FLUID PROCESSES IN SUBDUCTION ZONES: INSIGHTS FROM THE SIVRIHISAR (TURKEY) SUBDUCTION COMPLEX

A DISSERTATION
SUBMITTED TO THE FACULTY OF
UNIVERSITY OF MINNESOTA
BY

KATHERINE F. FORNASH

IN PARTIAL FULFILLMENT OF THE REQUIREMENTS
FOR THE DEGREE OF
DOCTOR OF PHILOSOPHY

DONNA L. WHITNEY, CHRISTIAN TEYSSIER, ADVISORS

AUGUST 2016

© KATHERINE F. FORNASH 2016

Table of Contents

Table of Contents……....i
List of Tables……....iv
List of Figures……vi
List of Supplementary Material……..ix

Chapter 1: Introduction……1
References…….……..…...8

Chapter 2: Tracking the timing of subduction and exhumation using $^{40}Ar/^{39}Ar$ phengite ages in blueschist- and eclogite-facies rocks (Sivrihisar, Turkey)……...13
Chapter Summary……..13
1. Introduction……....14
2. Geology of the Tavşanlı Zone……18
3. Age of HP metamorphism: results of previous geochronology……....20
4. Petrography and phengite composition……..21
4.1 Eclogite……22
4.2 Blueschist……....24
4.3 Quartzite……...26
5. *In situ* UV laser $^{40}Ar/^{39}Ar$ geochronology……27
5.1 *In situ* UV laser $^{40}Ar/^{39}Ar$ phengite geochronology methods……..27
5.2 Phengite $^{40}Ar/^{39}Ar$ geochronology results……...29
6. Discussion……..33
6.1 Evaluation of assumptions in $^{40}Ar/^{39}Ar$ age interpretation of Sivrihisar phengite……..34
6.1.1 Effects of contamination and mixed analyses……...38
6.1.2 Evaluation of ages with respect to phengite and bulk rock composition……40
6.1.3 Ages and structural position: effects of deformation……45
6.2 Timing of blueschist- and eclogite-facies metamorphism……...47
7. Conclusions……...52
References……....54
Tables……65
Figures……...72
Supplementary Material……87

Chapter 3: Lawsonite Composition and Zoning as an Archive of Metamorphic and Deformation Processes in Subduction Zones……...……...114
Chapter Summary……...……114

1.Introduction……...115
2. Regional Geology of the Tavşanlı Zone……..……117
2.1 Western Part of the Belt……..……...118
2.2 Eastern Part of the Belt……..……..……..119
3. Lawsonite in the Tavşanlı Zone…….……..…121
3.1 Lawsonite Eclogite…….……..……122
3.2 Lawsonite Blueschist……..……...125
3.3 Metasedimentary Rocks…….126
3.4 Lawsonite + Chlorite Rocks…….……127
3.5 Lawsonite-rich Veins and Layers……..128
4. Lawsonite Major and Trace Element Compositions and Zoning…….....128
4.1 Lawsonite Eclogite……..……..130
4.2 Lawsonite Blueschist……132
4.3 Metasedimentary Rocks……134
4.4 Lawsonite + Chlorite Rocks……..135
4.5 Lawsonite-rich Veins and Layers……..136
5. Lawsonite Crystallographic Orientation and Microstructures……137
5.1 EBSD Results……138
6. Discussion……140
6.1 Lawsonite Zoning Patterns……141
6.1.1 Core-to-rim Zoning……142
6.1.2 Oscillatory Zoning…….....146
6.1.3 Sector Zoning…….....148
6.1.4 Other Zoning……...150
6.2 Controls on Lawsonite Composition and its Variation…...……...151
7. Conclusions……..……...157
References…….……...159
Tables……...170
Figures……...……...179
Supplementary Material……...196

Chapter 4. Origin of Lawsonite-rich Veins and Layers in Eclogite and Blueschist, Sivrihisar Massif, Turkey……..197
Chapter Summary……197
1. Introduction……..198
2. Geology of the Sivrihisar Massif…….202
3. Methods……..……..204
3.1 Analysis of Whole-Rock and Mineral Compositions…….……...205
3.1.1 Bulk Rock Major and Trace Element Analysis…….……206
3.1.2 Mineral Major Element Analysis by Electron Microprobe……....206

3.1.3 Mineral Trace Element Analysis by LA-ICPMS……207
3.2 Microstructural Analysis of Lawsonite-rich Layer and Associated Host Rock……208
4. Petrography and Microstructures of the Lawsonite-rich Layer and Associated Host Rock……209
5. Bulk Rock and Mineral Composition……..212
5.1 Bulk Rock Major and Trace Element Analyses…….....212
5.2 Mineral Major and Trace Element Composition…….....215
5.2.1 Garnet……..……215
5.2.2 Clinopyroxene…….……218
5.2.3 Sodic Amphibole……...…….220
5.2.4 Lawsonite……221
5.2.5 Phengite……...…….....224
5.2.6 Rutile……...225
6. Discussion……226
6.1 Protolith……..……...227
6.2 Origin of the lawsonite-rich layer and associated glaucophane-rich margin……229
6.3 Fluid sources……..……236
7.Conclusions……...241
References……244
Tables……..……259
Figures……..……272
Supplementary Material……...…294

Chapter 5. Discussion…….……...299

Comprehensive Bibliography……...……303

List of Tables

Chapter 2: Tracking the timing of subduction and exhumation using $^{40}Ar/^{39}Ar$ phengite ages in blueschist- and eclogite-facies rocks (Sivrihisar, Turkey)

Table 2.1 Previous Geochronology in the Tavşanlı Zone……..……...65
Table 2.2 Representative major element compositions of phengite in eclogite and vein samples……...66
Table 2.3 Representative major element compositions of phengite in blueschist and quartzite samples……67
Table 2.4 *In situ* UV laser $^{40}Ar/^{39}Ar$ results……..68

Chapter 3: Lawsonite Composition and Zoning as an Archive of Metamorphic and Deformation Processes in Subduction Zones

Table 3.1 Representative major element compositions of lawsonite in lawsonite eclogite……...……..170
Table 3.2 Representative trace element compositions of lawsonite in lawsonite eclogite……...……..……171
Table 3.3 Representative trace element compositions of lawsonite in lawsonite blueschist……...……..……172
Table 3.4 Representative major element compositions of lawsonite in metasediments……..173
Table 3.5 Representative trace element compositions of lawsonite in metasediments……..174
Table 3.6 Representative major element compositions of lawsonite in lawsonite + chlorite rocks……...……...……..175
Table 3.7 Representative trace element compositions of lawsonite in lawsonite + chlorite rocks……...……...……..176
Table 3.8 Representative major element compositions of lawsonite in lawsonite-rich veins and layers……..……..177
Table 3.9 Representative trace element compositions of lawsonite in lawsonite-rich veins and layers……178

Chapter 4. Origin of Lawsonite-rich Veins and Layers in Eclogite and Blueschist, Sivrihisar Massif, Turkey

Table 4.1 Bulk rock major and trace element analyses……...259
Table 4.2 Representative major element compositions of garnet in eclogite core, eclogite margin, and glaucophane-rich margin…….……..……...260

Table 4.3 Representative major element compositions of garnet in lawsonite-rich layer……...……...261
Table 4.4 Representative trace element compositions of garnet……...……..262
Table 4.5 Representative major element compositions of omphacite……...……..263
Table 4.6 Representative trace element compositions of omphacite…..…..……..264
Table 4.7 Representative major element compositions of glaucophane.……..……..265
Table 4.8 Representative trace element compositions of glaucophane…...…….……..266
Table 4.9 Representative major element compositions of lawsonite……..267
Table 4.10 Representative trace element compositions of lawsonite……...……...268
Table 4.11 Representative major element compositions of phengite……...……...269
Table 4.12 Representative trace element compositions of phengite……....……..270
Table 4.13 Representative trace element compositions of rutile…..……..271

List of Figures

Chapter 2: Tracking the timing of subduction and exhumation using $^{40}Ar/^{39}Ar$ phengite ages in blueschist- and eclogite-facies rocks (Sivrihisar, Turkey)

Figure 2.1 Geologic Map of the Sivrihisar Massif, Tavşanlı Zone, Turkey and phengite sample locations……72
Figure 2.2 Overview of previous geochronologic estimates for the Tavşanlı Zone…….73
Figure 2.3 Photomicrographs of the lawsonite and epidote eclogite samples……..74
Figure 2.4 Plots of Si (p.f.u) vs. Altot (p.f.u) content of phengite in dated samples.....75
Figure 2.5 X-ray element maps of phengite in dated samples……..76
Figure 2.6 Photomicrographs of the vein and associated glaucophane-rich margin sample……77
Figure 2.7 Photomicrographs of the lawsonite blueschist samples……..78
Figure 2.8 Photomicrographs of the quartzite samples……79
Figure 2.9 Results of *in situ* UV laser $^{40}Ar/^{39}Ar$ geochronology for eclogite samples……...80
Figure 2.10 Results of *in situ* UV laser $^{40}Ar/^{39}Ar$ geochronology for lawsonite vein and associated glaucophane-rich margin sample……..81
Figure 2.11 Results of *in situ* UV laser $^{40}Ar/^{39}Ar$ geochronology for blueschist samples……...82
Figure 2.12 Results of *in situ* UV laser $^{40}Ar/^{39}Ar$ geochronology for quartzite Samples……..83
Figure 2.13 X-ray Computed Tomography imaging of rock chip used in *in situ* UV laser $^{40}Ar/^{39}Ar$ analysis……...84
Figure 2.14 Fe X-ray element maps of laser ablation pits in zoned phengite……...85
Figure 2.15 Relationship between $^{40}Ar/^{39}Ar$ age probability plot and structural position……...86

Chapter 3: Lawsonite Composition and Zoning as an Archive of Metamorphic and Deformation Processes in Subduction Zones

Figure 3.1 Distribution of lawsonite eclogite localities in the world……..179
Figure 3.2 Geologic Map of the Sivrihisar Massif, Tavşanlı Zone, Turkey and lawsonite sample locations……..180
Figure 3.3 Representative photomicrographs of metabasaltic samples…..…….....181
Figure 3.4 Representative photomicrographs of metasediment samples...……182
Figure 3.5 Field photographs and photomicrographs of lawsonite + chlorite rock

samples……..……...…183
Figure 3.6 Field photographs of lawsonite-rich vein and layer samples...…..……184
Figure 3.7 Representative Fe zoning in lawsonite…….……..…....185
Figure 3.8 REE patterns for lawsonite in lawsonite eclogite……...…….…….……186
Figure 3.9 REE patterns for lawsonite in lawsonite blueschist……..…...…...…..187
Figure 3.10 REE patterns for lawsonite in metasediments...……...…..……188
Figure 3.11 REE patterns for lawsonite in lawsonite + chlorite rocks……...…..……..189
Figure 3.12 REE patterns for lawsonite in lawsonite-rich veins and layers…...…….....190
Figure 3.13 Ti sector zoning in lawsonite……..…….…….....191
Figure 3.14 Relationship between Ti zoning and grain boundaries….……...192
Figure 3.15 Relationship between Ti and Fe zoning and subgrain boundaries……..193
Figure 3.16 Asymmetric Ti-rich overgrowth in lawsonite…….…194
Figure 3.17 Sr vs. Pb systematics in lawsonite……...……...195

Chapter 4. Origin of Lawsonite-rich Veins and Layers in Eclogite and Blueschist, Sivrihisar Massif, Turkey

Figure 4.1 Geologic Map of the Sivrihisar Massif, Tavşanlı Zone, Turkey and sample locations…….……..272
Figure 4.2 Field photographs of lawsonite-rich vein and layer samples…...…….273
Figure 4.3 Photomicrographs from the core of the lawsonite eclogite pod…….....274
Figure 4.4 X-ray Computed Tomography reconstruction of the lawsonite eclogite pod core and margin……...275
Figure 4.5 Photomicrographs from the margin of the lawsonite eclogite pod.……...276
Figure 4.6 Variation in bulk rock major and trace element concentrations along a pod transect……..……..277
Figure 4.7 Bulk rock chondrite- and N-MORB-normalized trace element diagrams……...278
Figure 4.8 Major and trace element zoning profiles for garnet in SV12-13E……....279
Figure 4.9 Major and trace element zoning profiles for garnet in SV03-103A……..…280
Figure 4.10 Major and trace element zoning profiles for garnet in SV03-103B……281
Figure 4.11 Variations in Cr and Zn content in garnet along a pod transect…….....282
Figure 4.12 Major and trace element zoning profiles for garnet in SV03-103C……283
Figure 4.13 Major and trace element zoning in omphacite……284
Figure 4.14 Major and trace element zoning in glaucophane…….……..……....285
Figure 4.15 Fe, Ti, and REE data for lawsonite in sample SV12-13E……...286
Figure 4.16 Fe, Ti, and REE data for lawsonite in sample SV03-103A……..……..…287
Figure 4.17 Fe, Ti, Cr, and REE data for lawsonite in sample SV03-103B…..……288
Figure 4.18 Fe, Ti, and REE data for lawsonite in sample SV03-103C…….……289

Figure 4.19 Variations in Pb, Cr, Sr, and V in lawsonite along a pod transect…..……290
Figure 4.20 Phengite zoning and trace element systematics……...291
Figure 4.21 Correlations between Zr content and Sn, Mn, Sb, V, W, and Hf content in rutile…….292
Figure 4.22 Plot of Nb (ppm) vs. Cr (ppm) content in rutile……..…293

List of Supplementary Material

Chapter 2: Tracking the timing of subduction and exhumation using $^{40}Ar/^{39}Ar$ phengite ages in blueschist- and eclogite-facies rocks (Sivrihisar, Turkey)

Supplementary Material 2.1 Sample locations……..87
Supplementary Material 2.2 X-Ray Computed Tomography (XRCT) Analytical Methods……..88
Supplementary Material 2.3 Reflected light images of analyzed phengite grains with their corresponding $^{40}Ar/^{39}Ar$ age…….89
Supplementary Material 2.4 ^{37}Ar and ^{39}Ar versus age plots for each sample……..105
Supplementary Material 2.5 36/40 vs. 39/40 plots for each sample…….109

Chapter 3: Lawsonite Composition and Zoning as an Archive of Metamorphic and Deformation Processes in Subduction Zones

Supplementary Material 3.1 Summary of sample locations and analytical methods...196

Chapter 4. Origin of Lawsonite-rich Veins and Layers in Eclogite and Blueschist, Sivrihisar Massif, Turkey

Supplementary Material 4.1 Sample locations…….294
Supplementary Material 4.2 XRCT scanning conditions…….295
Supplementary Material 4.3 Histograms of garnet volume (determined by XRCT)...297
Supplementary Material 4.4 Ni vs. Cr bulk rock systematics……..298

Chapter 1. Introduction

The subduction of hydrated oceanic lithosphere is accompanied by a series of dehydration reactions that transport and release significant quantities of fluids into the mantle. These fluids play a role in a number of fundamental geologic processes. Partial melting driven by fluid fluxing in the mantle has been invoked to explain the generation of arc magmas, with their distinctive enrichment in fluid mobile elements relative to high-field strength elements reflecting the addition of a subduction-related fluid to the overlying mantle wedge (McCulloch and Gamble 1991). The release of mineral bound H_2O during dehydration reactions has also been cited as potential trigger of intermediate-depth intraslab earthquakes (Kirby et al. 1996, Peacock 2001, Hacker et al. 2003, Abers et al. 2006) as well as episodic tremor and slip events (Obara 2002, Seno and Yamasaki 2003).

Despite the importance of fluids in subducted lithosphere, first-order questions remain about: (1) the depth(s) and nature (pulses vs. continuous) of fluid release, (2) the composition of the fluids, (3) the degree to which these fluids mobilize and redistribute particular groups/classes of elements (e.g., HFSE), (4) how these fluids migrate through the subducted slab to the slab-mantle interface, and (5) whether these fluids represent localized or large-scale transport.

Knowledge of fluid processes in modern subduction zones comes from inferences about subsurface processes based on constraints from numerical thermal models, laboratory experiments, geochemical studies of arc lavas, and geophysical imaging of active subduction zones. A complementary approach to understanding fluid and related

metamorphic and deformation processes in subduction zones is to study the record of fluid-rock interaction preserved in high-pressure (HP) and ultrahigh pressure rocks from exhumed subduction complexes. Evidence of fluid-rock interaction is present at all scales (μm-to-m) in exhumed subduction complexes and includes fluid inclusions, metamorphic veins consisting of HP minerals, metasomatic alteration rinds, hydrous mineral phases, and the presence of oscillatory zoning in minerals.

Although these features have been the focus of numerous geochemical, petrologic, isotopic, and field-based studies (Becker et al. 1999, Rubatto and Hermann 2003, Spandler and Hermann 2006, Gao et al. 2007, John et al. 2008, Beinlich et al. 2010, Spandler et al. 2011), our knowledge from the geologic record of metamorphic, deformation, and fluid processes operating in the deep forearc (> 30 km and <100 km) is limited by the fact that rocks that experienced high-pressure/low-temperature (HP/LT) conditions and that return from great depths relatively unaffected by lower pressure and/or higher temperature overprinting are rare; thus necessitating further studies in areas where rocks were exhumed from depths > 30 km and preserve their HP mineral assemblages and textures.

One place in the geologic record with exceptional preservation of HP/LT rocks, including lawsonite eclogite, is the Sivrihisar Massif, which is part of the Tavşanlı Zone HP/LT metamorphic belt exposed in northwest Turkey. The Sivrihisar Massif is an ideal place to examine the record of subduction processes preserved in high-pressure rocks from exhumed subduction complexes because in addition to being one of the largest and

best preserved HP/LT belts, it is also one of only ~19 known lawsonite eclogite localities in the world.

Although experimental studies and phase equilibria modeling predict that lawsonite should be stable at > 45 km depth in all but the hottest subduction zones (Schmidt and Poli 1994, Hacker et al. 2003), it is rarely exposed at the Earth's surface (Zack et al. 2004, Tsujimori et al. 2006, Whitney and Davis 2006, Tsujimori and Ernst 2014). Lawsonite, a Ca-Al-rich hydrous silicate that can hold up to 11.5 wt.% H_2O, is of critical importance to studies of fluid processes in subduction zones because it is likely the main hydrous phase at pressures exceeding 2.5 GPa. Lawsonite is also a significant reservoir for trace elements in high-pressure assemblages, particularly rare earth elements (REE), Sr, Pb, Th, and U (Tribuzio et al. 1996, Ueno 1999, Spandler et al. 2003, Mulcahy et al. 2009, Martin et al. 2011, 2014, Vitale Brovarone et al. 2014).

Of the ~ 19 known lawsonite eclogite localities, most occur as blocks in mélange (Altherr et al. 2004, Harlow et al. 2004), xenoliths (Usui et al. 2006), or as float (Zack et al. 2004). The Tavşanlı Zone is one of only a few lawsonite eclogite localities that occurs in a structurally coherent metabasaltic sequence that preserves contact relationships with its host rocks. It is also one of the deepest known lawsonite eclogite localities, recording maximum pressure conditions of 2.4 – 2.5 GPa (Davis and Whitney 2006, Whitney and Davis 2006).

The maximum P-T conditions recorded by the lawsonite eclogite (2.4 – 2.5 GPa, 550 °C; Davis and Whitney 2006) may also hold geodynamic significance because they correspond to the depths at which there is believed to be a slab-mantle coupling

transition. Heat flow observations from subduction zones show low heat flow in the fore-arc region and high heat flow in the arc to back-arc region. In order to reproduce these heat flow observations, most models have to impose a sharp transition from a decoupled to coupled slab-mantle interface at 70 – 80 km depth (Wada et al. 2008, Wada and Wang 2009, Syracuse et al. 2010). The mechanism responsible for this decoupling depth remains unknown, although it appears to be present in all subduction zones, regardless of their thermal state (Wada and Wang 2009), and corresponds to slab temperatures of ~ 550 ± 50 °C and pressures of 2.5 GPa (Syracuse et al. 2010). As the Sivrihisar lawsonite eclogites were metamorphosed at these P-T conditions, they may provide information about the nature of this transition and its implications for subduction and exhumation processes.

The high-pressure rocks of the Tavşanlı Zone therefore provide an accessible record of the complex geochemical, fluid, and deformation processes occurring at depths of 80 – 45 km in subduction zones. In this study, we present the results of a geochronologic (*in situ* UV laser $^{40}Ar/^{39}Ar$ phengite geochronology), geochemical (bulk rock and mineral major and trace element analysis), and microstructural (electron backscatter diffraction, X-ray computed tomography) study of the high-pressure rocks from the Sivrihisar Massif, Tavşanlı Zone, Turkey.

The second chapter, *Tracking the timing of subduction and exhumation using $^{40}Ar/^{39}Ar$ phengite ages in blueschist- and eclogite-facies rocks (Sivrihisar, Turkey)*, presents results from an *in situ* UV laser $^{40}Ar/^{39}Ar$ phengite geochronology study of a suite of lawsonite- blueschist and eclogite-facies rocks representing different protoliths

(metabasalt, metasediment), different structural levels (within and outside of a high strain zone) and different textural positions (eclogite pod core vs. eclogite pod margin) to (1) determine the timing of eclogite-facies metamorphism, (2) explore the age relationships of coexisting eclogite and blueschist, and (3) examine the effects of deformation, fluids, and protolith on $^{40}Ar/^{39}Ar$ systematics in HP/LT rocks, particularly in the context of previous results which documented large intra- and intersample age ranges (60 – 192 Ma). Results from this work suggest that peak, lawsonite eclogite-facies metamorphism occurred at 90 – 93 Ma, whereas retrograde metamorphism occurred at 82 ± 2 Ma. These ages are in agreement with existing geochronologic constraints in the region. Lawsonite blueschist and lawsonite-bearing quartzite layers record more variable $^{40}Ar/^{39}Ar$ ages that may reflect variations in deformation intensity, preservation of high-pressure mineral assemblages and fabrics, and/or the distribution of excess Ar.

The third chapter*, Lawsonite Composition and Zoning as an Archive of Metamorphic and Deformation Processes in Subduction Zones*, presents the results of a comprehensive geochemical (major and trace element) and microstructural (electron backscatter diffraction) study of lawsonite, with a focus on Sivrihisar lawsonite-bearing rocks. Although most studies of natural lawsonite have reported near end-member major element compositions, results from this study show that lawsonite can contain significant substitutions of FeO* (3 wt.%), TiO_2 (1 wt.%), and Cr_2O_3 (6 wt.%), and commonly displays zoning in these elements. Variations in the concentrations of these elements, as well as the types of zoning patterns displayed (oscillatory, sector, core-to-rim), are related to changes in the metamorphic assemblage and environment, as well as the

crystallographic orientation of the grain. In some cases, there is a correlation between intragrain variations in Fe and/or Ti content and microstructural features, such as subgrains or grain boundaries. These results indicate both crystallographic and environmental control on lawsonite composition and zoning. As similar zoning patterns have also been documented for the rare earth elements in lawsonite, these results also have implications for the interpretation and development of Lu-Hf lawsonite geochronology.

The fourth chapter, *Origin of Lawsonite-rich Veins and Layers in Eclogite and Blueschist, Sivrihisar Massif, Turkey*, presents a study of lawsonite-rich veins and layers from the Sivrihisar Massif, Turkey. Although lawsonite-rich veins and layers have been described in other HP/LT terranes, to date, no detailed study of their geochemistry or origins have been conducted. In this chapter, we present bulk rock major and trace element data for a monomineralic lawsonite vein from the margin of an epidote + chlorite-rich pod, as well as a detailed geochemical transect (bulk rock and mineral major and trace element) and X-ray Computed Tomography study of a lawsonite + garnet + phengite-rich layer associated with blueschist-facies assemblages and its lawsonite eclogite host rock to understand the petrogenesis of these volatile- and trace element-rich lawsonite layers and evaluate the significance (if any) of these layers for the eclogite-to-blueschist transition in the Sivrihisar Massif.

Together, these chapters provide insights into the timing of HP/LT metamorphic events in the Sivrihisar Massif, as well as evidence for possible fluid-rock interactions occurring between the interlayered lithologies of the massif (metasediments, mafic crust,

serpentinites) as documented by the zoning patterns, microstructures, and trace element geochemistry of lawsonite and lawsonite-bearing veins and layers.

REFERENCES

Abers GA, van Keken PE, Kneller EA, Ferris A, Stachnik JC (2006) The thermal structure of subduction zones constrained by seismic imaging: Implications for slab dehydration and wedge flow. Earth and Planetary Science Letters 241: 387 – 397.

Becker H, Jochum KP, Carlson RW (1999) Constraints from high-pressure veins in eclogites on the composition of hydrous fluids in subduction zones. Chemical Geology 160: 291 – 308.

Beinlich A, Klemd R, John T, Guo J (2010) Trace-element mobilization during Ca-metasomatism along a major fluid conduit: Eclogitization of blueschist as a consequence of fluid-rock interaction. Geochimica et Cosmochimica Acta 74: 1892 – 1922.

Davis PB, Whitney DL (2006) Petrogenesis of lawsonite and epidote eclogite and blueschist, Sivrihisar Massif, Turkey. Journal of Metamorphic Geology 24: 823 – 849.

Gao J, John T, Klemd R, Xiong X (2007) Mobilization of Ti-Nb-Ta during subduction: Evidence from rutile-bearing dehydration segregations and veins hosted in eclogite, Tianshan, NW China. Geochimica et Cosmochimica Acta 71: 4974 – 4996.

Hacker BR, Peacock SM, Abers GA, Holloway SD (2003) Subduction factory 2. Are intermediate-depth earthquakes in subducting slabs linked to metamorphic dehydration reactions? Journal of Geophysical Research 108: 1 – 16.

John T, Klemd R, Gao J, Garbe-Schonberg C-D (2008) Trace element mobilization in slabs due to non steady-state fluid-rock interaction: Constraints from an eclogite-facies transport vein in blueschist (Tianshan, China). Lithos 103: 1 – 24.

Kirby SH, Engdahl ER, Denlinger RP (1996) Intermediate-depth intraslab earthquakes and arc volcanism as physical expressions of crustal and uppermost mantle metamorphism in subducting slabs. In: Bebout, G.E., Scholl, D.W., Kirby, S.H., Platt, J.P. (Eds.), Subduction top to bottom. American Geophysical Union, Washington, pp. 195 – 214.

Martin LAJ, Rubatto D, Vitale Brovarone A, Hermann J (2011) Late Eocene lawsonite-eclogite facies metasomatism of a granulite sliver associated to ophiolites in Alpine Corsica. Lithos 125: 620 – 640.

Martin LAJ, Hermann J, Gauthiez-Putallaz L, Whitney DL, Vitale Brovarone A, Fornash KF, Evans NJ (2014) Lawsonite geochemistry and stability – implication for trace element and water cycles in subduction zones. Journal of Metamorphic Geology 32: 455 – 487.

McCulloch MT, Gamble JA (1991) Geochemical and geodynamical constraints on subduction zone magmatism. Earth and Planetary Science Letters 102: 358 – 374.

Mulcahy SR, King RL, Vervoort JD (2009) Lawsonite Lu-Hf geochronology: A new geochronometer for subduction zone processes. Geology 37: 987 – 990.

Obara, K (2002) Nonvolcanic deep tremor associated with subduction in southwest Japan. Science 296: 1679 – 1681.

Peacock SM (2001) Are the lower planes of double seismic zones caused by serpentinite dehydration in subducting oceanic mantle? Geology 29: 299 – 302.

Rubatto D, Hermann J (2003) Zircon formation during fluid circulation in eclogites (Monviso, Western Alps): implications for Zr and Hf budget in subduction zones. Geochimica et Cosmochimica Acta 67: 2173 – 2187.

Schmidt MW, Poli S (1994) The stability of lawsonite and zoisite at high pressures: Experiments in CASH to 92 kbar and implications for the presence of hydrous phases in subducted lithosphere. Earth and Planetary Science Letters 124: 105 – 118.

Seno T, Yamasaki T (2003) Low-frequency tremors, intraslab and interpolate earthquakes in Southwest Japan-from a viewpoint of slab dehydration. Geophysical Research Letters 30: doi: 10.1029/2003GL018349

Spandler C, Hermann J, Arculus R, Mavrogenes J (2003) Redistribution of trace elements during prograde metamorphism from lawsonite blueschist to eclogite facies; implications for deep subduction-zone processes. Contributions to Mineralogy and Petrology 146: 205 – 222.

Spandler C, Hermann J (2006) High-pressure veins in eclogite from New Caledonia and their significance for fluid migration in subduction zones. Lithos 89: 135 – 153.

Spandler C, Pettke T, Rubatto D (2011) Internal and External Fluid Sources for Eclogite-facies Veins in the Monviso Meta-ophiolite, Western Alps: Implications for Fluid Flow in Subduction Zones. Journal of Petrology 52: 1207 – 1236.

Syracuse EM, van Keken PE, Abers GA (2010) The global range of subduction zone thermal models. Physics of the Earth and Planetary Interiors 183: 73 – 90.

Tribuzio R, Messiga B, Vannucci R, Bottazzi P (1996) Rare earth element redistribution during high-pressure – low-temperature metamorphism in ophiolitic Fe-gabbros (Liguria, northwestern Italy): Implications for light REE mobility in subduction zones. Geology 24: 711 – 714.

Tsujimori T, Sisson VB, Liou JG, Harlow GE, Sorensen SS (2006) Very-low-temperature record of the subduction process: A review of worldwide lawsonite eclogites. Lithos 92: 609 – 624.

Tsujimori T, Ernst WG (2014) Lawsonite blueschists and lawsonite eclogites as proxies for palaeo-subduction zone processes: a review. Journal of Metamorphic Geology 32: 455 – 478.

Ueno T (1999) REE-bearing sector-zoned lawsonite in the Sanbagawa politic schists of the eastern Kii Peninsula, central Japan. European Journal of Mineralogy 11: 993 – 998.

Usui T, Nakamura E, and Helmstaedt H (2006) Petrology and geochemistry of eclogite xenoliths from the Colorado Plateau: implications for the evolution of subducted oceanic crust. Journal of Petrology 47: 929-964.

Vitale Brovarone A, Alard O, Beyssac O, Martin L, Picatto M (2014) Lawsonite metasomatism and trace element recycling in subduction zones. Journal of Metamorphic Geology 32: 489 –514.

Wada I, Wang K, He J, Hyndman RD (2008) Weakening of the subduction interface and its effects on surface heat flow, slab dehydration, and mantle wedge serpentinization. Journal of Geophysical Research 113: doi:10.1029/2007JB005190.

Wada I, Wang K (2009) Common depth of slab-mantle decoupling: Reconciling diversity and uniformity of subduction zones. Geochemistry Geophysics Geosystems 10: doi:10.1029/2009GC002570.

Whitney DL, Davis PB (2006) Why is lawsonite eclogite so rare? Metamorphism and preservation of lawsonite eclogite, Sivrihisar, Turkey. Geology 34: 473 – 476

Zack T, Rivers T, Brumm R, Kronz A (2004) Cold subduction of oceanic crust: Implications from a lawsonite eclogite from the Dominican Republic. European Journal of Mineralogy 16: 909 – 916.

Chapter 2: Tracking the timing of subduction and exhumation using $^{40}Ar/^{39}Ar$ phengite ages in blueschist and eclogite facies rocks (Sivrihisar, Turkey)

Katherine F. Fornash[1], Michael A. Cosca[2], Donna L. Whitney[1]

[1] Department of Earth Sciences, University of Minnesota, Minneapolis MN 55455 USA

[2] United States Geological Survey, Central Mineral and Environmental Resources Science Center, Box 25046, Denver Federal Center, MS-963, Denver, CO 80225 USA

Chapter Summary

Geochronologic studies of high-pressure/low-temperature (HP/LT) rocks can be used to determine the timing and rates of burial and exhumation in subduction zones by dating different stages of the pressure-temperature history. In this study, we present new *in situ* UV laser ablation $^{40}Ar/^{39}Ar$ phengite ages from a suite of lawsonite blueschist- and eclogite-facies rocks representing different protoliths (metabasalt, metasediment), different structural levels (within and outside of a high strain zone), and different textural positions (eclogite pod core vs. margin) to understand the timing of these events in an exhumed Neo-tethyan subduction zone (Sivrihisar Massif, Tavşanlı Zone, Turkey). Weighted mean *in situ* $^{40}Ar/^{39}Ar$ ages of phengite from the cores of lawsonite eclogite pods (90 – 93 Ma) are distinctly older than phengite from retrogressed, epidote eclogite (82 ± 2 Ma). These ages are interpreted as the age of peak and retrograde metamorphism, respectively. Eclogite records the narrowest range of ages (10 – 14 m.y.) of any rock type

analyzed. Transitional eclogite-blueschist facies assemblages and glaucophane-rimmed lawsonite + garnet + phengite veins from eclogite pod margins record a much wider age range of $^{40}Ar/^{39}Ar$ ages (~ 20 m.y.) with weighted mean ages of ~ 91 Ma. Blueschists and quartzites record more variable $^{40}Ar/^{39}Ar$ ages that may in part be related to structural position: samples within a high-strain zone at the tectonic contact of the HP rocks with a meta-ultramafic unit have *in situ* UV laser ablation $^{40}Ar/^{39}Ar$ ages of 84.0 ± 1.3 – 103.7 ± 3.1 Ma, whereas samples outside this zone range to older ages (84.6 ± 2.4 – 116.7 ± 2.7 Ma) and record a greater age range (22 – 38 m.y.). The phengite ages can be correlated with the preservation of HP mineral assemblages and fabrics as well as the effects of deformation. Collectively, these results show that high spatial resolution UV laser ablation $^{40}Ar/^{39}Ar$ phengite data, when considered in a petrologic and structural context, may document prograde (burial) and retrograde (exhumation) stages of subduction metamorphism.

1. Introduction

White mica $^{40}Ar/^{39}Ar$ geochronology has been widely used to determine the timing of metamorphism in exhumed subduction complexes (e.g., Arnaud and Kelley 1995; Ruffet et al. 1995, 1997; Sherlock et al. 1999; Agard et al. 2002; Gray et al. 2004; Federico et al. 2005; Putlitz et al. 2005). This method is well suited to dating high-pressure/low-temperature (HP/LT) rocks because of the relatively low temperatures (<600 °C) of peak metamorphism and the common occurrence of white mica as a phase in subduction zone lithologies (blueschist- and eclogite-facies metasediments, metabasalts). Furthermore, white mica may grow or recrystallize during prograde, peak,

and/or retrograde parts of the pressure-temperature path, offering tremendous potential for recording different stages of subduction metamorphism and exhumation.

Linking $^{40}Ar/^{39}Ar$ white mica ages to subduction processes, however, is challenging because $^{40}Ar/^{39}Ar$ geochronology of HP/LT and ultrahigh-pressure (UHP) terranes commonly yield a large range of inter- and/or intrasample ages (Sherlock et al. 1999; Giorgis et al. 2000; Sherlock and Kelley 2002; Putlitz et al. 2005; Beltrando et al. 2009, 2013; Warren et al. 2011, 2012; Bröcker et al. 2013). In some instances, these variations have been attributed to analytical artifacts, such as contamination owing to the ablation of adjacent K-poor minerals or inclusions, the presence of excess argon, and/or factors related to the intrinsic properties of the rock (bulk rock composition, permeability) or mineral (Scaillet et al. 1992; Li et al. 1994; Arnaud and Kelley 1995; Dahl 1996; Scaillet 1996; Reddy et al. 1999; Sherlock et al. 1999; Giorgis et al. 2000; Baxter et al. 2002; Cosca et al. 2005; Warren et al. 2012). In other instances, however, these age variations have been used to infer the timing, duration and rates of processes associated with subduction metamorphism.

Putlitz et al. (2005), for example, used the apparent textural equilibrium between phengite and other HP phases, as well as the preservation of growth zoning in phengite, to argue that the *in situ* UV laser ablation $^{40}Ar/^{39}Ar$ age spreads of ~ 10 m.y. from an eclogite and omphacite-rich metagabbro from Syros (Cycladic Islands, Greece) recorded mica formation and growth on the prograde path, thus documenting the duration of prograde metamorphism. $^{40}Ar/^{39}Ar$ phengite age variations of 10 – 14 m.y. from elsewhere in the Cycladic belt (Bröcker et al. 2013) and in the Western Alps (Halama et

al. 2014) have also been attributed to extended periods of mica (re)crystallization and/or resetting along specific portions of the P-T path. In the latter study, *in situ* UV laser ablation $^{40}Ar/^{39}Ar$ geochronology was coupled with *in situ* boron isotope and lithium and boron trace element analyses to show that periods of phengite crystallization were linked to episodes of fluid-rock interaction. Other studies have taken advantage of the fact that white mica (phengite) is a common fabric-forming mineral in metamorphic rocks and applied *in situ* laser ablation and/or step-heating $^{40}Ar/^{39}Ar$ geochronology techniques to phengite from specific fabrics or microstructural sites to relate variations in $^{40}Ar/^{39}Ar$ age to different (P-T)-deformation events (Agard et al. 2002; Gray et al. 2004; Beltrando et al. 2009).

Measured $^{40}Ar/^{39}Ar$ age variations in a sample or terrane can therefore provide useful information about its metamorphic history and associated processes if the factors resulting in the variation can be determined. Understanding these factors requires high-precision and high-spatial resolution $^{40}Ar/^{39}Ar$ data combined with systematic petrologic and structural characterization of the dated crystals and host rocks. The relatively recent availability of high sensitivity and low volume commercial gas source mass spectrometers equipped with stable electronics and ion counting capability provides a means to acquire precise data, including the accurate determination of non-radiogenic argon isotopes (e.g. ^{36}Ar), from small sample volumes. The advent of these capabilities, combined with the ability to target specific microchemical and microstructural domains at both the grain- and sample-scale using high-spatial resolution laser ablation techniques

may assist in interpreting the geological significance of phengite $^{40}Ar/^{39}Ar$ data from HP/LT rocks.

In this study, we present new high-precision and high-spatial resolution *in situ* UV laser ablation $^{40}Ar/^{39}Ar$ ages for phengite in a suite of blueschist- and eclogite-facies metabasaltic and metasedimentary rocks from the Sivrihisar region of the Tavşanlı Zone HP/LT terrane, Turkey (Figure 1). Sivrihisar blueschists and eclogites have been well studied for P-T conditions of metamorphism and deformation (e.g., Davis and Whitney 2006, 2008; Whitney and Davis 2006; Çetinkaplan et al. 2008; Teyssier et al. 2010; Davis 2011; Whitney et al. 2014), as have blueschist facies rocks in the rest of the Tavşanlı Zone (e.g., Okay and Kelley 1994; Okay 2002; Plunder et al. 2013, 2015). The timing of HP/LT metamorphic events, however, is somewhat uncertain because geochronologic studies of the Tavşanlı blueschists have yielded a wide range of ages (60 – 192 Ma; Table 1, Figure 2) and the timing of eclogite metamorphism has not been well studied.

As the Sivrihisar region is the only locality in the Tavşanlı Zone to preserve eclogite, this site offers an excellent opportunity to determine the timing of the maximum pressure recorded by HP/LT rocks in the region and to explore the age, petrologic, and tectonic relationships of coexisting eclogite and blueschist. In addition to addressing outstanding questions about the timing of regional metamorphic and tectonic events, the results from this study also provide insight into the combined effects of deformation, fluids, and protolith on $^{40}Ar/^{39}Ar$ systematics in HP/LT rocks.

2. Geology of the Tavşanlı Zone

The Tavşanlı Zone is a Late Cretaceous subduction complex formed during closure of the Neo-Tethys ocean (Okay 1980, 1984, 1986). It is bordered on its northern margin by the Izmir-Ankara-Erzincan suture, the main Neo-Tethyan suture, where it is exposed as a 50-km wide and >350-km long structurally coherent blueschist (and, locally, eclogite) facies belt (Figure 1). The belt is composed of a blueschist facies sequence overlain by an accretionary complex and large ophiolite slabs (Okay et al. 1998; Okay and Whitney 2010). Undeformed Eocene granitoids (~48 – 53 Ma; Harris et al. 1994; Okay et al. 1998; Sherlock et al. 1999) locally intruded the HP/LT sequence and the overlying ophiolite at shallow crustal levels.

The degree to which HP mineral assemblages and peak metamorphic conditions are preserved varies along the belt. Maximum recorded P-T conditions were 430 °C (Okay and Kelley 1994; Okay 2002) to 470 – 550 °C (Plunder et al. 2013) at ~ 2.4 GPa in the blueschist facies rocks of the western Tavşanlı Zone, and ~ 550 °C at ~2.4 ± 0.1 GPa in the lawsonite eclogite facies rocks of the Sivrihisar Massif (Figure 1) (Davis and Whitney 2006, 2008).

The Sivrihisar Massif is the only site in the Tavşanlı Zone in which eclogite facies rocks are preserved (Kulaksız 1978; Gautier 1984; Whitney 2002; Davis and Whitney 2006, 2008; Whitney and Davis 2006; Çetinkaplan et al. 2008; Seaton et al. 2009, 2014; Whitney et al. 2011; 2014) (Figure 1). The massif consists of interlayered mica schist and marble with a structural thickness > 3 km (Sivrihisar Formation), overlain (possibly tectonically) by a series of metabasite, metachert (quartzite), and marble (Halilbağı

Formation) (Okay and Whitney 2010). The Halilbağı Formation, which is the focus of this study, has well-preserved lawsonite eclogite- and blueschist-facies mineral assemblages in both the metabasaltic and metasedimentary units, making it an excellent location for investigating the timing of blueschist- and eclogite-facies metamorphism and evaluating the compositional and textural record of these events in rocks with different protoliths (quartzite, metabasalt).

The Halilbağı Formation consists of meter to kilometer scale metasedimentary units interlayered with blueschist containing eclogite layers and pods (Figure 1). Metasedimentary rock types include marble, calc-silicate, mica schist, and quartzite. Locally, these rocks contain HP minerals such as lawsonite, sodic amphibole (primarily glaucophane), sodic pyroxene (primarily omphacite), garnet, and phengitic white mica, and in quartzite also piemontite (Mn-rich epidote). Marble also contains calcite pseudomorphs after aragonite (Davis and Whitney 2006; Seaton et al. 2009; Whitney et al. 2014).

The northern margin of the HP terrane is a ~200 m thick high-strain (mylonite) zone that developed at high-pressure conditions (lawsonite, glaucophane, and omphacite were stable during deformation) and is in fault contact with a metamorphosed ultramafic and mafic complex to the north (Teyssier et al. 2010; Whitney et al. 2014). Within a few hundred meters of the northern margin of the HP/LT unit, antigorite serpentinite occurs as meter-scale lenses within the blueschist- and eclogite-facies rocks (Figure 1). These lenses are surrounded by metasomatic zones consisting of lawsonite + chlorite ± garnet (Zack 2013, Whitney et al. 2014).

3. Age of HP metamorphism: Results of previous geochronology

Previous attempts to determine the timing of high-pressure metamorphism in the Tavşanlı Zone have largely focused on the blueschist-facies metasedimentary rocks in the western portion of the belt, and have yielded a wide range of results: 60 – 192 Ma (Table 1, Figure 2). Despite this range of ages, there is consensus that HP metamorphism was Late Cretaceous; ages between 80 – 88 Ma have been obtained from blueschists throughout the Tavşanlı Zone using a variety of techniques (Okay and Kelley 1994; Okay et al. 1998; Sherlock et al. 1999; Seaton et al. 2009; 2014; Mulcahy et al. 2014), and an age of 91.1 ± 1.3 Ma was obtained from a lawsonite eclogite in the Sivrihisar Massif (Lu-Hf garnet-lawsonite-whole rock isochron; Mulcahy et al. 2014).

In the Tavşanlı Zone, the geologic significance (if any) of $^{40}Ar/^{39}Ar$ white mica ages older than 80 – 88 Ma is uncertain. Sherlock et al. (1999) interpreted older $^{40}Ar/^{39}Ar$ ages as resulting from the incorporation of excess Ar based on the fact that Rb-Sr ages (with higher nominal closure temperatures for radiogenic Sr) from the same samples were younger (Table 1, Figure 2). This observation, combined with the spatial distribution of $^{40}Ar/^{39}Ar$ ages within phengite grains (younger ages in the cores, older ages near the rims), and the presence of radiogenic argon in K-free minerals such as lawsonite and quartz (Sherlock et al. 1999; Sherlock and Kelley 2002), further supported their interpretation.

Owing to uncertainty about the age of peak HP metamorphism (blueschist vs. eclogite) and the geologic significance of $^{40}Ar/^{39}Ar$ ages >88 Ma, we conducted *in situ*

UV laser ablation $^{40}Ar/^{39}Ar$ geochronology of phengite in petrographically- and structurally-controlled samples of blueschist- and eclogite- facies rocks (metabasalt and quartzite) from the Sivrihisar Massif using a new generation of multi-collector mass spectrometer.

4. Petrography and Phengite Composition

To assess the distribution and significance of $^{40}Ar/^{39}Ar$ phengite ages in the HP rocks of the Halilbağı unit, we analyzed phengite grains in lawsonite eclogite- and blueschist-facies rocks from different structural positions and protoliths, and with different phengite textures and coexisting mineral assemblages. To guide decisions during *in situ* laser ablation $^{40}Ar/^{39}Ar$ analyses, petrographic observations and electron microprobe analyses of polished thin sections (derived from the opposite face of the rock chip used for $^{40}Ar/^{39}Ar$ dating) were carried out prior to $^{40}Ar/^{39}Ar$ analyses to determine if the phengite grains were compositionally zoned and/or if multiple phengite populations were present in the sample.

Phengite compositions were determined with a JEOL JXA-8900 electron microprobe in the Department of Earth Sciences at the University of Minnesota (Tables 2, 3). Quantitative microprobe analyses (wavelength dispersive spectroscopy) were performed with a 15-kV accelerating voltage, 15 nA beam current, and a defocused 5 μm beam diameter to minimize Na and K loss and beam damage to minerals. Natural mineral standards were used in calibrations. O and OH were calculated by cation stoichiometry and included in the ZAF matrix corrections. Qualitative (energy-dispersive spectroscopy)

element maps were acquired using a 15 kV accelerating voltage, 100 nA beam current, a focused beam, and stage-rastering step sizes ranging from 1 to 3 μm depending on grain size.

4.1 Eclogite

A lawsonite eclogite (SV12-13E) and a lawsonite + phengite + garnet vein (SV03-103) were sampled from a 1.25 m x 0.7 m eclogite pod hosted within calc-silicate schist near the village of Halilbağı (Figure 1c). This eclogite pod was the subject of a previous petrologic and microstructural study ("composite pod" of Davis and Whitney 2008). The lawsonite eclogite sample was collected from the core of the pod, and the lawsonite-rich vein (with its 3 mm-thick glaucophane-rich reaction zone) was collected from the lithologically complex margin of the pod. The pod margin consists of finely interlayered (cm-scale) lawsonite eclogite and blueschist assemblages in which glaucophane has partially replaced omphacite (Davis and Whitney 2008).

Lawsonite eclogite sample SV12-13E is composed of omphacite, garnet, lawsonite, phengite, texturally late glaucophane, minor amounts of epidote, and accessory florencite, zircon and rutile (in some cases rimmed by titanite) (Figure 3). Phengite occurs as individual grains in the matrix, as well as larger, elongate aggregates that are aligned with omphacite and define the foliation (Figure 3). Phengite crystals are 0.5 to 1.0 mm long, with straight grain boundaries and no evidence of strain. Slight compositional zoning can be detected in backscattered electron (BSE) images; X-ray element maps confirm variations in Si and Fe (Figure 4, 5). Within individual phengite grains, Si contents range from 3.45 – 3.52 p.f.u., although some phengite inclusions in

garnet have higher Si contents (~3.67 p.f.u.) (Table 2). Zircon and epidote commonly occur as inclusions in phengite.

The lawsonite-rich vein (SV03-103) consists of lawsonite, phengite, and garnet, with minor amounts of allanite (rimmed by epidote) and accessory zircon and rutile (Figure 6). Phengite is zoned: cores are Na-rich (~ 1 wt. %), Ti-rich (~0.5 wt. %), and Fe-poor (~2.4 wt. %) compared to rims (Na_2O: ~0.10 – 0.15 wt. %, TiO_2: ~0.10 – 0.20 wt. %, FeO*: ~3.5 wt. %). Vein phengite shows a core-to-rim increase in Si content, from 3.22 – 3.32 Si p.f.u. in the cores to 3.38 – 3.50 near the rims (Table 2, Figure 4, 5). The glaucophane-rich margin of the lawsonite vein consists of glaucophane, garnet, lawsonite, minor amounts of phengite and allanite, and accessory rutile (Figure 6). Phengite in this region is compositionally similar to the rims of phengite in the vein, and contains rutile inclusions.

Eclogite SV12-10B is composed of omphacite, garnet, phengite, talc, chlorite, minor lawsonite, and accessory rutile and apatite. It has a strong lineation and foliation defined by elongate omphacite (0.5 mm long) and phengite (Figure 3). Phengite is coarse-grained (0.5 – 1.5 mm in length), undeformed, and occurs as individual grains in the matrix and as intergrowths with talc (Mg# = 0.87) in pressure shadows surrounding ~ 1 – 2.5 mm diameter garnet porphyroblasts. Texturally, phengite appears to be in equilibrium with the peak eclogite facies assemblage. Similar to phengite in the lawsonite-garnet-phengite vein (SV03-103), phengite in this sample is strongly zoned, with Na-rich, Ti-rich, and Fe-poor cores relative to rims (Figure 4, 5). In some phengite, this zoning is truncated at the grain boundary (Figure 5).

An epidote eclogite (SV12-15A) was collected from a metabasaltic pod hosted in calc-silicate schist, 22 m SE of the lawsonite eclogite pod from which samples SV12-13E and SV03-103 were collected (Figure 1). The epidote eclogite consists of omphacite, garnet, epidote, phengite, chlorite, and accessory apatite, zircon and rutile (rimmed by titanite). In contrast to the other eclogite samples, which have a strong lineation and foliation, this eclogite has a massive texture (Figure 3). Phengite occurs as large, radiating clusters (~ 600 μm x 400 μm) or as individual grains (0.5 mm long) dispersed throughout the omphacite- and epidote-rich matrix. Some individual phengite grains are inclusion-rich with irregular grain boundaries and some are inclusion-poor with generally straight grain boundaries, although these textural features do not correspond to changes in phengite composition or zoning patterns. Phengite in the epidote eclogite has Si contents of 3.35 – 3.46 (Table 2).

4.2 Blueschist

Three lawsonite blueschists were sampled near the villages of Halilbağı and İkipınar (Figure 1b, c). The two blueschists (SV13-06B, SV13-15) located near the village of Halilbağı were collected at different distances from the northern tectonic contact to investigate the potential effects of structural position and deformation intensity on $^{40}Ar/^{39}Ar$ ages (Figure 1c). The lawsonite blueschist (SV12-59) sample collected near the village of İkipınar, ~8 km NW of Halilbağı (Figure 1b), was selected to compare blueschists from different regions along strike in the HP unit.

Halilbağı lawsonite garnet blueschist SV13-06B is composed of glaucophane, garnet, lawsonite, phengite, omphacite, quartz, chlorite, minor allanite, and accessory Fe-

oxides, zircon, and rutile rimmed with titanite (Figure 7). This blueschist was collected ~ 215 m from the northern tectonic boundary (Figure 1c). Phengite in this sample occurs as bundles or layers that are generally parallel to the dominant foliation, although locally these layers are bent around lawsonite and garnet porphyroblasts. Phengite displays only minor variations in Si content (3.43 – 3.47 p.f.u) and Mg# (0.62 – 0.65) (Table 3, Figure 4).

Halilbağı lawsonite blueschist sample SV13-15 is composed of glaucophane, lawsonite, phengite, and accessory titanite and zircon (Figure 7). This blueschist was collected ~ 120 m from the northern tectonic boundary (Figure 1b). Phengite is sparse in this sample and occurs intergrown with glaucophane (in pressure shadows surrounding the large lawsonite porphyroblasts, Fig. 7d), or in lawsonite + phengite-rich layers that are parallel to the dominant foliation. Phengite in this sample has minor Fe zoning at the rims (Figure 5) and contains the highest Si content of any sample analyzed in this study (3.49 – 3.72 Si p.f.u.). The phengite grains with the highest Si content (> 3.55 Si p.f.u.) have Mg# > 0.70 (Table 3).

İkipınar lawsonite garnet blueschist sample SV12-59 consists of glaucophane, garnet, lawsonite, phengite, and accessory Fe-oxides, titanite, and zircon (Figure 7). Phengite occurs as slightly elongate clusters (~ 1 – 1.5 mm in length) spread throughout the matrix and intergrown with lawsonite and glaucophane, and in some cases, as small individual grains flanking the margins of lawsonite and garnet porphyroblasts. Phengite is deformed and displays undulatory extinction as well as kink bands. Si content is 3.53 – 3.56 p.f.u. (Table 3).

4.3 Quartzite

The two quartzite samples chosen for study were selected from the same structural levels as the two blueschist samples from Halilbağı to compare the $^{40}Ar/^{39}Ar$ phengite ages for rocks with different protoliths (metasediment vs. metabasalt). Sample SV10-06 was collected ~220 meters from the northern tectonic boundary at the same structural level as blueschist SV13-06B; quartzite sample SV10-08 was collected 70 meters away from the tectonic boundary, close to the structural level of blueschist sample ~SV13-15 (Figure 1c).

Quartzite SV10-06 consists of quartz, phengite, sodic amphibole, sodic pyroxene, lawsonite, garnet, piemontite, and accessory Fe-oxides. Phengite occurs in layers (0.5 mm thick) and as elongate, single grains or small clusters dispersed throughout the quartz matrix (Figure 8). High-pressure minerals are abundant, and occur throughout the quartz matrix, as well as in phengite-rich layers. The Mg# of phengite in this sample is the lowest of any sample analyzed (Table 3). Intragrain variations in Mg# range between 0.56 – 0.66 and intragrain variations in Si content ranges between 3.37 – 3.50 p.f.u. There is no significant difference between the compositions of phengite that occurs in layers versus as single grains (Table 3). There is also no difference in the compositional zoning patterns of phengite that occurs in layers versus as single grains; all phengite grains have slightly Na- and Fe-richer core regions (Figure 5).

Quartzite sample SV10-08 consists of quartz, phengite, sodic amphibole, lawsonite, garnet, and accessory Fe-oxides. Similar to quartzite SV10-06, phengite in this sample occurs both as phengite-rich layers and individual phengite grains, although the

grain size in this sample is smaller than in SV10-06 (Figure 8), consistent with the location of this quartzite in the high-strain zone. The smaller, individual phengite grains tend to be concentrated in domains of recrystallized quartz aggregates. High-pressure minerals in this sample also tend to be finer-grained and less abundant than in SV10-06, and they are mostly found in phengite-rich layers. Phengite in this sample is unzoned, and intragrain variations in Si content range between 3.48 – 3.55 p.f.u.

In addition to representing different structural levels and protoliths, these two quartzite samples were also selected because they preserve different quartz crystallographic fabrics. Sample SV10-06 records a quartz c-axis pattern that is consistent with rhomb<a> slip, whereas sample SV10-08 records basal<a> slip (Whitney et al. 2014). This has been interpreted to indicate a fabric transition during exhumation from higher pressure (possibly eclogite facies) to lower pressures (possibly blueschist facies) (Whitney et al. 2014); a hypothesis that can be tested, in part, by dating the phengite from these samples.

5. *In situ* UV Laser Ablation $^{40}Ar/^{39}Ar$ Geochronology

5.1 In situ UV Laser $^{40}Ar/^{39}Ar$ Phengite Geochronology Methods

A rock chip approximately 0.5 x 1 x 1 cm in dimensions was prepared from each sample, and one side of the chip was polished to 1 μm roughness for *in situ* UV laser ablation $^{40}Ar/^{39}Ar$ geochronology. Analyses were conducted in two analytical sessions (March 2013 and June 2014) in the $^{40}Ar/^{39}Ar$ laboratory at the USGS in Denver, CO, USA, with sample SV03-103 serving as an internal standard between the two sessions. Each rock chip and standards of Fish Canyon sanidine (Kuiper et al. 2008) with an age of

28.201 ± 0.023 (1σ) were packaged and irradiated for 11 and 32.65 hours, respectively, in the central thimble position of the USGS TRIGA reactor in Denver, CO, USA using cadmium shielding to minimize any nucleogenic ^{40}Ar production from ^{40}K.

Analyses were conducted with an ArF exciplex laser (193 nm) operating at conditions of 20 Hz, with a spot diameter of 48 μm and a continuous duration of ablation for 120 seconds to extract gas from the samples. Blanks varied little throughout the $^{40}Ar/^{39}Ar$ experiments, and were run at the start of every session and after every 4 – 5 unknowns; representative blanks from each analytical session are reported in Table 4. Data were collected by ion counting and peak hopping on a Thermo Scientific ARGUS VI. Data were corrected for blanks, mass discrimination (= 0.9942 ± 0.0013 per dalton), and nucleogenic isotopic interferences from irradiated CaF_2 and zero age K-glass. Typical values (and uncertainties) were measured as follows: ($^{36}Ar/^{37}Ar$)Ca = 2.673e-4 ± 1.27e-6, ($^{39}Ar/^{37}Ar$)Ca = 9.37e-4 ± 4.6e-6, ($^{38}Ar/^{39}Ar$)K = 1.29e-2 ± 2.6e-4, and ($^{40}Ar/^{39}Ar$)K = not detected. Non-radiogenic argon was corrected to an atmospheric value of 298.56 ± 0.31 (Lee et al. 2006), and ages were calculated using the decay constants in Min et al. (2000).

Following the $^{40}Ar/^{39}Ar$ analyses, rock chips were imaged using the electron microprobe in the Department of Earth Sciences at the University of Minnesota to (1) verify (in two dimensions) that all analyses were conducted entirely within white mica grains, and (2) locate the position of the ablation pits relative to any compositional zoning features to evaluate possible correlations between $^{40}Ar/^{39}Ar$ age and phengite composition. One rock chip, from epidote eclogite sample SV12-15A, was also imaged

using X-ray Computed Tomography (XRCT) to determine the depth and geometry of the ablation pits and to evaluate whether any analysis pits intersected another phase at depth or occurred entirely within phengite. The rock chip was scanned at the University of Minnesota XRCT Laboratory in the Department of Earth Sciences using an accelerating voltage of 110 kV and a current of 250 μA. Data were reconstructed to a voxel size of 2.93 μm. Additional details about the analytical conditions are supplied in Supplementary Material 2.

5.2 Phengite $^{40}Ar/^{39}Ar$ Geochronology Results

In situ UV laser ablation $^{40}Ar/^{39}Ar$ phengite ages were obtained for 9 samples (Table 4). Here, and elsewhere throughout the text, ages from individual analysis pits are reported at the 1-sigma error level and, for samples yielding a single age mode, the mean weighted ages for individual samples are reported at the 2-sigma error level. Age probability plots for each sample (Figures 9 – 12) highlight the spread and distribution of ages from each sample, although we caution that no statistical or geologic significance is inferred from the individual age modes.

For most samples, 12 individual $^{40}Ar/^{39}Ar$ analyses were determined from circular analysis pits (48 μm diameter) ablated in a total of 3 – 5 grains, yielding ~2 – 4 analyses per grain (depending on phengite grain size). In samples that displayed complex lithologic layering (vein sample SV03-103), or evidence for multiple age populations after 12 analyses had been conducted (samples SV10-06, SV13-06B), additional $^{40}Ar/^{39}Ar$ analyses were performed. For samples containing coarse-grained phengite (> 150 μm), UV laser ablation pits were spaced across the grains to determine whether there

were any spatially correlated intragrain variations in $^{40}Ar/^{39}Ar$ age, as had been previously suggested in other geochronologic studies of phengite from the Tavşanlı Zone (Sherlock et al. 1999; Sherlock and Kelley 2002). Reflected light images for all spot analyses, along with their corresponding $^{40}Ar/^{39}Ar$ phengite ages, are presented in Supplementary Material 3.

In situ UV laser ablation $^{40}Ar/^{39}Ar$ ages from individual analysis pits in lawsonite eclogite SV12-13E range from 87.7 ± 2.5 Ma to 99.8 ± 3.7 Ma, yielding a mean weighted age of 93.0 ± 1.8 Ma (n = 12, MSWD = 1.70, p = 0.075; Figure 9). These ages overlap with a Lu-Hf isochron (garnet-lawsonite-whole rock) age of 91.1 ± 1.3 Ma Mulcahy et al. (2014) obtained for the same lawsonite eclogite, which we provided to Mulcahy et al. for their analysis. Despite an overall range in $^{40}Ar/^{39}Ar$ phengite ages of ~12 m.y. in the sample, there is no clear correlation between age and the location of individual ablation pits relative to phengite grain boundaries; all intragrain $^{40}Ar/^{39}Ar$ age variations are within error of each other (Figure 9a). Instead, the ~12 m.y. age range records intergrain age variations, with some grains yielding ages between 90.2 ± 2.8 – 90.7 ± 3.0 Ma and others yielding ages between 99.5 ± 3.2 – 99.7 ± 3.7 Ma.

In situ UV laser ablation $^{40}Ar/^{39}Ar$ ages of phengite in the talc-bearing lawsonite eclogite (SV12-10B) range from 84.5 ± 2.3 Ma to 95.4 ± 3.0 Ma, yielding a mean weighted age of 90.2 ± 1.4 Ma (n = 12, MSWD = 1.60, p = 0.092; Figure 9). Twelve analyses were conducted across four grains: 3 phengite grains in the matrix, and 1 phengite grain, intergrown with talc, in a pressure shadow surrounding a garnet porphyroblast. Analyses from phengite in the pressure shadow yield a consistent set of

$^{40}Ar/^{39}Ar$ ages ranging from 84.5 ± 2.3 Ma – 87.6 ± 2.3 Ma. Six analyses conducted across a coarse-grained phengite grain in the matrix showed core-to-rim age differences, with younger $^{40}Ar/^{39}Ar$ ages in the core (87.6 ± 2.4 Ma, 89.9 ± 2.2 Ma) and older $^{40}Ar/^{39}Ar$ ages in the rim (91.1 ± 2.5 Ma – 95.4 ± 3.0 Ma).

In situ UV laser ablation $^{40}Ar/^{39}Ar$ ages of phengite in the epidote eclogite (SV12-15A) range from 75.0 ± 3.9 Ma to 89.4 ± 5.0 Ma, yielding a mean weighted age of 81.8 ± 2.2 Ma (n = 11, MSWD = 1.4, p = 0.18; Figure 9). The radiogenic argon ($^{40}Ar^*$) signals for this sample were lower than in most other samples, so in addition to the 9 analysis pits ablated, two oblong trenches (~ 48 x 400 μm) were also ablated to try to obtain higher $^{40}Ar^*$ signals. No variation was observed between ages obtained from the trenches and ages obtained from individual analysis pits. One phengite grain (Supplementary Material 3) yielded a younger $^{40}Ar/^{39}Ar$ age in the core (75.0 ± 3.9 Ma), and older $^{40}Ar/^{39}Ar$ ages near the rim (87.4 ± 4.7 Ma, 86.6 ± 4.9 Ma), but with the exception of this grain there are no clear relationships between age and position of the ablation pit. All grains yielded a consistent set of $^{40}Ar/^{39}Ar$ ages that are within error of each other.

In situ UV laser ablation $^{40}Ar/^{39}Ar$ ages from the lawsonite vein sample (SV03-103) generally range from 81.2 ± 2.9 Ma to 103.3 ± 4.5 Ma (n = 34; Figure 10). A $^{40}Ar/^{39}Ar$ age of 127.1 ± 2.6 Ma was obtained from one analysis spot of phengite in the lawsonite-rich vein. With the exception of this one older $^{40}Ar/^{39}Ar$ age, similar age ranges are seen in phengite from both within the vein (86.1 ± 3.7 Ma – 102.8 ± 3.9 Ma) and in the adjacent glaucophane-rich margin (81.2 ± 2.9 Ma – 103.3 ± 4.5 Ma) (Figure 10). Because the vein phengite occurs in a phengite-rich domain, and not as discrete grains in

a matrix, it is difficult to identify clear grain boundaries in reflected light and backscattered electron (BSE) images, and therefore any spatial trends in $^{40}Ar/^{39}Ar$ ages. Phengite in the glaucophane-rich margin was generally not coarse-grained enough to permit multiple UV laser ablation analyses per grain. No trends were observed between the position of the analysis within the individual lithologic layers (i.e., center of the vein vs. margin of the vein near the glaucophane-rich reaction zone) and $^{40}Ar/^{39}Ar$ age or position of the analysis with respect to other porphyroblasts (e.g., pressure shadows) and $^{40}Ar/^{39}Ar$ age.

In situ UV laser ablation $^{40}Ar/^{39}Ar$ ages from phengite in the lawsonite garnet blueschist (SV13-06B) from Halilbağı range from 84.6 ± 2.4 Ma to 108.0 ± 2.7 Ma (n = 17; Figure 11). The $^{40}Ar/^{39}Ar$ age probability plot for this sample shows that 3 age modes can be discerned: at 85 Ma, 98 Ma, and 107 Ma (Figure 11). As in the lawsonite vein (SV03-103), the phengite in this sample occurs within phengite-rich layers and bundles that do not permit easy identification of grain boundaries or intra-grain $^{40}Ar/^{39}Ar$ age variations, however, $^{40}Ar/^{39}Ar$ age variations of up to 23 m.y. are observed at scales of ~300 μm.

In situ UV laser ablation $^{40}Ar/^{39}Ar$ ages from individual analysis pits in the lawsonite blueschist (SV13-15) range from 84.6 ± 7.9 Ma to 103.7 ± 3.1 Ma, yielding a mean weighted $^{40}Ar/^{39}Ar$ age of 95.8 ± 1.5 (n = 16, MSWD = 1.52, p = 0.088; Figure 11). Analyses were conducted in both phengite + lawsonite-rich layers and matrix phengite, although no variation was observed between $^{40}Ar/^{39}Ar$ ages obtained from phengite in the

lawsonite + phengite-rich layers or phengite in pressure shadows surrounding lawsonite porphyroblasts.

In situ UV laser ablation $^{40}Ar/^{39}Ar$ ages of phengite in the lawsonite garnet blueschist (SV12-59) from İkipınar range from 80.1 ± 2.5 Ma to 87.8 ± 2.7 Ma (n = 10; Figure 11). Two UV laser ablation spots returned older $^{40}Ar/^{39}Ar$ ages of 93.3 ± 2.8 Ma and 94.8 ± 2.8 Ma. Given the small grain size of phengite occurring in pressure shadows surrounding garnet and lawsonite porphyroblasts, $^{40}Ar/^{39}Ar$ age analyses were conducted exclusively in phengite occurring within the phengite-rich clusters.

In situ UV laser ablation $^{40}Ar/^{39}Ar$ ages of phengite in quartzite sample SV10-06 range from 87.6 ± 3.1 Ma to 125.4 ± 2.3 Ma (n = 19; Figure 12). Similar to the lawsonite garnet blueschist (SV13-06B) from the same structural level, the $^{40}Ar/^{39}Ar$ age probability plot for this sample exhibits multiple age modes: at 88 Ma, 100 Ma, 110 Ma, and 125 Ma (Figure 11). Analyses were conducted in both single phengite grains and phengite-rich layers. The $^{40}Ar/^{39}Ar$ ages from individual phengite grains range from 97.3 ± 2.8 – 116.7 ± 2.7 Ma, whereas $^{40}Ar/^{39}Ar$ ages from phengite in layers yield slightly older ages that range from 100.9 ± 2.0 – 124.4 ± 2.3 Ma. No correlation could be made between $^{40}Ar/^{39}Ar$ age and spatial position within the grain, as individual grains generally narrowed at the tips, permitting only a single analysis spot in their cores, and phengite-rich layers commonly contained other high-pressure mineral phases that restricted locations for $^{40}Ar/^{39}Ar$ analyses.

In situ UV laser ablation $^{40}Ar/^{39}Ar$ ages of phengite in quartzite SV10-08 range from 84.0 ± 1.3 Ma to 97.7 ± 1.8 Ma (n = 18; Figure 12). Results yield a $^{40}Ar/^{39}Ar$ age probability plot with two age modes: 84 Ma and 92 Ma.

6. Discussion

Results from the *in situ* UV laser ablation $^{40}Ar/^{39}Ar$ analyses show that phengite from blueschist- and eclogite-facies rocks in the Sivrihisar Massif record individual $^{40}Ar/^{39}Ar$ ages ranging from 75.0 ± 3.9 Ma to 127.1 ± 2.6 Ma. This age range is similar to the range of white mica ages documented in previous *in situ* UV laser ablation $^{40}Ar/^{39}Ar$ geochronology studies of the Tavşanlı Zone (Sherlock et al. 1999; Sherlock and Kelley 2002). Within our sample suite, there are no cases in which this age range is recorded in a single sample, instead, individual samples typically record either a comparatively narrow range of ages (<10 – 14 m.y.) that defines a single age mode or record a continuum of ages that spans 14 to 38 m.y. To understand the processes giving rise to the observed $^{40}Ar/^{39}Ar$ age variations, we explore factors affecting Ar systematics at both the grain- and sample-scale.

6.1 Evaluation of assumptions in $^{40}Ar/^{39}Ar$ age interpretation of Sivrihisar phengite

An important question in the interpretation of white mica $^{40}Ar/^{39}Ar$ ages is whether the ages represent the timing of crystallization or cooling. To interpret white mica $^{40}Ar/^{39}Ar$ geochronologic data as cooling ages, and therefore as the time at which the mica became closed to Ar diffusion, the following assumptions must be met: (1) all $^{40}Ar^*$ (radiogenic argon) present in the crystal lattice resulted from *in situ* decay of ^{40}K (i.e., no extraneous argon), (2) no $^{40}Ar^*$ accumulated within the mica at T> the closure

temperature and all $^{40}Ar^*$ was effectively removed from the mineral lattice (e.g., by fluids), and (3) the $^{40}Ar^*$ concentration in the mica is dependent only on the thermal history of the grain (temperature and residence time at that temperature). If the mica crystallized or experienced temperatures above the closure temperature for Ar in white mica (~ 350 – 400 °C), then the $^{40}Ar/^{39}Ar$ age should represent a cooling age that is younger than the crystallization age of the mica (Wijbrans and McDougall 1986).

In HP/LT terranes, however, $^{40}Ar/^{39}Ar$ white mica (phengite) ages commonly overlap with, or exceed, ages obtained from geochronometers with higher closure temperatures, such as Sm-Nd and Lu-Hf garnet ages or U-Pb zircon ages, even for rocks in which metamorphic temperatures were as high as 600 ± 50 °C (Li et al. 1994; Di Vincenzo et al. 2001, 2004, 2006; Bosse et al. 2005; Putlitz et al. 2005). These observations suggest that either the assumed nominal bulk closure temperature of 350 – 400 °C is incorrect for phengitic white mica and/or that one or more of the assumptions used in the interpretation of $^{40}Ar/^{39}Ar$ white mica ages as cooling ages are not valid for blueschist and eclogite facies rocks.

Nominal closure temperatures (T_c) for any mineral with a known grain size, geometry, and cooling rate can be approximated using Dodson's formula (Dodson 1973), provided reliable diffusion parameters are known. As diffusion parameters for phengite have not yet been experimentally determined, values for muscovite are commonly used. However, estimates for argon diffusion parameters in phengite using Arrhenius data obtained from step-heating experiments of natural phengite suggest that it is highly retentive of argon compared to muscovite and may be capable of recording the timing of

metamorphic growth and recrystallization (Forster and Lister 2014, Lister and Forster 2016). Theoretical and experimental studies also suggest that argon diffusivity may be pressure dependent, such that $^{40}Ar^*$ retention (and closure temperature) in white mica increases with increasing pressure (Lister and Baldwin 1996; Harrison et al. 2009). Using experimental data for muscovite from Harrison et al. (2009), Warren et al. (2012b) investigated the effects of this pressure dependence on the interpretation of $^{40}Ar/^{39}Ar$ ages from rocks that were metamorphosed under different P-T conditions. Results from numerical diffusion models showed that muscovite that experienced peak conditions in the blueschist- and low-temperature eclogite facies (400 – 550 °C, $P \leq 3$ GPa) could be capable of retaining $^{40}Ar^*$ during its prograde history.

The P-T conditions for blueschist-facies metamorphism in the Halilbağı unit are estimated at 380 – 500 °C and 1.2 – 1.6 GPa, the P-T conditions for epidote eclogite-facies metamorphism are estimated at up to 600 °C and 1.8 GPa, and peak metamorphic conditions for lawsonite eclogite-facies metamorphism are estimated at 500 – 550 °C and up to 2.6 GPa, although some lawsonite blueschists record the same P-T conditions as coexisting lawsonite eclogites (Davis and Whitney 2006, 2008). Based on these existing P-T data, the models of Warren et al. (2012b) predict that: (1) phengite from the lawsonite-bearing eclogites should yield $^{40}Ar/^{39}Ar$ crystallization ages for peak metamorphism, (2) phengite from the epidote eclogite should yield a $^{40}Ar/^{39}Ar$ cooling age (assuming metamorphic temperatures of ~ 600 °C), and (3) phengite from the lower temperature blueschists should theoretically be capable of preserving $^{40}Ar/^{39}Ar$ ages from the prograde path and possibly earlier. Although there are uncertainties in the

metamorphic paths of the dated samples (i.e., residence time at peak conditions and for some samples with high-variance assemblages, the peak P-T conditions), and there is evidence that volume diffusion was not the sole mechanism affecting Ar systematics in these rocks (i.e., presence of deformation features and compositional zoning), these predictions nonetheless provide a useful framework for exploring what behavior might be expected in rocks metamorphosed at these P-T conditions.

A comparison of the model predictions with existing geochronological results and the new *in situ* UV laser ablation $^{40}Ar/^{39}Ar$ geochronology obtained here show that, to a first-order, there is agreement between the predictions of the model and the observed ages. The *in situ* UV laser ablation $^{40}Ar/^{39}Ar$ data from the two lawsonite-bearing eclogite samples have mean weighted ages of 92.9 ± 1.9 Ma and 90.2 ± 1.4 Ma, in close agreement with the Lu-Hf isochron age of 91.1 ± 1.3 Ma obtained for one of the same samples dated in this study (SV12-13E) and interpreted as dating the timing of HP metamorphism (Mulcahy et al. 2014). The *in situ* UV laser ablation $^{40}Ar/^{39}Ar$ data from the epidote eclogite yield a younger mean weighted age of 81.8 ± 2.2 Ma, in agreement with Rb-Sr white mica ages of 78.5 ± 1.6 Ma – 82.8 ± 1.7 Ma from blueschist-facies rocks in the Tavşanlı Zone that have been interpreted as the age of retrograde metamorphism (Sherlock et al. 1999). The agreement between the $^{40}Ar/^{39}Ar$ age of retrograde (blueschist) metamorphism and the age obtained for the epidote eclogite is consistent with the interpretation that the epidote eclogite may record a cooling age.

In contrast to the eclogites, which yield a relatively narrow range of $^{40}Ar/^{39}Ar$ ages (<10 – 14 m.y. age spread) and a single age mode (Figure 9), blueschist and

quartzite tend to yield a much larger range of $^{40}Ar/^{39}Ar$ ages (from 14 to 38 m.y. in a given sample) (Figures 11, 12). Previously, large age ranges were interpreted as resulting from heterogeneous excess Ar contamination (Sherlock et al. 1999; Sherlock and Kelley 2002). Indeed, a couple of grains from this investigation recorded older UV laser $^{40}Ar/^{39}Ar$ ages in the rims compared with the cores, which could be argued for ingress of extraneous (excess) argon. However, given the inefficiency of argon diffusion at these P-T conditions and the complex zoning patterns and deformation features observed in these phengite crystals, an alternative interpretation is that the phengite preserves an age record of earlier geologic growth or metamorphic events, and that age variations within a sample reflect either continuous (re)crystallization in an open system following initial mica growth or the preservation of distinct mica populations or generations. To evaluate these possibilities, we examine the correlation between different $^{40}Ar/^{39}Ar$ age ranges and age modes and various physical and chemical factors, such as phengite composition and zoning patterns, host rock lithology, and structural position in the terrane. We also evaluate the possible effects of mixed analyses on the observed $^{40}Ar/^{39}Ar$ age spread.

6.1.1 Effects of contamination and mixed analyses

One possible cause for the observed spread of $^{40}Ar/^{39}Ar$ ages is that the analysis pits intersected another phase at depth, such that the analyses consist of both phengite and a K-free phase ("contaminated analysis"). Radiogenic argon yields ($\%^{40}Ar^*$ column, Table 4) can serve as a proxy for contaminated analyses because radiogenic argon should only be produced in K-bearing phases (micas), so analyses that consist of only K-rich minerals should have high $\%^{40}Ar^*$, whereas those consisting of a K-rich mineral and a K-

poor mineral should have lower $\%^{40}Ar^*$. However, previous *in situ* $^{40}Ar/^{39}Ar$ geochronology studies of HP/LT and UHP rocks have shown that K-free minerals (quartz, epidote, lawsonite, garnet, omphacite) can incorporate measurable amounts of extraneous ^{40}Ar (Giorgis et al. 2000; Sherlock and Kelley 2002). Therefore, in addition to monitoring the radiogenic argon yields, we also examined plots of ^{37}Ar and ^{38}Ar (derived from nucleogenic reactions with calcium and chlorine) versus $^{40}Ar/^{39}Ar$ age to identify extraneous argon contamination from Ca- or Cl-rich matrix phases, such as lawsonite, epidote, or chlorite (Supplementary Material 4).

Radiogenic argon yields for all analyzed samples are high (>70%), suggesting that contamination from K-free phases was negligible. Likewise, plots of ^{37}Ar and ^{38}Ar versus age (Supplementary Material 4) show that for most samples there are no consistent trends between the ^{37}Ar or ^{38}Ar content and measured age, and analyses with little to no measurable ^{37}Ar or ^{38}Ar yield a similar range of ages as analyses with higher ^{37}Ar or ^{38}Ar content. Although two of the eclogite samples (SV12-13E, SV12-10B) show some evidence for increasing age with increasing ^{37}Ar content and errors on the measured age in one of the blueschist samples (SV13-15) increase with increasing ^{37}Ar content, it is difficult to attribute these trends strictly to contamination with Ca-rich phases, as electron microprobe analyses show that phengite in several of these samples contains small, but measurable Ca contents (Table 2, 3).

Backscattered electron imaging of the analyzed rock chips in the electron microprobe following *in situ* laser ablation $^{40}Ar/^{39}Ar$ analyses provided additional confirmation, in two dimensions, that all analyses included in the age calculations were

conducted in phengite. To ensure that K-free phases were not intersected at depth, X-Ray Computed Tomography was used to image the sample that contained the lowest overall $\%^{40}Ar^*$ yields of any sample and that was therefore the sample most likely to contain analyses contaminated by K-poor phases. Of the 12 analysis pits imaged, only one pit showed evidence of intersecting another phase (omphacite + epidote matrix) at depth (Figure 13), confirming that the effects of intersecting another phase at depth were minimal and likely not the source of the inter- and intrasample age variability in this dataset.

6.1.2 Evaluation of Ages with Respect to Phengite and Bulk Rock Composition

Empirical studies of white mica from HP/LT terranes have suggested that white mica $^{40}Ar/^{39}Ar$ age variations may be compositionally controlled, such that particular compositions of mica (e.g., more Mg-rich) are more likely to retain Ar than others, or that variations in white mica composition are related to the presence of different mica generations or growth of mica at different P-T conditions (e.g., Scaillet et al. 1992; Dahl 1996; Giorgis et al. 2000). To examine the possible correlations between variations in phengite composition and $^{40}Ar/^{39}Ar$ age variability in the samples, compositional profiles and X-ray element maps were obtained across several grains in each sample to examine both intra- and inter-grain compositional variations (Figure 4, 5).

In comparing the phengite composition and $^{40}Ar/^{39}Ar$ geochronology results it is worth noting that (1) the phengite compositions were acquired on polished thin sections and the $^{40}Ar/^{39}Ar$ geochronology results were acquired on polished rock chips cut from the opposite face of the rock chip used to make the thin section, and (2) the sample

volumes analyzed by the EMPA (a few μm^3) and the *in situ* UV laser used for geochronology (~60 μm3, based on a conical pit geometry with a diameter of 48 μm and a depth of ~100 μm as estimated from XRCT images) are quite different. With regards to point (1), although the compositional analyses were conducted on thin sections and not the actual rock chip used for analyses (and thus different phengite grains), it is likely that the phengite analyzed by UV laser ablation $^{40}Ar/^{39}Ar$ geochronology had the same compositional variability and zoning patterns as the phengite analyzed in the thin section because most of the observed compositional variability was the result of intragrain zoning, not intergrain zoning (Figure 4, 5). The implications of point (2) are that only compositional features >48 μm in diameter will be able to be targeted for $^{40}Ar/^{39}Ar$ geochronology and linked unequivocally to a particular age. For the two samples (SV12-10B, SV03-103) in which compositional variations were large enough to be specifically targeted using the UV laser, X-ray element maps of the rock chips analyzed for $^{40}Ar/^{39}Ar$ geochronology were obtained after age analyses to relate the obtained $^{40}Ar/^{39}Ar$ age to a particular compositional domain (Figure 14).

With the exception of the lawsonite vein (SV03-103) and eclogite sample SV12-10B, in which phengite displays core-to-rim zoning in Si, Fe, Mg, Na, and Ti (Figure 4, 5, Table 2), most phengite displays only subtle compositional variations or zoning patterns (Figure 4, 5). These zoning patterns are characterized by irregular or patchy variations in Si and Fe (Figure 5), and in the case of quartzite SV10-06, Na as well. Phengite in some samples also shows thin, discontinuous Fe-poor rims (SV12-13E); in blueschist sample SV12-59 these Fe-poor growths are only found along the tips of mica

grains (Figure 5). The causes of such zoning are unknown, as little is known about how mica grows or recrystallizes under (U)HP/LT conditions, but could be related to recrystallization of the phengite as a result of fluids, deformation, or changes in P-T conditions. All of these factors can theoretically affect the mobility of argon at the grain scale, and could thus lead to the observed grain scale heterogeneities in $^{40}Ar/^{39}Ar$ ages.

In the case of phengite in vein sample SV03-103 and phengite in eclogite sample SV12-10B, the core-to-rim increase in Si content is qualitatively consistent with an increase in pressure conditions during phengite growth. If this is the case, one might expect the core to yield an older age and the rim to yield a younger age. However, X-ray element maps of the rock chips analyzed for $^{40}Ar/^{39}Ar$ geochronology show that there is no clear correlation between the composition of the phengite and $^{40}Ar/^{39}Ar$ age (Figure 14). For example, in eclogite SV12-10B, an $^{40}Ar/^{39}Ar$ age of 87.6 ± 2.4 Ma was obtained within the lower-Si core (3.3 p.f.u.) core of a phengite, and an $^{40}Ar/^{39}Ar$ age of 88.5 ± 2.3 Ma was obtained for the higher-Si rim (3.5 p.f.u.) (Figure 14). These values are statistically identical, and suggest that either the mechanism responsible for the change in mica composition may have been of too short a duration to be recorded by the *in situ* UV laser ablation $^{40}Ar/^{39}Ar$ method or that these phengite were affected by the uptake of excess Ar along grain boundaries.

Another possible reason for the lack of correlation between zoning and $^{40}Ar/^{39}Ar$ age may be related to unconstrained three-dimensional effects. The high magnification Fe X-ray element map (Figure 14) shows that the Fe-rich mica is not restricted to the rims, but is also found along some cleavage planes. Given the fine-scale zoning (~15- μm

scale) present in these phengite, it is likely that even though we imaged the rock chips after analyses to check the position of the analysis relative to phengite grain boundaries and zoning features, that some of the smaller scale zoning features may have been ablated away during analysis and thus are no longer visible. However, even had the rock chips been imaged prior to analysis to selectively target or avoid such features, it is likely that such small-scale heterogeneities would have also existed at depth and remained otherwise unnoticed, as the density contrast between phengite of two different compositions is not large enough to be detected with XRCT. Therefore, it is possible that most of our analyses represent, to some extent, mixed analyses.

Nonetheless, the important observation is that phengite preserves compositional variability at the grain scale, and that for most samples, the compositional variability does not conform to a simple core-to-rim zoning pattern. This indicates that a core-to-rim growth model for phengite may not be appropriate and that there is no reason to expect a symmetrical core-to-rim decreasing trend in $^{40}Ar/^{39}Ar$ ages for these phengite grains.

In addition to $^{40}Ar/^{39}Ar$ age variations at the grain scale, the samples in this study also show inter-sample $^{40}Ar/^{39}Ar$ age variations, so it also important to consider factors that could affect argon behavior at a larger scale. In some cases, variations in bulk rock K_2O have been correlated with $^{40}Ar/^{39}Ar$ age, such that samples with higher K_2O yield older ages than samples with lower K_2O (Foland 1979; Kelley and Wartho 2000; Sherlock and Kelley 2002). This indicates that differences in bulk rock composition (e.g., owing to differences in protolith type) could potentially account for intersample $^{40}Ar/^{39}Ar$ ages. This observation was made in previous studies of the Tavşanlı Zone, where

Sherlock and Kelley (2002) suggested that low-K metabasites might serve as the best candidates for obtaining geologically meaningful $^{40}Ar/^{39}Ar$ ages. However, in many other HP/LT and ultrahigh-pressure terranes, a common observation is that $^{40}Ar/^{39}Ar$ ages from metasedimentary rocks tend to be younger than ages of coexisting metabasaltic rocks (Baxter et al. 2002; Cosca et al. 2005; Di Vincenzo et al. 2006; Warren et al. 2011, 2012). This behavior has been attributed to the "armoring" effect of eclogite (Cosca et al. 2005), and the increased permeability and fluid production capacity of rocks with higher modal abundances of white mica, such as metapelites (Warren et al. 2012; Smye et al. 2013).

In the Sivrihisar Massif, there is no clear trend between mean weighted age or complexity of the $^{40}Ar/^{39}Ar$ age probability plot (one age mode versus multiple apparent age modes) and bulk rock composition or protolith. In general, eclogites record the narrowest range of ages (~ 10 – 14 m.y.) of any rock type, although the mean weighted $^{40}Ar/^{39}Ar$ age varies between individual eclogite samples depending on whether they are lawsonite-bearing (90 – 93 Ma) or epidote-bearing (~82 Ma). The fact that the eclogites, on the whole, tend to yield the narrowest range of ages of any rock type and lack the > 100 Ma ages that are documented in other samples is an interesting result in the context of previous studies and may be related to the history of fluid-rock interaction experienced by the Sivrihisar eclogites. Phengite from many of the eclogite samples display zoning features that are truncated at the grain boundary and may be indicative of dissolution-reprecipitation processes (Figure 5), and preliminary *in situ* oxygen isotope studies of garnets from the Halilbağı region suggest that at least some of the eclogites record interactions with metasedimentary-derived fluids (Gauthiez-Putallaz et al. 2014).

Although quartzite SV10-06 on average yielded the oldest $^{40}Ar/^{39}Ar$ ages, blueschist SV13-06B has $^{40}Ar/^{39}Ar$ ages that are older than those recorded in the other quartzite, SV10-08. The fact that quartzite SV10-06 and blueschist SV13-06B consistently record the oldest $^{40}Ar/^{39}Ar$ ages of the dated samples, and the fact that they were sampled from the same structural level, suggests that there is no simple correlation between $^{40}Ar/^{39}Ar$ age and protolith or rock type, but that the preservation of older $^{40}Ar/^{39}Ar$ ages may instead be related to the structural position of the sample. The preservation of slightly older $^{40}Ar/^{39}Ar$ ages (> 108 Ma) in quartzite is consistent with observations from the SE part of the Sivrihisar Massif, where petrologic data indicate that quartzite was less affected than metabasalt by overprinting and retained a more robust record of earlier metamorphic events (Whitney et al., 2011).

6.1.3 Ages and Structural Position: Effects of Deformation

To investigate the potential effects of structural position on $^{40}Ar/^{39}Ar$ ages, two quartzite and two blueschist samples collected from outcrops at different distances (< 200 m, within the high-strain zone; and > 200 m, not in the high-strain zone) from the northern tectonic boundary were analyzed (Figure 15). Regardless of rock type, the samples closest to the boundary (quartzite SV10-08, blueschist SV13-15) contained a narrower spread of $^{40}Ar/^{39}Ar$ ages and a simpler $^{40}Ar/^{39}Ar$ age probability plot than samples located farther away from the boundary (quartzite SV10-06, blueschist SV13-06B). In addition to differences in the complexity of the $^{40}Ar/^{39}Ar$ age probability plot, samples closest to the tectonic contact also generally contained younger $^{40}Ar/^{39}Ar$ ages;

only two $^{40}Ar/^{39}Ar$ ages > 100 Ma were obtained, whereas in the samples located farther from the boundary, > 60% of the obtained $^{40}Ar/^{39}Ar$ ages were > 100 Ma.

There is not evidence that different structural levels represent distinct crustal slices that experienced different metamorphic histories and were tectonically juxtaposed. Therefore, we consider the hypothesis that different structural levels experienced a similar tectonic history and older $^{40}Ar/^{39}Ar$ ages were largely "erased" in blueschist and quartzite deformed in the high-strain zone near the tectonic boundary; i.e., the $^{40}Ar^*$ systematics were affected by deformation-driven phengite recrystallization. In this case, the oldest $^{40}Ar/^{39}Ar$ ages recorded by phengite in rocks located closest to the tectonic boundary should provide a minimum age for the timing of deformation.

Field and petrographic observations, such as a reduction in grain size in rocks within vs. outside of the high strain zone, highly fractured and chloritized garnet, and the abundance of cross-cutting veins in rocks at the highest structural levels support this interpretation. Similar trends have been documented in other $^{40}Ar/^{39}Ar$ studies of white mica and biotite from fluid- and/or deformation-rich environments, such as high-strain zones and lithologic contacts in which $^{40}Ar/^{39}Ar$ ages were systematically younger near the contact or high strain zone (Baxter et al. 2002; Mulch et al. 2002; Warren et al. 2012), and in the case of some $^{40}Ar/^{39}Ar$ laserprobe studies, a narrower range of ages was also documented (Halama et al. 2014).

In addition to variations in the preservation of $^{40}Ar/^{39}Ar$ ages with distance from the northern tectonic boundary, there are also variations in the preservation of high-pressure mineral assemblages, and in the case of the quartzite samples, c-axis fabrics.

Blueschist (SV13-06B) and quartzite (SV10-06) from outside of the high-strain zone both preserve omphacite-rich domains and garnet, whereas blueschist (SV13-15) and quartzite (SV10-08) sampled within the high-strain zone lack omphacite, and in the case of blueschist SV13-15, also lack garnet. The presence of higher grade (eclogite-facies) assemblages in the quartzite sampled outside of the high strain zone is also consistent with the preservation of a higher-pressure quartz c-axis fabric (rhomb <a>) in that sample (SV10-06) (Whitney et al. 2014).

6.2 Timing of blueschist and eclogite facies metamorphism

The timing of metamorphism in the Tavşanlı Zone has been bracketed by estimates for the age of subduction initiation in the region and intrusion of HP/LT rocks by shallow crustal granitoids. In the Sivrihisar Massif, a Barrovian overprint of the HP/LT metamorphic rocks slightly predated intrusion by late granitoids and provides a further bracket on the end of subduction metamorphism (~ 63 Ma $^{40}Ar/^{39}Ar$ muscovite cooling age; Seaton et al. 2014). Previous estimates for the timing of subduction initiation in the region are based on $^{40}Ar/^{39}Ar$ dating of metamorphic sole rocks exposed along the length of the Tavşanlı Zone; these yielded ages of 93. 0 ± 2.0 Ma (Önen 2003) and 101.1 ± 3.8 Ma (Harris et al. 1994). If these rocks are interpreted as forming as a result of the initiation of intra-oceanic subduction during the closure of the Neo-Tethys, then these ages should pre-date HP/LT metamorphic events. However, geochronologic studies of the HP/LT rocks in the Tavşanlı Zone commonly yield ages that are the same as, or older than, the age of metamorphic sole rocks (this study; Sherlock et al. 1999; Sherlock and Kelley 2002; Mulcahy et al. 2014).

One possible reason for discrepancies between these metamorphic sole and Sivrihisar datasets is that the $^{40}Ar/^{39}Ar$ ages recorded by the metamorphic soles do not correspond to the age of the high-temperature amphibolite-facies metamorphic event, but instead indicate the timing of an HP/LT overprint. Indeed, many of the amphibolitic soles in the Tavşanlı Zone and nearby regions in Anatolia display evidence for an incipient blueschist-facies overprint (Dilek and Whitney 1997; Okay et al. 1998; Önen and Hall 2000; Plunder et al. 2013, 2015), as seen in glaucophane rims on hornblende and lawsonite replacing plagioclase (Plunder et al. 2013).

Although the possibility of contamination by extraneous argon cannot be ruled out entirely, if the $^{40}Ar/^{39}Ar$ ages recorded by metamorphic soles date the timing of or were disturbed by an early HP/LT event, then the oldest $^{40}Ar/^{39}Ar$ ages (> 93 Ma) recorded by the Sivrihisar metabasalts in this study could document prograde phengite crystallization. This interpretation is consistent with a preliminary Lu-Hf garnet isochron age of ~ 110 Ma for a garnet amphibolite from the Tavşanlı Zone (Pourteau et al. 2014). These results suggest that subduction initiation in the region could have started 10 – 17 Ma earlier than previously proposed by some authors.

If the timing of subduction initiation is tentatively taken as ~110 Ma, and the end of subduction-related metamorphism is taken as ~63 Ma (the oldest $^{40}Ar/^{39}Ar$ muscovite cooling age determined for the Barrovian overprint), then any $^{40}Ar/^{39}Ar$ age between 110 Ma and 63 Ma could be related to the HP/LT event in the region. With the exception of quartzite SV10-06, no sample records $^{40}Ar/^{39}Ar$ ages that are older or younger than this

age range; the oldest $^{40}Ar/^{39}Ar$ age is 108.0 ± 2.7 Ma in lawsonite blueschist SV13-06B and the youngest $^{40}Ar/^{39}Ar$ age is 75.0 ± 3.9 Ma in epidote eclogite SV12-15A.

The geologic significance (if any) of the $^{40}Ar/^{39}Ar$ ages >110 Ma in the SV10-06 quartzite are uncertain. It is unlikely that these 'old' phengite grains are detrital, as all analyzed white mica is high-Si phengite (> 3.3 Si p.f.u., Table 3). However, it is possible that the phengite grains incorporated small amounts of 'inherited' argon from the protolith. Although the $^{40}Ar/^{39}Ar$ ages yielded by the sample are younger than the age of the protolith, subsequent deformation during HP/LT metamorphism could have resulted in variable degrees of argon loss. Heterogeneous uptake of externally-derived Ar could also account for the observed $^{40}Ar/^{39}Ar$ ages.

The only existing estimate for the timing of eclogite-facies metamorphism in the Tavşanlı Zone is a Lu-Hf lawsonite-garnet-whole rock isochron age of 91.1 ± 1.3 Ma (Mulcahy et al. 2014) obtained from one of the lawsonite eclogite samples (SV12-13E) dated in this study. The *in situ* UV laser ablation $^{40}Ar/^{39}Ar$ phengite ages from this lawsonite eclogite range from 87.7 ± 2.5 Ma to 99.8 ± 3.7 Ma. Eclogite sample SV12-10B yields a similar range of $^{40}Ar/^{39}Ar$ ages: 84.5 ± 2.3 Ma to 95.4 ± 3.0 Ma. These $^{40}Ar/^{39}Ar$ phengite ages overlap with the reported Lu-Hf age, suggesting that phengite in these samples are likely recording crystallization ages. Although there is some evidence that the phengite $^{40}Ar/^{39}Ar$ ages recorded in eclogite SV12-10B may have been affected by uptake of extraneous argon, we tentatively suggest that lawsonite eclogite-facies metamorphism may have been occurring as early as 99.8 ± 3.7 Ma and as late as 84.5 ± 2.3 Ma. Similar $^{40}Ar/^{39}Ar$ age ranges have been documented in phengite from HP/LT

rocks in the Cycladic Islands (Aegean) and the western Alps (Putlitz et al. 2005; Bröcker et al. 2013; Halama et al. 2014)

The *in situ* UV laser ablation $^{40}Ar/^{39}Ar$ phengite ages from the epidote eclogite (SV12-15A) are consistently younger than those obtained in the lawsonite-bearing eclogites, ranging from 75.0 ± 3.9 Ma to 89.4 ± 5.0 Ma. One explanation for younger $^{40}Ar/^{39}Ar$ ages in epidote versus lawsonite eclogite is that the $^{40}Ar/^{39}Ar$ ages in the epidote eclogite are cooling ages, not crystallization ages. The higher temperatures recorded by the epidote eclogites (~ 600 °C; Davis and Whitney 2006) does not preclude this possibility. An alternative interpretation is that the phengite in the epidote eclogite records crystallization ages related to the timing of a retrograde overprint of the epidote eclogite-facies assemblage. The lower Si content of phengite (~3.4 Si p.f.u.), as well as the presence of secondary alteration minerals such as chlorite (Figure 3f) and widespread replacement of rutile by titanite, are consistent with this interpretation. Regardless of whether the ages are cooling or crystallization ages, they place constraints on the timing of exhumation and retrogression-related metamorphism in the terrane.

Estimates for the timing of blueschist-facies metamorphism using Lu-Hf and Rb-Sr geochronology yield ages of 78.5 ± 1.6 – 83.3 ± 1.8 Ma (Sherlock et al. 1999; Mulcahy et al. 2014). These ages are consistently younger than the timing of peak eclogite facies metamorphism in the region (this study; Mulcahy et al. 2014). The relationship between the co-existing eclogite- and blueschist-facies rocks in the Tavşanlı Zone is in some cases uncertain. There is evidence for local replacement of omphacite by glaucophane (Davis and Whitney 2006; 2008) and transformation of eclogite to

blueschist surrounding lawsonite-rich veins at pod margins (sample SV03-103; this study; Davis and Whitney 2008), however, some blueschists record similar P-T conditions as eclogite (Davis and Whitney 2006; 2008) and some blueschists lack evidence (reaction textures, inclusions) for former eclogite facies conditions. Therefore, although some blueschists are clearly retrogressed eclogite, this interpretation may not apply to all blueschists in the Sivrihisar Massif, and therefore it is not necessarily the case that all blueschists in the region are expected to be younger than eclogite.

Evidence for retrograde transformation of lawsonite eclogite to blueschist is most common at the margins of eclogite pods. Pod margins are chemically and structurally complex, reflecting the interaction of deformation, fluids, and metamorphism. A common feature of many of the lawsonite eclogite pods in the field area is the presence of mm- to cm-scale lawsonite veins and layers at or near the margins of the pods (e.g., sample SV03-103). In the Halilbağı area, these veins are commonly surrounded by transitional blueschist-eclogite assemblages (Davis and Whitney 2008); that is, partial transformation of eclogite to blueschist. Glaucophane-rich zones adjacent to lawsonite-rich veins are evidence of vein-related local transformation of eclogite to blueschist. Lawsonite, phengite, and garnet are stable in eclogite, veins, and blueschist.

The *in situ* UV laser ablation $^{40}Ar/^{39}Ar$ phengite ages from the lawsonite + garnet + phengite vein (SV03-103) ranged from 86.1 ± 3.7 Ma to 102.8 ± 3.9 Ma; phengite $^{40}Ar/^{39}Ar$ ages from the adjacent glaucophane-rich margin ranged from 81.2 ± 2.9 Ma to 103.3 ± 4.5 Ma. The fact that the lawsonite + garnet + phengite vein and the glaucophane-rich margin preserve a similar range of $^{40}Ar/^{39}Ar$ ages is consistent with

their being petrogenetically related. Assuming that the age of peak HP metamorphism is ~ 90 – 93 Ma (based on the lawsonite eclogite ages), this suggests that phengite crystallization in the vein was broadly coeval with lawsonite eclogite-facies metamorphism and the early stages of retrograde blueschist-facies metamorphism. The slightly larger age range recorded by phengite from the margin of the pod (~ 20 m.y.) could be the result of the localization of deformation and fluid flow at the contact between the pod and host schist.

7. Conclusions

In situ UV laser ablation $^{40}Ar/^{39}Ar$ analyses of phengite from a suite of blueschist- and eclogite-facies metabasaltic and metasedimentary rocks from the Sivrihisar Massif, Tavşanlı Zone, Turkey record individual spot ages ranging from 75.0 ± 3.9 Ma to 127.1 ± 2.6 Ma. Intrasample variations range from 10 to 14 m.y. in lawsonite- and epidote-bearing eclogites, and from 14 to 38 m.y. in blueschists and quartzites. Variations in bulk rock composition (K_2O content) and protolith (metabasalt vs. metasediment) do not appear to explain the observed intersample $^{40}Ar/^{39}Ar$ ages and age ranges, nor are they explained by the presence of contaminated analyses. Instead, the observed intersample age variations may be related, in part, to variations in the peak P-T conditions of metamorphism, degree of fluid-rock interaction and deformation related to the structural and textural position of the sample.

The $^{40}Ar/^{39}Ar$ ages obtained for the lawsonite eclogites (90-92 Ma) in which phengite is in apparent textural equilibrium with the peak eclogite facies assemblage (omphacite + garnet + lawsonite) and the $^{40}Ar/^{39}Ar$ ages obtained for the epidote eclogite (~ 81 Ma) in which phengite is in apparent textural equilibrium with the retrograde

minerals (chlorite, titanite) agree well with existing estimates for the timing of peak and retrograde metamorphism, respectively. The coarse-grained (0.5 – 1.5 mm), undeformed phengite from these samples display both patchy zoning and zoning features that are truncated at the grain boundary, suggesting that the samples may have experienced a period of fluid-rock interaction that may have facilitated removal of argon from the grain boundaries, resulting in a more narrow range of ages and a single age mode.

In the blueschist and quartzite samples located close the northern tectonic boundary (SV12-59, SV13-15, SV10-08), where phengite is restricted to a particular textural habit and the host rocks have been strongly deformed, the $^{40}Ar/^{39}Ar$ age probability plots are also relatively simple. In the quartzite (SV10-06) and blueschist (SV13-06B) samples located > 200 m from the tectonic contact with the metamorphosed mafic and ultramafic unit, where the host rocks have been less strongly deformed and preserve relicts of eclogite facies metamorphism, the phengite records both older $^{40}Ar/^{39}Ar$ ages and a greater range of $^{40}Ar/^{39}Ar$ ages.

Although we cannot rule out the presence of extraneous (excess) argon, the correlation between the distribution of $^{40}Ar/^{39}Ar$ ages and age ranges and the petrographic and (micro)structural context of the phengite and their dated host rocks suggests that processes other than the uptake of excess argon may be affecting argon distribution at both the grain- and sample-scale in the Tavşanlı Zone. If the ages recorded by the phengite document varying degrees of recrystallization occurring as a result of subduction-related metamorphism and deformation, then this suggests that subduction initiation in the region likely predated ~ 90 – 95 Ma.

REFERENCES

Agard P, Monie P, Jolivet L, Goffe B (2002) Exhumation of the Schistes Lustres complex: in situ laser probe $^{40}Ar/^{39}Ar$ constraints and implications for the Western Alps. J Metamorph Geol 20:599 – 618.

Arnaud NO, Kelley SP (1995) Evidence for excess argon during high pressure metamorphism in the Dora Maira Massif (western Alps, Italy), using an ultra-violet laser ablation microprobe ^{40}Ar-^{39}Ar technique. Contrib Mineral Petr 121:1 – 11.

Baxter EF, DePaolo DJ, Renne PR (2002) Spatially correlated anomalous $^{40}Ar/^{39}Ar$ "age" variations in biotites about a lithologic contact near Simplon Pass, Switzerland: A mechanistic explanation for excess Ar. Geochim Cosmochim Ac 66:1067 – 1083.

Beltrando M, Lister GS, Forster M, Dunlap WJ, Fraser G, Hermann J (2009) Dating microstructures by the $^{40}Ar/^{39}Ar$ step-heating technique: Deformation-pressure-temperature-time history of the Penninic Units of the Western Alps. Lithos 113:801 – 819.

Beltrando M, Di Vincenzo G, Ferraris C (2013) Preservation of sub-microscopic structural relicts in micas from the Gran Paradiso Massif (Western Alps): Implications for Ar-40-Ar-39 geochronology. Geochim Cosmochim Ac 119:359 – 380.

Bosse V, Feraud G, Ballevre M, Peucat J, Corsini M (2005) Rb-Sr and $^{40}Ar/^{39}Ar$ ages in blueschists from the Ile de Groix (Armorican Massif, France): Implications for closure mechanisms in isotopic systems. Chem Geol 220:21 – 45.

Bröcker M, Baldwin S, Arkudas R (2013) The geological significance of $^{40}Ar/^{39}Ar$ and Rb-Sr white mica ages from Syros and Sifnos, Greece: a record of continuous (re)crystallization during exhumation? J Metamorph Geol 31: doi: 0.1111/jmg.12037.

Çetinkaplan M, Candan O, Oberhansli R, Bousquet R (2008) Pressure-temperature evolution of lawsonite eclogite in Sivrihisar; Tavşanlı Zone-Turkey. Lithos 104:12 – 32.

Coğulu E, Krummenacher D (1967) Problemes geochronometriques dans la partie NW de l'Anatolie Centrale (Turquie). Schweizerische mineralogische und petrographische Mitteilungen 47: 825 – 833.

Cosca MA, Giorgis D, Rumble D, Liou JG (2005) Limiting effects of UHP Metamorphism on Length Scales of Oxygen, Hydrogen, and Argon Isotope Exchange: An Example from the Qinglongshan UHP Eclogites, Sulu Terrain, China. Int Geol Rev 47:716 – 749.

Cosca MA, Stunitz H, Bourgeix A, Lee JP (2011) $^{40}Ar^*$ loss in experimentally deformed muscovite and biotite with implications for $^{40}Ar/^{39}Ar$ geochronology of naturally deformed rocks. Geochim Cosmochim Ac 75: 7759 – 7778.

Dahl PS (1996) The crystal-chemical basis for Ar retention in micas: inferences from interlayer partitioning and implications for geochronology. Contrib Mineral Petr 123:22 – 39.

Davis PB, Whitney DL (2006) Petrogenesis of lawsonite and epidote eclogite and blueschist, Sivrihisar Massif, Turkey. J Metamorph Geol 24:823- 849.

Davis PB, Whitney DL (2008) Petrogenesis and structural petrology of high-pressure metabasalt pods, Sivrihisar, Turkey. Contrib Mineral Petr 156:217 – 241.

Davis PB (2011) Petrotectonics of lawsonite eclogite exhumation: Insights from the Sivrihisar massif, Turkey. Tectonics 30: TC1006, doi:10.1029/2010TC002713.

Delaloye M, Bingol E (2000) Granitoids from Western and Northwestern Anatolia: Geochemistry and Modeling of Geodynamic Evolution. Int Geol Rev 42:241 – 268.

Dempster TJ (1992) Zoning and recrystallization of phengitic micas: implications for metamorphic equilibrium. Contrib Mineral Petr 109:526 – 537.

Dilek Y, Whitney DL (1997) Counterclockwise P-T-t trajectory from the metamorphic sole of a Neo-Tethyan ophiolite (Turkey). Tectonophysics 280: 295 – 310.

Di Vincenzo G, Ghiribelli B, Giorgetti G, Palmeri R (2001) Evidence of a close link between petrology and isotope records: constraints from SEM, EMP, TEM and in situ ^{40}Ar-^{39}Ar laser analyses on multiple generations of white micas (Lanterman Range, Antarctica). Earth Planet Sc Lett 192:389- 405.

Di Vincenzo G, Carosi R, Palmeri R (2004) The Relationship between Tectono-metamorphic Evolution and Argon Isotope Records in White Mica: Constraints from in situ ^{40}Ar-^{39}Ar Laser Analysis of the Variscan Basement of Sardinia. J Petrol 45:1013 – 1043.

Di Vincenzo G, Tonarini S, Lombardo B, Castelli D, Ottolini L (2006) Comparison of ^{40}Ar-^{39}Ar and Rb-Sr Data on Phengites from the UHP Brossasco-Isasca Unit (Dora Maira Massif, Italy): Implications for Dating White Mica. J Petrol 47: 1439 – 1465.

Dodson MH (1973) Closure Temperature in Cooling Geochronological and Petrological Systems. Contrib Mineral Petr 40: 259 – 274.

Federico L, Capponi G, Crispini L, Scambelluri M, Villa I.M (2005) $^{39}Ar/^{40}Ar$ dating of high-pressure rocks from the Ligurian Alps: Evidence for a continuous subduction-exhumation cycle. Earth Planet Sc Lett 240:668 – 680.

Foland KA (1979) Limited mobility of argon in a metamorphic terrain. Geochim Cosmochim Ac 43:793 – 801.

Forster MA, Lister GS (2014) $^{40}Ar/^{39}Ar$ geochronology and the diffusion of ^{39}Ar in phengite-muscovite intergrowths during step-heating experiments *in vacuo*. In: Jourdan F, Mark DF, Verati C (eds) Advances in $^{40}Ar/^{39}Ar$ Dating: from Archaology to Planetary Sciences, Geological Society, London, Special Publications, 378, pp 117 – 135.

Gauthiez-Putallaz L, Rubatto D, Hermann J, Martin L, Fornash KF, Whitney D (2014) Sediment-Eclogite Fluid Exchanges during Subduction in the Tavşanlı Zone, Turkey. Goldschmidt Abstracts, 778.

Gautier Y (1984) Deformations et Metamorphismes Associes a la Fermeture Tethysienne en Anatolie Centrale (Region de Sivrihisar, Turquie. Ph.D. Thesis University Paris-Sud, 236 pp.

Giorgis D, Cosca MA, Li S (2000) Distribution and significance of extraneous argon in UHP eclogite (Sulu terrain, China): insight from in situ $^{40}Ar/^{39}Ar$ UV-laser ablation analysis. Earth Planet Sc Lett 181:605- 615.

Gray DR, Miller J, Foster DA, Gregory RT (2004) Transition from subduction- to exhumation-related fabrics in glaucophane-bearing eclogites, Oman: evidence from relative fabric chronology and 40Ar/39Ar ages. Tectonophysics 389:35 – 64.

Halama R, Konrad-Schmolke M, Sudo M, Marschall HR, Wiedenback M (2014) Effects of fluid-rock interaction on $^{40}Ar/^{39}Ar$ geochronology in high-pressure rocks (Sesia-Lanzo Zone, Western Alps). Geochim Cosmochim Ac 126:475 – 494.

Harris NBW, Kelley S, Okay AI (1994) Post-collision magmatism and tectonics in northwest Anatolia. Contrib Mineral Petr 117:241 – 252.

Harrison TM, Celerier J, Aikman AB, Hermann J, Heizler MT (2009) Diffusion of ^{40}Ar in muscovite. Geochim Cosmochim Ac 73:1039 – 1051.

Kelley SP, Wartho JA (2000) Rapid kimberlite ascent and the significance of Ar-Ar ages in xenolith phlogopites. Science 289:609 – 611.

Kramar N, Cosca MA, Hunziker JC (2001) Heterogeneous $^{40}Ar^*$ distributions in naturally deformed muscovite: in situ UV-laser ablation evidence for microstructurally controlled intragrain diffusion. Earth Planet Sc Lett 192:377 – 388.

Kuiper KF, Deino A, Hilgen FJ, Krijgsman W, Renne PR, Wijbrans JR (2008) Synchronizing rock clocks of Earth history. Science 320, 500 – 504.

Kulaksız S (1978) Sivrihisar kuzeybatı eklojitleri. Yerbilimleri 4:89 – 94.

Lee J-Y, Marti K, Severinghaus JP, Kawamura K, Yoo H-S, Lee JB, Kim JS (2006) A redetermination of the isotopic abundances of atmospheric Ar. Geochim Cosmochim Ac 70: 4507 – 4512.

Li S, Wang S, Chen Y, Liu D, Qui J, Zhou H, Zhang Z (1994) Excess argon in phengite from eclogite: Evidence from dating of eclogite minerals by Sm-Nd, Rb-Sr, and $^{40}Ar/^{39}Ar$ methods. Chem Geol 112:343 – 350.

Lister GS, Baldwin SL (1996) Modelling the effect of arbitrary P-T-t histories on argon diffusion in minerals using the MacArgon program for the Apple Macintosh. Tectonophysics 253:83 -109.

Lister GS, Forster MA (2016) White mica $^{40}Ar/^{39}Ar$ age spectra and the timing of multiple episodes of high-P metamorphic mineral growth in the Cycladic eclogite-blueschist belt, Syros, Aegean Sea, Greece. J Metamorph Geol. doi: 10.1111/jmg.12178.

Min K, Mundil R, Renne PR, Ludwig KR (2000) A test for systematic errors in $^{40}Ar/^{39}Ar$ geochronology through comparison with U/Pb analysis of a 1.1-Ga rhyolite. Geochim Cosmochim Ac 64:73 – 98.

Mulcahy SR, Vervoort JD, Renne PR (2014) Dating subduction-zone metamorphism with combined garnet and lawsonite Lu-Hf geochronology. J Metamorph Geol 32:515 – 533.

Mulch A, Cosca MA, Handy MR (2002) In-situ UV-laser $^{40}Ar/^{39}Ar$ geochronology of a micaceous mylonite: an example of defect-enhanced argon loss. Contrib Mineral Petr 142: 738 – 752.

Okay AI (1980) Mineralogy, petrology and phase relations of glaucophane-lawsonite zone blueschist from the Tavşanlı region, north-west Turkey. Contrib Mineral Petr 72:243 – 255.

Okay AI (1984) Distribution and characteristics of the northwest Turkish blueschist. In: The Geological Evolution of the Eastern Mediterranean, Special Publication 17 (eds Dixon, J.E. & Robertson, A.H.F.), pp. 455–466. Geological Society, London.

Okay AI (1986) High-pressure/low-temperature metamorphic rocks of Turkey. In: Blueschists and Eclogites (eds Evans, B.W. & Brown, E.H.), Geological Society of America Memoir, 164, 333- 347.

Okay AI, Kelley SP (1994) Tectonic setting, petrology, and geochronology of jadeite + glaucophane and chloritoid + glaucophane schists from north-west Turkey. J Metamorph Geol 12:455 – 466.

Okay AI, Harris NBW, Kelley SP (1998) Exhumation of blueschists along a Tethyan suture in northwest Turkey. Tectonophysics 285:275 – 299.

Okay AI (2002) Jadeite-chloritoid-glaucophane-lawsonite blueschists in northwest Turkey: unusually high P/T ratios in continental crust. J Metamorph Geol 20:757 – 768.

Okay AI, Whitney DL (2010) Blueschists, Eclogites, Ophiolites, and Suture Zones in Northwest Turkey: A Review and A Field Excursion Guide. Ofioliti 35:131 – 172.

Önen AP, Hall R (2000) Sub-ophiolite metamorphic rocks from NW Anatolia, Turkey. J Metamorph Geol 18:483 – 495.

Önen AP (2003) Neotethyan ophiolitic rocks of the Anatolides of NW Turkey and comparison with Tauride ophiolites. Journal of the Geological Society 160: 947 – 962.

Plunder A, Agard P, Chopin C, Okay AI (2013) Geodynamics of the Tavşanlı zone, western Turkey: Insights into subduction/obduction processes. Tectonophysics 608:884 – 903.

Plunder A, Agard P, Chopin C, Pourteau A, Okay AI (2015) Accretion, underplating and exhumation along a subduction interface: From subduction initiation to continental subduction (Tavşanlı Zone, W. Turkey). Lithos: http://dx.doi.org/10.1016/j.lithos.2015.01.007.

Pourteau, A., Scherer E. E., Schmidt, A., Bast, R., 2014. Internal P-T-t Structure of Subduction Complexes- Insights from Lu-Hf Geochronology on Garnet and Lawsonite (Halilbağı, Central Anatolia). Abstract #V24C-02 presented at 2014 Fall Meeting, AGU, San Francisco, Calif., 15 -19 Dec.

Putlitz B, Cosca MA, Schumacher JC (2005) Prograde mica $^{40}Ar/^{39}Ar$ growth ages recorded in high pressure rocks (Syros, Cyclades, Greece). Chem Geol 214:79- 98.

Reddy SM, Kelley SP, Wheeler J (1996) A $^{40}Ar/^{39}Ar$ laser probe study of micas from the Sesia Zone, Italian Alps: implications for metamorphic and deformation histories. J Metamorph Geol 14:493 – 508.

Ruffet G, Feraud G, Balevre M, Kienast J-R (1995) Plateau ages and excess argon in phengites: an 40Ar-39Ar laser probe study of Alpine micas (Sesia Zone, Western Alps, northern Italy). Chem Geol 121:327 – 343.

Ruffet G, Gruau G, Ballevre M, Feraud G, Philippot P (1997) Rb-Sr and 40Ar-39Ar laser probe dating of high-pressure phengites from the Sesia Zone (Western Alps):

underscoring of excess argon and new age constraints on the high-pressure metamorphism. Chem Geol 141:1 – 18.

Scaillet S, Feraud F, Ballevre M, Amouric M (1992) Mg/Fe and [(Mg,Fe)Si-Al_2] compositional control on argon behavior in high-pressure white micas: A $^{40}Ar/^{39}Ar$ continuous laser-probe study from the Dora-Maira nappe of the internal western Alps, Italy. Geochim Cosmochim Ac 56:2851 – 2872.

Scaillet S (1996) Excess ^{40}Ar transport scale and mechanism in high-pressure phengites: A case study from an eclogitized metabasite of the Dora-Maira nappe, western Alps. Geochim Cosmochim Ac 60:1075 - 1090.

Seaton NCA, Whitney DL, Teyssier C, Toraman E, Heizler M (2009) Recrystallization of high-pressure marble (Sivrihisar, Turkey). Tectonophysics 479:241- 253.

Seaton NCA, Teyssier C, Whitney DL, Heizler MT (2014) Quartzite and calcite microfabric transitions in a pressure and temperature gradient, Sivrihisar, Turkey. Geodinamica Acta 26:191 – 206.

Sherlock S, Kelley S, Inger S, Harris N, Okay A (1999) ^{40}Ar-^{39}Ar and Rb-Sr geochronology of high-pressure metamorphism and exhumation history of the Tavşanlı Zone, NW Turkey. Contrib Mineral Petr 137:46 – 58.

Sherlock S, Kelley S (2002) Excess argon evolution in HP-LT rocks: a UVLAMP study of phengite and K-free minerals, NW Turkey. Chem Geol 182:619 – 636.

Shin TA, Catlos EJ, Jacob L, Black K (2012) Relationships between very high pressure subduction complex assemblages and intrusive granitoids in the Tavşanlı Zone, Sivrihisar Massif, central Anatolia. Tectonophysics 595:183 – 197.

Smye AJ, Warren CJ, Bickle MJ (2013) The signature of devolatisation: Extraneous ^{40}Ar systematics in high-pressure metamorphic rocks. Geochim Cosmochim Ac 113:94 – 112.

Teyssier C, Whitney DL, Toraman E, Seaton NCA (2010) Lawsonite vorticity and subduction kinematics. Geology 38:1123-1126.

Warren CJ, Sherlock SC, Kelley SP (2011) Interpreting high-pressure phengite $^{40}Ar/^{39}Ar$ laserprobe ages: an example from Saih Hatat, NE Oman. Contrib Mineral Petr 161:991 – 1009.

Warren CJ, Smye AJ, Kelley SP, Sherlock SC (2012a) Using white mica $^{40}Ar/^{39}Ar$ data as a tracer for fluid flow and permeability under high-P conditions: Tauern Window, Eastern Alps. J Metamorph Geol 30:63 – 80.

Warren CJ, Hanke F, Kelley SP (2012b) When can muscovite $^{40}Ar/^{39}Ar$ dating constrain the timing of metamorphic exhumation? Chem Geol 291:79- 86.

Whitney DL (2002) Coexisting andalusite, kyanite, and sillimanite: Sequential formation of three Al2SiO5 polymorphs during progressive metamorphism near the triple point, Sivrihisar, Turkey. Am Mineral 87:405 – 416.

Whitney DL, Davis PB (2006) Why is lawsonite eclogite so rare? Metamorphism and preservation of lawsonite eclogite, Sivrihisar, Turkey. Geology 34:473 – 476.

Whitney DL, Evans BW (2010) Abbreviations for names of rock-forming minerals. Am Mineral 95:185-187.

Whitney DL, Teyssier C, Toraman E, Seaton NCA, Fayon AK (2011) Metamorphic and tectonic evolution of a structurally continuous blueschist-to-Barrovian terrane, Sivrihisar Massif, Turkey. J Metamorph Geol 29:193 – 212.

Whitney DL, Teyssier C, Seaton NCA, Fornash KF (2014) Petrofabrics of high-pressure rocks exhumed at the slab-mantle interface from the 'point of no return' in an oceanic subduction zone (Sivrihisar, Turkey). Tectonics 33:2315-2341, doi: 10/1002/2014TC003677.

Wijbrans JR, McDougall I (1986) $^{40}Ar/^{39}Ar$ dating of white micas from an Alpine high-pressure metamorphic belt on Naxos (Greece): the resetting of the argon isotopic system. Contrib Mineral Petr 93:187 – 194.

Zack TA (2013) Cold slab-mantle interface: constraints from exceptionally well preserved lawsonite eclogites. Mineralogical Magazine 77:2574.

Table 1. Previous Geochronology in the Tavşanli Zone

Metamorphic Sole Rocks

Rock Type	Isotope System	Mineral	Age (Ma)	Location	Reference
Garnet Amphibolite	$^{40}Ar/^{39}Ar$[b]	amphibole	101.1 ± 3.8	Orhaneli	Harris et al. 1994
Amphibolite	$^{40}Ar/^{39}Ar$	amphibole	93 ± 2	Kütahya	Önen 2003

High-Pressure/Low Temperature Metamorphism

Rock Type	Isotope System	Mineral	Age (Ma)	Location	Reference
Lawsonite Grt Blueschist	Lu-Hf[e]	Lws, Grt	83.3 ± 1.8	Halilbağı	Mulcahy et al. 2014
Lawsonite Eclogite	Lu-Hf[e]	Lws, Grt	91.1 ± 1.3	Halilbağı	Mulcahy et al. 2014
Blueschist	K-Ar	white mica	65 ± 2	Mihaliçcik	Coğolu and Krummenacher 1967
Blueschist	K-Ar	white mica	82 ± 2	Mihaliçcik	Coğolu and Krummenacher 1967
Metachert	Rb-Sr[a]	white mica	78.5 ± 1.6	Tavşanli	Sherlock et al. 1999
	$^{40}Ar/^{39}Ar$[b]	white mica	75 ± 6 – 89 ± 1	Tavşanli	Sherlock et al. 1999
	$^{40}Ar/^{39}Ar$[d]	glaucophane	95 ± 9 – 117 ± 3	Tavşanli	Sherlock et al. 1999
	$^{40}Ar/^{39}Ar$[d]	white mica	20 ± 3 – 90 ± 2	Tavşanli	Sherlock et al. 1999
Foliated Metabasite	Rb-Sr[a]	white mica	79.7 ± 1.6	Tavşanli	Sherlock et al. 1999
	$^{40}Ar/^{39}Ar$[b]	white mica	86 ± 3 – 111 ± 3	Tavşanli	Sherlock et al. 1999
	$^{40}Ar/^{39}Ar$[b]	white mica	86 ± 3 – 123 ± 7	Tavşanli	Sherlock and Kelley 2002
Metachert	Rb-Sr[a]	white mica	80.1 ± 1.6	Sivrihisar	Sherlock et al. 1999
	$^{40}Ar/^{39}Ar$[b]	white mica	78 ± 2 – 109 ± 3	Sivrihisar	Sherlock et al. 1999
	$^{40}Ar/^{39}Ar$[d]	glaucophane	113 ± 11 – 192 ± 10	Sivrihisar	Sherlock et al. 1999
Foliated Metabasite	Rb-Sr[a]	white mica	82.8 ± 1.7	Sivrihisar	Sherlock et al. 1999
	$^{40}Ar/^{39}Ar$[b]	white mica	72 ± 3 – 109 ± 7	Sivrihisar	Sherlock et al. 1999
Metachert	$^{40}Ar/^{39}Ar$[b]	white mica	84.6 ± 6 – 124 ± 6	Orhaneli	Sherlock et al. 1999
	$^{40}Ar/^{39}Ar$[b]	white mica	84 ± 6 – 154 ± 7	Orhaneli	Sherlock and Kelley 2002
Metapelite	$^{40}Ar/^{39}Ar$[b]	white mica	94 ± 2 – 114 ± 2	Tavşanli	Sherlock et al. 1999
	$^{40}Ar/^{39}Ar$[c]	white mica	92 ± 11 – 192 ± 8	Tavşanli	Sherlock et al. 1999
Metapelite	$^{40}Ar/^{39}Ar$[b]	white mica	102 ± 4 – 118 ± 3	Tavşanli	Sherlock et al. 1999
	$^{40}Ar/^{39}Ar$[b]	white mica	90 ± 5 – 108 ± 3	Tavşanli	Sherlock and Kelley 2002
Marble	$^{40}Ar/^{39}Ar$[d]	white mica	87.9 ± 0.3	Sivrihisar	Seaton et al. 2009
Jadeite-Schist	$^{40}Ar/^{39}Ar$[b]	white mica	88.5 ± 1	Kocasu	Okay and Kelley 1994
Jadeite-Schist	$^{40}Ar/^{39}Ar$[b]	white mica	70.0 ± 1.2 – 83.5 ± 1.6	Kocasu	Okay and Kelley 1994
Glaucophane- Lawsonite Metachert	$^{40}Ar/^{39}Ar$[b]	sodic amphibole	108 ± 8	Orhaneli	Harris et al. 1994
Quartzite	$^{40}Ar/^{39}Ar$[d]	white mica	82.73 ± 0.30	Sivrihisar	Seaton et al. 2014
Quartzite	$^{40}Ar/^{39}Ar$[d]	white mica	88.76 ± 0.32	Sivrihisar	Seaton et al. 2014
Marble	$^{40}Ar/^{39}Ar$[d]	white mica	82.10 ± 0.28	Sivrihisar	Seaton et al. 2014

Barrovian Metamorphism

Rock Type	Isotope System	Mineral	Age (Ma)	Location	Reference
Marble	$^{40}Ar/^{39}Ar$[d]	white mica	58.8 ± 0.1 Ma	Sivrihisar	Seaton et al. 2009
Quartzite	$^{40}Ar/^{39}Ar$[d]	white mica	63.02 ± 0.41 Ma	Sivrihisar	Seaton et al. 2014
Quartzite	$^{40}Ar/^{39}Ar$[d]	white mica	60.36 ± 1.05 Ma	Sivrihisar	Seaton et al. 2014
Quartzite	$^{40}Ar/^{39}Ar$[d]	white mica	69.41 ± 0.65 Ma	Sivrihisar	Seaton et al. 2014
Quartzite	$^{40}Ar/^{39}Ar$[d]	white mica	59.46 ± 0.12 Ma	Sivrihisar	Seaton et al. 2014

Granitoid Intrusion

Rock Type	Isotope System	Mineral	Age (Ma)	Location	Reference
Sivrihisar granitoid (Syeno-monzonite)	K-Ar	hornblende	71 ± 3	Sivrihisar	Coğolu and Krummenacher 1967
Sivrihisar granitoid (monzonite)	U-Pb	zircon	90.82 ± 2.14	Sivrihisar	Gautier 1984
Sivrihisar granitoid (monzonite)	U-Pb	apatite	48.95 ± 4.49	Sivrihisar	Gautier 1984
Sivrihisar granitoid (Granodiorite)	$^{40}Ar/^{39}Ar$[c]	hornblende	53 ± 3	Sivrihisar	Sherlock et al. 1999
Sivrihisar granitoid	K-Ar	hornblende	56.8 ± 1.2	Sivrhisar	Delaloye and Bingöl 2000
	K-Ar	biotite	62.9 ± 1.3	Sivrihisar	Delaloye and Bingöl 2000
Sivrihisar granitoid	U-Pb	zircon	78.4 ± 8.5 – 42.4 ± 2.3	Sivrihisar	Shin et al. 2013
Kaymaz granitoid	U-Pb	zircon	84.98 ± 6.27	Sivrihisar	Gautier 1984
Kaymaz granitoid	U-Pb	zircon	42.5 ± 2.2 – 33.3 ± 2.0	Sivrihisar	Shin et al. 2013
Orhaneli granitoid (Granodiorite)	$^{40}Ar/^{39}Ar$[b]	biotite	52.6 ± 0.4	Orhaneli	Harris et al. 1994
Orhaneli granitoid	K-Ar	biotite	51.7 1.0 – 57.9 1.2	Orhaneli	Delaloye and Bingöl 2000
		hornblende	31.4 ± 0.6	Orhaneli	Delaloye and Bingöl 2000
Topuk granitoid (Granodiorite)	$^{40}Ar/^{39}Ar$[b]	biotite, hbl	47.8 ± 0.4	Orhaneli	Harris et al. 1994
Topuk granitoid	K-Ar	biotite	43.0 ± 2.7 – 50.9 ± 1.0	Orhaneli	Delaloye and Bingöl 2000
		hornblende	56.1 ± 1.1	Orhaneli	Delaloye and Bingöl 2000

[a] Whole-rock-mineral isochron ages.

[b] Ages reported are from *in situ* $^{40}Ar/^{39}Ar$ UV laser methods, represent age ranges obtained in a single sample.

[c] Ages reported are from samples analyzed by step-heating with an infrared (IR) laser.

[d] Ages reported are from samples analyzed by step-heating in a furnace.

Note: Rock names follow those reported in the literature.

Table 2. Major Element Composition of Phengite in Eclogite and Vein Samples

Lithology	Lawsonite Eclogite			Eclogite				Epidote Eclogite			Lawsonite Vein				Vein Margin		
Sample #	SV12-13e	SV12-13e	SV12-13e	SV12-10b	SV12-10b	SV12-10b	SV12-10b	SV12-15a	SV12-15a	SV12-15a	SV03-103	SV03-103	SV03-103	SV03-103	SV03-103	SV03-103	SV03-103
Textural Position				Core	Core	Rim	Rim				Core	Core	Rim	Rim			
SiO_2	51.87	51.18	51.58	48.31	48.28	50.59	51.39	50.72	50.02	51.59	48.47	48.30	51.34	51.45	50.75	51.33	50.66
TiO_2	0.16	0.19	0.19	0.55	0.60	0.18	0.18	0.16	0.16	0.14	0.44	0.46	0.21	0.11	0.19	0.23	0.21
Al_2O_3	23.73	23.72	24.33	30.60	30.72	25.44	25.07	26.06	26.93	24.94	30.43	30.13	24.27	23.65	24.78	24.15	24.64
Cr_2O_3	bdl	0.01	0.05	0.09	0.05	0.03	0.02	0.03	0.02	0.05	bdl	0.02	0.01	0.07	0.12	0.04	0.05
FeO*	3.69	3.77	3.58	2.46	2.35	4.26	4.07	3.01	3.06	3.10	2.64	2.65	3.48	3.87	4.16	3.52	3.59
MnO	bdl	bdl	0.01	0.01	bdl	bdl	bdl	0.01	0.03	0.04	0.01	bdl	bdl	0.03	0.03	0.03	bdl
MgO	4.29	4.30	4.42	3.00	2.93	4.38	4.55	3.98	3.85	4.39	2.46	2.49	4.33	4.40	4.26	4.29	4.21
CaO	bdl	0.05	0.02	0.01	0.02	0.01	0.03	0.02	0.01	0.16	bdl	0.01	0.02	bdl	0.01	0.05	0.04
Na_2O	0.16	0.19	0.19	1.12	1.11	0.17	0.13	0.18	0.19	0.14	1.23	1.16	0.15	0.10	0.19	0.16	0.16
K_2O	11.11	11.26	10.95	8.84	8.95	10.09	10.03	11.09	11.14	10.96	9.65	9.73	11.22	11.27	11.09	11.11	11.04
Total (Wt. %)	95.01	94.67	95.32	94.99	95.01	95.15	95.47	95.26	95.41	95.51	95.33	94.95	95.03	94.95	95.58	94.91	94.60
Cations calculated on 11 oxygen basis																	
Si	3.51	3.48	3.47	3.22	3.22	3.41	3.44	3.41	3.36	3.46	3.24	3.24	3.47	3.49	3.43	3.48	3.44
Al	1.89	1.90	1.93	2.41	2.41	2.02	1.98	2.07	2.14	1.97	2.40	2.38	1.94	1.89	1.97	1.93	1.97
Ti	0.01	0.01	0.01	0.03	0.03	0.01	0.01	0.01	0.01	0.01	0.02	0.02	0.01	0.01	0.01	0.01	0.01
Cr	0.00	0.00	0.00	0.00	0.00	0.00	0.00	0.00	0.00	0.00	0.00	0.00	0.00	0.00	0.01	0.00	0.00
Fe	0.21	0.21	0.20	0.14	0.13	0.24	0.22	0.17	0.17	0.17	0.15	0.15	0.20	0.22	0.24	0.20	0.20
Mn	0.00	0.00	0.00	0.00	0.00	0.00	0.00	0.00	0.00	0.00	0.00	0.00	0.00	0.00	0.00	0.00	0.00
Mg	0.43	0.44	0.44	0.30	0.29	0.44	0.45	0.40	0.39	0.44	0.25	0.25	0.44	0.44	0.43	0.43	0.43
Ca	0.00	0.00	0.00	0.00	0.00	0.00	0.00	0.00	0.00	0.01	0.00	0.00	0.00	0.00	0.00	0.00	0.00
Na	0.02	0.02	0.02	0.14	0.14	0.02	0.02	0.02	0.02	0.02	0.16	0.15	0.02	0.01	0.02	0.02	0.02
K	0.96	0.98	0.94	0.75	0.76	0.87	0.86	0.95	0.96	0.94	0.82	0.83	0.97	0.98	0.96	0.96	0.96
Na/Na + K	0.02	0.02	0.02	0.16	0.16	0.02	0.02	0.02	0.02	0.02	0.16	0.15	0.02	0.01	0.02	0.02	0.02
X_{Mg}	0.67	0.68	0.69	0.68	0.69	0.65	0.67	0.70	0.70	0.72	0.63	0.63	0.69	0.67	0.64	0.68	0.68

bdl = below detection limit

Table 3. Major Element Composition of Phengite in Blueschist and Quartzite Samples

Lithology	Lawsonite Garnet Blueschist			Lawsonite Blueschist			Lawsonite Garnet Blueschist			Quartzite			Quartzite		
Sample #	SV13-06b	SV13-06b	SV13-06b	SV13-15	SV13-15	SV13-15	SV12-59	SV12-59	SV12-59	SV10-06A1	SV10-06A1	SV10-06A1	SV10-08	SV10-08	SV10-08
Textural Position										Layer	Layer	Grain	Layer	Layer	Layer
SiO_2	50.16	50.32	50.26	51.39	52.57	51.25	52.26	52.23	52.10	51.41	50.02	51.54	52.15	52.30	52.52
TiO_2	0.18	0.18	0.16	0.10	0.03	0.12	0.18	0.18	0.17	0.05	0.11	0.10	0.10	0.09	0.11
Al_2O_3	23.29	23.43	23.90	21.66	21.63	23.00	22.02	22.58	22.97	24.14	25.51	24.95	22.96	23.72	23.61
Cr_2O_3	0.04	0.02	0.02	0.02	bdl	0.01	bdl	0.04	bdl	bdl	0.01	bdl	0.02	bdl	0.01
FeO*	4.41	4.37	4.07	4.77	3.80	4.72	4.37	4.13	4.24	4.05	3.71	4.32	3.47	3.55	4.32
MnO	0.02	bdl	bdl	0.03	0.08	0.01	bdl	0.02	0.01	0.13	0.09	0.07	0.09	0.09	0.05
MgO	4.36	4.41	4.20	4.91	5.10	4.49	4.60	4.54	4.54	3.86	3.90	3.72	5.07	4.95	5.18
CaO	0.07	0.09	0.20	0.06	0.06	0.09	0.03	bdl	bdl	0.03	0.03	0.02	0.06	0.04	0.06
Na_2O	0.11	0.11	0.20	0.08	0.07	0.09	0.10	0.09	0.08	0.05	0.29	0.08	0.03	0.05	0.09
K_2O	10.98	10.99	10.56	10.98	11.11	11.00	11.07	11.20	11.14	10.60	10.84	10.98	10.35	10.43	10.06
Total (Wt. %)	93.62	93.92	93.57	94.00	94.45	94.78	94.63	95.01	95.25	94.32	94.51	95.78	94.30	95.22	96.01
Cations calculated on 11 oxygen basis															
Si	3.47	3.46	3.46	3.54	3.58	3.50	3.56	3.54	3.53	3.50	3.41	3.46	3.53	3.51	3.50
Al	1.90	1.90	1.94	1.76	1.74	1.85	1.77	1.81	1.83	1.94	2.05	1.98	1.83	1.88	1.86
Ti	0.01	0.01	0.01	0.01	0.00	0.01	0.01	0.01	0.01	0.00	0.01	0.01	0.00	0.00	0.01
Cr	0.00	0.00	0.00	0.00	0.00	0.00	0.00	0.00	0.00	0.00	0.00	0.00	0.00	0.00	0.00
Fe	0.25	0.25	0.23	0.27	0.22	0.27	0.25	0.23	0.24	0.23	0.21	0.24	0.20	0.20	0.24
Mn	0.00	0.00	0.00	0.00	0.00	0.00	0.00	0.00	0.00	0.01	0.01	0.00	0.01	0.01	0.00
Mg	0.45	0.45	0.43	0.50	0.52	0.46	0.47	0.46	0.46	0.39	0.40	0.37	0.51	0.50	0.52
Ca	0.01	0.01	0.01	0.00	0.00	0.01	0.00	0.00	0.00	0.00	0.00	0.00	0.00	0.00	0.00
Na	0.01	0.01	0.03	0.01	0.01	0.01	0.01	0.01	0.01	0.01	0.04	0.01	0.00	0.01	0.01
K	0.97	0.96	0.93	0.96	0.97	0.96	0.96	0.97	0.96	0.92	0.94	0.94	0.89	0.89	0.86
Na/Na + K	0.01	0.01	0.03	0.01	0.01	0.01	0.01	0.01	0.01	0.01	0.04	0.01	0.00	0.01	0.01
X_{Mg}	0.64	0.64	0.65	0.65	0.70	0.63	0.65	0.67	0.66	0.63	0.66	0.61	0.72	0.71	0.68

bdl = below detection limit

Table 4. *In situ* UV Laser $^{40}Ar/^{39}Ar$ Results

Analysis #	^{40}Ar (fA)	±1s	^{39}Ar (fA)	±1s	^{38}Ar (fA)	±1s	^{37}Ar (fA)	±1s	^{36}Ar (fA)	±1s	^{39}Ar Mol x 10^{17}	$^{40}Ar^{*}/^{39}Ar$	±1s	$\%^{40}Ar^{*}$	Age (Ma)	±1s
Eclogite Samples																
SV12-13c: Lawsonite eclogite																
J = 0.002280 ± 0.000003																
1	15.01055	0.04653	0.57094	0.00796	0.01020	0.00129	0.00773	0.00191	0.00787	0.00118	2.7896	22.17	0.37	84.4	90.2	2.8
2	13.36620	0.05646	0.50406	0.00716	0.00877	0.00154	0.00360	0.00191	0.00709	0.00116	2.4628	22.31	0.39	84.2	90.8	3.0
3	11.61895	0.04022	0.48150	0.00707	0.00397	0.00117	0.03129	0.00214	0.00238	0.00115	2.3526	22.66	0.36	93.9	92.2	3.1
4	14.72016	0.04701	0.54856	0.00662	0.00687	0.00114	0.02165	0.00198	0.00601	0.00121	2.6803	23.56	0.33	87.8	95.8	2.9
5	14.45331	0.04528	0.61120	0.00689	0.00722	0.00127	0.00000	0.00184	0.00429	0.00120	2.9863	21.54	0.27	91.1	87.7	2.5
6	10.11061	0.04528	0.39559	0.00662	0.00382	0.00136	0.00480	0.00177	0.00485	0.00125	1.9329	21.89	0.44	85.7	89.1	4.0
7	10.78725	0.04876	0.41995	0.00762	0.00494	0.00127	0.00000	0.00198	0.00533	0.00123	2.0518	21.89	0.47	85.3	89.1	3.8
8	13.75664	0.04549	0.57176	0.00788	0.00593	0.00127	0.00000	0.00219	0.00181	0.00114	2.7936	23.10	0.34	96.1	93.9	2.7
9	11.46359	0.04383	0.43277	0.00716	0.00453	0.00127	0.01400	0.00212	0.00346	0.00112	2.1145	24.10	0.44	91.0	97.9	3.4
10	11.06845	0.04383	0.45874	0.00752	0.00774	0.00127	0.00000	0.00198	0.00190	0.00112	2.2414	22.88	0.40	94.9	93.0	3.3
11	12.86866	0.04528	0.49294	0.00815	0.00983	0.00122	0.01350	0.00184	0.00262	0.00118	2.4085	24.52	0.43	94.0	99.5	3.2
12	11.17447	0.04188	0.40461	0.00585	0.00726	0.00142	0.02581	0.00192	0.00411	0.00118	1.9769	24.59	0.41	89.1	99.8	3.7
SV12-10B: Eclogite																
J = 0.006889 ± 0.000004																
1	10.01632	0.06140	1.25792	0.01379	0.02745	0.00137	0.05676	0.00171	0.00360	0.00075	6.1459	7.11	0.10	89.4	87.6	2.4
2	7.71056	0.05547	0.93833	0.01226	0.01449	0.00120	0.13962	0.00214	0.00147	0.00071	4.5845	7.77	0.12	94.5	95.4	3.0
3	6.55075	0.04751	0.79280	0.01250	0.01305	0.00117	0.16836	0.00205	0.00154	0.00069	3.8735	7.71	0.14	93.3	94.7	3.5
4	10.68143	0.04314	1.39288	0.01366	0.01722	0.00152	0.00567	0.00139	0.00041	0.00072	6.8054	7.58	0.08	98.8	93.1	2.1
5	11.10480	0.04314	1.40431	0.01366	0.01934	0.00144	0.00000	0.00125	0.00284	0.00076	6.8612	7.30	0.08	92.4	89.8	2.2
6	8.68190	0.04245	1.09855	0.01287	0.01636	0.00129	0.07491	0.00163	0.00186	0.00070	5.3673	7.40	0.10	93.7	91.1	2.5
7	7.57875	0.02550	1.03265	0.00721	0.01114	0.00100	0.01181	0.00119	0.00087	0.00064	5.0453	7.09	0.06	96.6	87.2	2.3
8	7.73646	0.03191	1.02478	0.00877	0.01211	0.00105	0.01104	0.00110	0.00148	0.00062	5.0069	7.12	0.07	94.3	87.6	2.3
9	7.50498	0.02860	1.00580	0.00877	0.01265	0.00103	0.01135	0.00115	0.00202	0.00060	4.9142	6.86	0.07	92.0	84.5	2.3
10	9.00082	0.03106	1.17407	0.00868	0.01581	0.00115	0.00258	0.00112	0.00090	0.00063	5.7363	7.44	0.06	97.0	91.4	2.1
11	7.55120	0.02941	0.99293	0.00841	0.01160	0.00118	0.03010	0.00143	0.00126	0.00063	4.8513	7.23	0.07	95.1	88.9	2.4
12	7.95269	0.03191	1.05386	0.01012	0.01307	0.00112	0.04474	0.00134	0.00126	0.00064	5.1490	7.19	0.08	95.3	88.5	2.3
SV12-15a: Epidote eclogite																
J = 0.002288 ± 0.000003																
1	9.97567	0.04022	0.38564	0.00707	0.00335	0.00118	0.00075	0.00191	0.00976	0.00127	1.8842	18.30	0.48	70.8	75.1	4.2
2	8.68629	0.04123	0.41391	0.00666	0.00803	0.00122	0.00152	0.00191	0.00194	0.00114	2.0224	19.58	0.35	93.3	80.2	3.5
3	11.07070	0.04687	0.52910	0.00717	0.01068	0.00138	0.00039	0.00191	0.00055	0.00117	2.5852	20.61	0.29	98.5	84.3	2.9
4	16.66790	0.04771	0.80960	0.00960	0.01183	0.00146	0.00688	0.00184	0.00045	0.00137	3.9557	20.42	0.25	99.2	83.6	2.2
6	8.61848	0.04168	0.38447	0.00671	0.00390	0.00148	0.00100	0.00178	0.00456	0.00104	1.8785	18.87	0.40	84.2	77.4	3.5
7	8.32995	0.03581	0.34778	0.00573	0.00372	0.00119	0.00149	0.00205	0.00461	0.00108	1.6993	19.98	0.40	83.5	81.8	3.9
8	8.30620	0.03912	0.32993	0.00564	0.00526	0.00119	0.00121	0.00198	0.00640	0.00111	1.6120	19.37	0.44	77.0	79.4	4.3
9	10.04837	0.03912	0.36547	0.00635	0.00645	0.00116	0.02655	0.00220	0.01128	0.00111	1.7857	18.29	0.48	66.5	75.0	3.9
10	7.26159	0.03912	0.30737	0.00582	0.00509	0.00110	0.00000	0.00198	0.00230	0.00114	1.5018	21.38	0.46	90.6	87.4	4.7
11	9.79471	0.03912	0.32639	0.00633	0.00671	0.00115	0.00950	0.00184	0.00966	0.00125	1.5947	21.17	0.58	70.6	86.6	4.9
12	7.38490	0.03581	0.30620	0.00685	0.00501	0.00129	0.00304	0.00198	0.00230	0.00117	1.4961	21.87	0.54	90.7	89.4	5.0

Lawsonite Vein Sample

SV03-103: Lawsonite vein

J = 0.002275 ± 0.000003

1	8.19882	0.03774	0.33394	0.00806	0.00787	0.00152	0.00153	0.00234	0.00249	0.00116	1.6315	22.32	0.59	91.0	90.7	4.6
2	12.98269	0.04888	0.51937	0.00632	0.00813	0.00159	0.01757	0.00206	0.00190	0.00105	2.5376	23.90	0.31	95.7	96.9	2.7
3	9.84464	0.03754	0.39071	0.00595	0.00567	0.00119	0.00000	0.00191	0.00328	0.00109	1.9090	22.68	0.39	90.1	92.1	3.6
4	11.31449	0.04465	0.47244	0.01031	0.00659	0.00133	0.00283	0.00198	0.00404	0.00112	2.3083	21.39	0.52	89.3	87.0	3.4
5	10.13630	0.04305	0.38468	0.00664	0.00552	0.00145	0.00169	0.00191	0.00258	0.00103	1.8795	24.34	0.46	92.4	98.6	3.6
6	11.91638	0.04134	0.43717	0.01056	0.00779	0.00117	0.00018	0.00198	0.00272	0.00112	2.1360	25.39	0.65	93.2	102.8	3.9
7	10.86336	0.04478	0.45193	0.00751	0.00675	0.00119	0.00127	0.00170	0.00373	0.00106	2.2081	21.56	0.41	89.7	87.7	3.1
8	8.83022	0.04050	0.33931	0.00716	0.00580	0.00137	0.01736	0.00198	0.00496	0.00114	1.6579	21.66	0.55	83.3	88.0	4.4
9[M]	10.53203	0.04518	0.41422	0.00685	0.00706	0.00137	0.00345	0.00205	0.00526	0.00119	2.0239	21.63	0.43	85.1	87.9	3.7
10[M]	12.32783	0.04528	0.50371	0.00725	0.00853	0.00122	0.01523	0.00216	0.00041	0.00120	2.4611	24.23	0.36	99.0	98.2	3.1
11[M]	13.18074	0.04272	0.49345	0.00752	0.00674	0.00116	0.00867	0.00177	0.00495	0.00130	2.4110	23.71	0.41	88.8	96.2	3.4
12[M]	9.87122	0.03860	0.37398	0.00636	0.00616	0.00116	0.01450	0.00192	0.00108	0.00131	1.8273	25.53	0.45	96.8	103.3	4.5
13[M]	9.99169	0.03860	0.36646	0.00752	0.00612	0.00118	0.00909	0.00200	0.00309	0.00119	1.7905	24.74	0.56	90.8	100.2	4.3
14[M]	12.73470	0.03842	0.47408	0.00686	0.00700	0.00108	0.02789	0.00213	0.00541	0.00111	2.3164	23.46	0.39	87.4	95.1	3.1
15[M]	10.39875	0.03612	0.44123	0.00810	0.00725	0.00106	0.00838	0.00213	0.00169	0.00115	2.1559	22.42	0.43	95.2	91.0	3.5
16[M]	10.12732	0.04080	0.42916	0.00574	0.00887	0.00108	0.00995	0.00198	0.00523	0.00098	2.0969	19.95	0.33	84.6	81.2	2.9
17[M]	10.13015	0.04162	0.41261	0.00696	0.00520	0.00111	0.00376	0.00198	0.00517	0.00107	2.0160	20.80	0.42	84.8	84.6	3.4
18	10.23939	0.14204	0.33087	0.00658	0.00744	0.00164	0.00457	0.00228	0.00999	0.00104	1.6166	21.93	0.74	70.9	89.1	4.4
19	11.15649	0.04327	0.39785	0.00630	0.00880	0.00120	0.00601	0.00205	0.00568	0.00102	1.9439	23.77	0.45	84.8	96.4	3.4
20	10.83385	0.04494	0.40429	0.00583	0.00988	0.00115	0.00519	0.00191	0.00705	0.00108	1.9754	21.58	0.40	80.6	87.7	3.4
21	10.12859	0.04561	0.41726	0.00716	0.00592	0.00131	0.00000	0.00177	0.00432	0.00118	2.0387	21.18	0.42	87.3	86.1	3.7

J = 0.006842 ± 0.000047

2	15.78002	0.03489	1.24802	0.00598	0.01866	0.00113	0.05717	0.00137	0.00894	0.00090	6.0975	10.51	0.07	83.1	127.1	2.6
3	12.02904	0.03489	1.45222	0.00762	0.01969	0.00112	0.02230	0.00120	0.00444	0.00087	7.0952	7.37	0.05	89.0	90.0	2.2
4	9.37046	0.05382	1.09990	0.01487	0.01720	0.00160	0.00000	0.00147	0.00342	0.00079	5.3739	7.59	0.12	89.1	92.6	2.9
5	10.95970	0.04982	1.37036	0.01487	0.02078	0.00168	0.00000	0.00137	0.00232	0.00079	6.6953	7.49	0.09	93.7	91.4	2.3
6	11.02038	0.04827	1.41812	0.01487	0.02131	0.00160	0.01902	0.00147	0.00231	0.00078	6.9286	7.29	0.09	93.8	89.0	2.2
7	12.51260	0.04904	1.54471	0.01414	0.01831	0.00160	0.00000	0.00125	0.00388	0.00076	7.5471	7.35	0.08	90.7	89.8	2.0
8[M]	8.95890	0.03493	1.03854	0.00590	0.01542	0.00099	0.00225	0.00107	0.00439	0.00059	5.0742	7.36	0.06	85.4	89.9	2.1
9[M]	6.25029	0.03220	0.71644	0.00564	0.00927	0.00090	0.08063	0.00131	0.00348	0.00058	3.5004	7.29	0.08	83.6	89.1	3.0
10[M]	9.58952	0.02953	1.17235	0.00528	0.01638	0.00113	0.00230	0.00114	0.00308	0.00062	5.7279	7.39	0.05	90.4	90.3	2.0
11[M]	7.95533	0.03220	1.03549	0.00485	0.01465	0.00099	0.00245	0.00106	0.00307	0.00058	5.0593	6.80	0.05	88.5	83.2	2.1
12[M]	9.23933	0.03220	1.09535	0.00766	0.01247	0.00104	0.00786	0.00103	0.00376	0.00058	5.3517	7.41	0.07	87.9	90.5	2.0
13	8.03213	0.02953	0.97002	0.00520	0.01135	0.00098	0.00363	0.00103	0.00403	0.00061	4.7394	7.04	0.05	85.0	86.1	2.3
14	8.71004	0.03041	1.04835	0.00709	0.01459	0.00099	0.00153	0.00116	0.00231	0.00062	5.1221	7.65	0.06	92.1	93.3	2.2

Blueschist Samples

SV13-06B: Lawsonite garnet blueschist

J = 0.006964 ± 0.000009

1	10.48210	0.04771	1.16055	0.00693	0.01909	0.00113	0.00173	0.00110	0.00343	0.00066	5.6701	8.15	0.07	90.2	101.0	2.2
2	10.88437	0.03966	1.12735	0.00721	0.01677	0.00111	0.00714	0.00109	0.00349	0.00081	5.5079	8.73	0.07	90.4	108.0	2.7
3	10.82496	0.03640	1.28901	0.00570	0.01896	0.00111	0.00000	0.00111	0.00273	0.00083	6.2978	7.76	0.05	92.5	96.4	2.4
4	12.29540	0.03883	1.41405	0.00798	0.01972	0.00108	0.00455	0.00119	0.00360	0.00086	6.9087	7.93	0.06	91.3	98.4	2.3
5	13.29624	0.03801	1.44667	0.00655	0.02139	0.00098	0.00079	0.00101	0.00387	0.00086	7.0680	8.39	0.05	91.3	103.9	2.2
6	13.77501	0.03801	1.48566	0.00808	0.02190	0.00107	0.00000	0.00111	0.00347	0.00084	7.2585	8.57	0.06	92.5	106.1	2.1
7	12.86553	0.03689	1.36225	0.00776	0.01919	0.00101	0.00817	0.00119	0.00372	0.00095	6.6556	8.63	0.06	91.4	106.8	2.6
8	11.94765	0.03048	1.37646	0.00718	0.01972	0.00095	0.00072	0.00109	0.00465	0.00090	6.7250	7.67	0.05	88.4	95.2	2.4
9	10.64391	0.03441	1.27191	0.00671	0.01750	0.00106	0.00261	0.00113	0.00421	0.00090	6.2142	7.38	0.05	88.2	91.7	2.6
10	10.92795	0.02729	1.08736	0.00405	0.01463	0.00087	0.00577	0.00103	0.00494	0.00071	5.3126	8.69	0.05	86.5	107.5	2.4
11	8.81195	0.02385	1.12150	0.00590	0.01398	0.00082	0.00162	0.00105	0.00400	0.00071	5.4794	6.79	0.05	86.4	84.6	2.4
12	10.87665	0.03362	1.19539	0.00640	0.01480	0.00079	0.00269	0.00118	0.00594	0.00073	5.8404	7.61	0.06	83.7	94.5	2.3
13	7.99539	0.04163	0.95998	0.00824	0.01347	0.00116	0.00266	0.00112	0.00260	0.00064	4.6903	7.52	0.08	90.3	93.4	2.6
14	9.10009	0.03712	1.01453	0.00806	0.01447	0.00108	0.00382	0.00112	0.00290	0.00066	4.9569	8.11	0.08	90.5	100.6	2.5
15	9.61444	0.03448	1.04719	0.00610	0.01326	0.00115	0.00045	0.00112	0.00382	0.00064	5.1164	8.09	0.06	88.1	100.3	2.3
16	9.80165	0.03276	1.03615	0.00877	0.01533	0.00115	0.00111	0.00113	0.00270	0.00064	5.0624	8.68	0.09	91.8	107.4	2.4
17	7.95914	0.02780	0.96316	0.00798	0.01159	0.00106	0.00058	0.00118	0.00124	0.00069	4.7059	7.88	0.07	95.4	97.7	2.7

SV13-15: Lawsonite blueschist

J = 0.006947 ± 0.000018

1	3.40948	0.05061	0.35030	0.01287	0.00818	0.00132	0.15393	0.00188	0.00281	0.00076	1.7115	7.40	0.38	76.0	91.8	8.7
2	10.53242	0.05464	1.25292	0.01487	0.01738	0.00160	0.12724	0.00214	0.00279	0.00076	6.1215	7.75	0.11	92.3	96.0	2.5
3	5.75041	0.04751	0.63520	0.01262	0.01115	0.00130	0.27946	0.00259	0.00220	0.00078	3.1035	8.08	0.19	89.3	100.0	4.9
4	4.84142	0.05061	0.51474	0.01312	0.00855	0.00116	0.48064	0.00287	0.00363	0.00074	2.5149	7.44	0.25	79.0	92.2	5.8
5	8.81351	0.04601	1.02637	0.01352	0.01350	0.00137	0.10832	0.00188	0.00198	0.00073	5.0146	8.02	0.12	93.5	99.3	2.9
6	8.89783	0.04982	1.08231	0.01332	0.01516	0.00144	0.13478	0.00205	0.00197	0.00078	5.2879	7.69	0.11	93.6	95.3	2.9
7	8.92656	0.04601	1.06289	0.01325	0.01596	0.00130	0.14684	0.00205	0.00251	0.00072	5.1931	7.71	0.11	91.8	95.5	2.8
8	8.66792	0.04384	0.96905	0.01407	0.01307	0.00136	0.26593	0.00232	0.00191	0.00072	4.7346	8.40	0.14	93.9	103.7	3.1
9	8.33835	0.04384	1.00828	0.01366	0.01560	0.00135	0.02138	0.00147	0.00246	0.00074	4.9263	7.54	0.12	91.2	93.5	3.0
10	5.40276	0.03023	0.67731	0.00738	0.00962	0.00101	0.22657	0.00224	0.00180	0.00063	3.3092	7.23	0.10	90.7	89.7	3.5
11	5.87059	0.03191	0.72326	0.00772	0.00938	0.00112	0.13481	0.00151	0.00138	0.00064	3.5337	7.57	0.10	93.3	93.8	3.4
12	8.74912	0.03362	1.08228	0.00780	0.01080	0.00099	0.06002	0.00160	0.00190	0.00065	5.2878	7.57	0.07	93.6	93.8	2.3
13	2.63035	0.03106	0.29624	0.00648	0.00311	0.00098	0.29857	0.00224	0.00220	0.00062	1.4474	6.81	0.22	76.7	84.6	7.8
14	9.88285	0.03276	1.18680	0.00832	0.01425	0.00123	0.02843	0.00143	0.00217	0.00064	5.7985	7.78	0.06	93.5	96.4	2.1
15	8.17263	0.03362	0.95207	0.00552	0.01331	0.00102	0.14528	0.00160	0.00236	0.00062	4.6517	7.86	0.06	91.6	97.3	2.5
16	9.08837	0.03536	1.10231	0.00755	0.01325	0.00105	0.08440	0.00160	0.00369	0.00064	5.3857	7.25	0.06	88.0	90.0	2.2

SV12-59: Lawsonite garnet blueschist (Ikipinar)

J = 0.002283 ± 0.000002

1	12.73440	0.04219	0.58094	0.00878	0.01326	0.00162	0.00443	0.00184	0.00449	0.00107	2.8384	19.60	0.33	89.5	80.1	2.5
2	10.25258	0.04050	0.44330	0.00851	0.00863	0.00129	0.00680	0.00206	0.00503	0.00109	2.1659	19.73	0.45	85.4	80.6	3.3
3	10.47995	0.04478	0.46669	0.00655	0.00699	0.00137	0.00020	0.00198	0.00420	0.00118	2.2802	19.76	0.32	88.0	80.7	3.2
4	12.12479	0.04653	0.50508	0.00787	0.00920	0.00129	0.00012	0.00214	0.00734	0.00115	2.4678	19.66	0.38	81.9	80.3	3.0
5	13.31851	0.04168	0.52986	0.00783	0.00626	0.00126	0.00000	0.00205	0.00395	0.00111	2.5889	22.90	0.37	91.2	93.3	2.8
6	10.89688	0.04082	0.44250	0.00738	0.00719	0.00137	0.00150	0.00184	0.00694	0.00115	2.1621	19.94	0.41	81.0	81.4	3.4
7	14.10302	0.04050	0.52017	0.00747	0.00759	0.00108	0.00238	0.00200	0.00666	0.00110	2.5416	23.28	0.39	85.9	94.8	2.8
8	14.27480	0.04653	0.62005	0.00747	0.00881	0.00135	0.02645	0.00233	0.00439	0.00111	3.0296	20.91	0.28	90.9	85.3	2.4
9	13.22657	0.04305	0.56684	0.00858	0.01022	0.00126	0.02654	0.00219	0.00534	0.00103	2.7696	20.53	0.36	88.0	83.8	2.5
10	13.18270	0.04305	0.56679	0.00675	0.00849	0.00126	0.01305	0.00219	0.00622	0.00103	2.7694	19.98	0.28	85.9	81.6	2.4
11	13.58467	0.04549	0.61951	0.00779	0.00577	0.00127	0.00203	0.00205	0.00347	0.00114	3.0269	20.25	0.28	92.4	82.7	2.4
12	12.76235	0.04140	0.55510	0.00725	0.00630	0.00124	0.00581	0.00205	0.00271	0.00112	2.7122	21.53	0.31	93.7	87.8	2.7

Quartzite Samples

SV10-06A1: Quartzite

J = 0.006919 ± 0.000008

2	11.03973	0.02818	1.18509	0.00640	0.01624	0.00099	0.00417	0.00103	0.00556	0.00072	5.7901	7.91	0.06	85.0	97.5	2.3
3	10.36778	0.03087	1.03554	0.00522	0.01403	0.00102	0.00415	0.00102	0.00504	0.00076	5.0594	8.56	0.06	85.5	105.3	2.7
4	9.31867	0.02968	1.07234	0.00579	0.01563	0.00100	0.00295	0.00101	0.00576	0.00090	5.2392	7.09	0.05	81.6	87.6	3.1
5	14.68938	0.03312	1.45382	0.00665	0.02144	0.00107	0.00000	0.00100	0.00549	0.00089	7.1030	8.97	0.05	88.8	110.2	2.3
6	13.89021	0.03400	1.38657	0.00762	0.01883	0.00097	0.00057	0.00108	0.00620	0.00089	6.7745	8.68	0.06	86.7	106.7	2.4
7	13.62816	0.02802	1.30452	0.00513	0.01875	0.00095	0.00202	0.00104	0.00758	0.00089	6.3736	8.71	0.05	83.4	107.1	2.5
8	10.77142	0.03053	1.04945	0.00560	0.01606	0.00092	0.00235	0.00102	0.00579	0.00086	5.1274	8.61	0.06	84.0	105.9	3.0
9	12.90022	0.03225	1.24224	0.00494	0.01662	0.00103	0.00257	0.00105	0.00564	0.00090	6.0693	9.03	0.05	87.0	110.9	2.7
10	10.63101	0.03312	1.13098	0.00713	0.01619	0.00094	0.00029	0.00112	0.00572	0.00084	5.5257	7.89	0.07	83.9	97.3	2.8
11	12.93149	0.03053	1.19801	0.00732	0.01839	0.00091	0.00243	0.00097	0.00692	0.00092	5.8532	9.07	0.07	84.0	111.4	2.8
12	11.89293	0.02968	1.14974	0.00762	0.01621	0.00094	0.00011	0.00117	0.00492	0.00082	5.6174	9.06	0.07	87.7	111.3	2.7
13	6.99025	0.03362	0.63794	0.00696	0.00773	0.00105	0.01452	0.00122	0.00344	0.00067	3.1169	9.35	0.13	85.3	114.7	3.9
14	6.34331	0.02941	0.59051	0.00680	0.00717	0.00110	0.00013	0.00106	0.00272	0.00063	2.8851	9.37	0.13	87.2	114.9	4.0
15	9.68850	0.03191	0.90418	0.00772	0.01204	0.00139	0.00915	0.00119	0.00364	0.00064	4.4177	9.51	0.10	88.8	116.7	2.7
16	9.90219	0.02953	0.92936	0.00663	0.01340	0.00097	0.00757	0.00111	0.00547	0.00057	4.5407	8.90	0.08	83.5	109.3	2.3
17	9.53168	0.02865	0.87893	0.00672	0.01309	0.00112	0.00741	0.00115	0.00461	0.00058	4.2943	9.28	0.09	85.6	113.8	2.5
18	11.26495	0.02608	0.97900	0.00627	0.01334	0.00095	0.00231	0.00100	0.00412	0.00058	4.7833	10.25	0.08	89.1	125.4	2.3
19	10.93987	0.03220	1.04859	0.00766	0.01485	0.00082	0.00148	0.00118	0.00514	0.00058	5.1233	8.97	0.08	86.0	110.1	2.2
20	10.53359	0.02693	1.11757	0.00581	0.01387	0.00095	0.00018	0.00105	0.00461	0.00059	5.4603	8.19	0.06	86.9	100.9	2.0

SV10-08:Quartzite

J = 0.007019 ± 0.000006

1	4.50018	0.03097	0.54154	0.00391	0.00763	0.00093	0.00074	0.00107	0.00201	0.00065	2.6482	7.20	0.08	86.7	90.2	4.5
2	15.82645	0.05238	2.06982	0.00584	0.03185	0.00122	0.00113	0.00105	0.00658	0.00071	10.1218	6.69	0.03	87.6	84.0	1.3
3	12.95973	0.04380	1.67433	0.00825	0.02428	0.00112	0.00008	0.00107	0.00310	0.00072	8.1878	7.18	0.05	92.9	90.0	1.7
4	13.78936	0.04099	1.75153	0.00786	0.02506	0.00113	0.00079	0.00103	0.00241	0.00065	8.5652	7.45	0.04	94.8	93.3	1.4
5	13.62573	0.04855	1.72882	0.00786	0.02574	0.00122	0.00025	0.00104	0.00297	0.00070	8.4542	7.36	0.05	93.5	92.2	1.6
6	14.35348	0.03948	1.88977	0.00793	0.02759	0.00115	0.00266	0.00109	0.00302	0.00071	9.2413	7.11	0.04	93.8	89.2	1.5
7	12.60326	0.03509	1.65708	0.00486	0.02369	0.00114	0.00486	0.00113	0.00189	0.00065	8.1034	7.26	0.03	95.6	91.0	1.5
8	11.10657	0.03859	1.48351	0.00706	0.02126	0.00107	0.00202	0.00108	0.00273	0.00069	7.2546	6.93	0.04	92.7	86.9	1.8
9	9.13114	0.03254	1.14769	0.00505	0.01713	0.00115	0.00232	0.00116	0.00249	0.00069	5.6124	7.30	0.05	91.9	91.5	2.3
10	13.24886	0.04261	1.65814	0.00840	0.02492	0.00098	0.00201	0.00108	0.00269	0.00072	8.1086	7.50	0.05	94.0	93.9	1.7
11	11.62618	0.04807	1.41593	0.00511	0.02198	0.00104	0.00215	0.00111	0.00241	0.00070	6.9241	7.70	0.05	93.8	96.3	1.9
12	9.64929	0.03561	1.21754	0.00693	0.01825	0.00098	0.00013	0.00106	0.00215	0.00072	5.9540	7.39	0.05	93.4	92.6	2.2
13	11.92638	0.03477	1.50192	0.00752	0.02221	0.00108	0.00286	0.00106	0.00146	0.00069	7.3447	7.64	0.05	96.4	95.7	1.8
14	11.64491	0.03906	1.50497	0.00674	0.02271	0.00093	0.00000	0.00109	0.00191	0.00072	7.3596	7.35	0.04	95.1	92.1	1.8
16	11.01166	0.03732	1.43068	0.00626	0.01951	0.00088	0.00175	0.00106	0.00118	0.00070	6.9963	7.44	0.04	96.8	93.2	1.9
18	9.90909	0.03393	1.31351	0.00830	0.01916	0.00097	0.00084	0.00115	0.00108	0.00070	6.4233	7.29	0.05	96.8	91.3	2.0
19	11.06902	0.04083	1.40024	0.00483	0.02055	0.00094	0.00066	0.00109	0.00038	0.00068	6.8474	7.82	0.04	99.0	97.7	1.8
20	13.24562	0.04261	1.71729	0.00713	0.02139	0.00096	0.00181	0.00119	0.00102	0.00070	8.3979	7.53	0.04	97.7	94.2	1.6

Quartz Analyses

2.06043	0.03147	0.00762	0.00255	0.00266	0.00071	0.00232	0.00113	0.00317	0.00069	0.03728	147.26	89.00	54.3	
0.44893	0.02692	0.00395	0.00279	0.00085	0.00065	0	0.00108	0.00040	0.00070	0.01934	83.45	78.80	73.6	

Representative Blank Values for UV Laser Analyses

1.32930	0.01700	0.02407	0.00400	0.00543	0.00071	0.03082	0.00077	0.00643	0.00004	0.1180
1.21560	0.01300	0.01572	0.00110	0.00363	0.00045	0.02588	0.00074	0.00430	0.00057	0.07680
1.51450	0.01600	0.01848	0.00180	0.00426	0.00052	0.03026	0.00066	0.00491	0.00074	0.09030
1.32930	0.01700	0.02407	0.00400	0.00545	0.00071	0.03082	0.00077	0.00643	0.00044	0.11800
1.50960	0.01700	0.03123	0.00340	0.00402	0.00047	0.03000	0.00075	0.00683	0.00045	0.15300
1.28050	0.01400	0.02265	0.00260	0.00450	0.00052	0.02852	0.00072	0.00511	0.00036	0.11100

For analyses conducted in sample SV03-103, an [R] adjacent to the analysis number denotes an analysis that was conducted in the glaucophane-rich margin.

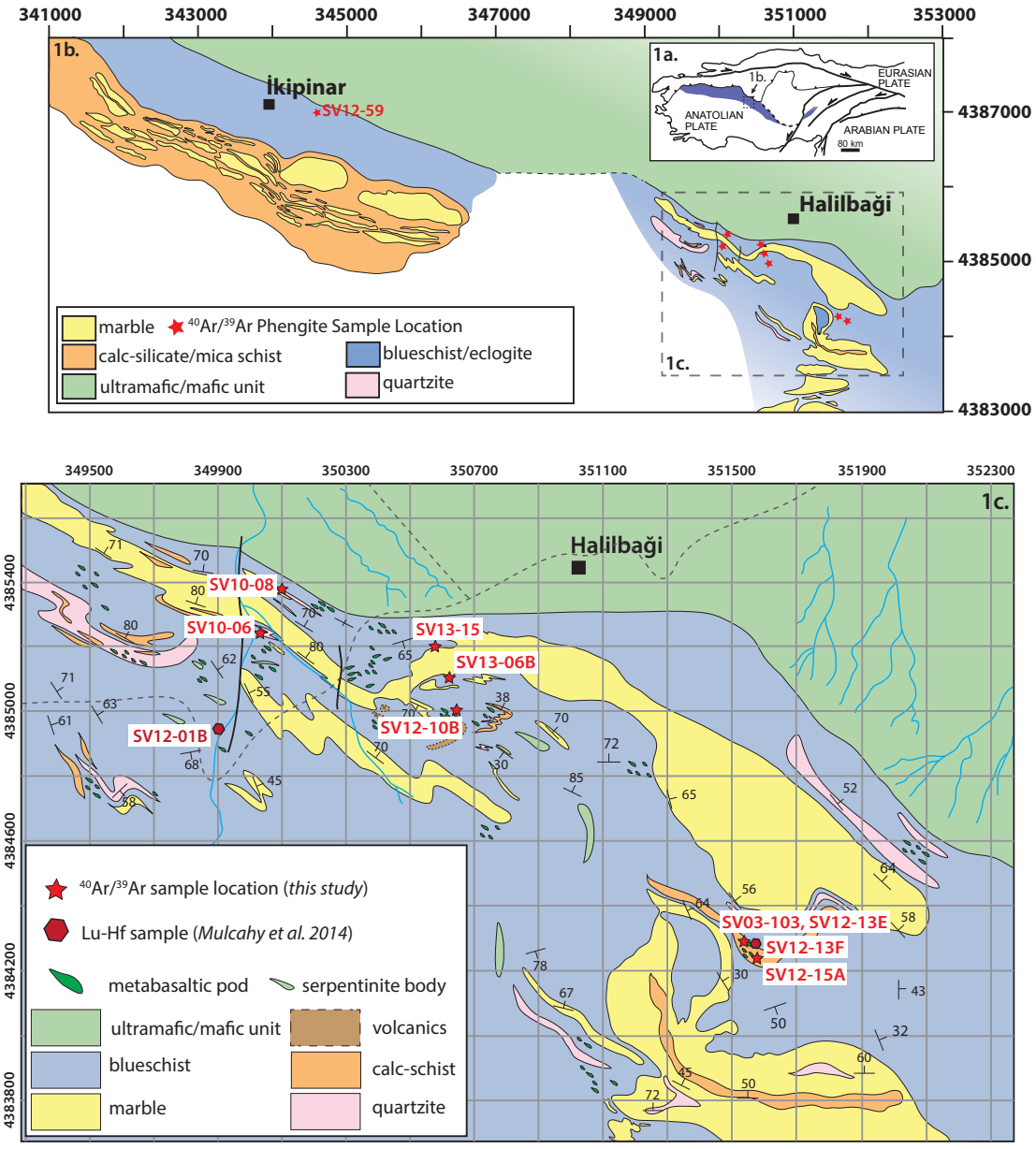

Figure 1. (a) Tectonic map showing the location of the Tavşanlı Zone HP/LT belt (shaded region) in Turkey. (b) Simplified geologic map of the Halilbağı Formation outcrops near the villages of Halilbağı and İkipınar; sample location for lawsonite garnet blueschist SV12-59 is shown. (c) Schematic geologic map of the Halilbağı region showing remaining $^{40}Ar/^{39}Ar$ sample locations, as well as the locations of the samples dated by Mulcahy et al. (2014) using the Lu-Hf method. Sample locations are provided in Supplementary Material 1.

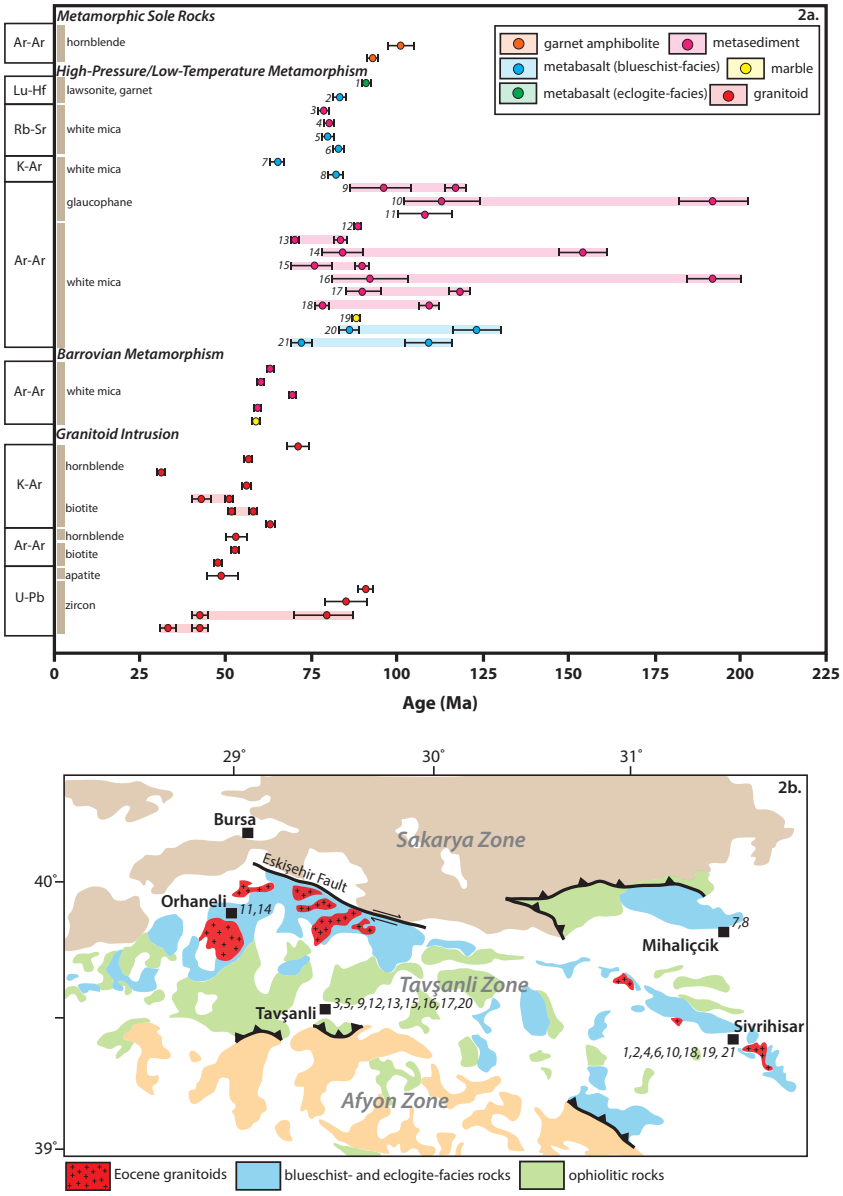

Figure 2. (a) Overview of previous geochronologic estimates for the timing of subduction initiation, HP/LT metamorphism, Barrovian metamorphism, and granitoid intrusion. Each line represents a different sample. For studies utilizing *in situ* geochronologic methods, the total intrasample variation is indicated by the length of the bar; the oldest and youngest analysis (and their corresponding error as reported in the literature) are shown. (b) Generalized geologic map of the Tavşanlı Zone showing the geographic distribution of the samples used for dating the timing of HP metamorphism. Sample locations are approximate and shown next to the closest city as GPS coordinates were not provided in all studies.

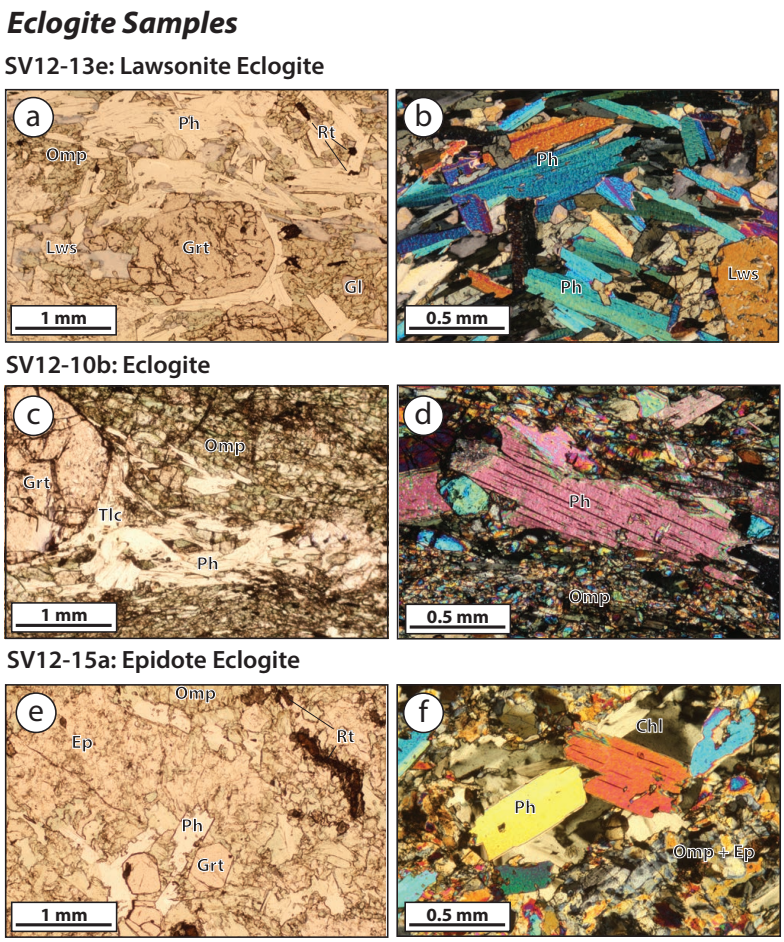

Figure 3. Photomicrographs of the lawsonite (a,b,c,d) and epidote (e,f) eclogite samples dated in this study. Phengite in the eclogite samples are coarse-grained, undeformed, and are in apparent textural equilibrium with the peak lawsonite eclogite assemblage (b,d) and the retrogressed, epidote eclogite assemblage (f). Mineral abbreviations follow the recommendations of Whitney and Evans (2010).

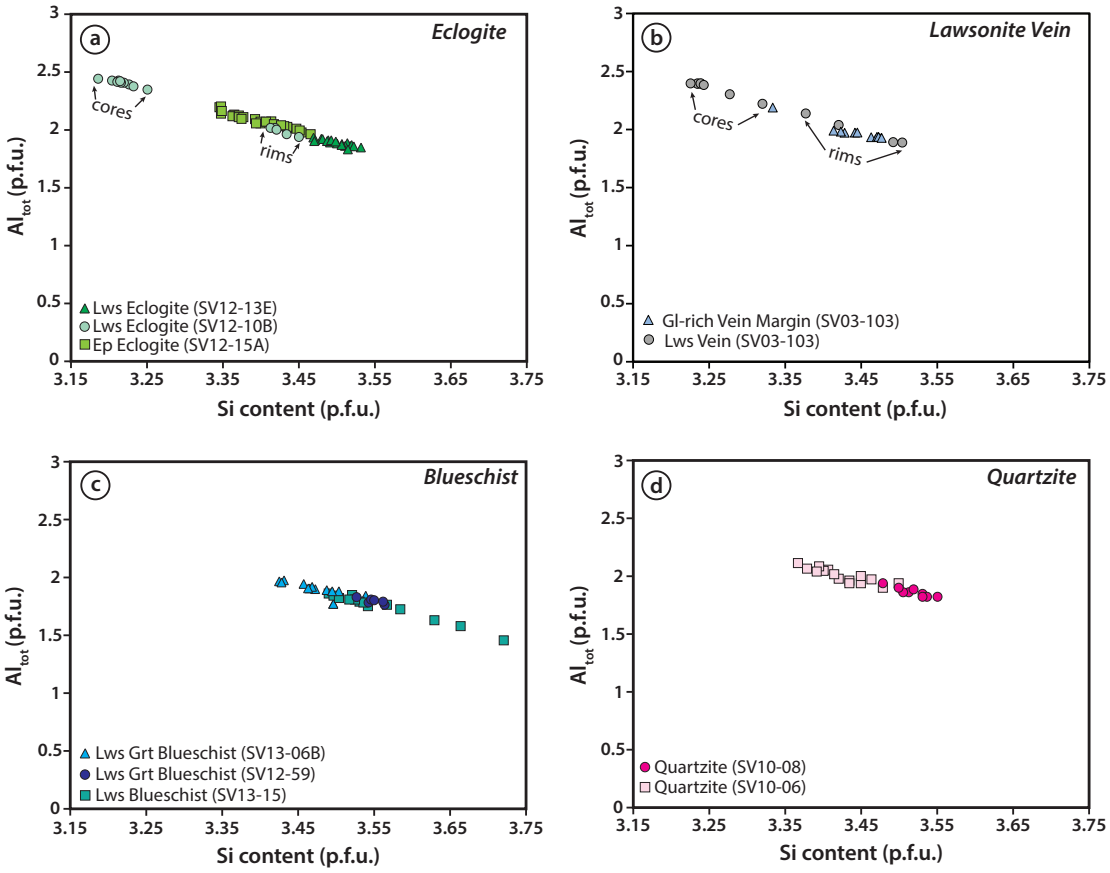

Figure 4. Plots of Si vs. Al_{tot} content of phengite in the eclogite samples (a), lawsonite vein and associated glaucophane-rich margin (b), blueschist samples (c), and quartzite samples (d).

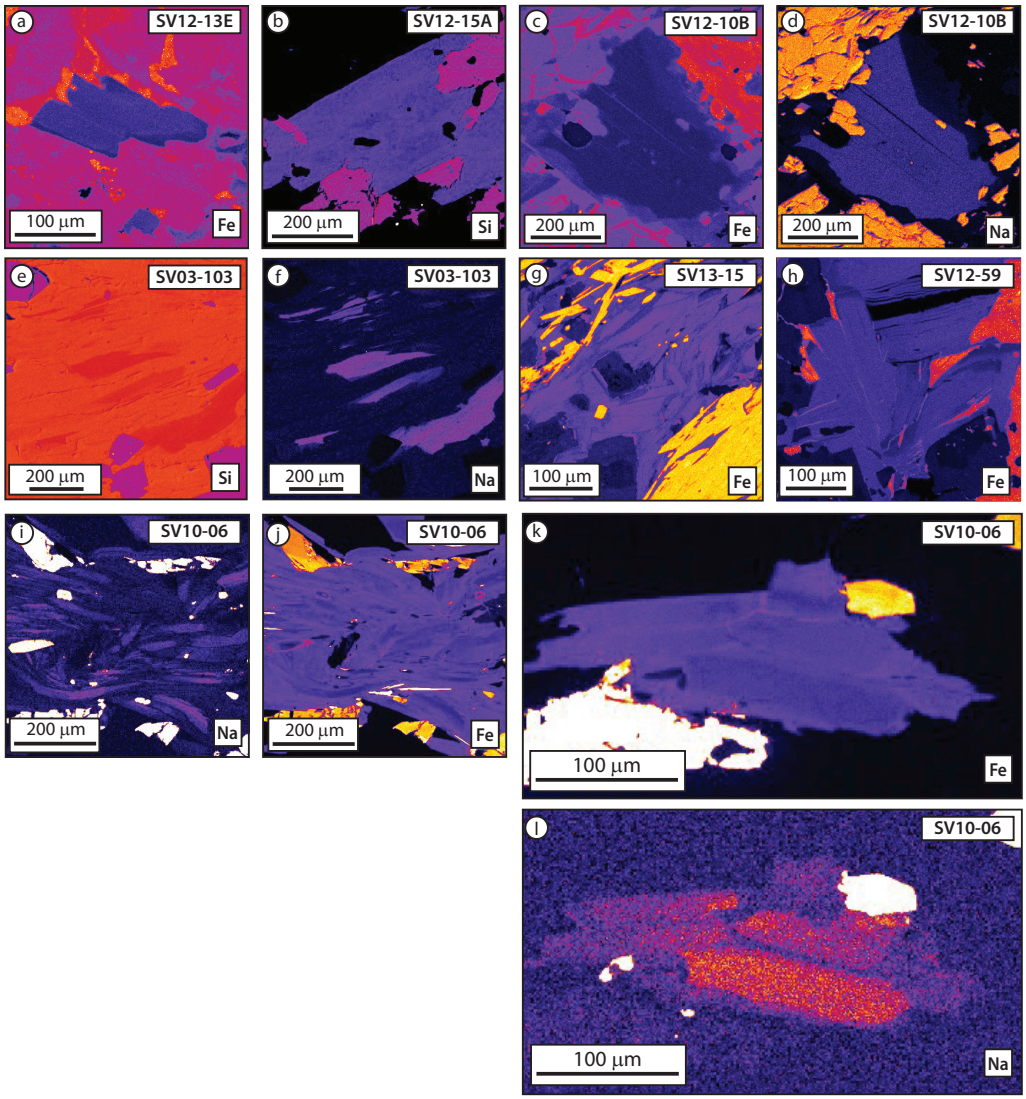

Figure 5. X-ray elements maps of phengite in the eclogite samples (a, b, c, d), lawsonite vein and associated glaucophane-rich margin (e, f), blueschist samples (g, h), and quartzite samples (i, j, k, l).

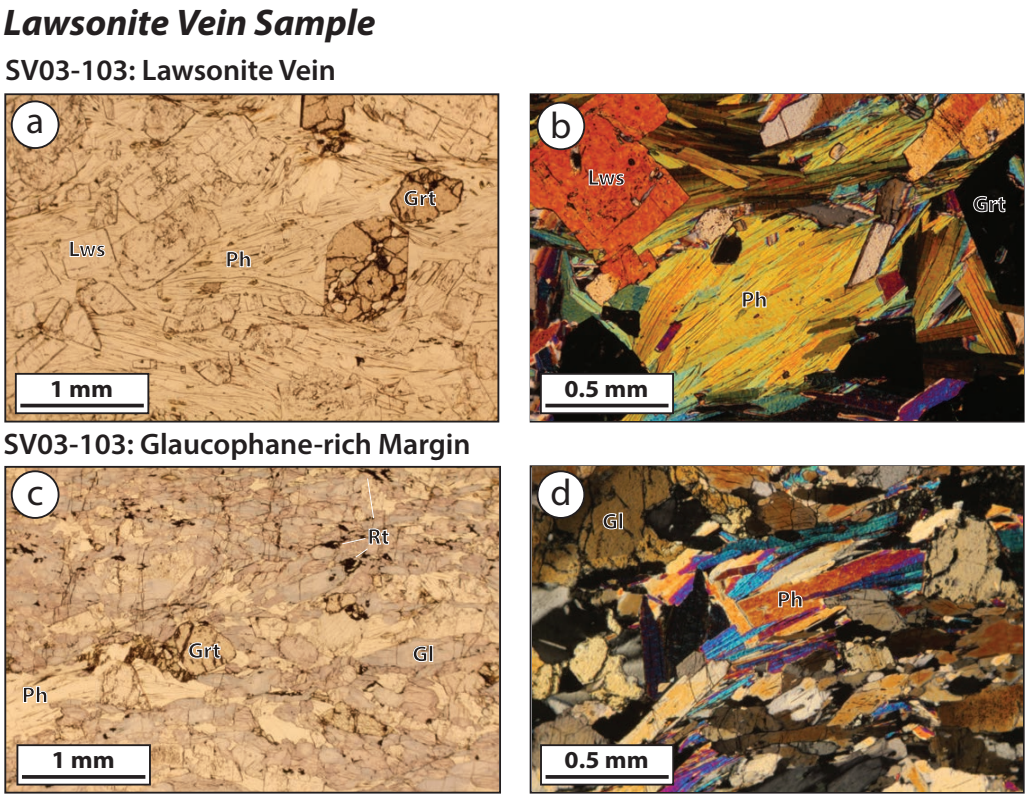

Figure 6. Photomicrographs of the vein (a,b) and associated glaucophane-rich margin (c,d) from the margin of the eclogite pod from which sample SV12-13E was collected.

Blueschist Samples

SV13-06B: Lawsonite Garnet Blueschist (Halilbağı)

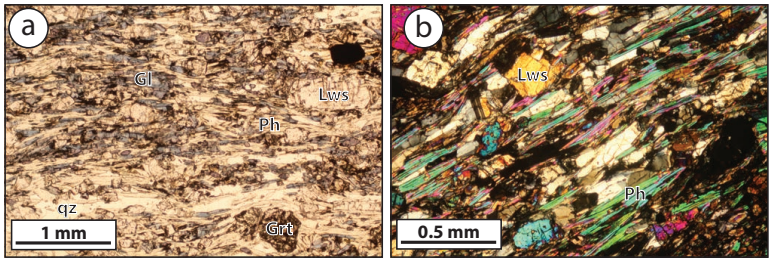

SV13-15: Lawsonite Blueschist (Halilbağı)

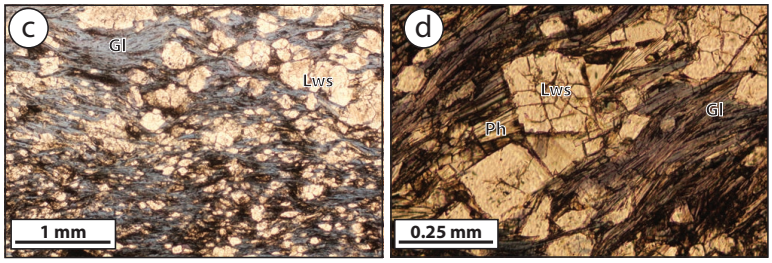

SV12-59: Lawsonite Garnet Blueschist (İkipinar)

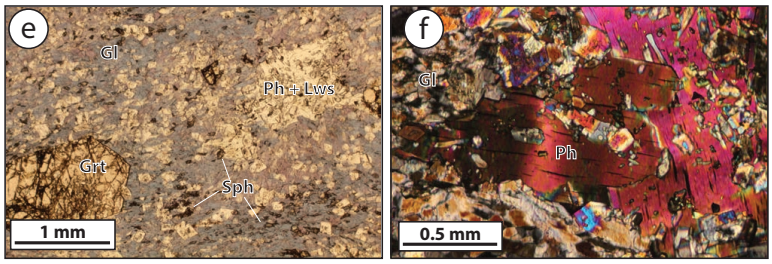

Figure 7. Photomicrographs of the lawsonite blueschist samples dated in this study. Phengite in the blueschist samples varies in size, modal abundance, and textural habit (foliation-parallel bundles or layers, b; intergrown with glaucophane in pressure shadows, d; deformed clusters intergrown with lawsonite and glaucophane, f).

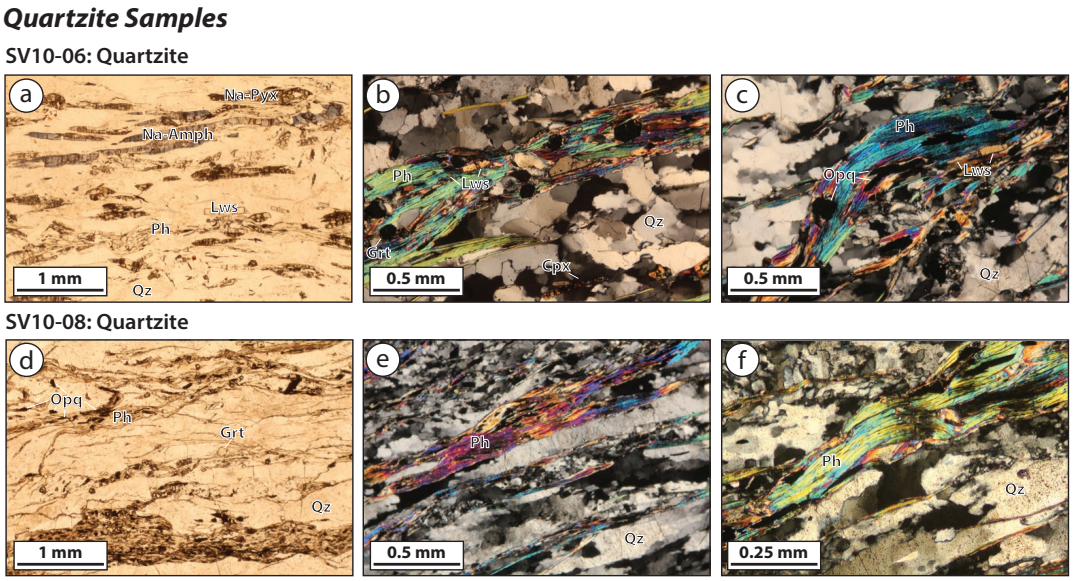

Figure 8. Photomicrographs of the quartzite samples dated in this study. Note the reduced grain size between sample SV10-06 (collected outside of the high-strain zone) and sample SV10-08 (collected from within the high-strain zone).

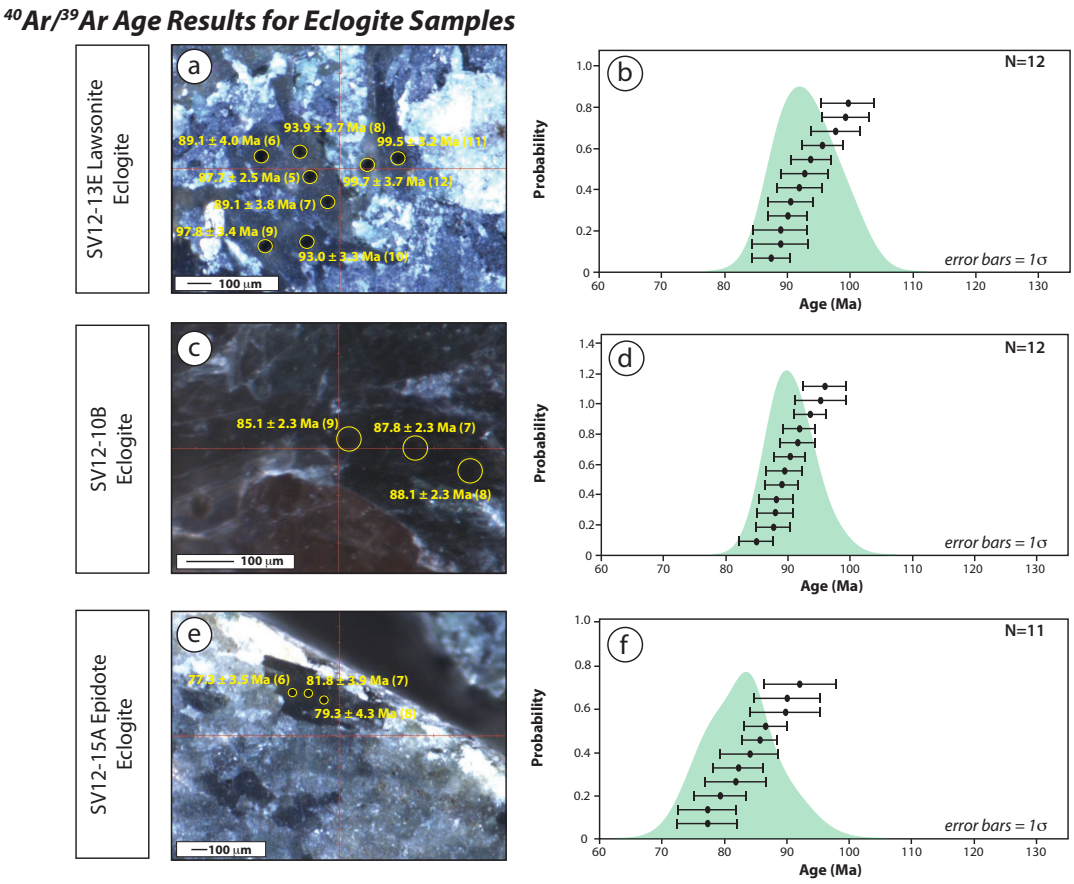

Figure 9. Results of *in situ* UV laser ablation $^{40}Ar/^{39}Ar$ geochronology for eclogite samples. Representative reflected light images of phengite with their respective $^{40}Ar/^{39}Ar$ age results are shown in a,c,and e. The distribution of phengite ages (and their corresponding 1-sigma error) are shown in b,d and f; the shaded region corresponds to the cumulative age probability plot for each sample.

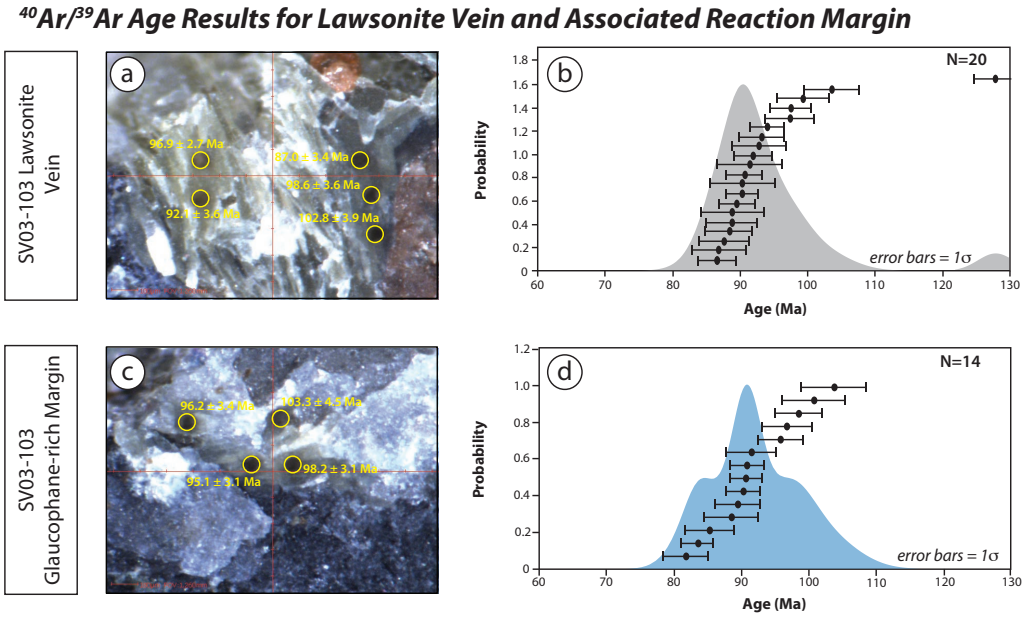

Figure 10. Results of *in situ* UV laser ablation $^{40}Ar/^{39}Ar$ geochronology for the lawsonite vein sample and associated glaucophane-rich margin. Representative reflected light images of phengite with their respective $^{40}Ar/^{39}Ar$ age results are shown in a and c. The distribution of phengite ages (and their corresponding 1-sigma error) are shown in b and d; the shaded region corresponds to the cumulative age probability plot for each sample.

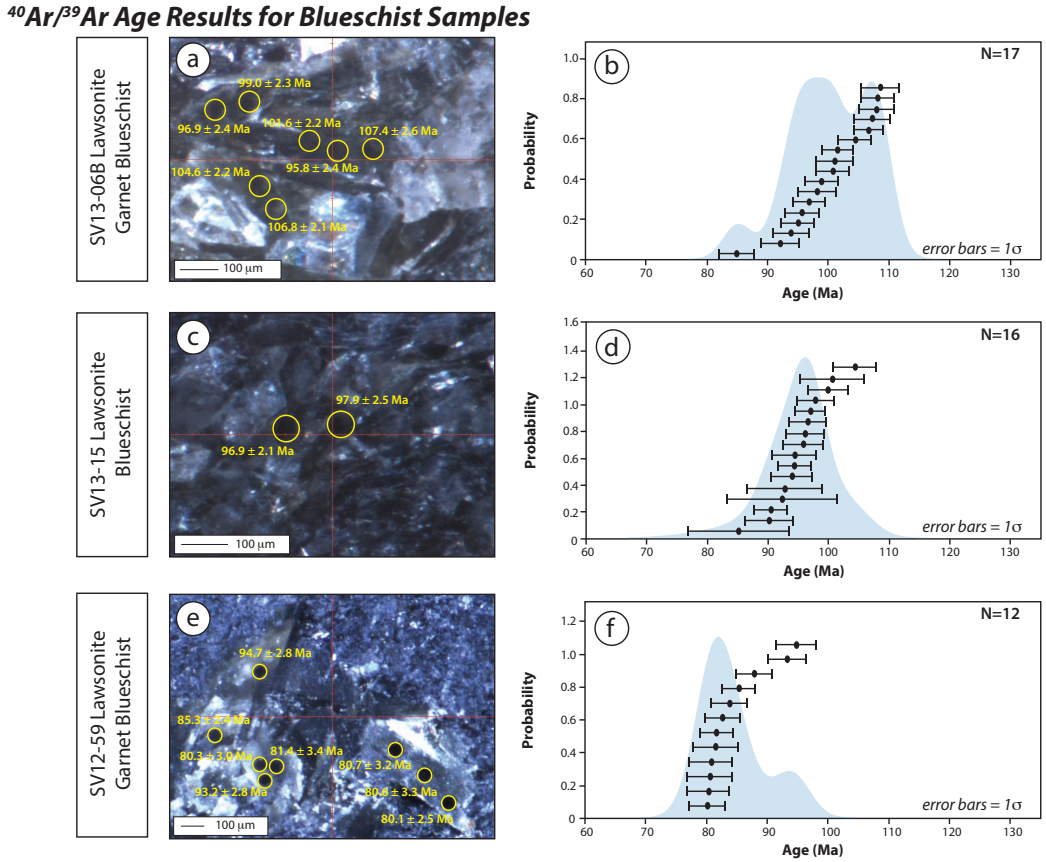

Figure 11. Results of *in situ* UV laser ablation $^{40}Ar/^{39}Ar$ geochronology for blueschist samples. Representative reflected light images of phengite with their respective $^{40}Ar/^{39}Ar$ age results are shown in a,c, and e. The distribution of phengite ages (and their corresponding 1-sigma error) are shown in b, d, and f; the shaded region corresponds to the cumulative age probability plot for each sample.

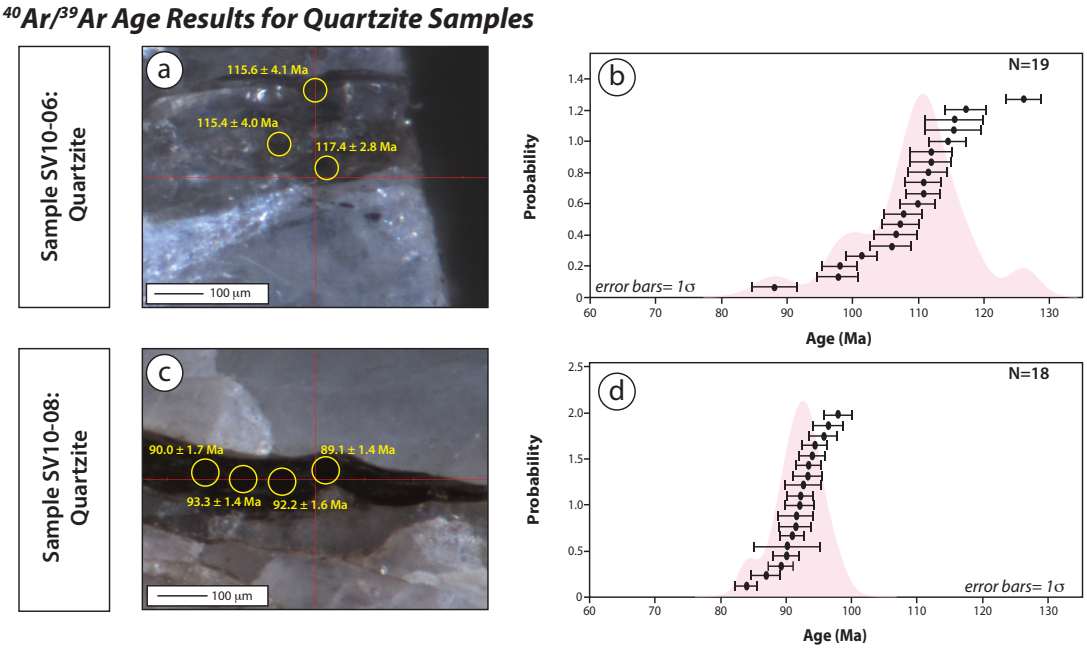

Figure 12. Results of *in situ* UV laser ablation $^{40}Ar/^{39}Ar$ geochronology for quartzite samples. Representative reflected light images of phengite with their respective $^{40}Ar/^{39}Ar$ age results are shown in a and c. The distribution of phengite ages (and their corresponding 1-sigma error) are shown in b and d; the shaded region corresponds to the cumulative age probability plot for each sample.

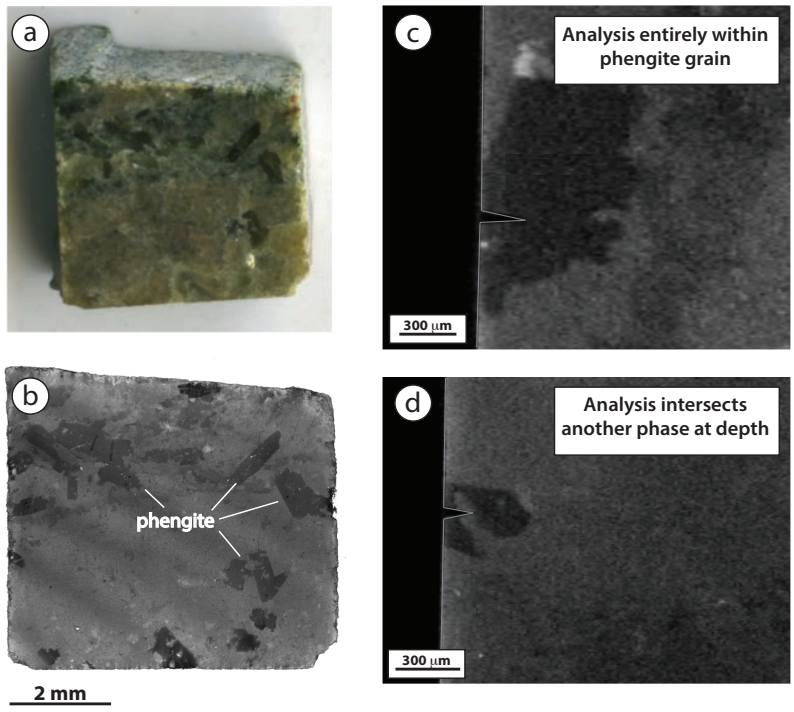

Figure 13. (a) Photomicrograph of the epidote eclogite (SV12-15A) rock chip analyzed for $^{40}Ar/^{39}Ar$ geochronology. (b) XRCT reconstruction of the rock chip; dark grains are phengite, the light matrix is omphacite + epidote, and bright grains are oxide phases (rutile, sphene). 2D slices through the rock chip (c, d) show the conical geometry of the ablation pits at depth and permit identification of "contaminated" analyses.

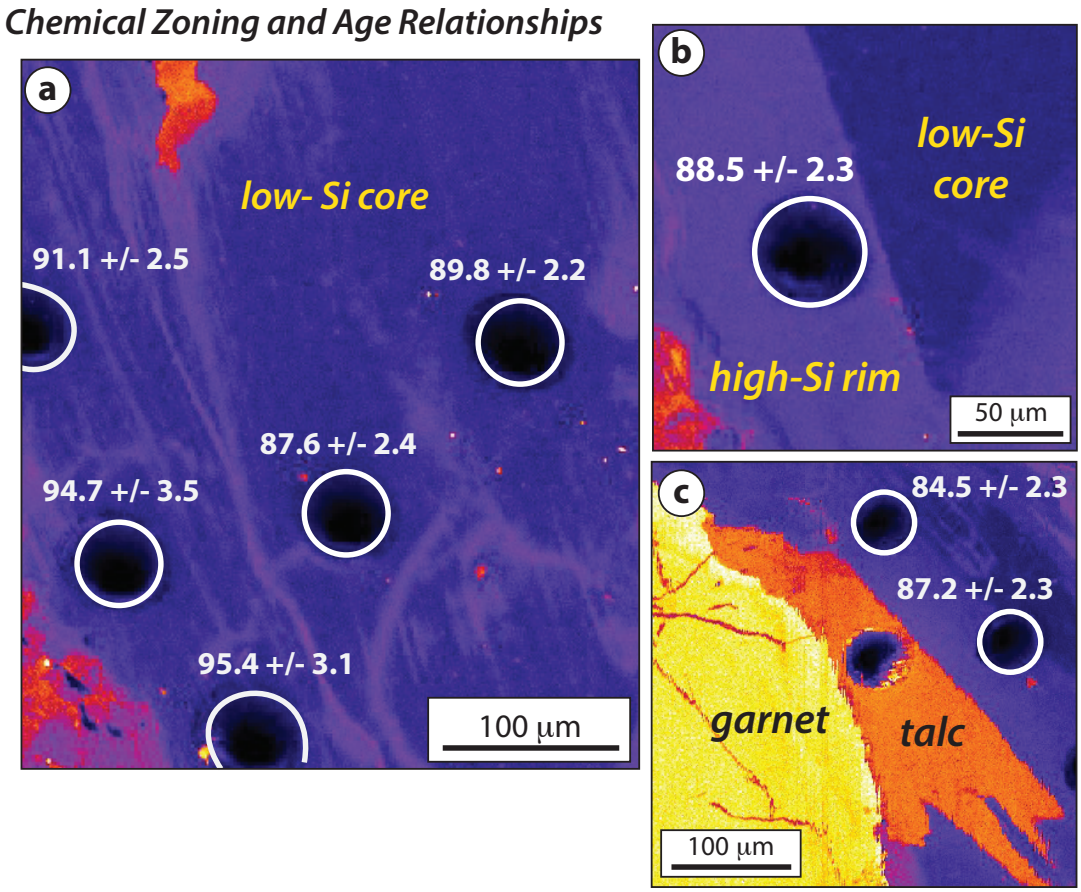

Figure 14. Fe X-ray element maps of *in situ* UV laser ablation pits in zoned phengite from sample SV12-10B with their respective $^{40}Ar/^{39}Ar$ ages and 1-sigma error.

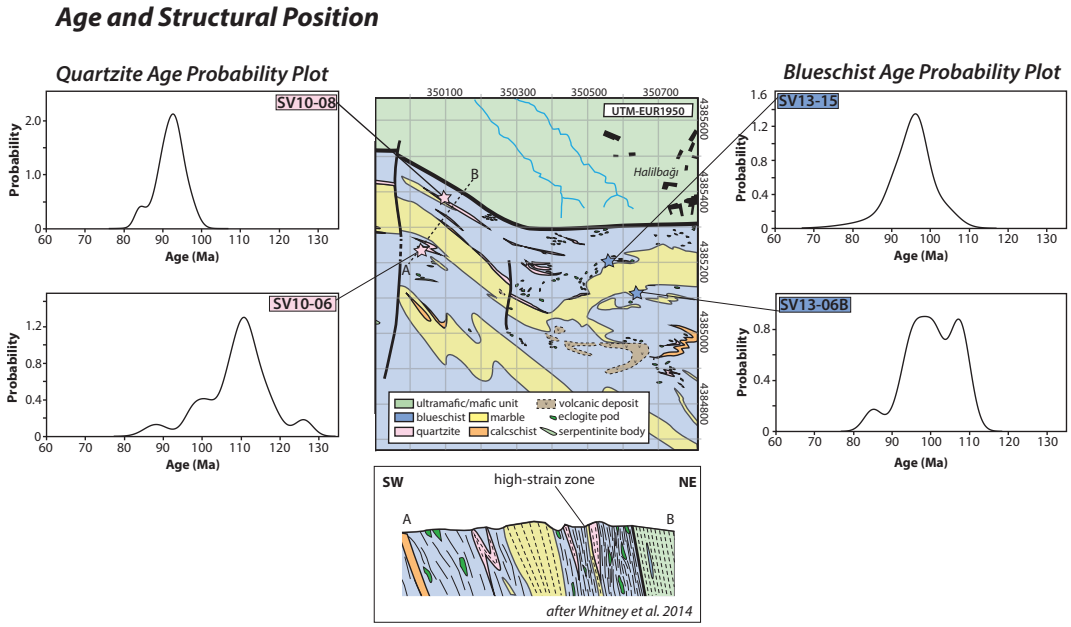

Figure 15. Age probability plots for quartzite and blueschist samples collected within the high-strain zone (SV10-08, SV13-15), and samples collected just outside of the high-strain zone (SV10-06, SV13-06B). Sample locations and the location of the cross-section through the high-strain zone (A – B) are shown in the map.

	UTM Coordinates[a]	
	Easting	**Northing**
Eclogite Samples		
SV12-13E	351574	4384265
SV12-10B	350615	4384978
SV12-15A	351591	4384250
Lawsonite Vein Sample		
SV03-103	351574	4384265
Blueschist Samples		
SV12-59	344596	4386992
SV13-15	350572	4385194
SV13-06B	350615	4385109
Quartzite Samples		
SV10-06	350070	4385416
SV10-08	350123	4385550

[a]Coordinates are reported using the ED 1950 (UTM) reference system, zone 36S

Supplementary Material 1. Sample locations

North Star Imaging, Inc.
CT Acquisition
Technique Sheet

Xray source: SV12-15A
voltage: 110 kV
current: 250 µA
focal spot size: 2 microns
focal spot mode: n/a

Detector: Dexela 2923 [2237]
pixel pitch: [75 x 75] microns
mode: Sequence (Low gain)
gain:
binning: 1x1
framerate: 1.35 fps (740.744 ms integration time)

flip: horizontal
rotation: 90 degree
crop: none

defect map: 88622 defective pixels (0.741551031692433%) (saved) (88622 defective pixels, 0.741551031692433%)
offset map: 0.0959, dev 0.00551, 170 fravg, 1.3 fps
gain map start gain map 0: 0.767, dev 0.0682, 170 fravg, 1.3 fps
gain map 1: 0.455, dev 0.0411, 170 fravg, 1.3 fps
gain map 2: 0.318, dev 0.0292, 170 fravg, 1.3 fps
gain map 3: 0.052, dev 0.00525, 170 fravg, 1.3 fps
gain map end
Distances:
ug start tube to detector: 446.556 [mm]
tube to part: 17.5 [mm]
calculated Ug: 0.04903 [mm](0.654 pixels)
zoom factor: x25.52
ug end
Fixturing: plastic tube (xm tube)
Filter: none (3W TXI)

CT Scan:
type: step
monitor xray down: max allowed image variation 5%
frames averaged: 4
delay: 0 ms
projections: 1440
start: 5/2/2013 1:15:12 PM
end: 5/2/2013 3:02:04 PM
duration: 1h46m51s

Notes:
2.93um voxel size
projections 1440
frame averaged 4
framerate 1.35 fps
tube to detector: 446.556 [mm]

tube to part: 17.5 [mm]
110kV @ 3W

Supplementary Material 2. X-ray Computed Tomography (XRCT) methods

Supplementary Material 3. Images of individual $^{40}Ar/^{39}Ar$ spot analyses

SV12-13E Lawsonite Eclogite

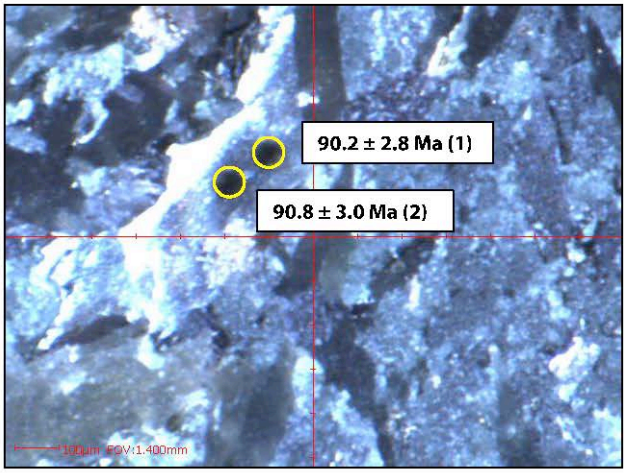

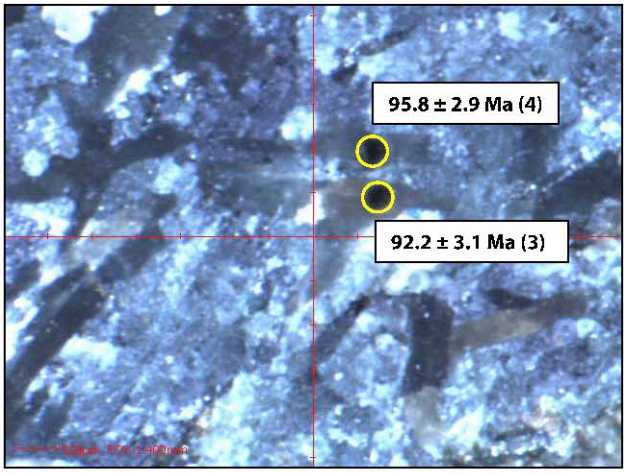

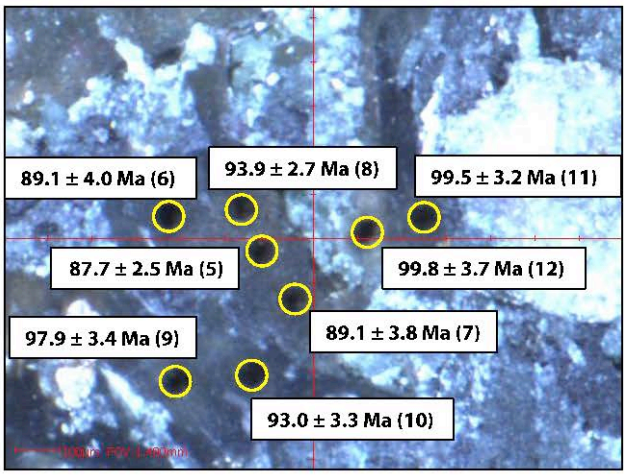

SV12-10B Eclogite

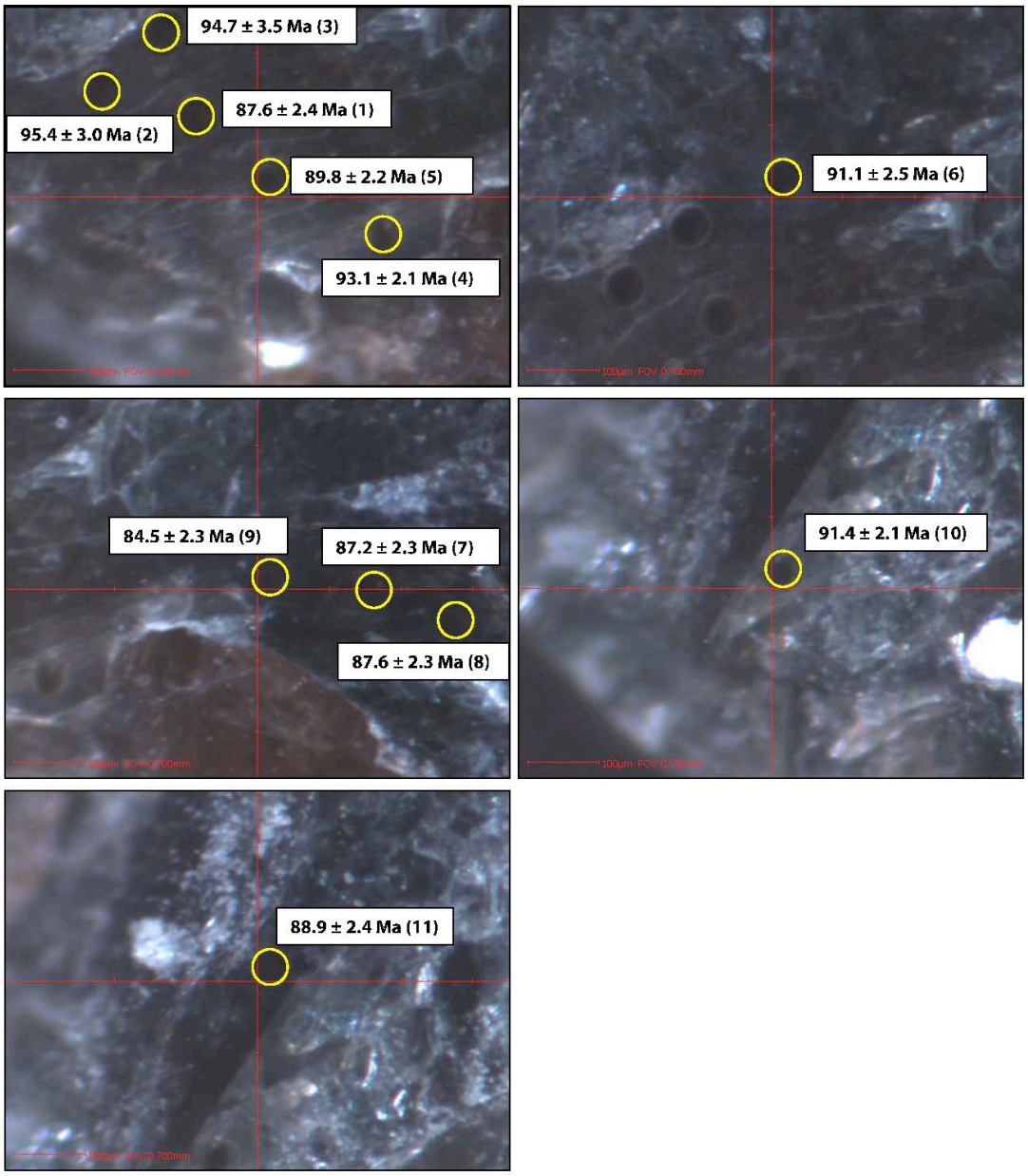

SV12-15A Epidote Eclogite

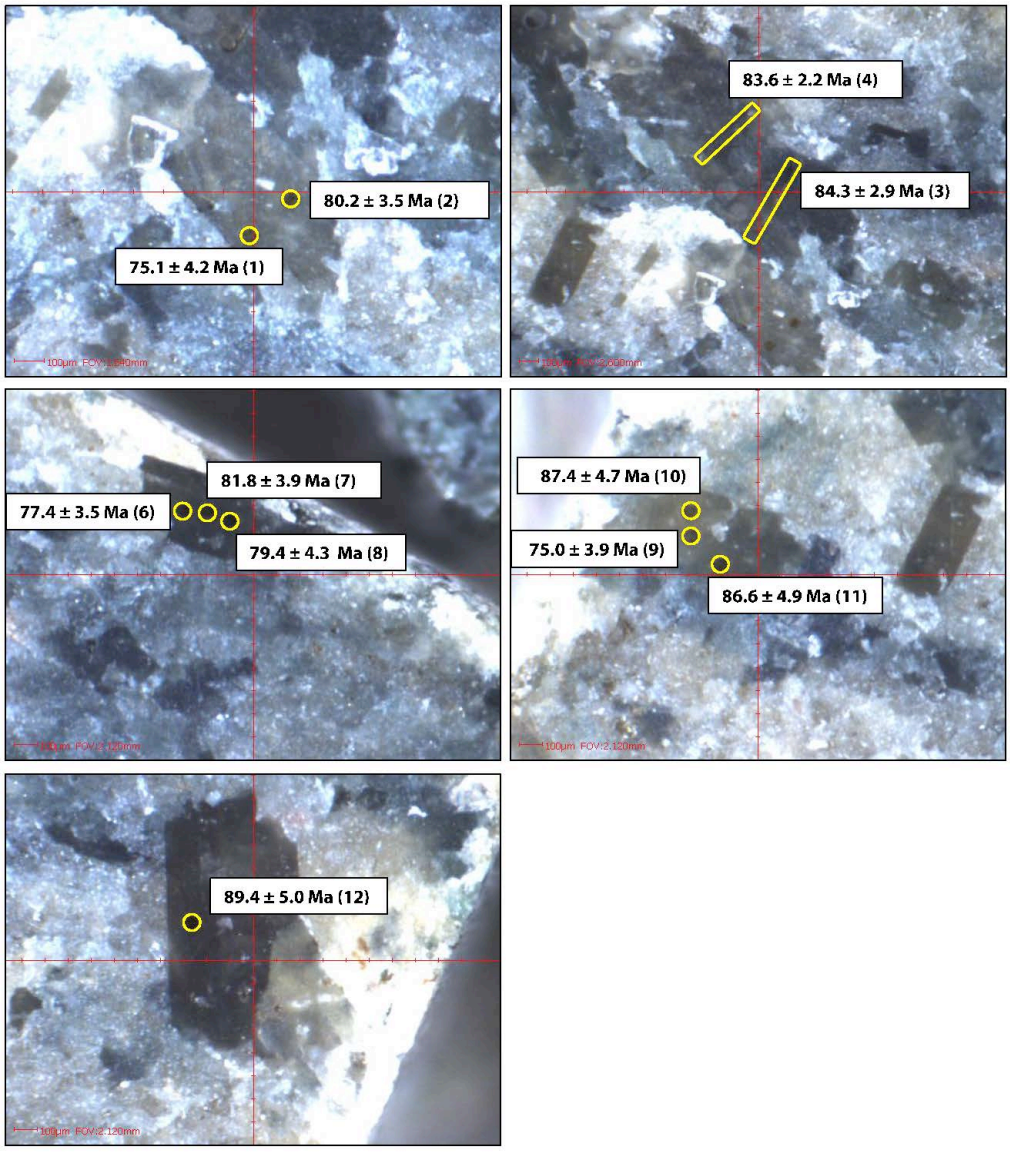

SV03-103 Lawsonite + Garnet + Phengite Vein

Analyses Within the Vein

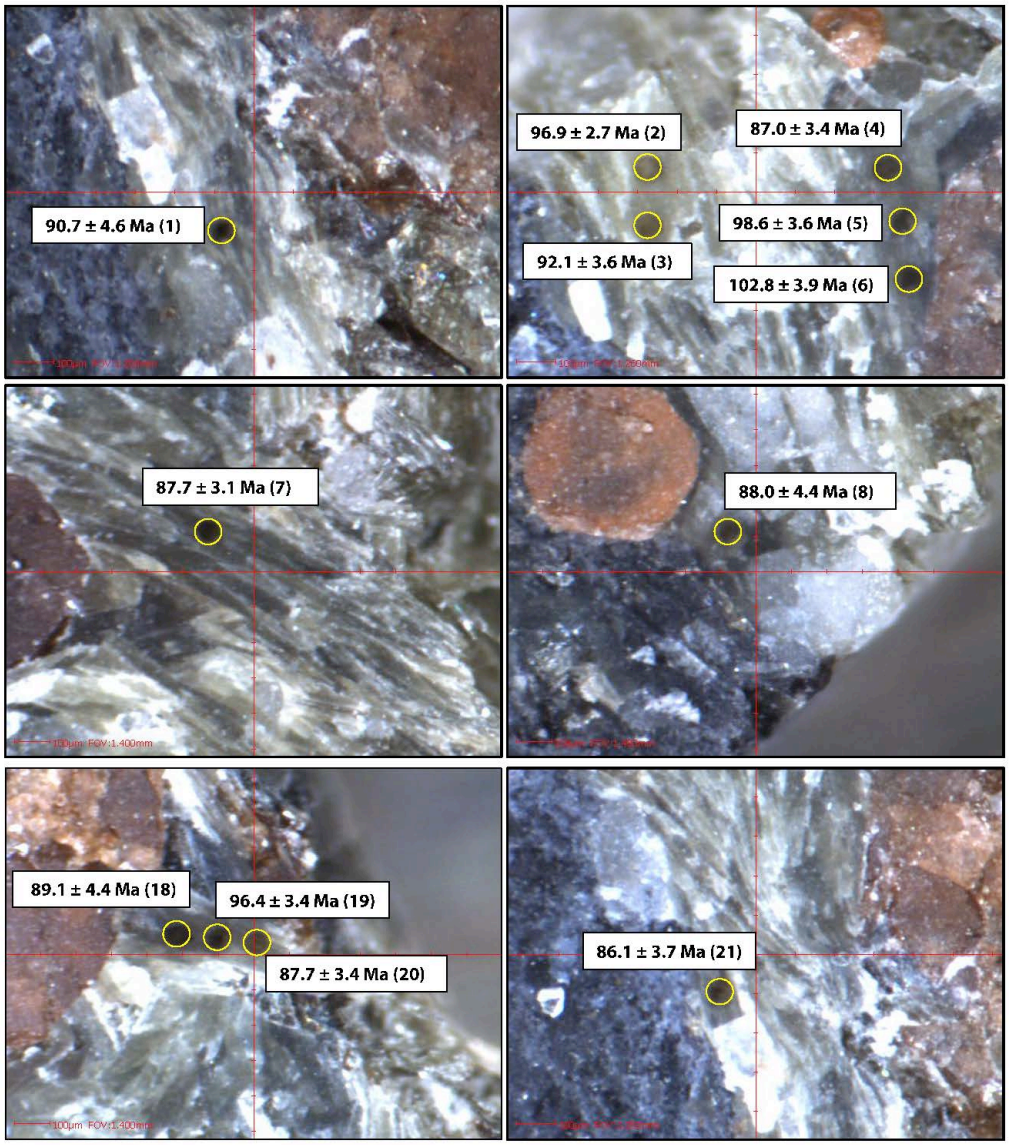

SV03-103 Lawsonite + Garnet + Phengite Vein, *continued*

Analyses Within the Vein

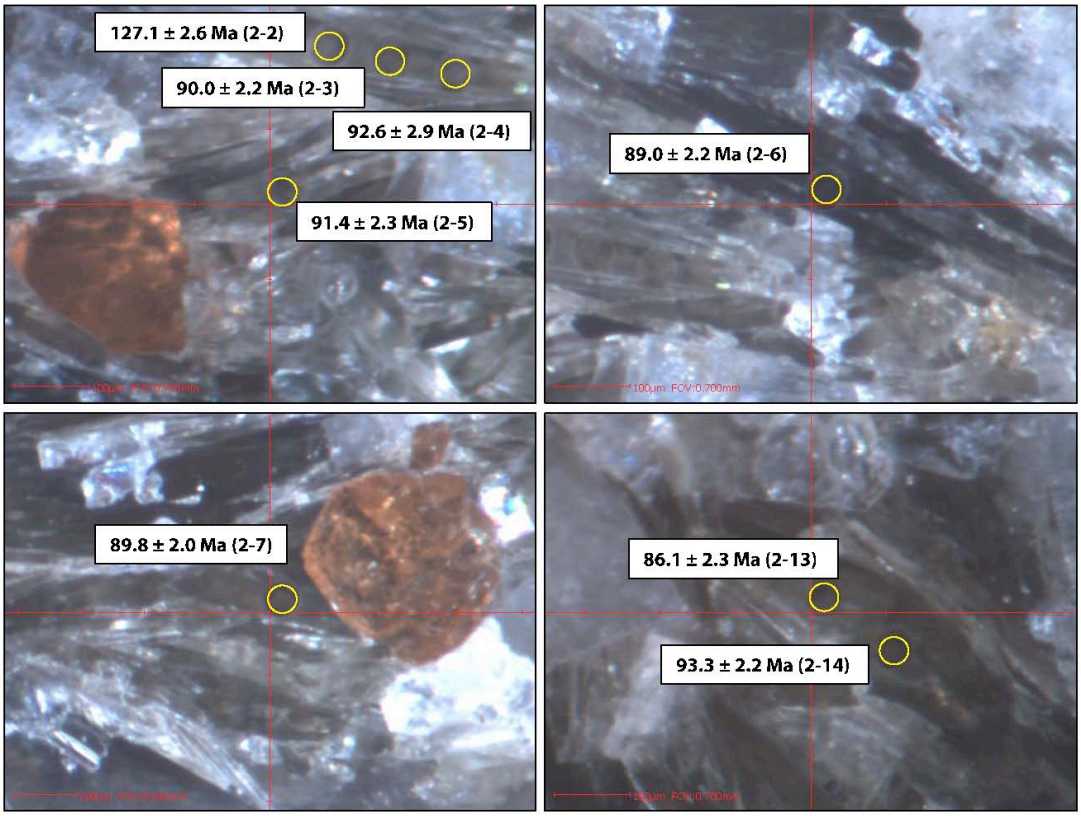

SV03-103 Lawsonite + Garnet + Phengite Vein, *continued*

Analyses Within the Glaucophane-rich Margin

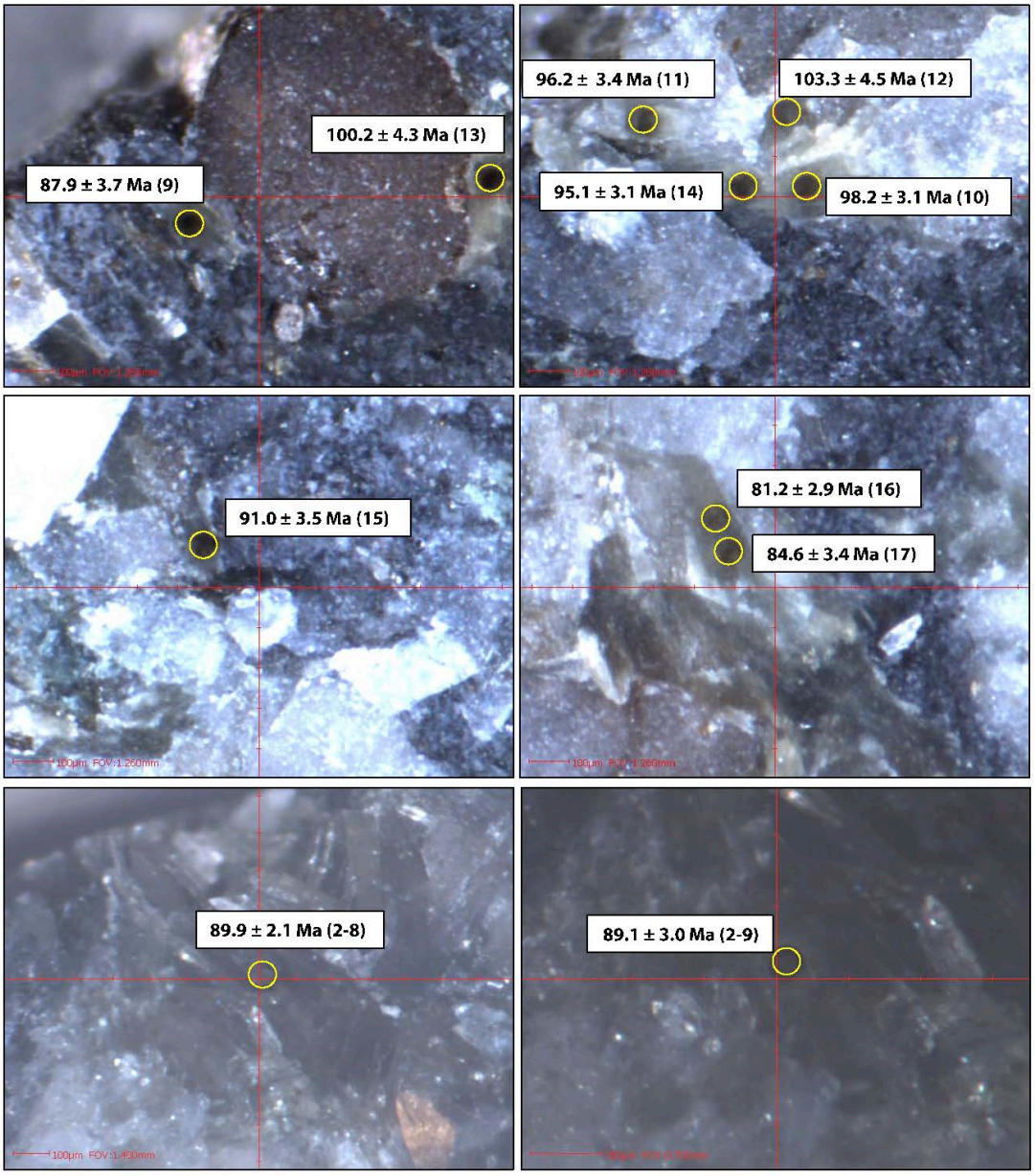

SV03-103 Lawsonite + Garnet + Phengite Vein, *continued*

Analyses Within the Glaucophane-rich Margin

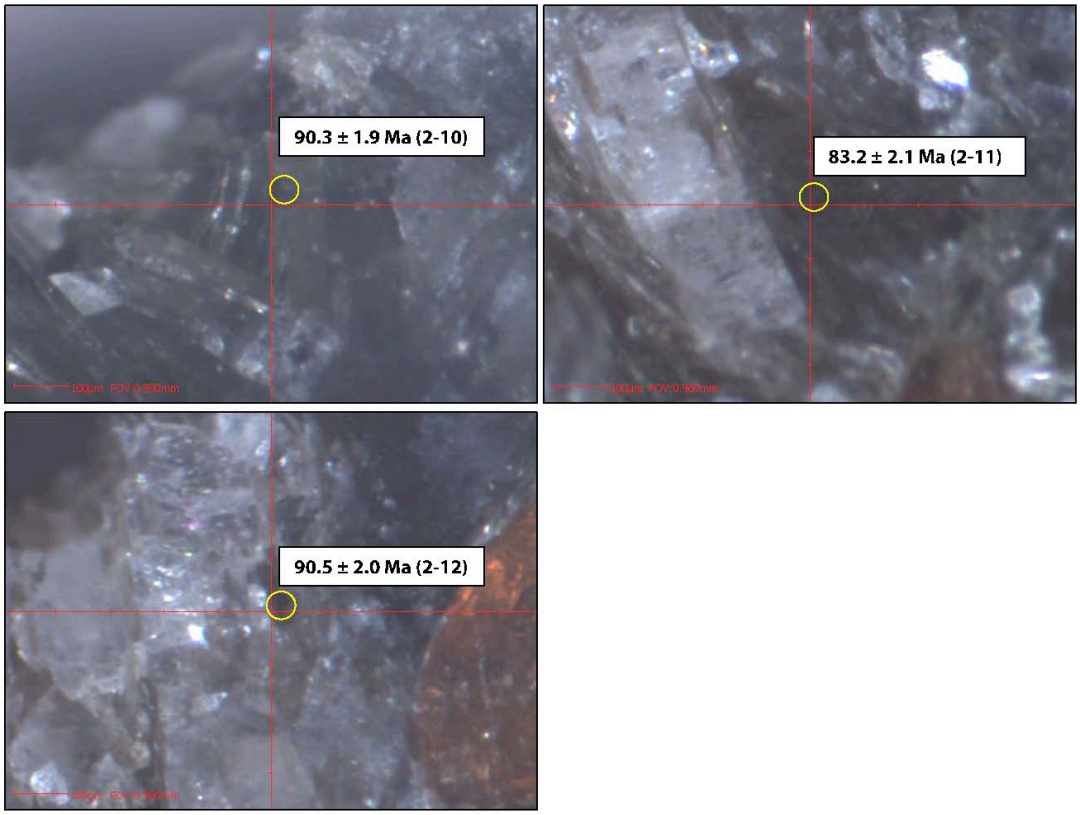

SV13-06B Lawsonite Garnet Blueschist

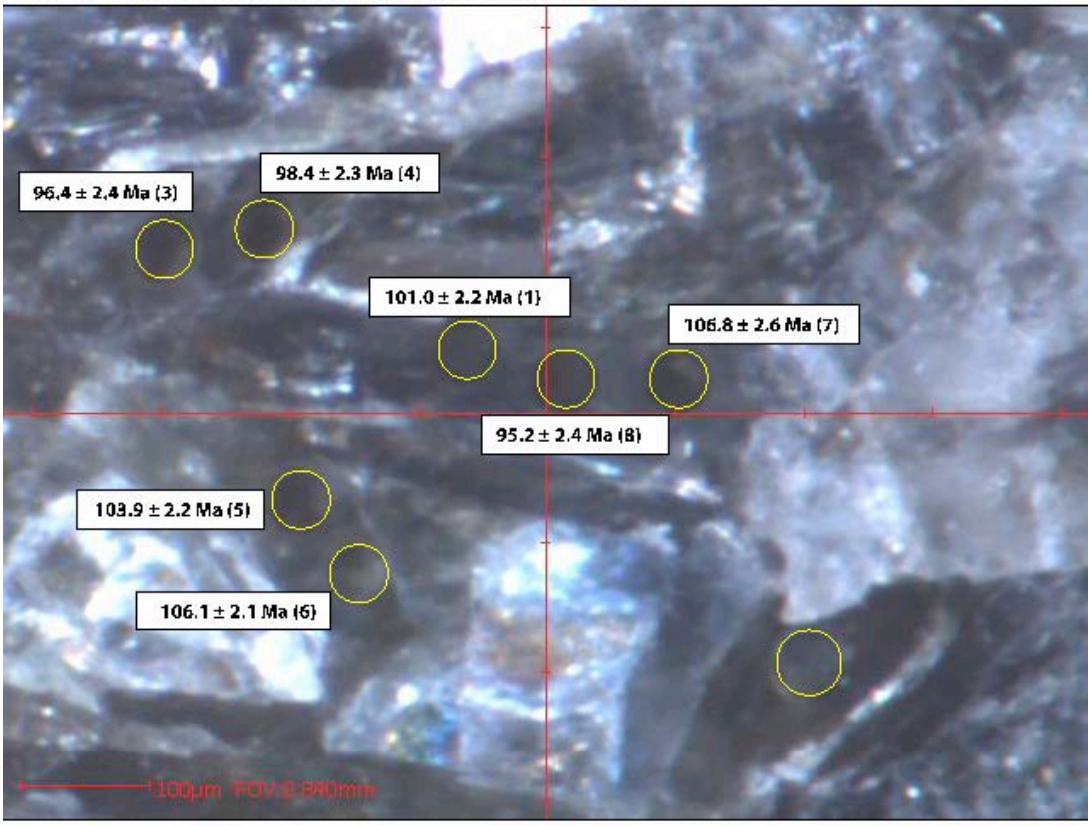

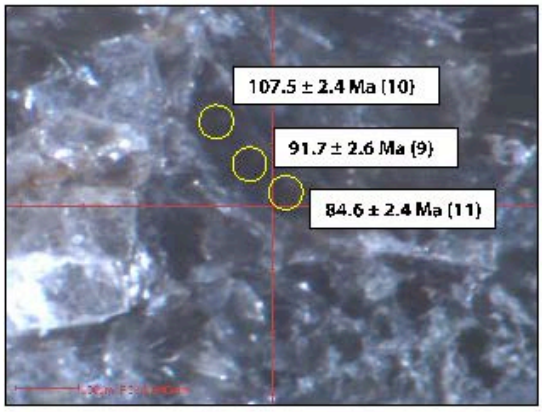

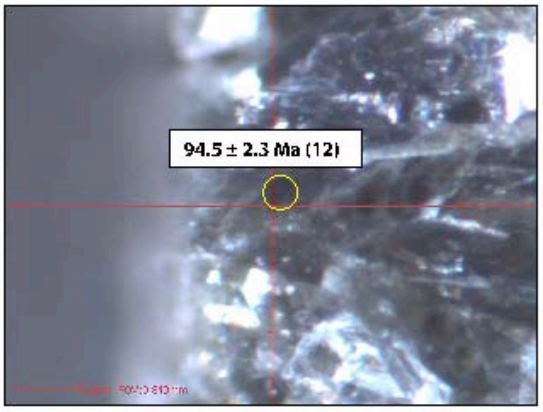

SV13-06B Lawsonite Garnet Blueschist, *continued*

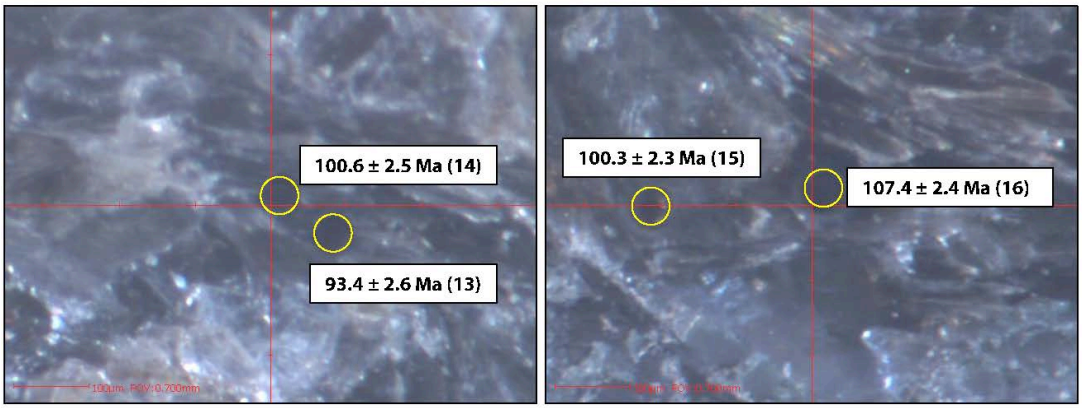

SV13-15 Lawsonite Blueschist

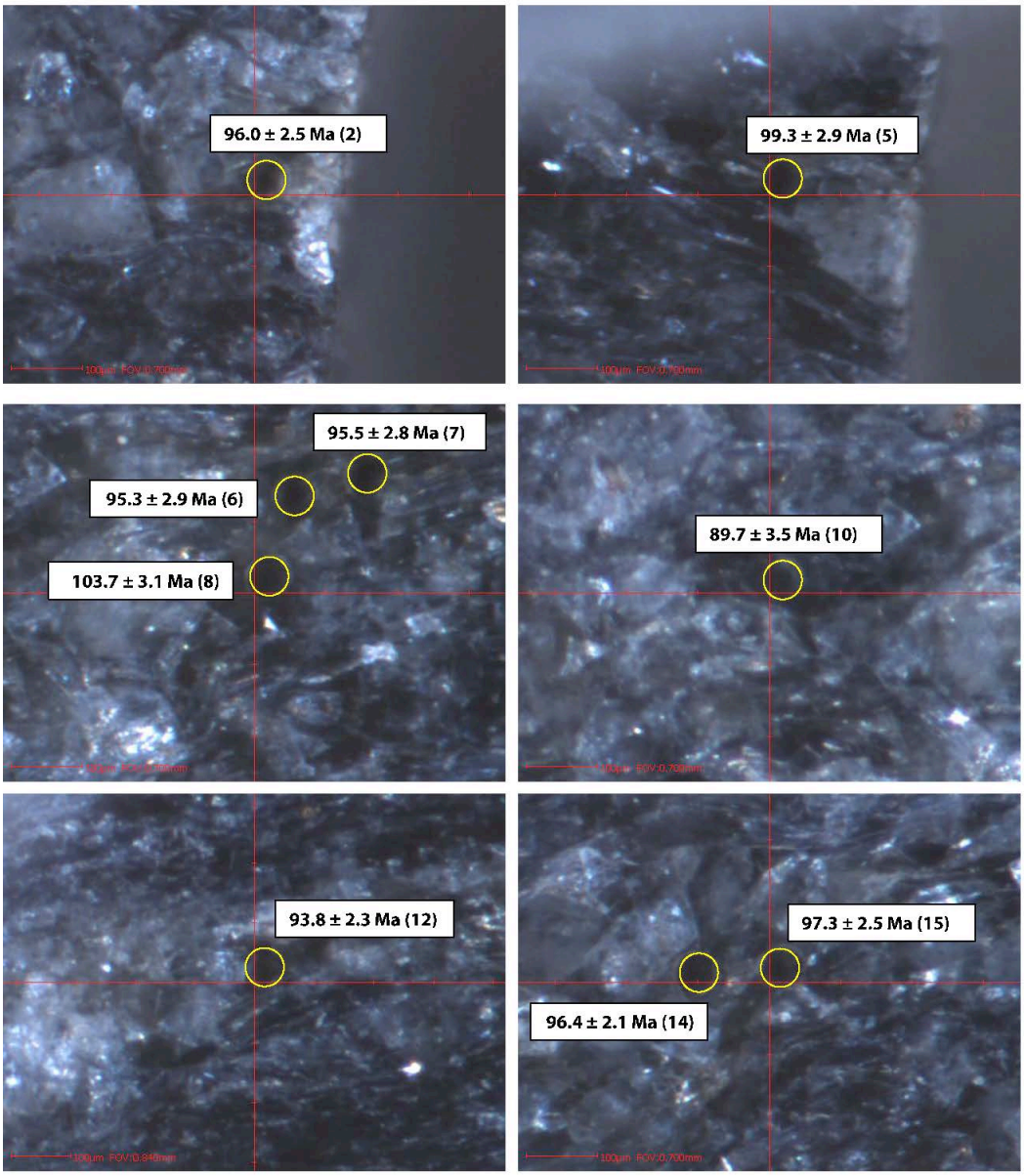

SV13-15 Lawsonite Blueschist, *continued*

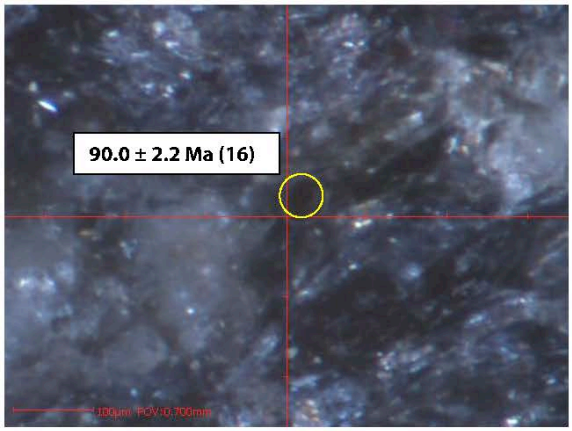

SV12-59 Lawsonite + Garnet Blueschist (İkipinar)

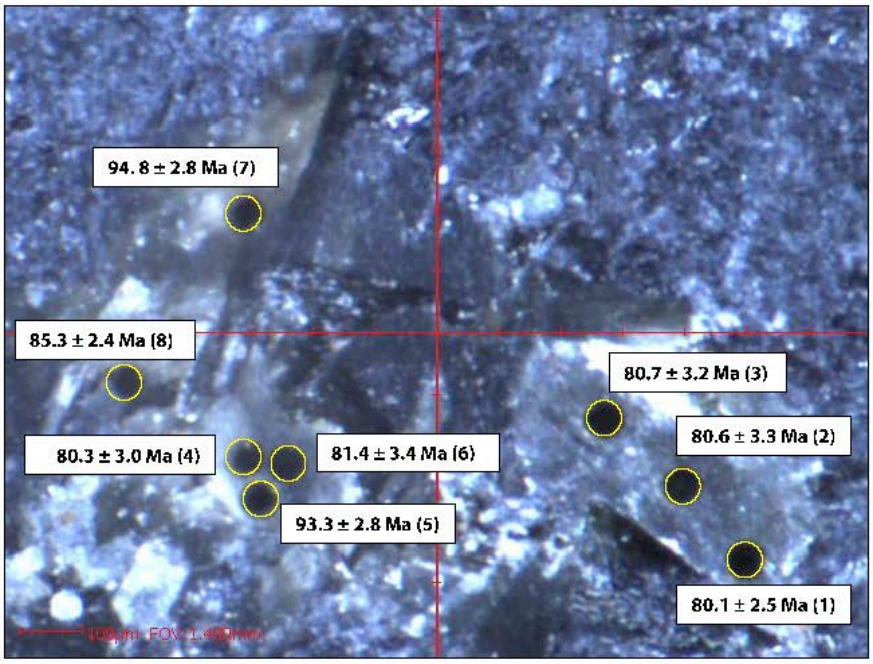

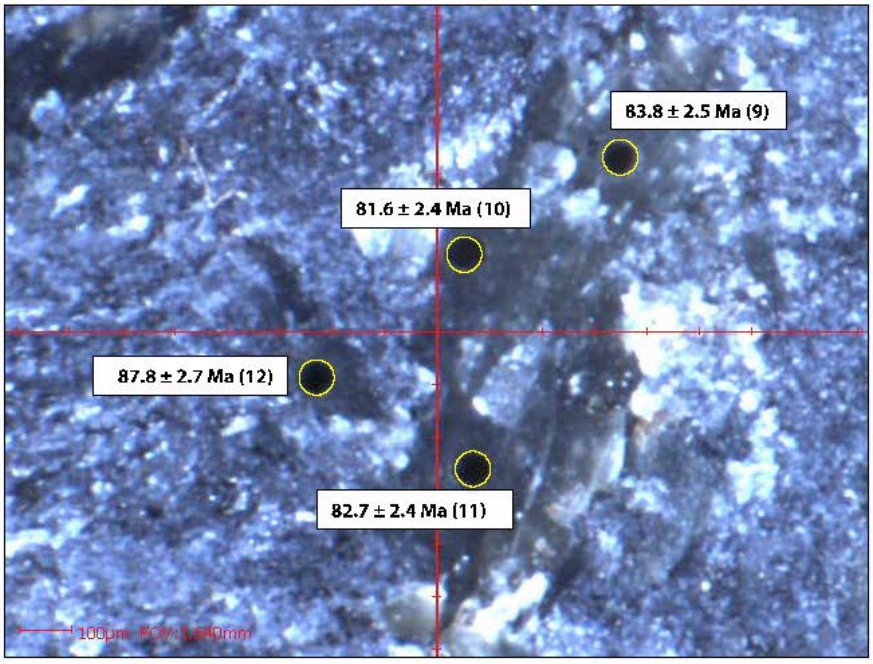

SV10-06 Quartzite

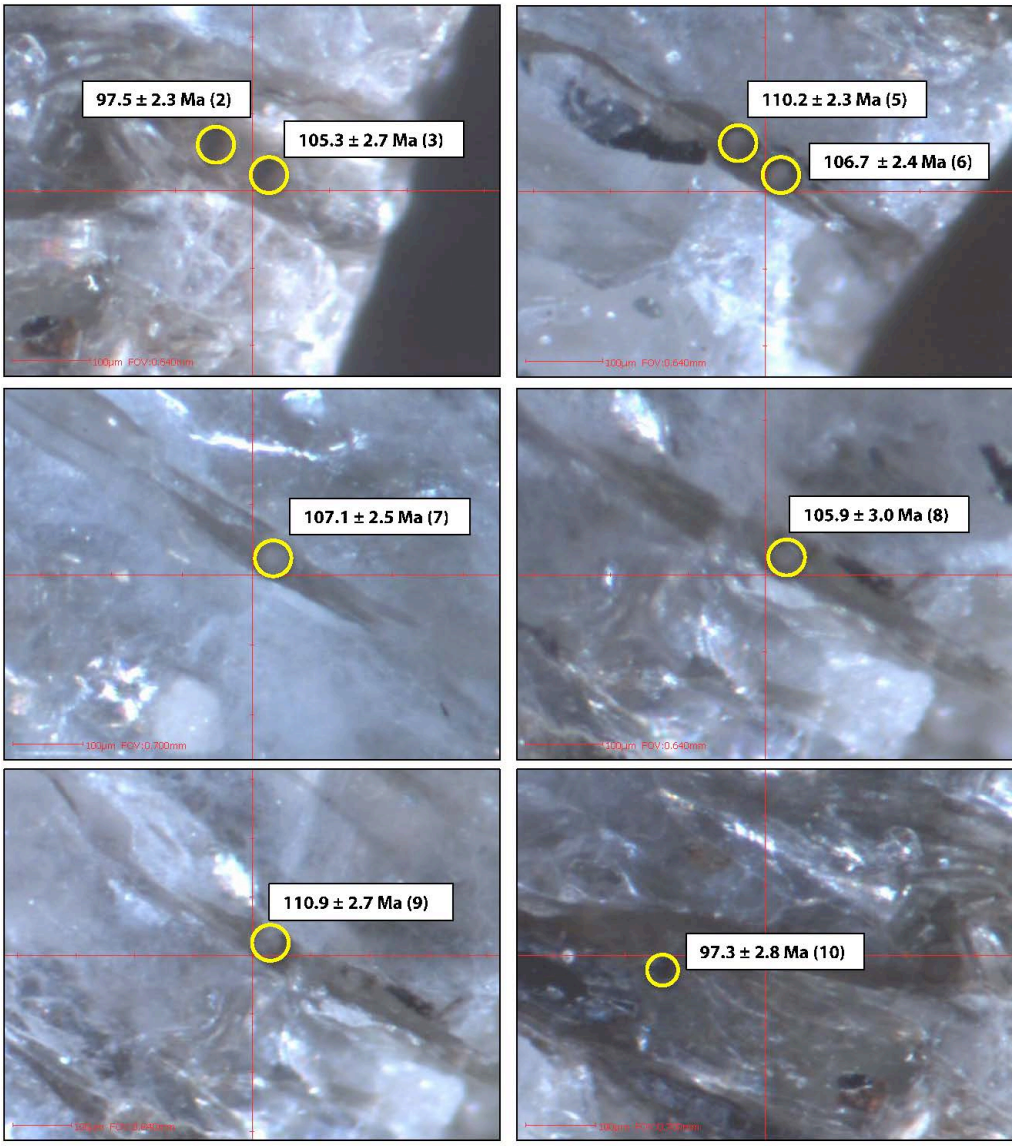

SV10-06 Quartzite, *continued*

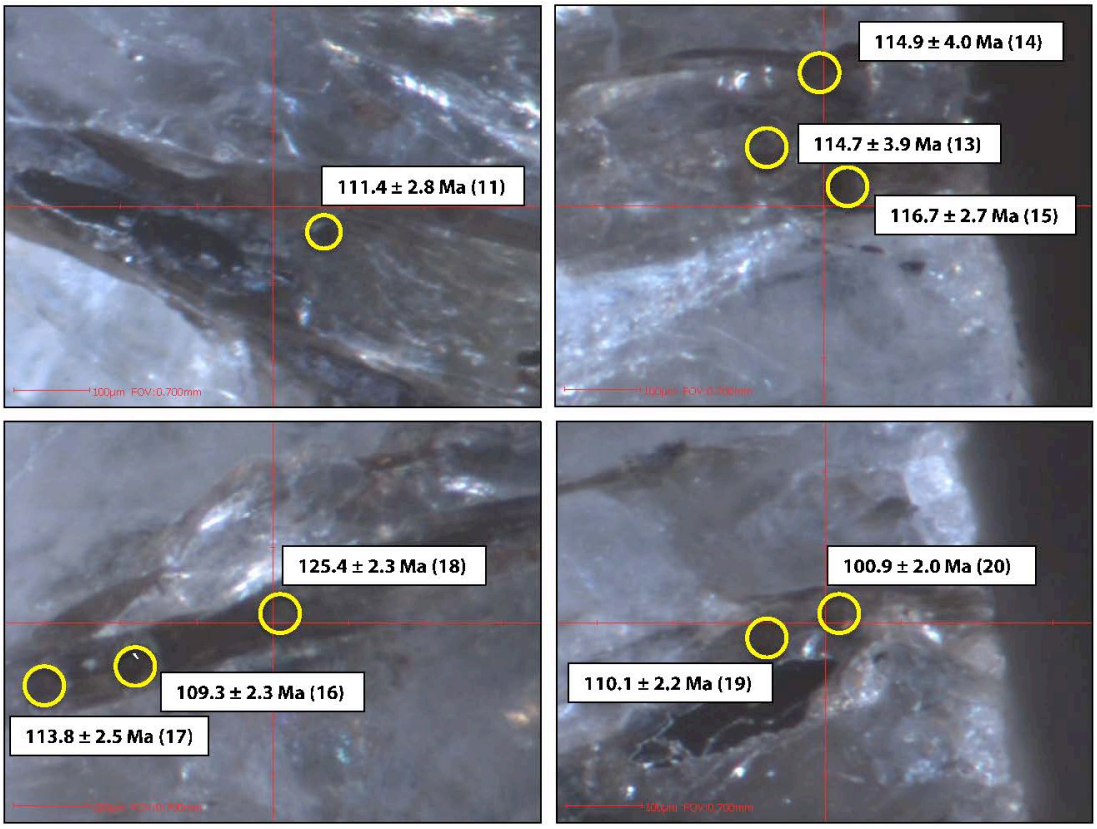

SV10-08 Quartzite

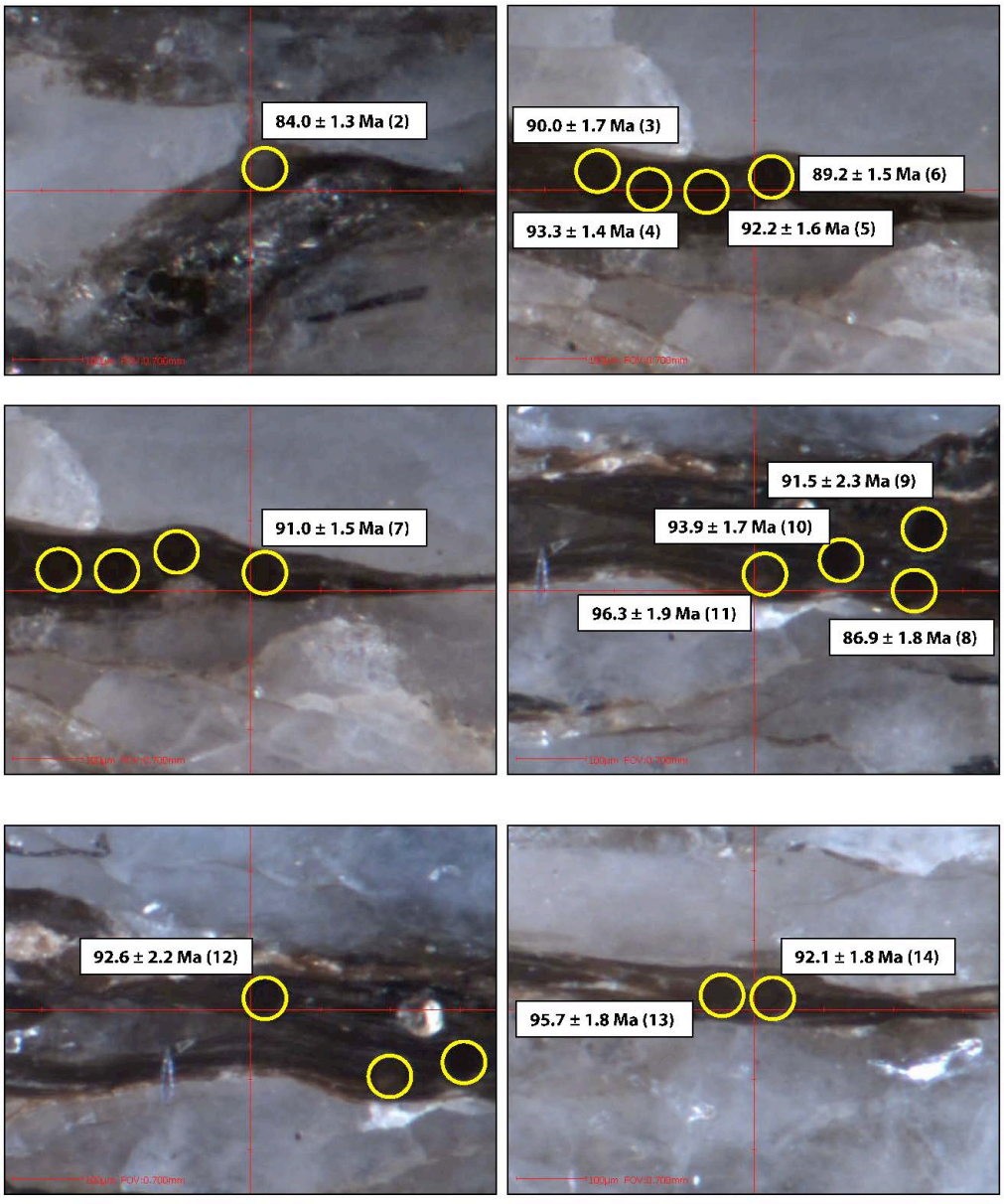

SV10-08 Quartzite, *continued*

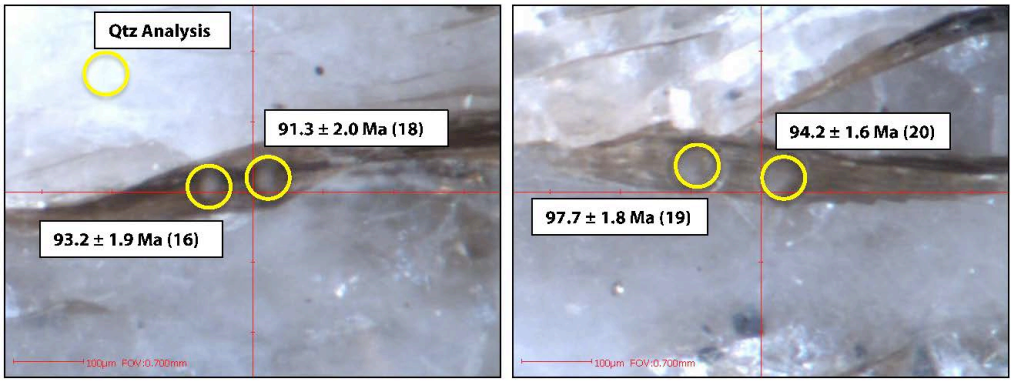

Supplementary Material 4. Plots and ^{36}Ar and ^{37}Ar vs Age

SV12-13E Lawsonite Eclogite

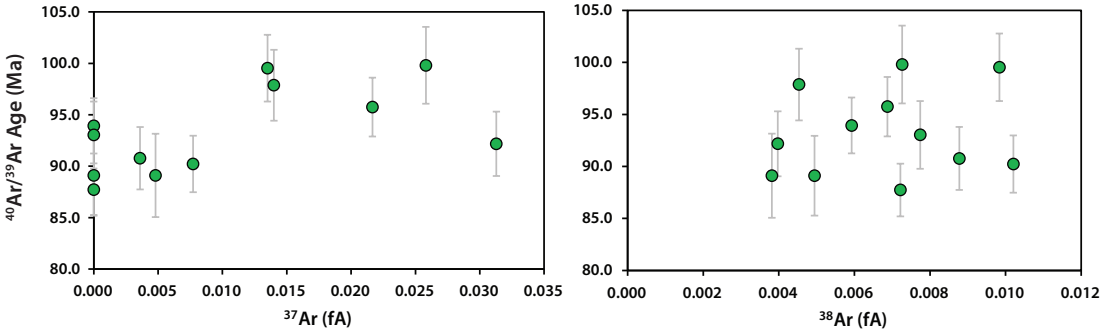

SV12-10B Eclogite

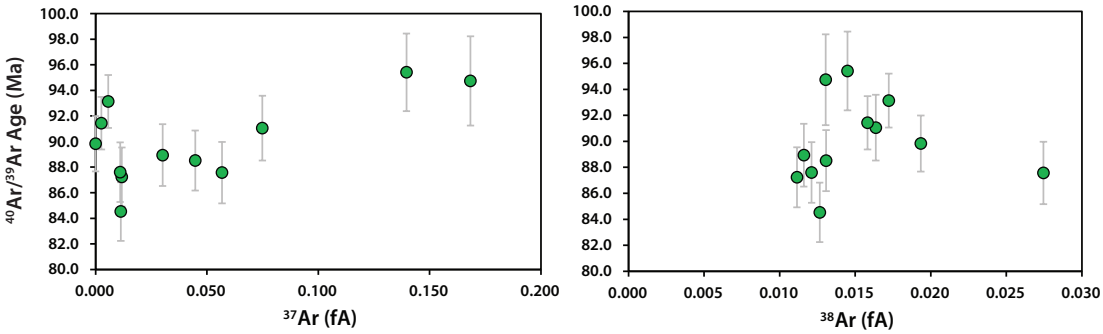

SV12-15A Epidote Eclogite

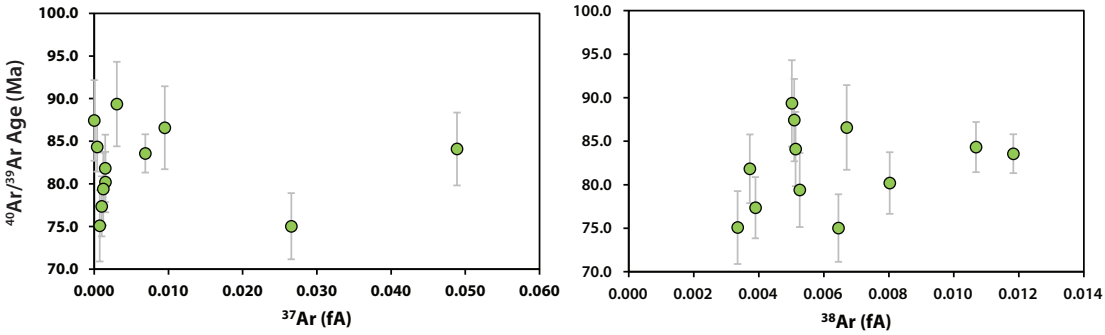

SV03-103 Lawsonite Vein (Session 1)

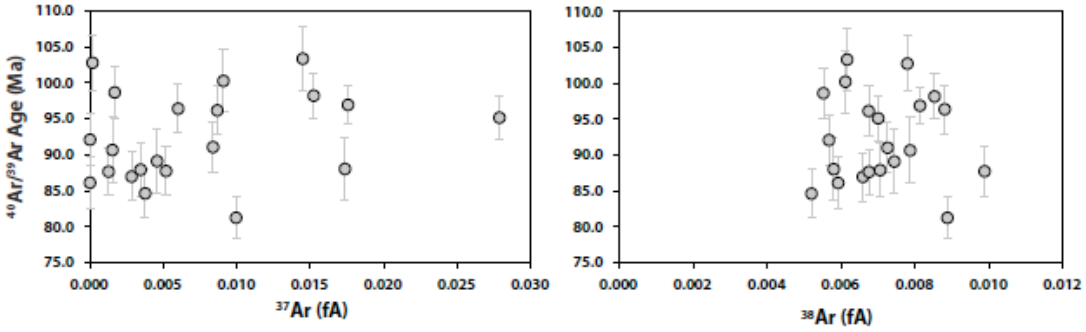

SV03-103 Lawsonite Vein (Session 2)

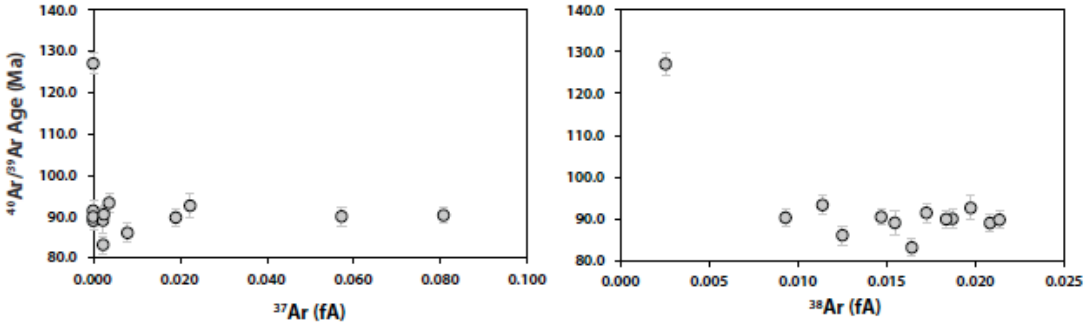

SV13-06B Lawsonite Garnet Blueschist (Halilbağı)

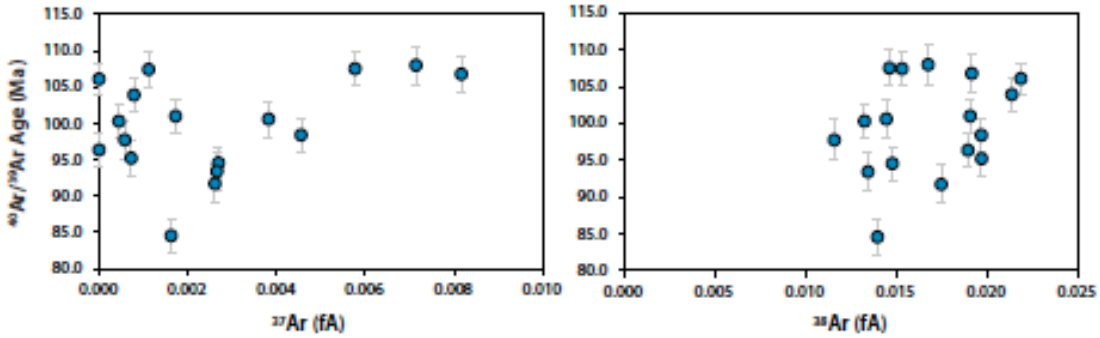

SV13-15 Lawsonite Blueschist (Halilbağı)

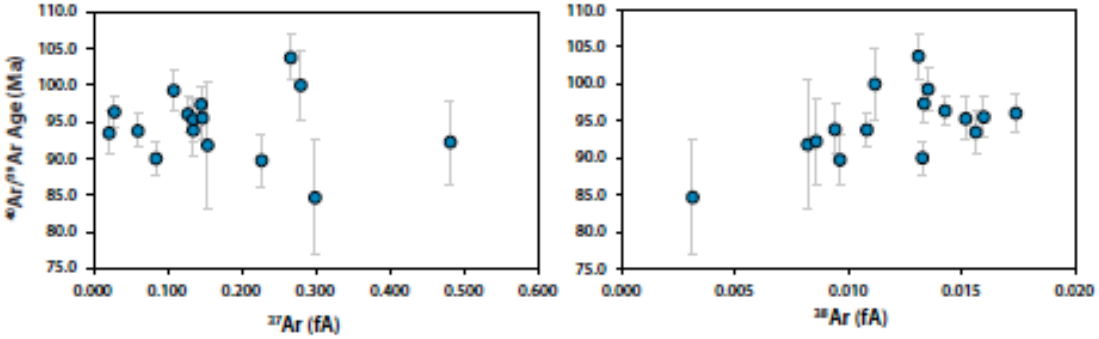

SV12-59 Lawsonite Garnet Blueschist (İkipınar)

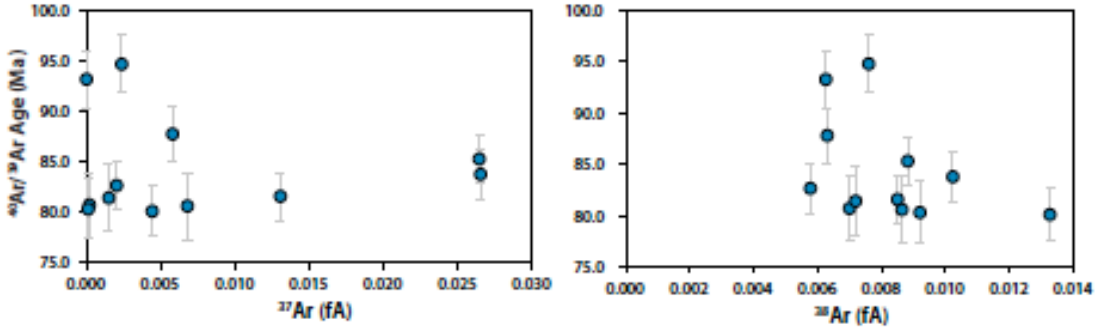

SV10-06 Quartzite

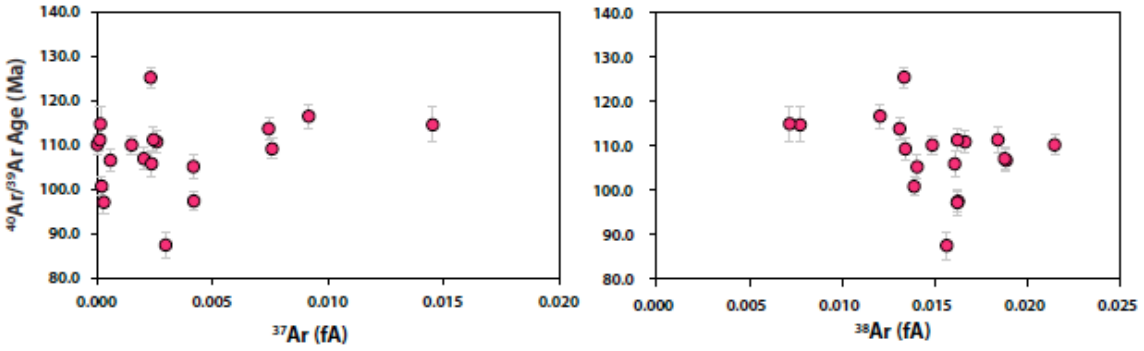

SV10-08 Quartzite

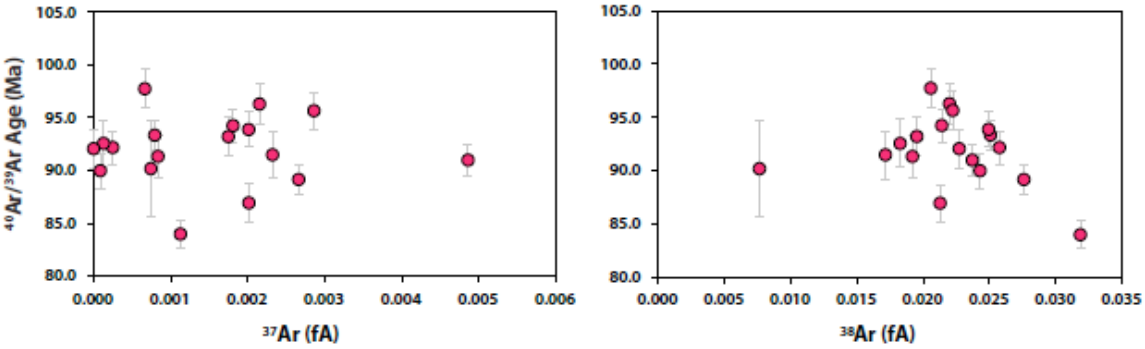

Supplementary Material 5. 36/40 vs. 39/40 Plots

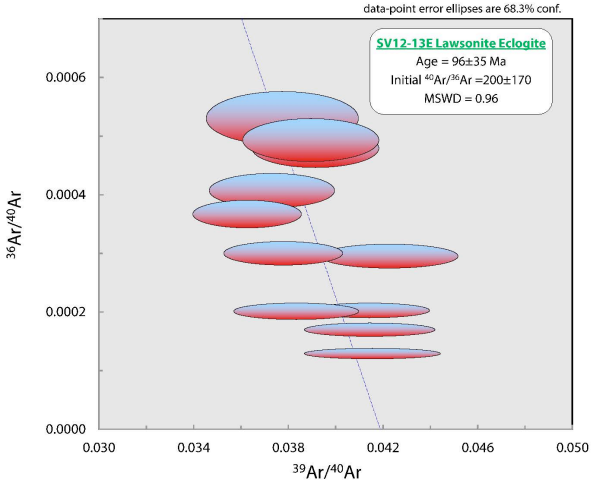

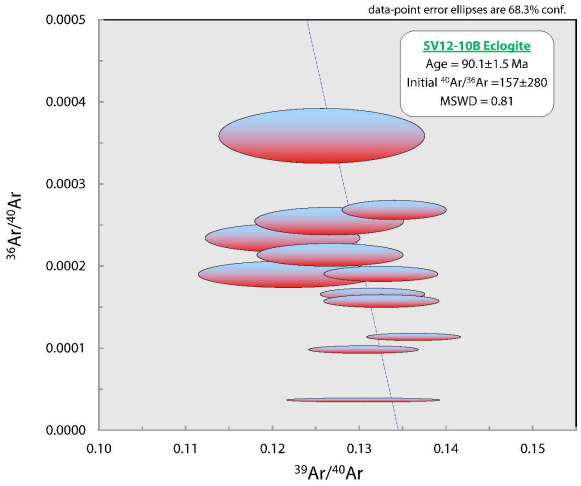

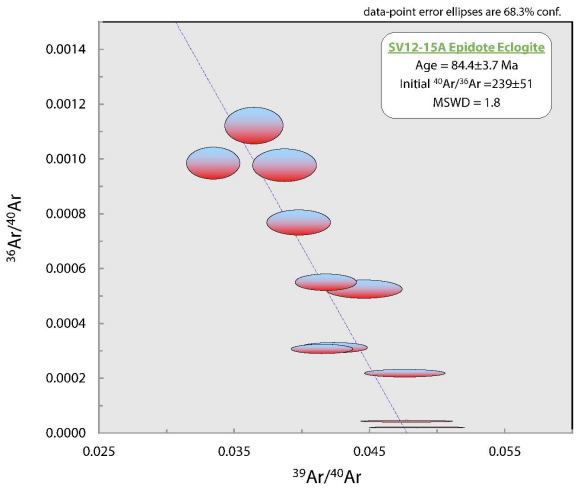
data-point error ellipses are 68.3% conf.
SV12-15A Epidote Eclogite
Age = 84.4±3.7 Ma
Initial $^{40}Ar/^{36}Ar$ =239±51
MSWD = 1.8
$^{36}Ar/^{40}Ar$
$^{39}Ar/^{40}Ar$
0.0014
0.0012
0.0010
0.0008
0.0006
0.0004
0.0002
0.0000
0.025
0.035
0.045
0.055

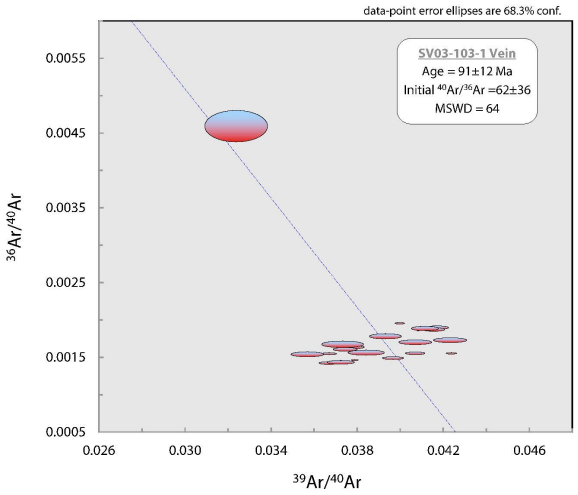
data-point error ellipses are 68.3% conf.
SV03-103-1 Vein
Age = 91±12 Ma
Initial $^{40}Ar/^{36}Ar$ =62±36
MSWD = 64
$^{36}Ar/^{40}Ar$
$^{39}Ar/^{40}Ar$
0.0055
0.0045
0.0035
0.0025
0.0015
0.0005
0.026
0.030
0.034
0.038
0.042
0.046

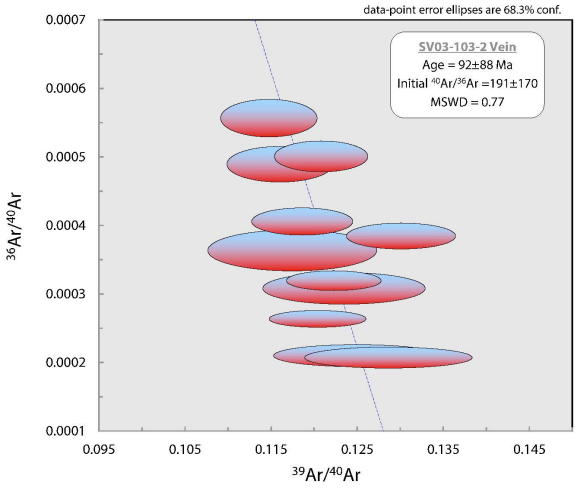
data-point error ellipses are 68.3% conf.
SV03-103-2 Vein
Age = 92±88 Ma
Initial 40Ar/36Ar =191±170
MSWD = 0.77
0.0007
0.0006
0.0005
0.0004
0.0003
0.0002
0.0001
36Ar/40Ar
0.095
0.105
0.115
0.125
0.135
0.145
39Ar/40Ar

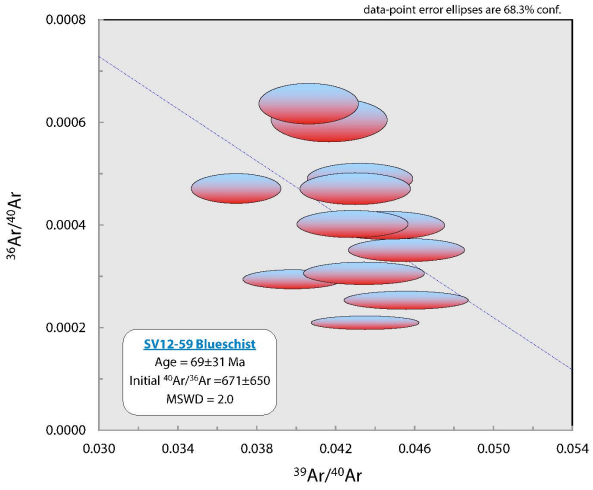
data-point error ellipses are 68.3% conf.
SV12-59 Blueschist
Age = 69±31 Ma
Initial 40Ar/36Ar =671±650
MSWD = 2.0
0.0008
0.0006
0.0004
0.0002
0.0000
36Ar/40Ar
0.030
0.034
0.038
0.042
0.046
0.050
0.054
39Ar/40Ar

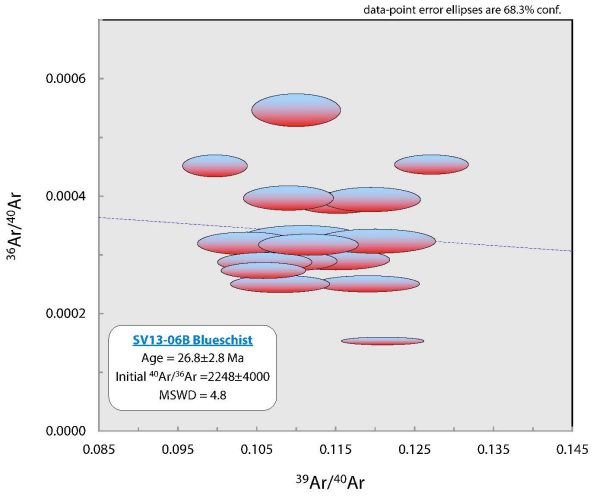
data-point error ellipses are 68.3% conf.
0.0006
0.0004
0.0002
0.0000
$^{36}Ar/^{40}Ar$
0.085
0.095
0.105
0.115
0.125
0.135
0.145
$^{39}Ar/^{40}Ar$
SV13-06B Blueschist
Age = 26.8±2.8 Ma
Initial $^{40}Ar/^{36}Ar$ =2248±4000
MSWD = 4.8

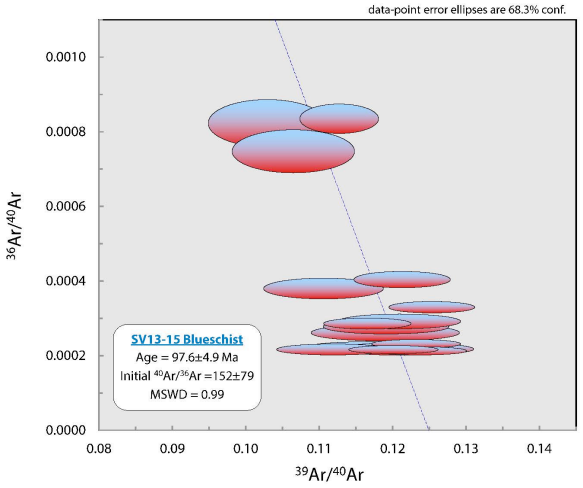
data-point error ellipses are 68.3% conf.
0.0010
0.0008
0.0006
0.0004
0.0002
0.0000
$^{36}Ar/^{40}Ar$
0.08
0.09
0.10
0.11
0.12
0.13
0.14
$^{39}Ar/^{40}Ar$
SV13-15 Blueschist
Age = 97.6±4.9 Ma
Initial $^{40}Ar/^{36}Ar$ =152±79
MSWD = 0.99

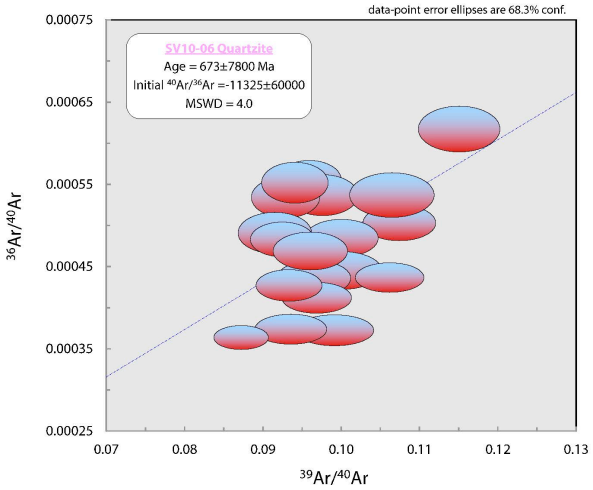
data-point error ellipses are 68.3% conf.
SV10-06 Quartzite
Age = 673±7800 Ma
Initial $^{40}Ar/^{36}Ar$ =-11325±60000
MSWD = 4.0
0.00075
0.00065
0.00055
0.00045
0.00035
0.00025
$^{36}Ar/^{40}Ar$
0.07
0.08
0.09
0.10
0.11
0.12
0.13
$^{39}Ar/^{40}Ar$

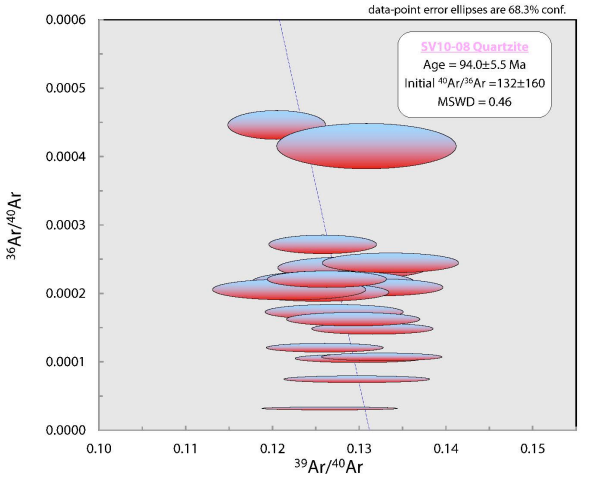
data-point error ellipses are 68.3% conf.
SV10-08 Quartzite
Age = 94.0±5.5 Ma
Initial $^{40}Ar/^{36}Ar$ =132±160
MSWD = 0.46
0.0006
0.0005
0.0004
0.0003
0.0002
0.0001
0.0000
$^{36}Ar/^{40}Ar$
0.10
0.11
0.12
0.13
0.14
0.15
$^{39}Ar/^{40}Ar$

Chapter 3. Lawsonite Composition and Zoning as an Archive of Metamorphic and Deformation Processes in Subduction Zones

Chapter Summary

Lawsonite is a hydrous, Ca-Al-rich silicate mineral that is important in volatile and element cycling between the crust and mantle, and may also influence the rheology and deformation behavior of the subducted crust and associated sediments. However, despite its potential geochemical and geodynamic significance for subduction zone processes, little is known about the trace element affinity and the types and origins of zoning patterns in lawsonite, or the relationship (if any) between compositional zoning and microstructures. To evaluate the significance of trace element abundance and zoning in lawsonite for subduction zone metamorphism and deformation, we conducted an integrated geochemical (major and trace element) and microstructural (electron backscatter diffraction) study of lawsonite in metabasaltic, metasedimentary, and metasomatic rocks, as well as lawsonite-bearing veins and layers, from the Sivrihisar Massif, Turkey, one of the few places in the world where pristine lawsonite has survived unaltered in eclogite during exhumation. Lawsonite from all rock types deviates from the end-member composition, incorporating FeO* (up to 3 wt.%), TiO_2 (up to 1 wt.%), and Cr_2O_3 (up to 6 wt.%), and commonly displays zoning (core-to-rim, sector, oscillatory) in these elements. Intragrain variations (up to 2 orders of magnitude) in trace (including rare earth) elements are also common, and in some cases display zoning that correlates with transition metal zoning. Within a single grain, different elements can display different zoning patterns, suggesting that different mechanisms affect the uptake and distribution

of different elements in lawsonite. In some cases, this is crystallographically-controlled (e.g., Ti), whereas in others (e.g. Fe, Cr) zoning may track changes in the metamorphic environment, such as changes in mineral assemblage, oxidation state, and/or fluid-rock interaction. Zoning in lawsonite can also be affected by processes acting after crystal growth (e.g., deformation, dissolution-reprecipitation) that may subsequently modify the original zoning patterns and/or grain shape.

1. Introduction

Water is transported into the deep parts of the subduction system via hydrous phases such as lawsonite, phengite, amphibole, epidote-group minerals, talc, chlorite, and serpentinite. Because these hydrous phases form as a result of fluid-rock interaction, their compositions and microstructures may provide a record of fluid compositions and sources, and their distribution may track fluid transport pathways in the subducted slab. Of these phases, lawsonite [$CaAl_2Si_2O_7(OH)_2 \cdot H_2O$] is of particular importance to fluid processes and element cycling in subduction zones because it is abundant over a wide range of depths (and may be the main hydrous phase at $P > 2.5$ GPa) (e.g., Pawley 1994, Schmidt and Poli, 1994), has a high water content (11.5 wt.%), and is a significant reservoir for trace elements in high-pressure assemblages, particularly rare earth elements (REE), Sr, Pb, Th, and U (Tribuzio et al. 1996, Ueno 1999, Spandler et al. 2003, Martin et al. 2014, Vitale Brovarone et al. 2014). It can also be used to date subduction metamorphism (Mulcahy et al. 2009, 2014, Vitale Brovarone and Herwartz 2013), to document the deformation and rheological behavior of subducted oceanic crust and

associated sedimentary rocks (Teyssier et al. 2010, Kim et al. 2013, 2015, Cao et al. 2014, 2016, Whitney et al. 2014), and to interpret seismic properties of subducted slabs (e.g., Abers and Sarker 1996, Hacker 1996, Connolly and Kerrick, 2002, Hacker et al. 2003, Fujimoto et al. 2010; Chantel et al. 2012; Mookherjee and Bezacier 2012, Reynard and Bass 2014). Lawsonite dehydration has also been proposed as a driving force for some slab earthquakes (e.g., Kita et al. 2006, Abers et al. 2013). It is therefore important to understand the chemical and physical properties and behavior of lawsonite.

In comparison to other hydrous phases that are important in subduction systems, however, relatively little is known about the compositional variations and zoning of lawsonite. This is in part because lawsonite has been proposed to exhibit very little compositional variation (e.g., Pawley 1994), and in part because it is rarely preserved in subduction-related rocks exhumed to the Earth's surface (Zack et al. 2004, Whitney and Davis 2006). Furthermore, many of the documented lawsonite-bearing localities preserve fresh lawsonite only in spatially- and/or texturally restricted sites, such as an inclusion in garnet (Zhang and Meng 2006, Tsujimori et al. 2006) or in a xenolith (Usui et al. 2006). In some cases, the (former) presence of lawsonite is only inferred from rectangular or prismatic-shaped aggregates of epidote + paragonite + quartz ± albite ± talc (at lower pressures; e.g., Ballevre et al. 2003) or epidote + kyanite + quartz/coesite ± garnet ± omphacite (at higher pressures), from phase equilibria modeling, or from mass balance calculations (e.g., Guo et al. 2013) (Figure 1). The scarcity of well-preserved lawsonite, particularly in eclogite, has prevented a comprehensive understanding of the

compositions, substitution mechanisms, trace element affinity, and the types and origins of zoning patterns in lawsonite.

One of the few places in the world with fresh, unaltered lawsonite in eclogite and blueschist facies rocks is the Sivrihisar Massif, Turkey, which contains a coherent sequence of lawsonite-bearing metabasaltic and metasedimentary rocks that provide an opportunity to systematically examine the range of compositional variations and zoning patterns in lawsonite. The lawsonite-bearing rocks of the Sivrihisar Massif were metamorphosed and deformed at or near the slab-mantle interface, and therefore lawsonite and associated minerals from these rocks are an archive of fluid-mineral interaction at the top of a subducting slab (Teyssier et al. 2010, Whitney et al. 2014).

In this study, we integrate results of major and trace element compositional analyses of lawsonite by electron microprobe (EMP) and laser ablation inductively coupled mass spectrometry (LA-ICPMS) with microstructural analysis of lawsonite by electron backscatter diffraction (EBSD) to characterize different types of zoning and document compositional variations in lawsonite from different rock types. This dataset is used to evaluate the controlling factors in lawsonite composition and zoning at eclogite and blueschist facies conditions, and therefore to understand the physical and chemical behavior of this important hydrous mineral during subduction.

2. Regional Geology of the Tavşanlı Zone

The Tavşanlı Zone is a Late Cretaceous (Okay and Kelley 1994, Okay 1998, Sherlock et al. 1999, Seaton et al. 2009, 2014, Mulcahy et al. 2014) paleosubduction zone formed during the closure of the Neo-Tethys Ocean (Okay 1980, 1984, 1986). It is

presently exposed just south of the Izmir-Ankara-Erzincan suture, the main Neo-Tethyan suture in Turkey, as a 50-km wide and 350-km long, east-west trending, structurally coherent high-pressure/low-temperature metamorphic belt. The belt is composed of a coherent continental blueschist facies sequence (Orhaneli Group) that is overlain by a Cretaceous accretionary complex (Ovacık Complex) and large ophiolite slabs (Okay 1998, Okay and Whitney 2010). Undeformed Eocene granitoids (~48 – 53 Ma; Harris et al. 1994, Okay 1998, Sherlock et al. 1999) locally intruded the blueschist sequence and the overlying ophiolite.

Blueschist facies rocks from the western part of the belt record pressures of up to 2.4 GPa and temperatures of 430 °C (Okay and Kelley 1994, Okay 2002) to 470 – 550 °C (Plunder et al. 2013), whereas blueschists from a more eastern portion of the belt record pressures of only 0.9 – 1.1 GPa and peak metamorphic temperatures ranging from 375 to 450 °C (Droop et al. 2005). Although the belt is dominated by blueschist facies rocks, lawsonite eclogite pods, ranging in size from 5 cm to 5 m, occur in the Sivrihisar Massif (Davis and Whitney 2006, Whitney and Davis 2006). Lawsonite eclogite from the Sivrihisar Massif records maximum pressure conditions of 2.4 – 2.5 GPa and temperatures of 550 °C (Davis and Whitney 2006, 2008), indicating depths of ~80 km in the subduction zone and making it one of the deepest known occurrences of fresh lawsonite eclogite in the world (Whitney et al. 2014).

2.1 Western Part of the Belt

In the western part of the belt, the Orhaneli Group is composed of metapelitic schists at the base (Kocasu Formation), several kilometers of marble in the middle (Inönü

Marble), and a series of metabasite (~80%), metachert, and phyllite layers at the top (Devlez Formation). Blueschist-facies minerals are well preserved in the rocks of the Kocasu and Devlez Formation. Metapelitic schists of the Kocasu Formation consist of quartz + phengite + chlorite + jadeite + chloritoid + lawsonite + albite (Okay and Kelley 1994, Okay 2002). The metabasaltic rocks of the Devlez Formation consist of sodic amphibole + lawsonite + phengite + titanite ± sodic pyroxene ± chlorite ± quartz ± albite ± carbonate minerals (Okay 1980, Plunder et al. 2015), and the metacherts consist of garnet ± sodic amphibole ± lawsonite ± phengite ± sodic pyroxene ± epidote ± oxides (hematite) (Plunder et al. 2015). Within the Devlez area, metasomatic zones consisting of lawsonite-bearing chloritite with minor sodic pyroxene and titanite are also found at the base of an oceanic-derived accretionary complex (Plunder et al. 2013). Garnet is rare in the western part of the belt, but when present, typically occurs as small, Mn-rich garnet in the metacherts of the Devlez Formation.

2.2 Eastern Part of the Belt

Although the Sivrihisar Massif is offset to the SSE from the main part of the belt and has more north-south oriented mineral lineations than the rest of the Tavşanlı Zone (Okay 1998), it has long been considered to be part of the Tavşanlı Zone and is currently the only site in the belt where unaltered lawsonite eclogite has been found. In the Sivrihisar Massif, the base of the Orhaneli Group is comprised of interlayered micaschist and marble with a structural thickness > 3 km (Sivrihisar Formation), overlain (possibly tectonically) by a series of metabasite, metachert, and marble called the Halilbağı Formation (Okay and Whitney 2010). Although the Sivrihisar Formation is generally

considered to be a lateral facies variation of the Kocasu Formation and the Inönü Marble (Okay and Whitney 2010), high-pressure mineral assemblages are not well preserved, although in a few locations highly altered jadeite (± chloritoid ± lawsonite) occurs (Çetinkaplan et al. 2008, Whitney et al. 2011). The Halilbağı Formation, however, has well-preserved HP minerals, including lawsonite, in metabasaltic and metasedimentary rocks as well as in metasomatic zones associated with serpentinite lenses (Whitney et al. 2014).

Near the villages of Halilbağı and İkipınar, the Halilbağı Formation consists of km-scale metasedimentary layers (marble, calc-schist, quartzite) interlayered with km-scale lawsonite blueschist layers (Figure 2). Hundreds of mafic pods (> 230), including lawsonite eclogite, occur throughout the field area, where they are hosted within schistose blueschist, calc-silicate, and quartzite (Davis and Whitney 2006). Lawsonite eclogite typically consists of omphacite + garnet + lawsonite + phengite + rutile ± glaucophane. Other common metabasaltic pod types include blueschist pods, omphacite + lawsonite + phengite pods, omphacite + garnet pods, and chlorite + epidote ± lawsonite pods, interpreted as retrogressed lawsonite eclogite pods (Davis and Whitney 2008). The margins of some mafic pods are dominated by chlorite + epidote, with coarse-grained patches of lawsonite and crosscutting, monomineralic lawsonite veins. Metasedimentary rock types include marble, calc-silicate, mica schist, and quartzite. With the exception of marble, these rock types locally contain HP minerals such as lawsonite, sodic pyroxene, sodic amphibole, piemontite (Mn-rich epidote), spessartine-rich garnets, and phengitic white mica.

This sequence of HP rocks is in fault contact with a low-grade metamorphosed ultramafic and mafic complex to the north (Figure 2). Within ~ 150 m of the fault contact a mylonite zone is preserved, and is interpreted to have developed under HP conditions (Teyssier et al. 2010, Whitney et al. 2014). Within several hundred meters of the fault contact, antigorite serpentinite lenses occur within the HP terrane. The serpentinite lenses are bordered by lawsonite + chlorite ± garnet assemblages (Zack 2013, Whitney et al. 2014), suggesting that they were emplaced at high-pressure conditions.

3. Lawsonite in the Tavşanlı Zone

Lawsonite is abundant in the Tavşanlı Zone (comprising 20 – 50% of the mode in some rocks; Okay 1980), and occurs in various rock types and textural/structural sites, including metabasalts (blueschist and eclogite), metasediments (calc schists and quartzites), and metasomatic zones of lawsonite + chlorite at the contact between metabasaltic rocks and serpentinite, as well as in lawsonite-rich veins and layers at pod margins. Petrographic and textural evidence suggests that lawsonite was stable along the prograde (inclusions in garnet), peak (matrix grains), and retrograde path (retrogressed chlorite + epidote-rich pod margins). Given the widespread occurrence of lawsonite in a variety of rock types and textural sites, the Tavşanlı Zone is an excellent field area to investigate the utility of lawsonite as a monitor of metamorphic fluid and deformation processes over a range of depths during subduction and exhumation.

Representative samples of blueschist- and eclogite-facies metabasaltic, metasedimentary, and metasomatic rocks and lawsonite-rich veins and metamorphic layers were chosen for major and trace element zoning and composition study, as well as

microstructural analysis. Given the structural continuity of outcrops in the Sivrihisar region of the Tavşanlı Zone, the preservation of lawsonite eclogite, and the wealth of existing structural and petrologic data from that region, most of our sampling was conducted there. However, one sample from the western part of the Tavşanlı Zone was also included for comparison with similar lithologies in the Sivrihisar region. The mineral assemblages and textures for samples in which multiple analytical techniques were used are described in the following sections. Sample locations and the analytical methods are provided in Supplementary Material 1 for all samples for which compositional (± microstructural) data are presented.

3.1 Lawsonite Eclogite

Four lawsonite eclogite samples from the Halilbağı area were studied: two samples of fresh lawsonite eclogite (SV12-13E, SV03-103) and two of retrogressed lawsonite eclogite (SV08-4A, SV12-24) (Figure 2). The two fresh lawsonite eclogites are from the same 3.5 meter-long pod (see also Davis and Whitney, 2008; their Fig. 4 and sample SV04-305): SV12-13E was collected from the core of the pod and sample SV03-103 was collected from the pod margin.

Pod-core lawsonite eclogite SV12-13E consists of omphacite + garnet + lawsonite + phengite, minor epidote-group minerals (Figure 3a, b), and accessory rutile (rimmed with titanite), apatite, florencite, and zircon. Minor glaucophane is also present, although it appears to be a texturally late phase. Modal abundances of garnet, omphacite, lawsonite and phengite vary within the sample at the thin section scale, with some regions containing more omphacite and garnet, and other regions containing more phengite and

lawsonite, although these regions do not form distinct bands or layers. The habit of lawsonite in each of these regions varies; in the more phengite-rich regions, lawsonite tends to be euhedral to subhedral, whereas in the more omphacite + garnet-rich regions, lawsonite tends to be irregularly shaped and polycrystalline, containing numerous high-angle (> 10 °) boundaries (Figure 3a ,b). Euhedral to subhedral lawsonite ranges in size from 0.25 to 0.5 mm in length, whereas polycrystalline lawsonite can form aggregates of up to 1.5 mm in length. Both lawsonite types contain abundant inclusions of epidote, glaucophane, and zircon.

Fresh lawsonite eclogite SV03-103A was sampled from the margin of the pod and consists of omphacite + garnet + lawsonite + phengite (Figure 3c), minor epidote with allanitic cores, and accessory rutile (rimmed with titanite). Compared to lawsonite from the pod core, lawsonite from the pod margin is typically coarser-grained (1 – 1.3 mm in length) and inclusion-poor, containing only sparse inclusions of epidote and zircon. Lawsonite from this region of the pod also tends to lack the internal high-angle grain boundaries found in some of the lawsonite from the core of the pod, and forms rectangular blocky crystals.

Retrogressed eclogite sample SV08-4A was collected from a small (0.5 m) pod in blueschist, in a region that also contains several serpentinite lenses and associated chlorite + lawsonite ± garnet metasomatic zones (D. Whitney, personal communication; Figure 2). The sample is foliated and layered, with some layers richer in omphacite, some in glaucophane, and some in chlorite. The studied sample consists largely consists of lawsonite + chlorite, with minor amounts of epidote (with allanitic cores), and accessory

rutile (rimmed with titanite) and zircon. Relict ompachite, zoned amphibole (actinolitic cores, glaucophane rims), and highly fractured garnet (partly replaced by chlorite) are also present. Lawsonite occurs both as inclusions in garnet and as a matrix phase (Figure 3d, e). Lawsonite inclusions in garnet are commonly equant, whereas lawsonite in the chlorite-rich matrix varies from more equant grains to irregularly shaped aggregates of lawsonite. As viewed in thin section, lawsonite grain size varies within the chlorite-rich matrix, from 0.1 mm to 0.5 mm.

The margin of a chlorite + epidote-rich pod (SV12-24) was collected ~ 720 m E of the village of İkipınar (Figure 2). As these pods were previously interpreted as representing highly retrogressed eclogite pods based on their bulk compositions and the presence of relict clinopyroxene (Davis and Whitney 2006), we use the lawsonite from this sample as another comparison to lawsonite from unaltered lawsonite eclogite pods. This sample contains lawsonite + chlorite + epidote-group minerals, relict clinopyroxene and accessory Fe-Ti oxides, apatite, and titanite (Figure 3f). Common inclusions in lawsonite are Fe-Ti oxides, apatite, and epidote-group minerals. Lawsonite in this sample forms coarse-grained (up to ~ 1 cm in length), blocky to lath-like crystals that are most commonly white (in outcrop), but pink colored crystals also occur. Lawsonite most commonly occurs as scattered grains within the more fine-grained chlorite + epidote-rich matrix, although some lawsonite displays a radiating texture. A cm-scale, cross-cutting, monomineralic lawsonite vein (SV12-24B) was also collected from the margin of this pod.

3.2 Lawsonite Blueschist

Three lawsonite blueschists were sampled from coherent metabasaltic layers near the villages of Halilbağı (SV13-15, SV13-06B) and İkipınar (SV12-59) (Figure 2). Lawsonite blueschist sample SV13-15 was collected in the high-strain zone, ~ 120 meters south of the fault contact at the northern margin of the HP unit, and consists of glaucophane + lawsonite + phengite, and accessory titanite and zircon (Figure 3g). The blueschist displays strong compositional layering at the thin section scale, with mm-scale bands of lawsonite and phengite, alternating with layers of lawsonite and glaucophane (with minor phengite occurring only in pressure shadows surrounding lawsonite porphyroblasts) (Figure 3g). Lawsonite grain size and habit also vary in the different layers. In the lawsonite + phengite-rich bands, lawsonite forms equant grains that are all roughly the same size (~ 100 μm), whereas lawsonite in the glaucophane-rich layers ranges from more fine-grained, equant grains to more coarse-grained, irregularly shaped aggregates of lawsonite.

Lawsonite garnet blueschist sample SV13-06B was collected just outside of the high-strain zone, ~ 215 meters south of the fault contact (Figure 2), and consists of glaucophane + omphacite + garnet + lawsonite + phengite, and quartz, chlorite, minor allanite, and accessory rutile (rimmed with titanite), Fe-oxides, and zircon. Lawsonite in this sample forms tabular crystals that are generally oriented parallel to the dominant foliation and contain inclusions of zircon, epidote, quartz, rutile (with titanite rims), and rare garnet (Figure 3h).

Lawsonite garnet blueschist sample SV12-59 was collected near the village of İkipınar, ~ 8 km NW of Halilbağı (Figure 2) and consists of glaucophane + garnet + lawsonite + phengite, and accessory Fe-Ti oxides, titanite, and zircon. Lawsonite forms equant grains (~ 0.8 mm for matrix grains) that occur in a variety of textural positions within the sample, including as an inclusion in garnet, as part of deformed phengite-rich clusters, and as a matrix phase (Figure 3i).

3.3 Metasedimentary rocks

Blueschist-facies calc-schist SV13-01a was sampled in the high-strain zone, ~ 180 meters south of the fault contact (Figure 2), and consists of quartz + calcite + lawsonite + phengite (intergrown with chlorite) + glaucophane, and accessory epidote (with allanitic rims), apatite, and titanite. Lawsonite is sparse in this sample and occurs as porphyroblasts (0.5 – 3 mm in length) dispersed throughout the matrix (Figure 4a). The lawsonite is typically oriented at an angle to the dominant foliation, although locally the foliation is bent around the lawsonite porphyroblasts (Figure 4b).

Quartzite sample SV10-06 was collected ~220 meters from the northern tectonic boundary at the same structural level as blueschist SV13-06B (Figure 2). It consists of quartz + phengite + clinopyroxene + sodic amphibole + lawsonite + garnet, minor amounts of piemontite, and accessory Fe-Ti oxides. Phengite occurs as elongate single grains or small clusters dispersed throughout the quartz matrix, as well as in layers (~ 0.5 mm thick) containing lawsonite, garnet, and Fe-Ti oxides (Figure 4c). Lawsonite typically forms elongate (~0.5 mm in length), boudinaged grains that are parallel to the dominant foliation (Figure 4c, d).

3.4 Lawsonite + Chlorite Rocks

Lawsonite + chlorite-rich rocks are found throughout the Tavşanlı Zone (Zack 2013, Plunder et al. 2013, Whitney et al. 2014), and are typically associated with serpentinite lenses (Figure 5a; Zack 2013, Whitney et al. 2014). Although these rocks are largely comprised of lawsonite in a chlorite-rich matrix, some samples also contain epidote-group minerals, amphibole, garnet, and accessory titanite. Lawsonite is typically coarse-grained (> 0.5 mm, Figure 5b - d) and slightly pink in hand sample (Figure 5c). Three lawsonite + chlorite-rich rocks were sampled for this study: two from the Halilbağı region of the Sivrihisar Massif (SV12-21d, SV13-17a) and one from further west in the Tavşanlı Zone (TZ10-2.2; for map of location see Stop 2.2 in Okay and Whitney 2010; Supplementary Material 1).

Sample SV12-21d consists of lawsonite + chlorite and accessory titanite (Figure 5b). Lawsonite occurs as coarse-grained (~ 1 x 0.75 mm), blocky crystals dispersed in a chlorite matrix. The modal abundance of lawsonite varies widely throughout the rock, with some regions containing largely chlorite (> 90%) and others containing ~50% lawsonite and 50% chlorite. Regardless of variations in modal abundance, the rock overall lacks a pervasive fabric and lawsonite is scattered within the matrix.

Sample SV13-17a consists of lawsonite + garnet + epidote-group minerals + chlorite and accessory titanite. Lawsonite is present as a matrix phase where it forms grains that range from elongate (~0.5 by ~0.2 mm) to equant (~ 0.5 by ~0.4 mm).

Inclusions of REE-rich epidote are common, and typically occur in the core regions of lawsonite grains.

The lawsonite + chlorite-rich sample (TZ10-2.2) was collected from a boulder in the western region of the Tavşanlı Zone, and consists of lawsonite + chlorite and accessory titanite. Lawsonite forms elongate, light pink laths that range from 1 – 5 mm in length and that are scattered throughout the chlorite matrix (Figure 5c, d). Lawsonite cores contain abundant inclusions of titanite, epidote-group minerals, and apatite, whereas the rims are generally inclusion-poor.

3.5 Lawsonite-rich Veins and Layers

Lawsonite-rich layer SV03-103C is from the margin of the lawsonite eclogite pod studied by Davis and Whitney (2008), and from which fresh lawsonite eclogite samples SV12-13E (core) and SV03-103A (margin) were collected (Figure 6a). The sample consists of lawsonite + garnet + phengite, minor epidote with allanite cores, and accessory rutile (rimmed with titanite) and zircon. Lawsonite is coarse-grained (0.5 to 1.0 mm in length), and forms rectangular, blocky crystals. Rutile, epidote, and/or zircon are common inclusions in lawsonite. Major and trace element analyses of lawsonite in lawsonite vein SV03-103 were previously presented by Martin et al. 2014. A monomineralic lawsonite vein (SV12-24B) was also collected from the epidote + chlorite-rich pod margin from which sample SV12-24 was collected (Figure 6b).

4. Lawsonite Major and Trace Element Compositions and Zoning

To characterize the composition and zoning patterns of lawsonite, we obtained major and trace element maps to determine the most common zoning types and to guide decisions during subsequent quantitative major and trace element analyses of lawsonite.

Major element compositions were determined with a JEOL JXA-8900 electron microprobe in the Department of Earth Sciences at the University of Minnesota. Quantitative microprobe analyses were performed with a 15-kV accelerating voltage, 15 nA beam current, and a defocused 5 - 10 μm beam diameter to minimize beam damage to minerals. Natural mineral standards were used in calibrations. O and OH were calculated by cation stoichiometry and included in the ZAF matrix calibrations. X-ray element maps were acquired using a 15-kV accelerating voltage, 100 nA beam current, a focused beam, and stage-rastering step sizes ranging from 1 to 6 depending on lawsonite grain size.

LA-ICPMS analyses of lawsonite were acquired at the Research School of Earth Sciences, Australian National University. Trace elements were measured on an ArF excimer laser coupled to a quadrupole ICPMS Agilent 7700, using the set-up described in Eggins et al. (1998). The laser was tuned to a frequency of 5 Hz and energy of 50 mJ (corresponding to an HV of around 26 – 27 kV), and spot sizes ranged from 28 μm to 47 μm depending on the size of the grain and compositional zoning features. Counting times were 20 s for the background and 50 s for sample analysis. The internal isotope used to quantify the analyses was ^{29}Si. The NIST 612 glass was used as a primary standard, and the BCR glass was used as a secondary standard. The effects of small inclusions of rutile, zircon, and allanite on the analyses were removed manually by examining the time-resolved spectra for each analysis prior to data reduction. The data were reduced with the

freeware Iolite (Paton et al. 2011) and its data reduction scheme for trace elements (Woodhead et al. 2007). Accuracy and reproducibility of the secondary standard were generally within 10% of the reference value.

The results of the major and trace element zoning and composition analyses are presented below, organized by rock type. For samples where Fe, Ti, and/or Cr content is ≥ 0.5 wt.%, composition data from microprobe analyses are reported, and for samples where Fe, Ti, and/or Cr content is < 0.5 wt.%, composition data from LA-ICPMS analyses are reported.

4.1. Lawsonite Eclogite

Although two texturally different types of lawsonite are present in the core of the eclogite pod (SV12-13E), both lawsonite types display similar major and trace element compositions. They deviate from end-member lawsonite composition in that they contain FeO* (~1.2 – 1.5 wt.%), Ti (375 – 4000 ppm), and Cr (200 – 400 ppm) (Table 1, 2). With the exception of Fe and Ti, which display irregular zoning, no other systematic major or trace element zoning is detected in X-ray element maps (Figure 7a, b). However, chondrite-normalized lawsonite REE patterns from the core of the pod show that REE concentrations vary by 1 – 2 orders of magnitude (1 – 100 times chondrite) at both the sample and individual grain scale (Figure 8a), documenting that lawsonite is also zoned in the REE. There does not appear to be any detectable correlation between variations in REE concentrations or the shape of the REE pattern and the spatial position of the analysis (i.e., core vs. rim), Fe or Ti concentrations, or the textural type of lawsonite (Figure 8a).

Lawsonite from eclogite at the pod margin (SV03-103) also displays irregular Fe and Ti zoning, and contains similar FeO* and Ti contents as lawsonite from the core of the eclogite pod: intragrain Fe contents range from 1.0 – 1.6 wt.%, and Ti-rich regions of the lawsonite contain 1750 – 4200 ppm Ti, whereas Ti-poor regions of the lawsonite contain only 350 – 375 ppm Ti (Table 1, 2). Cr contents vary little across the grains, ranging from 30 – 150 ppm. Although lawsonite from the eclogite pod margin displays similar chondrite-normalized REE concentrations as lawsonite from the pod core (ranging from 1 – 100 times chondrite), the REE patterns tend to lack the enrichment in the MREE seen in lawsonite from the pod core and are overall more flat (Figure 8b).

Lawsonite from retrogressed lawsonite eclogite sample SV08-4A is zoned, as seen in backscattered electron images that show a lighter gray hourglass-shaped feature in the core of matrix lawsonite. Chondrite-normalized REE patterns suggest that there may be core-to-rim zoning in trace elements as well, with core regions containing higher concentrations of REE than rim regions in the same grain (Figure 8c). One grain yielded a "core" region with REE concentrations similar to those observed in the "rim", however, this may reflect either a sectioning effect or a "core" that is no longer located in the geometric center of the grain as a result of dissolution-reprecipitation processes. Inclusions of lawsonite in garnet yield REE concentrations similar to those observed in the core regions of matrix lawsonite (100 to 1000 times chondrite) (Figure 8c).

Chondrite-normalized REE patterns from lawsonite in the chlorite + epidote-rich pod (SV12-24) display two trends; one set of REE patterns has a flat trend ($[La/Yb]_N$ = 1 – 3) whereas the other set is LREE-enriched ($[La/Yb]_N$ = 8 – 20) with overall higher

concentrations of REE (10 – 1000 times chondrite) (Figure 8d). The flat REE patterns were all obtained from a single grain of blocky lawsonite.

Bulk rock analysis of the monomineralic lawsonite vein (SV12-24B) sampled from this pod shows a similar REE pattern to the LREE-enriched lawsonite population, both in terms of concentration (~20 – 400 times chondrite) and the overall shape of the pattern (Table 9). The concentrations of trace elements such as Sr, Pb, V, and Ti in lawsonite from the monomineralic vein and lawsonite from the pod are also similar (Table 2, 9).

4.2. Lawsonite Blueschist

Lawsonite from blueschists in the Tavşanlı Zone displays a variety of zoning types, such as core-to-rim zoning in Fe and sector zoning in Ti, and in some cases, core-to-rim zoning that transitions to more oscillatory zoning near the rims (Figure 7c-f). Lawsonite from a blueschist in the high-strain zone (SV01-75A) also displays oscillatory zoning in Cr.

Lawsonite from blueschist SV13-15 displays zoning in Fe and Ti. Fe zoning patterns appear to vary based on the textural location of the lawsonite: lawsonite from phengite-rich layers displays a core-to-rim increase in Fe (Figure 7d), whereas lawsonite from the glaucophane-rich matrix shows irregular variations in Fe content. Lawsonite from the glaucophane-rich matrix shows increased concentrations of Ti and Cr, and decreased P contents compared to lawsonite in the lawsonite + phengite rich bands (Table 3). Chondrite-normalized REE patterns from lawsonite in blueschist SV13-15 are generally LREE-enriched, although two analyses yield relatively flat REE patterns

(Figure 9a). No difference is observed in the concentration of REE or the shape of the REE pattern and the textural position of the analysis (lawsonite in the lawsonite + phengite-rich bands vs. in the glaucophane-rich matrix) (Figure 9a). Compared to the other lawsonite blueschists analyzed, this sample yielded overall higher REE concentrations (10 – 1000 times chondrite) (Figure 9).

Lawsonite from lawsonite garnet blueschist SV12-59 displays zoning in Fe and Ti. Fe zoning is characterized by a transition from an Fe-poor "core" (~ 0.70 to 1 wt.% FeO*) to an Fe-rich "rim" (~ 1.3 to 1.9 wt.% FeO*), although Fe zoning in this sample is not symmetric with respect to grain boundaries, and in some cases, is truncated at the grain boundary. Ti displays irregular zoning patterns that vary from grain to grain; Ti contents vary from ~ 300 to 3000 ppm across the sample (Table 3). No difference in trace element content was observed between lawsonite from lawsonite + phengite-rich clusters and lawsonite from the matrix (Table 3). Lawsonite from all regions displays chondrite-normalized REE patterns that are slightly enriched in the LREE compared to the HREE, with REE concentrations of 10 – 100 times chondrite (Figure 9b).

Lawsonite from lawsonite garnet blueschist SV13-06B displays zoning in Fe and Ti: Fe zoning is characterized by a core-to-rim increase in Fe concentrations, whereas Ti displays an irregular distribution. Trace element analyses of lawsonite from this sample show core-to-rim variations in Y and the shape of the REE pattern; these core-to-rim variations in trace elements correlate with core-to-rim zoning in Fe (Figure 9c). Fe-poor cores typically contain lower concentrations of Y (13 – 23 ppm) and display a steep REE

pattern compared to the Fe-rich rims, which are characterized by higher concentrations of Y (48 – 72 ppm) and a relative enrichment in the MREE (Table 3, Figure 9c).

4.3. Metasedimentary Rocks

On the basis of major element compositions and zoning patterns, there appears to be two populations of lawsonite in calc-schist sample SV13-01a. One displays pronounced oscillatory zoning in Cr, with Cr concentrations reaching up to 6 wt.%, Cr_2O_3 and the second has lower Cr contents (max. concentrations are ~ 1.00 wt.% Cr_2O_3), but has Ti and Fe sector zoning (Table 4, Figure 7g). Chondrite-normalized REE patterns from lawsonite from this calc-schist also display two trends: one set of REE patterns is flat, whereas the other shows enrichment in LREE (Figure 10a). In general, the Cr-rich lawsonite population contains higher concentrations of REE (10 to 1000 times chondrite) and steeper LREE patterns ($[La/Gd]_N$ = 3 – 12) relative to the Cr-poor population.

In contrast to the observations of Ueno (1999) for sector zoned lawsonite from the Sanbagawa pelitic schists, variations in the concentrations of the LREE do not appear to be related to whether the analysis was conducted in a Ti-poor or Ti-rich sector. The Cr-rich lawsonite population also displays an increased concentration of Sr, Y, Ni, and Pb relative to the Cr-poor lawsonite population (Table 5).

Compared to lawsonite from the other investigated rock types, which show a variety of zoning patterns in the transition metals, lawsonite from the quartz-rich rocks analyzed here display little to no zoning in the transition metals (Fe, Ti, Cr) (Figure 7h). Lawsonite from quartzite SV10-06 show chondrite-normalized REE patterns that are enriched in the LREE relative to the HREE ($[La/Yb]_N$ = 3 – 200), and contain a negative

Eu anomaly (Figure 10b). Lawsonite from this sample contains the highest concentrations of REE measured in this study, showing enrichments of up to ~ 1,000 to ~10,000 times chondrite, as well as the highest concentrations of Pb (100 – 220 ppm) (Table 5).

4.4. Lawsonite + Chlorite Rocks

Lawsonite from lawsonite + chlorite rock SV12-21D displays an asymmetric, localized Fe- and Ti-rich overgrowth. The boundary between the Fe- and Ti-rich overgrowth and the Fe- and Ti-poor region is sharp, although the absolute concentrations of Fe and Ti can vary within a compositional domain. In the Fe- and Ti-rich region, FeO* concentrations range from 1.80 – 2.00 wt.% and TiO_2 concentrations range from 0.5 to 1.00 wt.%, whereas in the Fe- and Ti-poor regions, FeO* ranges from 1.00 – 1.50 wt.% and Ti from 200 – 500 ppm (Table 6). Cr contents are generally low (50 – 140 ppm) and do not display any systematic zoning patterns (Table 7). Chondrite-normalized REE patterns from lawsonite display two trends: REE patterns from the Ti- and Fe-rich lawsonite overgrowth are flat, whereas REE patterns from the Ti- and Fe-poor region are HREE-enriched with flat LREE and MREE (Figure 11a). The two compositionally distinct regions also display variations in other trace elements such as Y and Sr, with Ti- and Fe-rich regions having slightly higher concentrations of Y and Sr compared to the Ti- and Fe-poor region (Table 7).

Lawsonite from lawsonite + chlorite rock SV13-17A displays compositional zoning in Fe, Ti, and Cr (Figure 7i, j). Fe zoning in this sample is complex and typically consists of an Fe-poor core region (1.00 – 1.20 wt.% FeO*) that transitions to an Fe-rich rim that displays oscillatory variations in Fe content (1.60 – 2.00 wt.% FeO*) (Figure 7i,

j; Table 6). REE-rich epidote-group mineral inclusions in the lawsonite generally occur outside of the Fe-poor core (Figure 7i). Sector zoning in Ti is observed in all analyzed grains; Ti-rich sectors contain 1500 – 3000 ppm Ti, whereas Ti-poor sectors contain 200 – 500 ppm Ti (Table 7). Cr displays oscillatory zoning in this sample, with concentrations ranging from 500 – 1500 ppm (Table 7). Regardless of intragrain variations in these elements, all trace element analyses of lawsonite from this sample yielded REE patterns that are MREE-enriched (Figure 11b). In contrast to most lawsonite analyzed, this lawsonite is also relatively enriched in the HREE compared to the LREE. Similar to the observations made for Ti sector-zoned lawsonite in calc-schist SV13-01a, variations in REE concentrations do not appear to vary depending on Ti content.

Lawsonite from lawsonite + chlorite rock TZ10-2.2c shows compositional zoning in Ti and Fe. Although the intra- and intergrain distribution of Ti within lawsonite is locally heterogeneous in this sample, inclusion-rich regions are generally Ti-poor, whereas inclusion-poor regions generally show a higher concentration of Ti. Lawsonite in this sample displays chondrite-normalized REE patterns that are generally flat ($[La/Yb]_N$ = 0.5 – 7) and 10 to 100 times enriched in the REE relative to chondrite (Figure 11c). The relative enrichment in REE does not appear to be related to the textural position of the analysis (Ti-poor vs. Ti-rich region, core vs. rim).

4.5. Lawsonite-rich Veins and Layers

Lawsonite from the lawsonite + garnet + phengite layer (SV03-103C) hosted in interlayered lawsonite eclogite and blueschist at an eclogite pod margin displays prominent zoning in Fe and Ti (Figure 7k, l). Fe zoning is characterized by a transition

from an Fe-poor core (~ 0.5 wt.% FeO*) to an Fe-rich rim; Fe-rich rims display oscillatory variations in FeO* content ranging from 0.8 – 1.5 wt.%. Ti displays patchy sector zoning, with Ti-rich sectors containing 1170 – 3060 ppm Ti, and Ti-poor sectors containing < 950 ppm Ti (Table 8, 9). Within a sector the Ti concentrations appear to vary in an oscillatory manner. Weakly developed oscillatory Cr zoning (Cr contents range from 320 to 1050 ppm) is present in lawsonite adjacent to the glaucophane-rich margin, but is not observed in lawsonite from the more interior regions of the layer; this lawsonite contains little to no Cr (< 100 ppm). Chondrite-normalized REE patterns for lawsonite in this sample show concentrations that are enriched in the LREE ($[La/Yb]_N$ = 4 - 41) compared to the HREE (Figure 12a).

Bulk rock analysis of the monomineralic lawsonite vein (SV12-24B) yielded a composition that is similar to that of pure lawsonite, with small amounts of FeO* (2. 69 wt.%) and TiO_2 (0.13 wt.%) (Table 8). The chondrite-normalized REE pattern for the monomineralic lawsonite vein is characterized by an enrichment in the LREE relative to the HREE ($[La/Yb]_N$ = 13.4) and REE concentrations of up to 360 times chondrite (Figure 12b). Compared to lawsonite from the lawsonite + garnet + phengite-rich layer (SV03-103C) collected from the margin of the fresh lawsonite eclogite pod, the REE patterns from this sample lack a negative Eu anomaly and contain higher concentrations of V, Y, REE, Pb, Th, and U (Table 9, Figure 12).

5. Lawsonite Crystallographic Orientation and Microstructures

To evaluate whether some lawsonite zoning types are crystallographically controlled and whether deformation affects the trace-element distribution in lawsonite,

the crystallographic orientations of lawsonite crystals displaying different zoning types were determined using electron backscatter diffraction (EBSD). In addition to determining the crystallographic orientation of individual lawsonite crystals, grain-scale EBSD maps and orientation contrast images for lawsonite crystals displaying irregular zoning features (particularly in Ti) were also obtained to determine whether there was any relationship between microstructural features (subgrains, grain boundaries, twinning) and zoning patterns.

The crystallographic orientation and microstructures of lawsonite were analyzed with a JEOL 6500 FEG-SEM and the Oxford Instruments/HKL Channel 5 software in the Characterization Facility (College of Science and Engineering, University of Minnesota-Twin Cities). SEM conditions were 70° tilt, 20 kV accelerating voltage, and ~ 15 nA beam current.

5.1 EBSD Results

To determine whether particular zoning types (e.g. sector zoning) are crystallographically controlled, we measured the crystallographic orientation of lawsonite grains displaying core-to-rim, sector, and oscillatory zoning from across 10 samples representing different rock types (metabasalt, metasediment, metasomatic lawsonite + chlorite rocks, lawsonite-rich layers; Supplementary Material 1). Lawsonite grains cut perpendicular to the a-, b-, or c-axis displayed core-to-rim and/or oscillatory zoning, however, only lawsonite grains cut perpendicular to the a- or b- axis displayed sector zoning (Figure 13).

To determine whether there was any relationship between microstructural features and intragrain compositional variations in lawsonite, ~30 grains of lawsonite from across 10 samples representing different rock types and lawsonite textures (euhedral grains, lawsonite aggregates, polycrystalline lawsonite) were analyzed using EBSD and EMP. Orientation contrast and Euler maps from these grains show that the most commonly observed microstructural features in lawsonite are twinning (polysynthetic), subgrains (misorientation < 10°), and grain boundaries (misorientation > 10°). Total misorientation across most grains ranges from 1 to 5°, although, some grains display higher misorientations of > 8°.

The presence or absence of twinning does not appear to affect the type of zoning pattern observed (core-to-rim, sector, oscillatory), nor does the orientation of the twinning have any relationship to the orientation of particular zoning features (i.e., the position or orientation of the Ti-rich sectors). However, a comparison of X-ray element maps and results from EBSD analyses show that in some cases there is a correlation between the observed zoning patterns and the presence of subgrain or grain boundaries and/or regions with abundant polysynthetic twinning. In sample SV03-305, for example, variations in Ti concentration correlate with the position of grain boundaries and polysynthetic twinning features, such that the regions of high Ti concentrations tend to be located adjacent to the high angle grain boundaries (20° – 26° misorientation) and regions with abundant polysynthetic twinning (Figure 14). However, variations in the Fe or Cr content in the lawsonite do not appear to be similarly affected by the presence of grain boundaries. The development of subgrains may also modify zoning patterns in lawsonite,

as seen in the Ti sector-zoned lawsonite in layered eclogite and blueschist sample SV08-76, where the development of a subgrain appears to distort the hourglass shape of the Ti-rich sector (Figure 15). In this case, the core-to-rim zoning in Fe also appears to be affected by subgrain development and shows an irregular transition between the Fe-poor core and the Fe-rich rim in the region of the subgrain (Figure 15).

In other cases, however, lawsonite grains with little to no misorientation (< 1°) can display distinct zoning features. For example, a lawsonite crystal in lawsonite + chlorite rock sample SV12-21D shows the presence of an Fe- and Ti-rich region that is separated from the Fe- and Ti-poor region of the grain by a sharp boundary (Figure 16). As there is no measured misorientation across this boundary, the change in lawsonite composition likely reflects continuous growth during changes in the metamorphic conditions (P-T) or reaction history of the rock.

6. Discussion

Lawsonite from all rock types displays large variations in the concentrations of transition metals (Fe, Ti, Cr) and other trace elements (Sr), and commonly displays zoning in these elements. Within a sample, and even within a single lawsonite grain, chondrite-normalized REE concentrations can vary by 1 – 2 orders of magnitude, consistent with the results of trace and REE analyses conducted on lawsonite from other HP/LT terranes (e.g., Martin et al. 2011, Martin et al. 2014, Vitale-Brovarone et al. 2014). In addition to variations in the concentrations of REE at both the sample and grain scale, the trends of the REE patterns can also vary markedly, displaying patterns that range from flat to LREE-, MREE-, and/or HREE-enriched.

To understand the processes giving rise to the observed intra-grain and intersample compositional variations in lawsonite, we first examine the types of zoning patterns observed in lawsonite and their relationship to microstructural features (if any) to consider processes acting at the grain scale. We then consider processes that may have operated at the sample scale to affect the major and trace element systematics of lawsonite, such as the bulk rock composition/protolith, changes in metamorphic assemblage, fluid-rock interactions amongst the different interlayered rock types, as well as the effects of deformation on element mobility in lawsonite.

6.1 Lawsonite Zoning Patterns

Some studies of synthetic and natural lawsonite have assumed or reported near end-member major element composition (Pawley 1994, Okay and Kelley 1994). However, lawsonite can contain Fe, Ti, and Cr at the weight percent level, and commonly displays zoning in these elements. The most common zoning types are oscillatory (Sherlock and Okay 1999, Vitale Brovarone et al. 2014; this study) core-to-rim (this study), and sector (Ueno 1999, Tsujimori and Ernst 2014, Vitale Brovarone et al. 2014; this study). Similar zoning patterns have also been observed for trace elements (Y, Sr, Th, REE) in lawsonite (Ueno 1999, Martin et al. 2011, 2014, Tsujimori and Ernst 2014, Vitale Brovarone et al. 2014; this study). As these and other trace elements have been used in previous studies of lawsonite to track changes in mineral parageneses (Martin et al. 2011), monitor metamorphic grade (Maruyama and Liou 1988, Vitale Brovarone et al. 2014), and date subduction zone metamorphism (Mulcahy et al. 2009, 2014, Vitale Brovarone and Herwartz 2013), an understanding of the types and causes of the different

zoning patterns in lawsonite is important for interpretations of metamorphic reactions involving lawsonite.

Individual lawsonite grains can display similar zoning patterns in different elements (e.g., core-to-rim zoning in Fe, Ti, and Cr), or display different zoning patterns in different elements (e.g., core-to-rim zoning in Fe, sector zoning in Ti, and oscillatory zoning in Cr), suggesting that the uptake and distribution of different elements may be controlled by different parameters. In the following sections, we discuss each zoning type observed in Sivrihisar lawsonite and consider the mechanisms, both crystallographic and environmental, that may have resulted in such zoning.

6.1.1 Core -to -rim Zoning

Lawsonite from nearly every rock type studied displays core-to-rim zoning in Fe, with Fe-poor cores and Fe-rich rims (Figure 7). The absolute variation in Fe content from core-to-rim varies both between different samples and between different grains within a sample, although the latter may reflect sectioning effects. In contrast to the core-to-rim zoning observed in other metamorphic minerals, such as garnet, where the compositional change from core-to-rim is commonly continuous, the change in Fe content from the core to the rim of lawsonite is typically abrupt, showing either a well-defined core and rim region or an Fe-poor core that transitions to a rim with oscillatory variations in Fe content (Figure 7). In these cases, the core-to-rim transition is also typically marked by a change in inclusion assemblage. For example, lawsonite from blueschist SV13-07 shows an Fe-poor core that contains glaucophane and rutile inclusions and a relatively inclusion-poor Fe-rich rim (Figure 7f). Lawsonite from lawsonite + chlorite rock SV13-17A, on the

other hand, has a relatively inclusion-poor Fe-poor core and inclusions of REE-rich epidote-group minerals in its Fe-rich rim (Figure 7i). This suggests that the change in zoning may be related to changes in reaction history along the P-T path. This interpretation is also consistent with the fact that lawsonite inclusions in garnet in some samples display contrasting zoning from lawsonite in the matrix. For example, in blueschist SV13-07, lawsonite inclusions in garnet show Ti-rich and rutile-bearing rims, whereas matrix lawsonite displays Ti-rich and rutile-bearing cores.

In other studies, increasing Fe content in lawsonite at both the sample (Maruyama and Liou 1988) and grain (Vitale Brovarone et al. 2014) scale has been correlated with an increase in metamorphic grade. As most Sivrihisar lawsonite displays a core-to-rim increase in Fe content, this would suggest that lawsonite growth in the terrane records an overall increase in metamorphic grade.

Another possibility, however, is that the core-to-rim increase in Fe content is tracking a change in the oxidation state of the metamorphic environment, as all Fe in lawsonite is commonly assumed to be ferric. At the sample scale, there also appears to be a relationship between lawsonite Fe content and oxide mineral assemblages, further suggesting that variations in Fe content in lawsonite in most cases probably represent variations in oxidation state, either related to variations that occur during metamorphism or inherited from the protolith. In the Sivrihisar Massif, lawsonite in the chlorite + epidote-rich pod margin (SV12-24) that is interpreted as retrogressed eclogite (Davis and Whitney 2008), and in quartz-rich metasedimentary rocks contains the highest overall FeO* contents (~1.5 – 3 wt.%). With the exception of these samples, FeO* contents

measured in most other samples ranges from ~0.5 to 2 wt.%. Notably, the rocks with the highest overall Fe contents contain Fe-Ti oxides, whereas the other rock types contain rutile and/or titanite. Similar relationships between Fe content and oxide assemblages were observed in lawsonite from the western part of the Tavşanlı Zone, where lawsonite from the metabasalts (whose primary oxide/accessory phase is titanite) has FeO* contents ranging from 0 to 1.5 wt.% and lawsonite from the metacherts (whose primary oxide phase is hematite) has FeO* contents ranging from 1 – 2.2 wt.% (Plunder et al. 2015).

In addition to Fe, trace element results from the suite of lawsonite-bearing rocks studied here demonstrate that lawsonite can also serve as a host for other redox-sensitive elements, such as V. With the exception of lawsonite from the lawsonite + garnet + phengite-rich layer (SV03-103C) and some of the lawsonite + chlorite-rich rocks (SV12-21D), lawsonite V concentrations also show a correlation with the dominant oxide assemblage, with lawsonite from the epidote + chlorite-rich pod (SV12-24) and quartz-rich metasedimentary rocks (SV08-281C, SV10-06) containing lower V concentrations (130 – 260 ppm) than lawsonite from the other samples (216 – 1551 ppm V). Although V has, to date, only been used as a monitor of redox conditions in igneous environments (Li and Lee 2004, Mallmann and O'Neill 2009), the correlation between low V concentrations and high ferric iron concentrations observed in lawsonite from the quartz-rich metasedimentary rocks and the epidote + chlorite-rich pod margin is consistent with observations from these studies that V generally becomes more incompatible in minerals with increases in fO_2. Further study would be needed to determine whether V could be used as an fO_2 sensor in metamorphic environments as well.

Core-to-rim zoning in trace elements, including REE, has been documented in lawsonite in metasomatic rocks from Alpine Corsica (Martin et al. 2011) and in metasedimentary rocks from the Tavşanlı Zone (Martin et al. 2014). In the Corsica study, Martin et al. (2011) documented core-to-rim variations in the Eu anomaly that they attributed to lawsonite growth during prograde, blueschist-facies (plagioclase stable) conditions (recorded in lawsonite cores) and peak, eclogite-facies (plagioclase absent) conditions (recorded near rims), suggesting that lawsonite zoning can be used to track changes in P-T conditions. In our study, core-to-rim reversals in the Eu anomaly were observed in lawsonite from lawsonite-rich layer sample SV03-103C, but the trend is opposite to that of lawsonite in the Corsica metasomatic rock: in the Sivrihisar sample, the core records a weak positive Eu anomaly, whereas the rim has a negative Eu anomaly. Although there is some textural evidence in the Sivrihisar Massif for retrograde transformation of eclogite to blueschist (Davis and Whitney 2006, 2008; Whitney et al. 2014), there is no plagioclase present in this sample or Sivrihisar blueschists in general (Davis and Whitney 2006, 2008), so it is unlikely that the core-to-rim change in the Eu anomaly is related to a transition from plagioclase-absent (eclogite-facies) to plagioclase-stable (blueschist-facies) conditions. In this case, the shift in the Eu anomaly may be related to a change in the oxidation state, as the switch in the Eu anomaly also correlates with core-to-rim zoning in Fe. Correlations between the Eu anomaly and oxidation state have been documented in other minerals, such as zircon (Burnham and Berry 2012, Trail et al. 2012).

In addition to core-to-rim variations in the Eu anomaly and Fe content, this lawsonite grain also records a core-to-rim increase in the concentration of the REE. In a closed system, continued lawsonite growth should result in a core-to-rim decrease in the REE, so the trend observed in this lawsonite grain requires either the addition of an external REE-rich source (e.g., fluids from an adjacent rock unit) or the breakdown of another REE-rich phase with the system, such as allanite, during lawsonite growth.

Core-to-rim variations in the concentrations of the REE are also documented in other samples. In lawsonite garnet blueschist SV13-06B, the Fe-rich rim shows an enrichment in the MREE that likely results from the breakdown of an MREE-rich phase (Figure 9c), such as rutile or titanite, whereas lawsonite from quartzite SV10-06 records a core-to-rim decrease in REE concentrations (Figure 10b) that likely reflects progressive lawsonite growth.

6.1.2 Oscillatory Zoning

Oscillatory zoning in lawsonite was first documented by Sherlock and Okay (1999) in blueschist-facies metabasaltic rocks from the Tavşanlı Zone. In their samples, oscillatory variations in Cr (ranging from 3 – 6 wt.% Cr_2O_3) were attributed to the breakdown of inferred Cr-rich phases such as chromite in the protolith, and concomitant fluid-rock interaction during subduction metamorphism. Oscillatory Cr zoning in lawsonite has since been documented in eclogite-facies veins from Alpine Corsica (Vitale Brovarone et al. 2014), where the high Cr_2O_3 contents (up to 8 wt.%) were interpreted as resulting from interactions with adjacent serpentinite units.

Oscillatory Cr zoning in Sivrihisar lawsonite occurs in metabasaltic rocks (Davis and Whitney 2006), including in finely interlayered lawsonite-rich layers and glaucophane-rich assemblages at eclogite pod-margins, as well as in metasedimentary rocks and in some of the metasomatic lawsonite + chlorite-rich rocks adjacent to serpentinites, although the Cr contents do not in every case approach weight percent levels. Cr-rich (wt.% levels Cr_2O_3) lawsonite with oscillatory zoning was observed in a calc-schist (SV13-01a) and a glaucophane-lawsonite-garnet blueschist (SV01-75). In the calc-schist, only a subset of the lawsonite grains are Cr-rich (with Cr_2O_3 contents up to ~ 6 wt.%). The Cr-rich lawsonite also tends to contain overall higher concentrations of Ni, Sr, Y, and Pb than the Cr-poor lawsonite (Table 5), and also lacks the Ti and Fe zoning observed in Cr-poor lawsonite. The co-enrichment of Cr and Ni in Cr-rich lawsonite from the calc-schist, together with the structural position of both Cr-rich lawsonite-bearing samples in a high-strain zone in proximity to serpentinites, suggest that at least some of the Cr-rich Sivrihisar lawsonite may result from fluid-rock interactions with serpentinite. Within both these samples, other phases (garnet, glaucophane) also show evidence for fluid-rock interaction, such as the presence of late oscillatory rims on the garnets (SV01-75) and patchy zoning in the glaucophane. In the case of the calc-schist sample, it is also unlikely that the protolith would contain chromite or other Cr-rich phases from which the Cr could be locally or internally sourced.

Oscillatory zoning in other elements, such as Fe and Sr were also documented in Sivrihisar lawsonite. In the case of oscillatory Fe zoning, variations in Fe content can occur across the entire grain or only in the Fe-rich rim of the grain. When both Fe and Cr

zoning are present within a single grain, the Fe and Cr contents are anti-correlated, indicating that there may be a substitution relationship between Fe and Cr. It is unknown if oscillatory zoning occurs in other elements, such as the REE, but the lack of clear core-to-rim zoning trends in the REE in many of the samples could be explained by the presence of oscillatory zoning or variations in these elements at scales smaller than the spot size used for LA-ICPMS analysis (28 – 48 μm).

6.1.3 Sector Zoning

Ca, Ti, and REE sector zoning in lawsonite was reported by Ueno (1999) from the Sanbagawa pelitic schists in Japan. Ueno (1999) suggested that the distribution of these elements in lawsonite were crystallographically-controlled, with the {100} sector showing enrichment in REE, the {001} sector showing enrichment in Ti, and the {010} sector recording a near ideal lawsonite composition (following the nomenclature adopted by Ueno (1999), in which the sectors are denoted as {100}, {010}, and {001} according to the axis along which they grew). However, these conclusions were based on observations of the two-dimensional shape of the lawsonite crystal and not analytical determination of crystallographic orientation.

Although lawsonite typically forms euhedral rhombs, it can be difficult to identify particular crystallographic axes from petrographic observation alone, in part because the 2D cross-sectional geometry of lawsonite crystals can vary and/or be modified by post-crystallization processes. For example, Cao and Jung (2016) hypothesized that the activation of different slip planes in lawsonite could affect the aspect ratio of lawsonite grains. Several of the lawsonite grains studied here show Fe zoning that has been

truncated at the grain boundary, such that the core is no longer in the geometric center of the grain, indicating that the original shape of the grain has been affected by post-crystallization processes such as dissolution-reprecipitation. Furthermore, crystallographically controlled zoning such as Ti sector zoning may influence preferential growth directions and therefore may affect which crystallographic axis is the long direction in orthorhombic lawsonite.

Results from EBSD analysis of the crystallographic orientation of lawsonite displaying Ti sector zoning shows that Ti-rich sectors tend to grow in the direction of the {100} axis (observed if the lawsonite grain is intersected perpendicular to the a-axis), or in the direction of the {010} axis (observed if the lawsonite grain is intersected perpendicular to the b-axis) (Figure 13). This crystallographic relationship holds true for all rock types (metabasalts, calc-schist, lawsonite-rich layers, and metasomatic lawsonite + chlorite-rich rocks) in which sector zoning was observed.

A notable feature of Ti sector zoning in Sivrihisar lawsonite is the irregularity of Ti concentrations within Ti-rich sectors, which generally vary from ~1000 to 4000 ppm (Table 5, 7, 9, Figure 13). Typical misorientations across grains displaying sector zoning are less than 3°, suggesting that these variations were not caused by intracrystalline deformation. In some cases, Ti variation within a sector is oscillatory, suggesting that the intrasector variations in Ti may be related to periodic or cyclic variations in Ti availability.

Other elements, such as Fe and Sr, can also display sector zoning in lawsonite (Tsujimori and Ernst 2014, this study), although this is less common in the Sivrihisar

Massif and typically does not occur in the hourglass-type sectors observed in the Ti zoning patterns. When present, the Fe- and Sr-rich sectors tend to occur in the Ti-poor regions of lawsonite (i.e. opposite the Ti-rich sectors). Some lawsonite grains that display Ti sector zoning have Ti-poor sectors that have high LREE concentrations; however, this is not true for every sample or even every grain within a sample. For example, the chondrite-normalized REE patterns for Ti-sector zoned lawsonite in the lawsonite-rich layer found at the eclogite pod-margin (SV03-103) shows similar REE patterns and concentrations regardless of whether the analysis was in a Ti-rich or Ti-poor sector. This suggests that either there is no clear substitution mechanism relating REE, Ti, Sr, and Fe in lawsonite, as proposed by Ueno (1999), or that substitution relationships among these elements are obscured in some lawsonite by the presence of contrasting zoning types in different elements.

6.1.4 Other Zoning

Some lawsonite grains display irregular compositional variation, including in elements such as Ti that in other cases display geometrically organized zoning (core/rim, oscillatory, sector). In eclogite pod-margin sample SV03-305 (Davis and Whitney 2008), collected from the same pod as samples SV12-13E and SV03-103, Ti (but not Fe or Cr) is concentrated along lawsonite grain boundaries and regions with abundant polysynthetic twinning (Figure 14). A possible explanation for this observation is that Ti was mobilized as a result of fluid-related processes, and became concentrated along grain boundaries that served as pathways for fluid transport. The fact that Fe and Cr concentrations are not similarly affected by the presence of the grain boundaries suggests that the Ti may have

been released by the breakdown of a Ti-rich phase such as rutile; e.g. during reaction of rutile to titanite, as has been proposed by Vitale Brovarone et al. 2014 for metasomatic lawsonite from Corsica. In the Corsica samples, Ti-rich regions in lawsonite were also co-enriched in Nb, lending further support to the interpretation that the source of the Ti was rutile. However, no correlation between Ti and Nb concentrations, or for that matter, any other HFSE element, has been observed in Sivrihisar lawsonite, although the common presence of rutile (and zircon) inclusions in lawsonite from Tavşanlı Zone would make it difficult to rule out the possibility that any observed correlation between high Ti and HFSE concentrations were not the result of ablating an inclusion.

6.2 Controls on Lawsonite Composition and its Variation

Experimental studies of phase relations in bulk compositions relevant for subducting lithologies and field-based studies of high-pressure/low-temperature rocks from exhumed subduction complexes have demonstrated that lawsonite is stable in different rock types, including metabasaltic, metasedimentary, and metasomatically-derived rocks, as well as lawsonite-rich veins and layers, and is also a major reservoir for trace elements in all of these rock types. Despite the stability of lawsonite in a variety of different rock types and bulk compositions and its ability to serve as a host for trace elements, most previous studies of lawsonite geochemistry have focused on the composition of lawsonite in blueschist-facies metabasaltic rocks, and/or have only presented compositional results for a limited suite of trace elements. In addition to providing new trace element data for lawsonite in eclogite-facies metabasalt, metasedimentary rocks, and lawsonite-rich veins and layers, which are not well

represented in the literature, results from this study also provide the first geochemical data for the lawsonite + chlorite-bearing lithologies from the Tavşanlı Zone.

Trace element analysis of lawsonite from metabasaltic rocks in the Sivrihisar Massif shows that they generally contain chondrite-normalized REE concentrations of ~ 10 – 1000 times chondrite (Figure 8, 9). These concentrations are similar to what has been documented in lawsonite in metabasaltic rocks from other oceanic subduction complexes, such as the Franciscan (Mulcahy et al. 2009), New Caledonia (Spandler et al. 2003), the Ligurian Alps (Tribuzio et al. 1996), as well as blueschist-facies mafic material from the North Qilian belt in northwest China (Xiao et al. 2013). Although the concentrations of REE amongst the metabasaltic rocks are similar, the shape of the chondrite-normalized REE pattern varies. For example, in metabasalt from the Franciscan, lawsonite displays high MREE to HREE concentrations relative to the LREE, whereas lawsonite from the metabasaltic rocks in the Sivrihisar Massif display more LREE-enriched patterns (Figure 8, 9). This difference may reflect variations in reaction history, as the lawsonite blueschist analyzed by Mulcahy et al. (2009) was interpreted to form on the retrograde path after garnet breakdown, so lawsonite likely incorporated the HREE liberated by garnet. In the Sivrihisar Massif, on the other hand, lawsonite may have grown either concurrently with garnet or after significant garnet growth, resulting in a relative depletion in the HREE.

Compared to lawsonite from metabasalt, lawsonite from metasedimentary rocks typically yields higher trace element contents (100 – 10,000 times chondrite; Figure 10), similar to results obtained for lawsonite in metasedimentary rocks in other HP/LT

terranes (Ueno 1999, Spandler et al. 2003, Martin et al. 2014). One explanation for the observed enrichment in trace (including rare earth) element concentrations in lawsonite in metasedimentary rocks is that there are fewer phases competing with lawsonite for available trace elements (e.g., if titanite and/or epidote are absent) (Martin et al. 2014). It is also possible, however, that variations in trace element content in lawsonite from metabasaltic and metasedimentary rocks in the Sivrihisar Massif are related to a concentration-dilution effect. Generally, the modal abundance of lawsonite in metasedimentary rocks in the Sivrihisar Massif is low compared to that in the metabasalts (~ 5% in quartz-rich metasedimentary rocks vs. ≥ 20% in metabasaltic rocks) so the available trace elements are distributed over fewer lawsonite grains leading to higher concentrations in each individual grain.

Lawsonite also occurs in lawsonite + chlorite-rich rocks interpreted to represent metasomatic reaction between serpentinite and oceanic crustal lithologies. These rocks have been reported from the Tavşanlı Zone (Plunder et al. 2013, Zack 2013, Whitney et al. 2014) and from Alpine Corsica (Martin et al., 2011, Vitale Brovarone et al. 2014). Possible pseudomorphed equivalents have also been described in the Southern Ural Mountains, Russia (Beane and Liou 2005), suggesting that lawsonite + chlorite-rich lithologies may be a common product of subduction-related metamorphism and metasomatism but are not well-preserved in the geologic record.

Lawsonite in the lawsonite + chlorite-rich rocks from Alpine Corsica contain high REE (up to 1,000 – 10,000 times chondritic), Th, and U contents (Martin et al. 2011, Vitale-Brovarone et al. 2014). Compared to these rocks, however, the lawsonite +

chlorite-rich rocks in the Tavşanlı Zone overall contain much lower concentrations of trace elements (e.g., REE concentrations ~ 10 to 100 times chondrite), particularly the LREE (Table 7, Figure 11). One likely explanation for the variation in lawsonite trace and rare earth element abundance between Tavşanlı Zone and Corsica relates to the rock types involved in the generation of the metasomatic rocks. In Alpine Corsica, the lawsonite + chlorite rocks may have formed as a result of interaction between serpentinite and adjacent REE-enriched metasedimentary rocks (Martin et al. 2011, Vitale Brovarone et al. 2014), whereas in the Tavşanlı Zone, field relations in the Sivrihisar Massif suggest that the lawsonite + chlorite rocks likely formed as a result of metasomatic interactions between serpentinite and metabasalt (Zack 2013, Whitney et al. 2014). Indeed, lawsonite from Sivrihisar metabasalt has REE concentrations similar to those measured in lawsonite from the lawsonite + chlorite rocks (~ 10 – 1000 times chondrite; Figure 8, 9).

However, even within the Tavşanlı Zone there are large variations in the trace element content of lawsonite from lawsonite + chlorite rocks. For example, lawsonite from a sample (TZ10-.2.2) from the western part of the belt contains the highest V concentrations (> 1000 ppm) of any sample analyzed in this study, whereas a sample (SV12-21D) from the Halilbağı region contains some of the lowest V concentrations measured (< 300 ppm) (Table 7). The REE patterns of lawsonite also vary markedly, with lawsonite from the western Tavşanlı sample yielding flat chondrite-normalized REE patterns, whereas lawsonite from the lawsonite + chlorite rocks sampled in Halilbağı displays REE patterns that range from flat to MREE- and/or HREE-enriched (Figure 11). In SV12-21D, the shift from HREE-enriched patterns to flat REE patterns correlates with

Fe and Ti zoning in the grain, such that the Fe- and Ti-poor regions have HREE-enriched patterns and Fe- and Ti-rich regions have flat REE patterns (Figure 11). These intersample variations may stem from heterogeneities in the source rocks or to variations in the intensity of fluid-rock interaction with distance from the serpentinite lens during metasomatism.

A possible monitor of lawsonite compositional variation as a function of rock type and fluid-rock interaction is the Sr and Pb concentration of lawsonite. A global review of lawsonite composition shows that lawsonite may contain the majority of Sr and Pb in HP/LT mafic rocks: up to ~60% of the Pb and up to ~100% of the Sr (Martin et al. 2014). The concentrations of Sr and Pb in metabasalt are typically distinct from Sr and Pb concentrations in metasedimentary rocks (Martin et al. 2014): lawsonite from metabasaltic rocks (blueschist, eclogite) tends to yield high Sr/Pb ratios whereas lawsonite from metasedimentary rocks tends to yield lower Sr/Pb ratios (Figure 17a). In the Sivrihisar rocks, although there are variations in Sr/Pb ratios in lawsonite within and among grains/samples in general, these compositional variations define a linear array with lawsonite in each sample having a distinct slope, similar to what was documented by Martin et al. (2014). Where available, bulk rock Sr/Pb ratios appear to closely match lawsonite Sr/Pb ratios and plot along the linear array defined by the lawsonite in that sample (Figure 17), suggesting that the Sr/Pb ratio of lawsonite tracks bulk rock Sr/Pb systematics.

Although this trend applies to the majority of the analyzed samples, two samples from our dataset record lawsonite Sr/Pb ratios that are apparently inconsistent with their

rock type. One is a population of Cr-rich (up to 6 wt.% Cr_2O_3) lawsonite from a calc-schist (SV13-01) that was sampled from the high-strain zone, and the other is lawsonite from the retrogressed (chlorite + epidote-rich) margin of a metabasaltic pod (SV12-24) and its associated monomineralic lawsonite vein (SV12-24B). In the case of the calc-schist (SV13-01), lawsonite from the Cr-poor lawsonite population plots along the Sr/Pb trajectory for metasedimentary rocks, whereas the Cr-rich lawsonite population is displaced from that trend and contains Sr/Pb contents that are similar to those found in the metabasaltic rocks. Similar observations were made for some of the zoned lawsonite grains from the metasomatically-derived rocks from Alpine Corsica, where the lawsonite cores yielded Sr/Pb concentrations similar to metasedimentary rocks, and the rims yielded Sr/Pb concentrations similar to the metabasaltic rocks (sample COE5; Martin et al. 2014). In the Corsica rock, the core of the lawsonite was interpreted as forming prior to the metasomatic interaction with mafic- and ultramafic rocks, and the rim was interpreted as forming during the metasomatic event (Martin et al. 2011), therefore, the core-to-rim change in Sr/Pb ratios was interpreted as an indicator of the later metasomatic event (Martin et al. 2014). This suggests that the difference in Sr/Pb ratios recorded by the two populations of lawsonite in calc-schist SV13-01 could reflect fluid-rock interactions with adjacent mafic- or ultramafic sources. Further support for this hypothesis is provided by the presence of oscillatory Cr zoning in the lawsonite with the high Sr/Pb ratios as well as the co-enrichment of Ni.

The opposite trend is observed for the lawsonite from the epidote + chlorite-rich pod, where the lawsonite plot along the trajectory defined by the metasediments (Figure

17a). With the exception of one lawsonite grain that yielded flat chondrite-normalized REE patterns (~ 10 times chondrite), lawsonite from this sample also contain REE concentrations that are similar to those documented in metasedimentary rocks (~ 100 – 1000 times chondrite). This suggests that either the pod is incorrectly classified as a retrogressed eclogite (metabasaltic) pod, or that the pod may have experienced fluid-rock interactions with adjacent metasedimentary units.

A comparison of the Sr and Pb concentrations in lawsonite from the Tavşanlı Zone with published data for lawsonite from other HP/LT and UHP terranes (Figure 17b), shows that although the Sr and Pb contents seem to be correlated for lawsonite in most samples, the same relationship between Sr/Pb ratios and rock type (metabasalt vs. metasediment) does not appear to hold true. However, the scarcity of studies that have published lawsonite composition data that includes Sr and Pb, particularly in metasedimentary lithologies, and that have conducted texturally-controlled (i.e., accounted for intra- and intergrain zoning) compositional analyses of lawsonite, makes it difficult to reconcile these differences. Additional studies of lawsonite from other HP/LT terranes would be needed to fully understand the Sr/Pb systematics of lawsonite and their utility as a possible indicator of metasomatic events, especially in bulk compositions that contain carbonates that could serve as additional reservoirs for Sr and Pb.

7. Conclusions

(1) Lawsonite can display a variety of different zoning patterns, including core-to-rim zoning, sector zoning, oscillatory zoning, and irregular or patchy zoning, in both major (wt.%) and trace (ppm) elements. Within a single grain, different elements

can display contrasting zoning types, suggesting that the incorporation and distribution of individual elements within lawsonite is controlled by different mechanisms, both environmental and crystallographic.

(2) With the exception of the LILE, results from this and other studies demonstrate that lawsonite is a major reservoir for most trace elements and element groups across a variety of rock types. The ability of lawsonite to incorporate a wide variety of elements into its crystal lattice makes it a potentially useful monitor of changes in the metamorphic reaction history, fluid-rock interactions and possibly oxidation state.

(3) Although lawsonite is commonly assumed to behave as a rigid body in a weaker matrix, grain-scale EBSD maps of lawsonite reveal the presence of subgrains and internal grain boundaries. In some cases, subgrain development has modified the zoning patterns in lawsonite, suggesting that deformation may enhance the mobility of some elements within lawsonite, such as Ti, which is commonly thought to be relatively immobile in subduction zone environments.

(4) Given the large intra- and inter-grain variability possible in lawsonite REE patterns and concentrations, care should be taken in using REE data obtained from lawsonite to determine whether any given sample is suitable for Lu-Hf lawsonite geochronology and in interpreting the results obtained from lawsonite geochronology. Similarly, texturally-controlled compositional analyses of lawsonite should also be undertaken when using lawsonite trace element analyses to calculate trace element budgets for subducting lithologies.

REFERENCES

Abers GA, Sarker G (1996) Dispersion of regional body waves at 100-150 km depth beneath Alaska: in situ constraints on metamorphism of subducted crust. Geophysical Research Letters 23: 1171–1174.

Abers GA, Nakajima J, van Keken PE, Kita S, Hacker BR (2013) Thermal-petrological controls on the location of earthquakes within subducting plates. Earth and Planetary Science Letters 369: 178 – 187.

Ballevre M, Pitra P, Bohn M (2003) Lawsonite growth in epidote blueschists from the Ile de Groix (Armorican Massif, France): a potential geobarometer. Journal of Metamorphic Geology 21: 723 – 735.

Beane RJ, Liou JG (2005) Metasomatism in Serpentinite Melange Rocks from the High-Pressure Maksyutov Complex, Southern Ural Mountains, Russia. International Geology Review 47: 24 – 40.

Burnham AD, Berry AJ (2012) An experimental study of trace element partitioning between zircon and melt as a function of oxygen fugacity. Geochimica et Cosmochimica Acta 95: 196 – 212.

Cao Y, Jung H, Song S (2014) Microstructres and petro-fabrics of lawsonite blueschist in the North Qilian suture zone, NW China: Implications for seismic anisotropy of subducting oceanic crust. Tectonophysics 628: 140 – 157.

Cao Y, Jung H (2016) Seismic properties of subducting oceanic crust: Constraints from natural lawsonite-bearing blueschist and eclogite in Sivrihisar Massif, Turkey, Physics of the Earth and Planetary Interiors: doi:

http://dx.doi.org/10.1016/j.pepi.2015.10.003.

Çetinkaplan M, Candan O, Oberhansli R, Bousquet R (2008) Pressure-temperature evolution of lawsonite eclogite in Sivrihisar; Tavşanlı Zone-Turkey. Lithos 104:12 – 32.

Chantel J, Mookherjee M, Frost DJ (2012) The elasticity of lawsonite at high pressure and the origin of low velocity layers in subduction zones. Earth and Planetary Science Letters 349-350: 116-125.

Clarke GL, Powell R, Fitzherbert JA (2006) The lawsonite paradox: a comparison of field evidence and mineral equilibria modelling. Journal of Metamorphic Geology 24: 715 – 725.

Connolly JAD, Kerrick DM (2002) Metamorphic controls on seismic velocity of subducted oceanic crust at 100-250 km depth. Earth and Planetary Science Letters 204: 61–74.

Davis PB, Whitney DL (2006) Petrogenesis of lawsonite and epidote eclogite and blueschist, Sivrihisar Massif, Turkey. Journal of Metamorphic Geology 24: 823 – 849.

Davis PB, Whitney DL (2008) Petrogenesis and structural petrology of high-pressure metabasalt pods, Sivrihisar, Turkey. Contributions to Mineralogy and Petrology 156: 217 – 241.

Davis PB (2011) Petrotectonics of lawsonite eclogite exhumation: Insights from the Sivrihisar massif, Turkey. Tectonics 30:TC1006, doi:10.1029/2010TC002713.

Droop GTR, Karakaya MC, Eren Y, Karakaya N (2005) Metamorphic evolution of blueschists of the Altinekin Complex, Konya area, south central Turkey. Geological Journal 40: 127 – 153.

Eggins SM, Rudnick RL, McDonough WF (1998) The composition of peridotites and their minerals: a laser ablation ICP-MS study. Earth and Planetary Science Letters 154: 53 – 71.

Fujimoto Y, Kono Y, Hirajima T, Kanagawa K, Ishikawa M, Arima M (2010) P-wave velocity and anisotropy of lawsonite and epidote blueschists: constraints on water transportation along subducting oceanic crust. Physics of the Earth and Planetary Interiors 183: 219–228.

George A, Grapes R (1987) Lawsonite-bearing veins in Torlesse rocks. New Zealand Journal of Geology and Geophysics 30: 203 – 205.

Guo S, Ye K, Wu TF, Chen Y, Yang YH, Zhang LM, Liu JB, Mao Q, Ma YG (2013) A potential method to confirm the previous existence of lawsonite in eclogite: the mass imbalance of Sr and LREEs in multistage epidote (Ganghe, Dabie UHP terrane). Journal of Metamorphic Geology 31: 415 – 435.

Hacker BR (1996) Eclogite formation and the rheology, buoyancy, seismicity, and H2O content of oceanic crust. In: Subduction: Top to Bottom (eds Bebout, G.E., Scholl, D. & Kirby, S.), pp. 337–346. AGU, Washington, DC.

Hacker BR, Peacock SM, Abers GA, Holloway SD (2003) Subduction factory 2. Are intermediate-depth earthquakes in subducting slabs linked to metamorphic dehydration reactions? Journal of Geophysical Research 108: 1 – 16.

Harris NBW, Kelley S, Okay AI (1994) Post-collision magmatism and tectonics in northwest Anatolia. Contributions to Mineralogy and Petrology 117:241 – 252.

Kim D, Katayama I, Michibayashi K, Tsujimori T (2013) Rheological contrast between glaucophane and lawsonite in naturally deformed blueschist from Diablo Range, California. Island Arc 22: 63 – 73.

Kim D, Katayama I, Wallis S, Michibayashi K, Miyake A, Seto Y, Azuma S (2015) Deformation microstructures of glaucophane and lawsonite in experimentally deformed blueschists: implications for intermediate-depth intraplate earthquakes. Journal of Geophysical Research: Solid Earth 120: 1229 – 1242.

Kita S, Okada T, Nakajima J, Matsuzawa T, Hasegawa A (2006) Existence of a seismic belt in the upper plane of the double seismic zone extending in the along-arc direction at depths of 70-100 km beneath NE Japan. Geophysical Research Letters 33: L24310.

Li Z-X A, Lee C-T A (2004) The constancy of upper mantle fO_2 through time inferred from V/Sc ratios in basalts. Earth and Planetary Science Letters 228: 483 – 493.

Li J.-L, Gao J, John T, Klemd R, Su W (2013) Fluid-mediated metal transport in subduction zones and its link to arc-related giant ore deposits: Constraints from a sulfide-bearing HP vein in lawsonite eclogite (Tianshan, China). Geochimica et Cosmochimica Acta 120: 326 - 362.

Mallman G, O'Neill H St. C. (2009) The Crystal/Melt Partitioning of V during Mantle Melting as a Function of Oxygen Fugacity Compared with some other Elements (Al, P, Ca, Sc, Ti, Cr, Fe, Ga, Y, Zr, and Nb). Journal of Petrology 50: 1765 – 1794.

Martin LAJ, Rubatto D, Vitale Brovarone A, Hermann J (2011) Late Eocene lawsonite-eclogite facies metasomatism of a granulite sliver associated to ophiolites in Alpine Corsica. Lithos 125: 620 – 640.

Martin LAJ, Hermann J, Gauthiez-Putallaz L, Whitney DL, Vitale Brovarone A, Fornash KF, Evans NJ (2014) Lawsonite geochemistry and stability – implication for trace element and water cycles in subduction zones. Journal of Metamorphic Geology 32: 455 – 487.

Maruyama S, Liou JG (1988) Petrology of Franciscan Metabasites Along the Jadeite-Glaucophane Type Facies Series, Cazadero, California. Journal of Petrology 29: 1 – 37.

Mevel C, Kienast JR (1980) Chromian jadeite, phengite, pumpellyite, and lawsonite in a high-pressure metamorphosed gabbro from the French Alps. Mineralogical Magazine 43: 979 – 984.

Mookherjee M, Bezacier L (2012) The low velocity layer in subduction zone: structure and elasticity of glaucophane at high pressures. Physics of the Earth and Planetary Interiors 208–209: 50–58.

Mulcahy SR, King RL, Vervoort JD (2009) Lawsonite Lu-Hf geochronology: A new geochronometer for subduction zone processes. Geology 37: 987 – 990.

Mulcahy SR, Vervoort JD, Renne PR (2014) Dating subduction-zone metamorphism with combined garnet and lawsonite Lu-Hf geochronology. Journal of Metamorphic Geology 32: 515-533.

Okay AI (1980) Mineralogy, petrology and phase relations of glaucophane-lawsonite zone blueschist from the Tavşanlı region, north-west Turkey. Contributions to Mineralogy and Petrology 72: 243- 255.

Okay AI (1984) Distribution and characteristics of the northwest Turkish blueschist. In: The Geological Evolution of the Eastern Mediterranean, Special Publication 17 (eds Dixon, J.E. & Robertson, A.H.F.), pp. 455 – 466. Geological Society, London.

Okay AI (1986) High-pressure/low-temperature metamorphic rocks of Turkey. In: Blueschists and Eclogites (eds Evans, B.W. & Brown, E.H.), Geological Society of America Memoir 164: 333- 347.

Okay AI, Kelley SP (1994) Tectonic setting, petrology and geochronology of jadeite + glaucophane and chloritoid + glaucophane schists from northwest Turkey. Journal of Metamorphic Geology 12: 455 – 466.

Okay AI (1998) Exhumation of blueschists along a Tethyan suture in northwest Turkey. Tectonophysics 285: 275 – 299.

Okay AI (2002) Jadeite-chloritoid-glaucophane-lawsonite blueschists in northwest Turkey: unusually high P/T ratios in continental crust. Journal of Metamorphic Geology 20: 757 – 768.

Okay AI, Whitney DL (2010) Blueschists, Eclogites, Ophiolites, and Suture Zones in Northwest Turkey: A Review and A Field Excursion Guide. Ofioliti 35: 131 – 172.

Paton C, Hellstrom J, Paul B, Woodhead J, Hergt J (2011) Iolite: Freeware for the visualization and processing of mass spectrometric data. Journal of Analytical Atomic Spectrometry 26: 2508 – 2518.

Pawley AR (1994) The pressure and temperature stability limits of lawsonite: implications for H_2O recycling in subduction zones. Contributions to Mineralogy and Petrology 118: 99 – 108.

Philippon M, Gueydan F, Pitra P, Brun JP (2013) Preservation of subduction-related prograde deformation in lawsonite pseudomorph-bearing rocks. Journal of Metamorphic Geology 31: 571 – 583.

Plunder A, Agard P, Chopin C, Okay AI (2013) Geodynamics of the Tavşanlı Zone, western Turkey: Insights into subduction/obduction processes. Tectonophysics 608: 884 – 903.

Plunder A, Agard P, Chopin C, Pourteau A, Okay AI (2015) Accretion, underplating and exhumation along a subduction interface: From subduction initiation to continental subduction (Tavşanlı zone, W. Turkey). Lithos: http://dx.doi.org/10.1016/j.lithos.2015.01.007.

Reynard B, Bass JD (2014) Elasticity of lawsonite and seismological signature of metamorphism and water cycling in the subducting oceanic crust. Journal of Metamorphic Geology 32: 479 – 487.

Schmidt MW, Poli S (1994) The stability of lawsonite and zoisite at high pressures: Experiments in CASH to 92 kbar and implications for the presence of hydrous phases in subducted lithosphere. Earth and Planetary Science Letters 124: 105 – 118.

Schmidt MW, Poli S (1998) Experimentally based water budgets for dehydrating slabs and consequences for arc magma generation. Earth and Planetary Science letters 163: 361 – 379.

Seaton NCA, Whitney DL, Teyssier C, Toraman E, Heizler M (2009) Recrystallization of high-pressure marble (Sivrihisar, Turkey). Tectonophysics 479: 241 – 253.

Seaton NCA, Teyssier C, Whitney DL, Heizler MT (2014) Quartzite and calcite microfabric transitions in a pressure and temperature gradient, Sivrihisar, Turkey. Geodinamica Acta 26: 191 – 206.

Sherlock S, Kelley S, Inger S, Harris N, Okay A (1999) ^{40}Ar-^{39}Ar and Rb-Sr geochronology of high-pressure metamorphism and exhumation history of the Tavşanlı Zone, NW Turkey. Contributions to Mineralogy and Petrology 137:46 – 58.

Sherlock SC, Okay AI (1999) Oscillatory zoned chrome lawsonite in the Tavşanlı Zone, northwest Turkey. Mineralogical Magazine 63: 687 – 692.

Spandler C, Hermann J, Arculus R, Mavrogenes J (2003) Redistribution of trace elements during prograde metamorphism from lawsonite blueschist to eclogite facies; implications for deep subduction-zone processes. Contributions to Mineralogy and Petrology 146: 205 – 222.

Sun SS, McDonough WF (1989) Chemical and isotopic systematic of oceanic basalts; implications for mantle composition and processes. In: Saunders, A.D., Norry, M.J., (Eds.), Magmatism in the Ocean Basins. Special Publications of the Geological Society of London, vol. 42, pp. 313 – 345.

Teyssier C, Whitney DL, Toraman E, Seaton NCA (2010) Lawsonite vorticity and subduction kinematics. Geology 38: 1123 – 1126.

Trail D, Watson EB, Tailby ND (2012) Ce and Eu anomalies in zircon as proxies for the oxidation state of magmas. Geochimica et Cosmochimica Acta 97: 70 – 87.

Tribuzio R, Messiga B, Vannucci R, Bottazzi P (1996) Rare earth element redistribution during high-pressure – low-temperature metamorphism in ophiolitic Fe-gabbros (Liguria, northwestern Italy): Implications for light REE mobility in subduction zones. Geology 24: 711 – 714.

Tsujimori T, Sisson VB, Liou JG, Harlow GE, Sorensen SS (2006) Very-low-temperature record of the subduction process: A review of worldwide lawsonite eclogites. Lithos 92: 609 – 624.

Tsujimori T, Ernst WG (2014) Lawsonite blueschists and lawsonite eclogites as proxies for palaeo-subduction zone processes: a review. Journal of Metamorphic Geology 32: 455 – 478.

Ueno T (1999) REE-bearing sector-zoned lawsonite in the Sanbagawa politic schists of the eastern Kii Peninsula, central Japan. European Journal of Mineralogy 11: 993 – 998.

Usui T, Nakamura E, Helmstaedt H (2006) Petrology and geochemistry of eclogite xenoliths from the Colorado Plateau: implications for the evolution of subducted oceanic crust. Journal of Petrology 47: 929-964.

Vitale Brovarone A, Herwartz D (2013) Timing of HP metamorphism in the Schistes Lustres of Alpine Corsica: New Lu-Hf garnet and lawsonite ages. Lithos 172 – 173: 175 – 191.

Vitale Brovarone A, Alard O, Beyssac O, Martin L, Picatto M (2014) Lawsonite metasomatism and trace element recycling in subduction zones. Journal of Metamorphic Geology 32: 489 – 514.

Wei CJ, Clarke GL (2011) Calculated phase equilibria for MORB compositions: a reappraisal of the metamorphic evolution of lawsonite eclogite. Journal of Metamorphic Geology 29: 939 – 952.

Whitney DL, Davis PB (2006) Why is lawsonite eclogite so rare? Metamorphism and preservation of lawsonite eclogite, Sivrihisar, Turkey. Geology 34: 473 – 476.

Whitney DL, Teyssier C, Toraman E, Seaton NCA, Fayon AK (2011) Metamorphic and tectonic evolution of a structurally continuous blueschist-to-Barrovian terrane, Sivrihisar Massif, Turkey. Journal of Metamorphic Geology 29:193 – 212.

Whitney DL, Teyssier C, Seaton NCA, Fornash KF (2014) Petrofabrics of high-pressure rocks exhumed at the slab-mantle interface from the 'point of no return' in an oceanic subduction zone (Sivrihisar, Turkey). Tectonics 33: 2315-2341.

Woodhead JD, Hellstrom J, Hergt JM, Grieg A, Maas R (2007) Isotopic and elemental imaging of geological materials by laser ablation inductively coupled plasma-mass spectrometry. Geostandards and Geoanalytical Research 31: 331 – 343.

Xiao Y, Niu Y, Song S, Davidson J, Liu X (2013) Elemental responses to subduction-zone metamorphism: Constraints from the North Qilian Mountain, NW China. Lithos, 160-161, 55 – 67.

Zack T, Rivers T, Brumm R, Kronz A (2004) Cold subduction of oceanic crust: Implications from a lawsonite eclogite from the Dominican Republic. European Journal of Mineralogy 16: 909 – 916.

Zack TA (2013) Cold slab-mantle interface: constraints from exceptionally well preserved lawsonite eclogites. Mineralogical Magazine 77:2574.

Zheng J, Meng F (2006) Lawsonite-bearing eclogites in the north Qilian and north Altyn Tagh: Evidence for cold subduction of oceanic crust. Chinese Science Bulletin 51: 1238 – 1244.

Table 1. Representative major element compositions of lawsonite from lawsonite eclogite

Lithology	Lawsonite Eclogite (core)		Lawsonite Eclogite (margin)		Retrogressed Lawsonite Eclogite			Retrogressed Lawsonite Eclogite	
Sample #	SV12-13E	SV12-13E	SV03-103	SV03-103	SV08-4A	SV08-4A	SV08-4A	SV12-24	SV12-24
Textural Position	Ti-rich	Ti-poor	Ti-rich	Ti-poor	grt inclusion	core	rim	Ti-rich	Ti-poor
SiO_2	37.94	38.29	38.44	38.42	38.59	38.96	38.39	38.17	38.55
TiO_2	0.31	0.07	0.26	0.04	0.02	0.20	0.36	0.73	0.03
Al_2O_3	31.21	31.99	31.96	31.97	31.72	32.06	31.93	30.40	31.88
Cr_2O_3	0.02	0.01	0.01	0.01	0.04	0.06	0.06	0.00	0.02
FeO*	1.45	1.47	1.08	1.31	1.20	1.29	1.28	2.54	2.01
MnO	bdl	bdl	bdl	bdl	0.04	bdl	bdl	bdl	bdl
MgO	bdl	bdl	bdl	bdl	0.03	bdl	bdl	0.04	bdl
CaO	17.92	17.86	17.95	17.75	17.75	17.95	17.92	17.75	17.80
Na_2O	bdl	bdl	bdl	bdl	bdl	bdl	bdl	bdl	bdl
K_2O	bdl	bdl	bdl	bdl	bdl	bdl	bdl	bdl	bdl
Total (Wt.%)	88.85	89.69	89.70	89.50	89.39	90.52	89.94	89.63	90.29
Cations calculated on 8 oxygen basis									
Si	2.00	1.99	2.00	2.00	2.01	2.01	1.99	2.00	2.00
Ti	0.01	0.00	0.01	0.00	0.00	0.01	0.01	0.03	0.00
Al	1.94	1.96	1.96	1.96	1.95	1.95	1.95	1.88	1.95
Fe^{3+}	0.06	0.06	0.05	0.06	0.05	0.06	0.06	0.11	0.09
Cr	0.00	0.00	0.00	0.00	0.00	0.00	0.00	0.00	0.00
Mn	0.00	0.00	0.00	0.00	0.00	0.00	0.00	0.00	0.00
Mg	0.00	0.00	0.00	0.00	0.00	0.00	0.00	0.00	0.00
Ca	1.01	1.00	1.00	0.99	0.99	0.99	1.00	1.00	0.99
Na	0.00	0.00	0.00	0.00	0.00	0.00	0.00	0.00	0.00
K	0.00	0.00	0.00	0.00	0.00	0.00	0.00	0.00	0.00
Total (cations)	5.02	5.01	5.02	5.01	5.00	5.02	5.01	5.03	5.03

bdl, below detection level

Table 2. Representative trace element compositions of lawsonite from lawsonite eclogite

Lithology	Lawsonite Eclogite (Fresh, pod core)				Lawsonite Eclogite (Fresh, pod margin)				Lawsonite Eclogite (Retrogressed)			Lawsonite Eclogite (Retrogressed)			
Sample #	SV12-13e	SV12-13e	SV12-13e	SV12-13e	SV03-103	SV03-103	SV03-103	SV03-103	SV08-4A	SV08-4A	SV08-4a	SV12-24	SV12-24	SV12-24	SV12-24
Textural Position	high Ti	high Ti	low Ti	low Ti	high Ti	high Ti	low Ti	low Ti	grt inclusion	core	rim	high Ti blocky	low Ti blocky	high Ti fan	low Ti fan
(ppm)															
P	25	21.7	18.2	23.2	17	21	28	22	17	41	24	29.4	24.5	25.3	71
Sc	2.38	3.59	2.55	3.18	4.22	3.14	2.41	2.43	2	1.14	1.75	4.64	4.13	5.14	4.03
Ti	1437	976	455	375	4230	2222	364	374	468	322	1197	2338	236.6	1740	765
V	262.2	231.8	429.3	268.9	305.9	239.4	250.7	247.1	559	725	668	213.7	227	229.1	188.7
Cr	305.2	255.6	317.2	404.8	96.7	245.4	91.9	41.1	24.7	249.5	680	112.7	163.2	203	152.9
Mn	12.77	14.15	17.2	16.75	23.9	20.8	18.5	22.5	480	18.4	26.4	45.9	31.19	35.8	57.19
Sr	1326	1211	1567	1358	533	443.9	669	1096	418.7	484	633	534	772	626	657
Y	18.84	27.1	8.41	56	32.7	23.5	20.51	26.1	94.4	87	10.42	5.75	11.69	24.6	133.4
Zr	bdl	0.012	bdl	bdl	0.026	bdl	0.18	0.2	0.078	bdl	bdl	bdl	bdl	bdl	bdl
Nb	0.035	0.0053	bdl	0.0015	0.78	bdl	bdl	bdl	0.021	bdl	bdl	bdl	bdl	0.43	0.309
Cs	bdl	0.041	bdl	bdl	bdl	bdl	bdl	bdl	bdl	bdl	bdl	bdl	bdl	bdl	bdl
Ba	bdl	0.077	0.23	0.65	0.5	0.09	0.1	0.04	0.87	bdl	bdl	0.82	bdl	0.77	1.45
La	0.956	6.77	0.98	10.13	5.13	2.88	3.52	11.1	148.2	133.9	4.5	2.21	3.59	43.1	185.2
Ce	2.86	16.51	2.29	25.12	11.72	7.59	8.62	28.3	348	327	12.91	4.37	7.98	75.2	324.7
Pr	0.426	2.07	0.241	3.65	1.5	1.09	1.15	3.85	43.1	45.2	2.17	0.586	0.969	8.1	33.9
Nd	1.75	8.34	1.05	18.17	7.67	5.4	6.02	19.7	202	217.4	11.9	2.36	4.62	27.6	127.3
Sm	0.54	1.76	0.21	6.3	2.14	1.07	1.46	5.94	40	46.1	2.68	0.49	1.08	5.1	24.86
Eu	0.18	0.375	0.068	1.94	0.55	0.389	0.351	1.49	10.2	12.73	0.84	0.189	0.398	1.66	8.47
Gd	0.92	1.67	0.36	9.01	2.59	2.09	2.32	6.67	37.9	41.7	2.79	0.61	1.47	4.16	22.42
Tb	0.244	0.386	0.069	1.8	0.544	0.33	0.534	0.96	4.39	3.9	0.54	0.107	0.202	0.696	3.46
Dy	2.55	3.74	0.73	12.18	4.22	3.25	2.95	4.97	23.6	21.4	2.17	0.67	1.89	4.3	23
Ho	0.557	0.91	0.221	1.98	0.95	0.74	0.64	1.07	3.14	3.23	0.34	0.168	0.455	0.95	4.55
Er	0.97	1.89	0.71	3.33	2.98	2.36	2.19	2.06	7.1	6.27	0.79	0.61	1.18	2.26	13.08
Tm	0.055	0.155	0.077	0.225	0.348	0.213	0.166	0.183	0.48	0.48	bdl	0.111	0.153	0.334	1.664
Yb	0.166	0.39	0.42	0.45	2.03	1.6	1.16	0.4	1.86	1.9	0.38	0.53	1.1	1.74	10.16
Lu	0.005	0.033	0.044	0.036	0.233	0.217	0.19	0.047	0.173	0.194	bdl	0.082	0.192	0.397	1.5
Hf	bdl	bdl	bdl	bdl	bdl	bdl	bdl	bdl	bdl	bdl	bdl	bdl	bdl	bdl	bdl
Ta	0.0015	bdl	bdl	bdl	0.144	bdl	bdl	bdl	bdl	bdl	bdl	bdl	bdl	bdl	bdl
Pb	34.89	35.7	35.7	37.28	11.76	10	14.11	27.41	9.94	12.62	28.5	68.9	94.2	70.2	86.6
Th	0.046	1.6	0.0087	0.052	0.152	0.174	0.113	0.84	7.87	52	0.53	0.304	0.208	1.64	7.05
U	0.0056	0.239	0.0067	0.076	0.097	0.0036	0.025	0.077	6.07	3.2	bdl	bdl	bdl	bdl	3.4

bdl, below detection level

Table 3. Representative trace element compositions of lawsonite from lawsonite blueschist

Lithology	Lawsonite Blueschist				Lawsonite Garnet Blueschist				Lawsonite Garnet Blueschist (Ikipinar)			
Sample #	SV13-15	SV13-15	SV13-15	SV13-15	SV13-06B	SV13-06B	SV13-06B	SV13-06B	SV12-59	SV12-59	SV12-59	SV12-59
Textural Position	matrix core	matrix rim	lws+ph layer core	lws+ph layer rim	matrix core	matrix core	matrix rim	matrix rim	ph+lws cluster	matrix Ti-poor	matrix Ti-rich	
(ppm)												
P	18.9	19.4	26.7	23.7	20.3	22.5	24	25.6	15.5	24.8	22.6	
Sc	5.65	3.82	2.94	3.09	3.67	5.13	3.22	3.57	4.24	4.06	5.05	
Ti	1370	1546	12	8.7	682	395	664	737	493	424	1118	
V	665	504.7	492	564	391.8	413.9	423.5	421	541	546.1	499.2	
Cr	7	37.2	9.4	9	783	532	852	633	31.7	140.3	189.8	
Mn	69.2	62.5	33.4	36.41	18.4	18.07	12.57	25.2	42.3	53.2	45.4	
Sr	624	410	862	1225	828	810	731	741	475.1	505	392.5	
Y	100	9.44	26.4	18.58	13.93	22.42	57	48.2	15.93	18.07	14.81	
Zr	0.011	0.018	0.038	0.001	bdl	0	0	bdl	bdl	0.071	0.038	
Nb	0.012	0.113	0.041	0.021	0.38	0.008	0.0017	0	bdl	bdl	bdl	
Cs	0	0.037	0.013	0	0.041	0.024	0	0.005	0.174	0.035	0.035	
Ba	0.095	0.032	0.97	0.59	0.69	0.23	0.044	0.32	13.2	1.83	0.46	
La	381	59.8	35.2	29.87	14.73	32.6	15.14	14.79	6.62	10.06	6.81	
Ce	615	118.5	73	63.7	38.1	75.5	40.4	41.9	18.26	28.9	19.73	
Pr	57.3	11.75	8.68	7.4	4.98	9.27	5.61	5.68	2.66	4.25	2.93	
Nd	197	38.7	8.68	7.4	24.2	42	27.8	28.7	14.17	22.2	15.14	
Sm	31	5.52	7.23	6.75	5.69	9.63	9.2	8.55	3.81	5.6	4.14	
Eu	14.3	1.56	2.46	1.94	1.68	3.12	3.21	2.63	1.17	1.63	1.27	
Gd	23.2	2.93	6.56	5.98	5.53	9.52	12.51	9.5	4.26	6.21	4.03	
Tb	2.85	0.358	0.81	0.758	0.688	1.186	2.33	1.53	0.594	0.707	0.542	
Dy	17.6	2.14	5.38	3.73	2.8	5.49	15.45	10.8	3.47	4.25	2.93	
Ho	3.14	0.417	0.865	0.651	0.522	0.944	2.314	1.77	0.57	0.686	0.52	
Er	9.3	0.78	2.61	1.34	1.23	1.56	3.3	4.45	1.23	1.56	1.36	
Tm	1.03	0.095	0.061	0.031	0.137	0.159	0.185	0.424	0.119	0.2	0.127	
Yb	5.97	0.56	1.94	0.89	0.57	0.46	0.33	1.38	0.42	0.75	1.14	
Lu	0.75	0.056	0.307	0.125	0.105	0.043	0.022	0.101	0.038	0.087	0.179	
Hf	0	0	0	0	0	0	0	0	bdl	bdl	bdl	
Ta	bdl	0	0	0	0.016	0	0	0	bdl	0	0	
Pb	28.68	18.71	28.53	31.2	25.28	28.79	25.28	23.2	2.67	2.76	1.97	
Th	1.28	0.272	0.083	0.051	0.36	2.62	0.381	1.34	bdl	0.088	0.042	
U	2.9	0.03	0.47	0.205	0.191	2.6	0.096	0.14	0.0064	bdl	0.021	

bdl, below detection limit

Table 4. Representative major element compositions of lawsonite from metasediments

Lithology	Blueschist-facies Calcschist				Quartz-rich Schist			Quartzite (Blueschist-facies)		
Sample #	SV13-01A	SV13-01A	SV13-01A	SV13-01A	SV08-281C	SV08-281C	SV08-281C	SV10-03B	SV10-03B	SV10-03B
Textural Position	Cr-rich	Cr-rich	Ti-rich sector	Ti-poor sector	core		rim	core		rim
SiO_2	37.41	37.67	38.15	38.28	37.76	37.26	37.26	37.85	37.95	37.69
TiO_2	0.80	0.45	0.75	0.02	0.06	0.06	0.10	0.09	0.09	0.07
Al_2O_3	25.79	26.53	30.37	31.09	31.03	30.83	30.03	31.40	31.43	30.98
Cr_2O_3	5.81	4.91	0.74	1.12	0.02	0.03	bdl	bdl	bdl	bdl
FeO*	2.12	2.04	1.86	1.38	1.71	1.86	1.79	1.89	1.91	1.89
MnO	0.01	0.02	bdl	bdl	0.01	0.05	0.04	bdl	bdl	bdl
MgO	0.01	0.03	0.02	0.02	bdl	0.01	0.01	bdl	0.01	0.02
CaO	17.26	16.78	17.56	17.59	18.00	17.80	17.35	17.77	17.73	17.74
Na_2O	bdl	0.03	bdl	0.03	bdl	bdl	0.01	0.03	bdl	0.01
K_2O	bdl	bdl	0.02	bdl	bdl	bdl	0.01	0.02	bdl	bdl
Total (Wt.%)	89.21	88.46	89.47	89.53	88.59	87.90	86.60	89.05	89.12	88.40
Cations calculated on 8 oxygen basis										
Si	2.01	2.03	2.00	2.00	2.00	1.99	2.02	1.99	1.99	2.00
Ti	0.03	0.02	0.03	0.00	0.00	0.00	0.00	0.00	0.00	0.00
Al	1.63	1.68	1.88	1.92	1.93	1.94	1.91	1.95	1.95	1.94
Fe^{3+}	0.10	0.09	0.08	0.06	0.08	0.08	0.08	0.08	0.08	0.08
Cr	0.25	0.21	0.03	0.05	0.00	0.00	0.00	0.00	0.00	0.00
Mn	0.00	0.00	0.00	0.00	0.00	0.00	0.00	0.00	0.00	0.00
Mg	0.00	0.00	0.00	0.00	0.00	0.00	0.00	0.00	0.00	0.00
Ca	1.00	0.97	0.99	0.99	1.02	1.02	1.01	1.00	1.00	1.01
Na	0.00	0.00	0.00	0.00	0.00	0.00	0.00	0.00	0.00	0.00
K	0.00	0.00	0.00	0.00	0.00	0.00	0.00	0.00	0.00	0.00
Total (cations)	5.02	5.00	5.01	5.02	5.03	5.03	5.02	5.02	5.02	5.03

bdl, below detection level

Table 5. Representative trace element compositions of lawsonite from metasediments

Lithology	Blueschist-facies Calc-schist					
Sample #	SV13-01A	SV13-01A	SV13-01A	SV13-01A	SV10-06	SV10-06
Textural Position	Cr-rich	Cr-rich	Ti-rich sector	Ti-poor sector	core	rim
(ppm)						
P	26	42	44	33	23.5	21.6
Sc	8.24	4.23	16.3	3.41	2.9	3.41
Ti	479	1337	2410	283	322	356
V	498.3	606.6	383.4	416.7	204.2	185.4
Cr			2993	1865	20.9	28.9
Mn	29.7	36.3	522	33.7	93.8	99.4
Sr	849	753	229.9	225	738	722
Y	51.6	139	21.6	19.9	112.9	118.5
Zr	0.048	0.03	0.59	0.016	bdl	bdl
Nb	0.02	0.069	0.48	0.048	bdl	bdl
Cs	bdl	bdl	bdl	0.2	0.023	0.006
Ba	0.74	1.03	0.74	0.44	0.022	0.034
La	52	73.1	32.9	3.24	220.1	289.7
Ce	104.1	155.2	68.5	9.67	537	633
Pr	10.85	18.33	7.75	1.23	57.1	63.2
Nd	41.6	74.3	32.9	6.6	227.6	236.7
Sm	7.99	17.3	5.8	1.99	45.7	45.4
Eu	2.77	5.82	1.53	0.66	10.08	9.82
Gd	6.44	16.8	5.2	3.35	42.3	38
Tb	1.19	3.08	0.65	0.372	5.93	5.79
Dy	8.65	25	4	3.1	30.5	30.8
Ho	1.97	4.98	0.83	0.67	4.21	4.19
Er	5.7	14.72	1.54	2.09	6.38	5.87
Tm	0.878	1.94	0.32	0.256	0.324	0.366
Yb	5.27	11.44	1.31	2	0.91	1.05
Lu	0.524	1.26	0.178	0.256	0.057	0.078
Hf	bdl	bdl	bdl	bdl	bdl	bdl
Ta	bdl	0.0024	0.073	bdl	bdl	bdl
Pb	35.47	34.93	16.5	9.83	136.4	127
Th	0.848	2.31	5.64	1.33	17.63	27
U	0.247	0.92	0.73	0.223	2.57	2.01

bdl, below detection limit

Table 6. Representative major element compositions of lawsonite in lawsonite + chlorite rocks

Lithology	Lawsonite + Chlorite (Halilbağı)				Lawsonite + Chlorite (Tavşanlı)			Lawsonite + Chlorite + Garnet (Halilbağı)			
Sample #	SV12-21D	SV12-21D	SV12-21D	SV12-21D	TZ10-2.2c	TZ10-2.2c	TZ10-2.2c	SV13-17A	SV13-17A	SV13-17A	SV13-17A
Textural Position	Ti-rich	Ti-rich	Ti-poor	Ti-poor	Ti-rich		Ti-poor	Fe-poor core	Fe-rich rim	Ti-rich sector	Ti-poor sector
SiO_2	37.80	37.84	38.13	37.79	38.39	38.49	37.87	38.62	38.19	38.24	38.53
TiO_2	0.54	1.03	0.05	bdl	0.32	0.15	0.01	0.50	0.60	0.87	0.05
Al_2O_3	30.96	30.51	31.73	31.58	31.09	31.44	31.23	31.90	30.77	30.93	31.48
Cr_2O_3	0.04	0.05	0.04	0.05	bdl	0.05	0.03	0.16	0.15	0.16	0.22
FeO*	2.06	1.87	1.40	1.28	1.31	1.24	1.47	1.04	2.08	1.61	1.40
MnO	0.03	0.01	bdl	0.01	bdl	bdl	bdl	0.03	bdl	bdl	bdl
MgO	0.01	0.02	bdl	0.01	bdl	bdl	0.01	0.03	0.01	0.05	0.01
CaO	17.55	17.76	17.87	17.69	17.94	17.90	18.02	17.73	17.54	17.64	17.17
Na_2O	0.01	0.01	0.03	0.04	0.01	0.01	0.03	bdl	0.02	0.01	bdl
K_2O	bdl	bdl	bdl	bdl	bdl	bdl	bdl	bdl	0.01	bdl	bdl
Total (Wt.%)	89.00	89.10	89.25	88.45	89.06	89.28	88.67	90.01	89.37	89.51	88.86
Cations calculated on 8 oxygen basis											
Si	1.99	1.99	2.00	1.99	2.01	2.01	1.99	2.00	2.00	1.99	2.02
Ti	0.02	0.04	0.00	0.00	0.01	0.01	0.00	0.02	0.02	0.03	0.00
Al	1.92	1.89	1.96	1.96	1.92	1.94	1.94	1.95	1.90	1.91	1.95
Fe^{3+}	0.09	0.08	0.06	0.06	0.06	0.05	0.07	0.05	0.09	0.07	0.06
Cr	0.00	0.00	0.00	0.00	0.00	0.00	0.00	0.01	0.01	0.01	0.01
Mn	0.00	0.00	0.00	0.00	0.00	0.00	0.00	0.00	0.00	0.00	0.00
Mg	0.00	0.00	0.00	0.00	0.00	0.00	0.00	0.00	0.00	0.00	0.00
Ca	0.99	1.00	1.00	1.00	1.01	1.00	1.02	0.98	0.99	0.99	0.96
Na	0.00	0.00	0.00	0.00	0.00	0.00	0.00	0.00	0.00	0.00	0.00
K	0.00	0.00	0.00	0.00	0.00	0.00	0.00	0.00	0.00	0.00	0.00
Total (cations)	5.01	5.00	5.02	5.01	5.01	5.01	5.02	5.01	5.01	5.00	5.00

bdl, below detection level

Table 7. Representative trace element compositions of lawsonite in lawsonite + chlorite rocks

Lithology	Lawsonite + Chlorite (Halilbağı)				Lawsonite + Chlorite (Tavşanlı)				Lawsonite + Chlorite + Garnet (Halilbağı)			
Sample #	SV12-21d	SV12-21d	SV12-21d	SV12-21d	TZ10-2.2c	TZ10-2.2c	TZ10-2.2c	TZ10-2.2c	SV13-17A	SV13-17A	SV13-17A	SV13-17A
Textural Position	high Ti	high Ti	low Ti	low Ti	high Ti	high Ti	low Ti	low Ti	Fe-poor core	Fe-rich rim	Ti-rich sector	Ti-poor sector
(ppm)												
P	36	27	61	85	16	25	15	21	21	8	24	1
Sc	4.89	3.54	2.32	2.71	26.07	27.10	19.68	18.97	46.3	23.1	26.4	11.9
Ti	5160.0	6470.0	265.0	277.0	1922.0	1716.0	292.0	171.9	2980	2640	2000	249
V	247.9	241.0	222.5	243.2	1424.0	1448.0	1023.0	1551.0	898	695	709	900
Cr	629.3	584	534	555	107	100	50	68	1349	637	1110	860
Mn	24.1	20.8	20.7	31.7	19.2	20.3	15.0	15.5	77.7	30.7	42.0	36.0
Sr	505	485	755	815	1212.0	1177.0	1035.0	1585.0	2294	1015	604	1380
Y	8.02	6.16	32.1	32.6	45.5	23.2	25.0	63.2	161	162.90	310	190
Zr	0.00	0.03	0.00	0.07	0.17	0.01	bdl	bdl	0.00	0.43	24	0.12
Nb	0.07	0.00	0.00	0.05	0.01	bdl	bdl	0.01	0.00	0.00	0.00	0.00
Cs	0.23	0.00	0.00	0.28	0.01	bdl	bdl	0.04	0.95	0.00	0.00	0.28
Ba	3.20	0.58	0.74	5.20	0.04	2.15	bdl	1.18	2.10	0.90	5.40	4.00
La	1.26	0.37	2.19	1.73	3.78	3.02	3.56	9.88	2.84	2.80	12.70	4.90
Ce	2.26	0.87	4.12	3.14	9.92	7.43	10.78	27.80	6.60	7.84	35.20	14.20
Pr	0.40	0.16	0.80	0.68	1.57	1.14	1.75	4.08	1.50	1.58	5.75	2.34
Nd	2.37	0.83	4.24	2.97	9.02	6.53	8.65	20.66	12.9	9	40.70	14.80
Sm	0.50	0.27	1.39	1.22	3.91	2.07	2.88	7.28	5.70	4.73	14.50	5.30
Eu	0.27	0.21	0.66	0.52	1.78	0.93	1.03	3.01	4.18	2.56	8.00	4.80
Gd	0.56	0.87	3.23	1.94	7.03	3.56	3.75	11.72	12.10	11.7	32.70	14.50
Tb	0.15	0.14	0.54	0.32	1.08	0.54	0.60	1.58	3.21	2.62	5.80	3.50
Dy	1.08	1.11	4.72	4.51	7.23	3.83	4.19	10.77	23	19.70	47.00	29.20
Ho	0.17	0.23	1.22	1.17	1.60	0.76	0.89	2.07	6.10	5.19	10.10	6.70
Er	0.72	0.75	4.88	5.18	4.24	2.03	2.42	5.37	11.80	13	23.30	20.10
Tm	0.10	0.06	0.81	1.01	0.46	0.20	0.24	0.49	1.83	1.59	2.41	2.60
Yb	0.74	0.59	6.16	8.49	2.55	1.29	1.57	2.95	9.20	9.40	13.60	13.90
Lu	0.06	0.07	1.22	1.76	0.39	0.24	0.18	0.48	1.26	1.45	1.52	2.73
Hf	0.00	0.00	0.00	0.00	0.02	bdl	0.00	0.00	0.05	0.00	0.97	0.00
Ta	0.00	0.00	0.00	0.00	0.00	bdl	bdl	bdl	0.00	0.00	0.00	0.00
Pb	18.70	18.10	22.22	26.84	27.84	28.7	25.16	32.91	71.10	38.8	25.80	47.00
Th	0.01	0.00	0.00	0.00	0.63	1.0	0.36	4.10	0.07	0.26	2.30	0.07
U	0.01	0.00	0.00	0.02	0.14	0.2	0.03	0.26	0.74	0.07	1.14	0.13

bdl, below detection level

Table 8. Representative major element compositions of lawsonite in lawsonite-rich veins and layers

Lithology	Lawsonite Vein (margin)		Lawsonite Vein (interior)		Lws Vein
Sample #	SV03-103	SV03-103	SV03-103	SV03-103	SV12-24B
Textural Position	Fe-poor core	Fe-rich rim	Fe-poor core	Fe-rich rim	Bulk[1]
SiO_2	38.36	38.31	38.36	38.54	38.00
TiO_2	0.48	0.41	0.03	0.38	0.13
Al_2O_3	32.18	31.97	32.67	31.70	27.92
Cr_2O_3	0.01	0.08	0.00	0.00	2.69
FeO*	0.67	1.45	0.65	1.45	0.01
MnO	bdl	bdl	bdl	bdl	0.05
MgO	bdl	bdl	bdl	bdl	18.93
CaO	17.91	17.67	18.00	17.83	0.05
Na_2O	bdl	bdl	bdl	bdl	0.07
K_2O	bdl	bdl	bdl	bdl	0.01
Total (Wt.%)	89.61	89.89	89.71	89.90	87.86
Cations calculated on 8 oxygen basis					
Si	1.99	1.99	1.99	2.00	
Ti	0.02	0.02	0.00	0.01	
Al	1.97	1.96	1.99	1.94	
Fe^{3+}	0.03	0.06	0.03	0.06	
Cr	0.00	0.00	0.00	0.00	
Mn	0.00	0.00	0.00	0.00	
Mg	0.00	0.00	0.00	0.00	
Ca	1.00	0.98	1.00	0.99	
Na	0.00	0.00	0.00	0.00	
K	0.00	0.00	0.00	0.00	
Total (cations)	5.01	5.01	5.01	5.00	

bdl, below detection level

[1]Data obtained from an ICP-OES bulk rock analysis of a mono-minerallic lawsonite vein

Table 9. Representative trace element compositions of lawsonite in lawsonite-rich veins and layers

Lithology	Lawsonite + Garnet + Phengite Vein				Lws Vein
Sample #	SV03-103	SV03-103	SV03-103	SV03-103	SV12-24B
Textural Position	Fe-poor core	Fe-rich rim	Ti-poor sector	Ti-rich sector	Bulk
(ppm)					
P	34	28.5	17	30.4	na
Sc	2.6	2.74	2.29	2.55	na
Ti	883	2368	200	3060	na
V	38.8	47.9	42.9	45.8	189
Cr	17.6	4.01	5.3	14.58	bdl
Mn	6.3	20.9	22.2	26.8	na
Sr	877	541.1	1137	626	740
Y	40.6	7.1	19.8	36.4	90.8
Zr	158	0.02	3.2	0	6
Nb	0.12	0.005	0	0.44	0.8
Cs	0.07	0.1	0	0	bdl
Ba	0	0	0.26	0.26	15
La	7.76	9.7	35.8	18.6	86.2
Ce	19.25	21.7	93.7	51.3	172
Pr	2.52	2.62	12.25	6.9	19.4
Nd	13	11.54	57.1	35.6	79.2
Sm	3.63	3.32	16.7	11.52	16.5
Eu	0.92	0.86	2.97	3.06	5.08
Gd	5.6	3.13	14.8	13.8	16.8
Tb	0.91	0.373	1.74	2.07	2.55
Dy	7.94	2.03	7.38	11.26	14.6
Ho	1.59	0.257	1.02	1.58	2.81
Er	3.88	0.51	1.66	3.1	7.69
Tm	0.32	0.055	0.183	0.315	0.914
Yb	1.27	0.47	1.17	1.58	4.63
Lu	0.273	0.025	0.113	0.158	0.66
Hf	3.9	0	0.12	0	0.2
Ta	0.051	0.0048	0	0.0097	2.88
Pb	22.2	10.97	34.4	17.65	59
Th	1.23	0.301	0.97	0.573	1.33
U	0.61	0.9	0.08	0.225	2.28

bdl, below detection limits
na, not analyzed

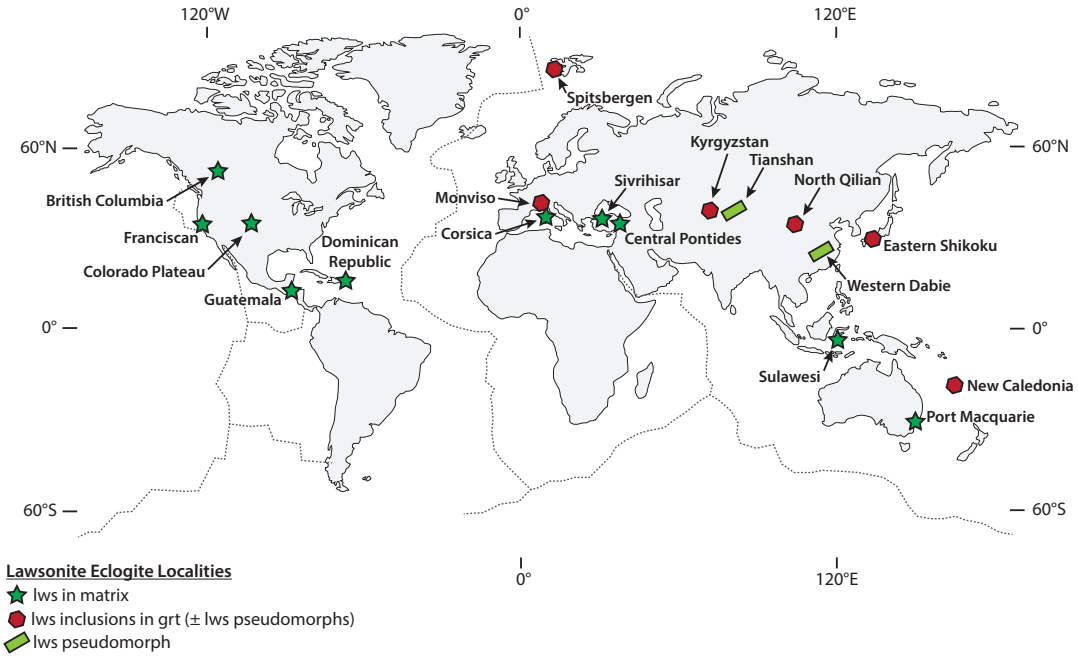

Figure 1. Distribution of lawsonite eclogite localities in the world, classified by the textural position of the lawsonite (matrix, inclusion in garnet, pseudomorph).

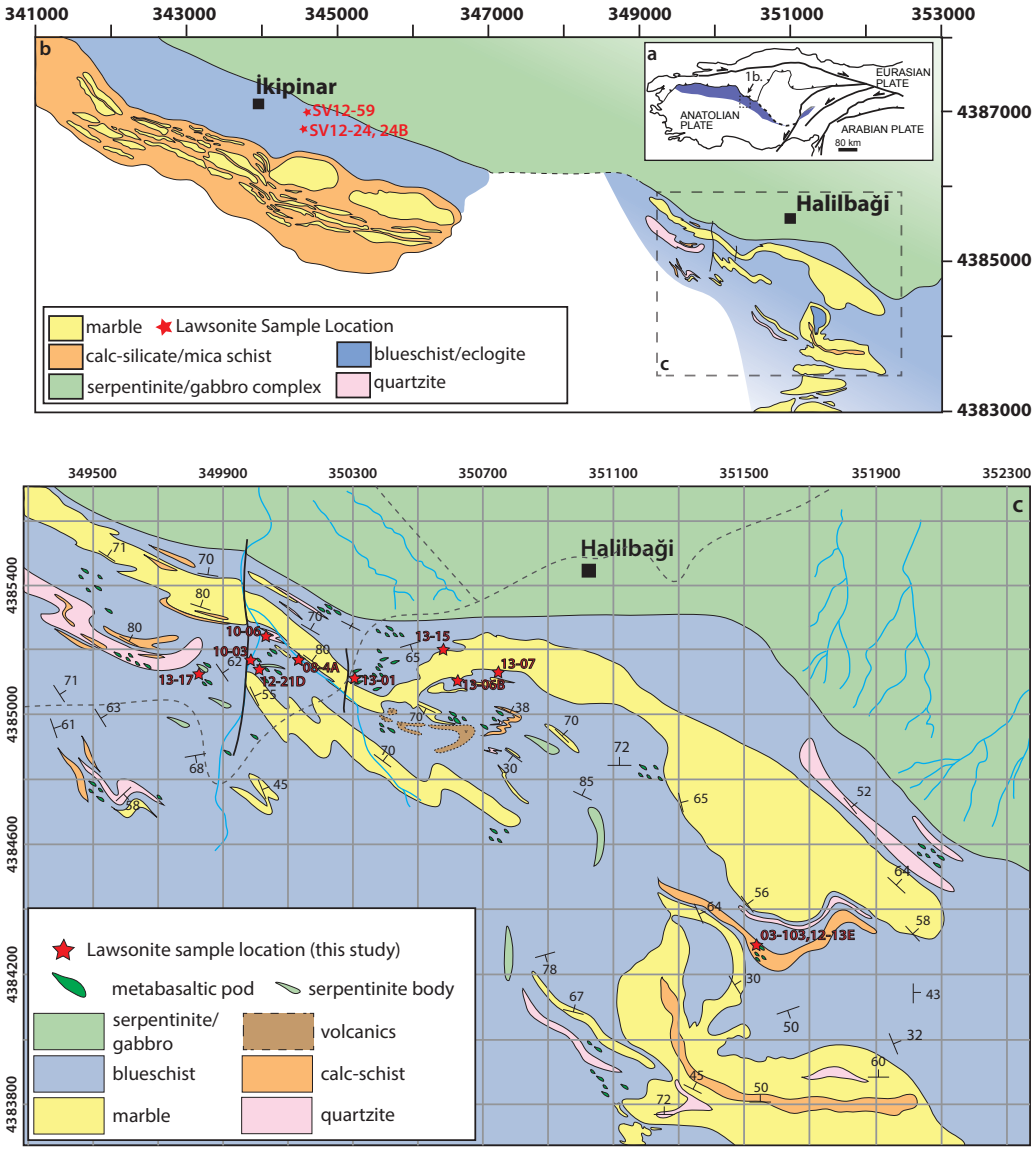

Figure 2. (a) Tectonic map showing the location of the Tavşanlı Zone HP/LT belt (shaded region) in Turkey. (b) Simplified geologic map of the Sivrihisar Massif near the villages of Halilbağı and İkipınar; sample location for lawsonite garnet blueschist SV12-59 and chlorite + epidote-rich pod and associated monomineralic vein (SV12-24, SV12-24B) is shown. (c) Schematic map of the Halilbağı region showing remaining lawsonite sample locations. Sample locations are provided in Supplementary Material 1.

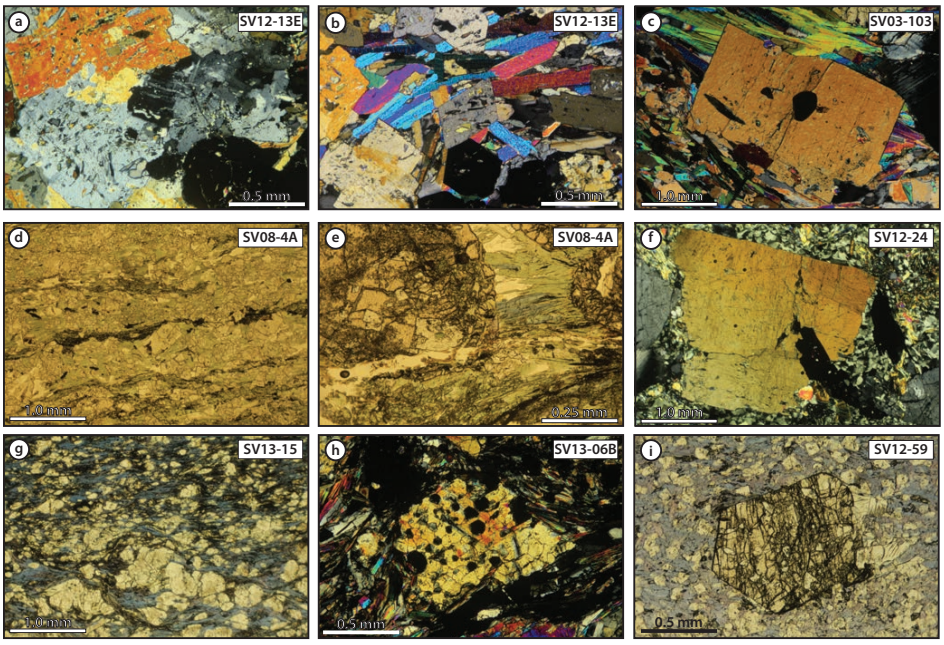

Figure 3. Representative photomicrographs of metabasaltic samples highlighting the different microstructures (euhedral, blocky crystals vs. aggregates), textural positions (matrix; inclusions in garnet, e, i), and inclusion assemblages (Fe-Ti oxides, f; garnet, h) in lawsonite.

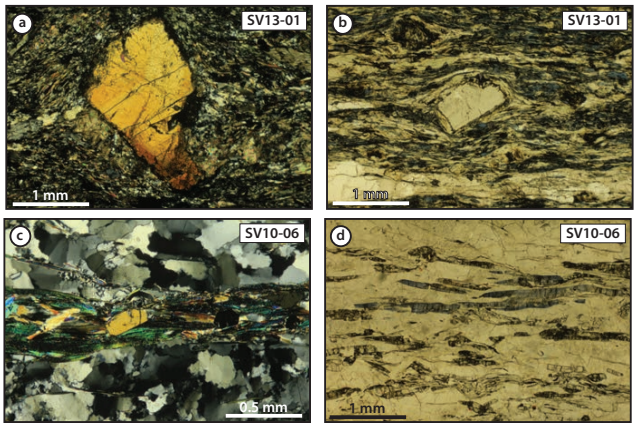

Figure 4. Photomicrographs of lawsonite from calc-schist sample SV13-01 (a, b) and quartzite sample SV10-06 (c, d).

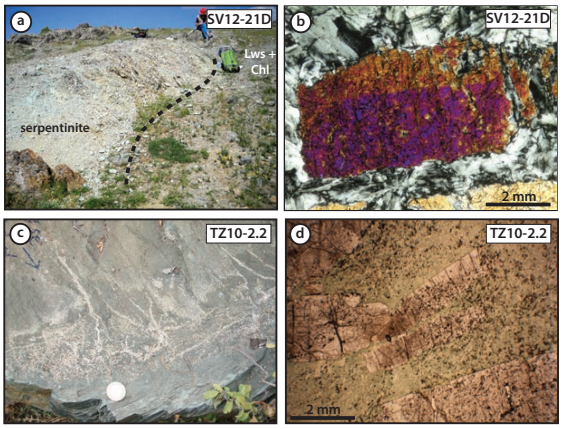

Figure 5. (a) Photograph from the Halilbağı region showing the field relationships between antigorite serpentinite lenses and the lawsonite + chlorite-rich rocks from which sample SV12-21D was collected (b). (c) Photograph of the lawsonite + chlorite-rich boulder from which sample TZ10-2.2c was collected (d).

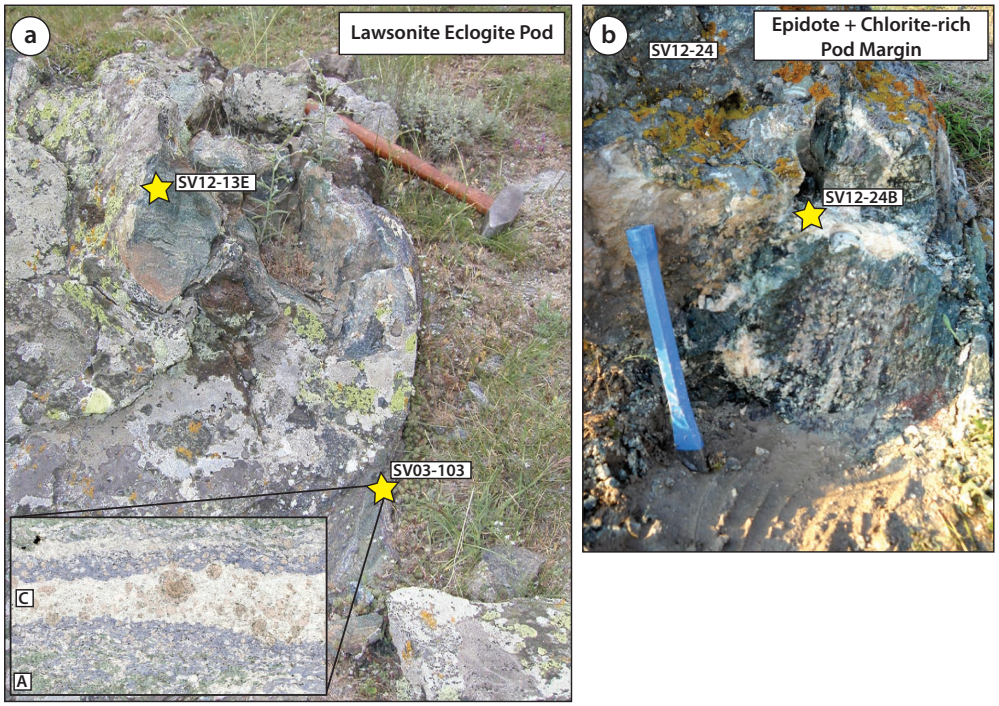

Figure 6. Photograph of the lawsonite eclogite pod from which samples SV12-13E (lawsonite eclogite pod core), SV03-103A (lawsonite eclogite pod margin), and SV03-103C (lawsonite + garnet + phengite-rich layer) were collected. Inset shows a thin section scan of the pod margin highlighting the mm-to-cm scale interlayering of blueschist and eclogite, as well as the relationship of these layers to the lawsonite + garnet + phengite-rich layer. Photograph of the epidote + chlorite-rich pod margin from which the monomineralic lawsonite vein (SV12-24B) and SV12-24 were sampled (b).

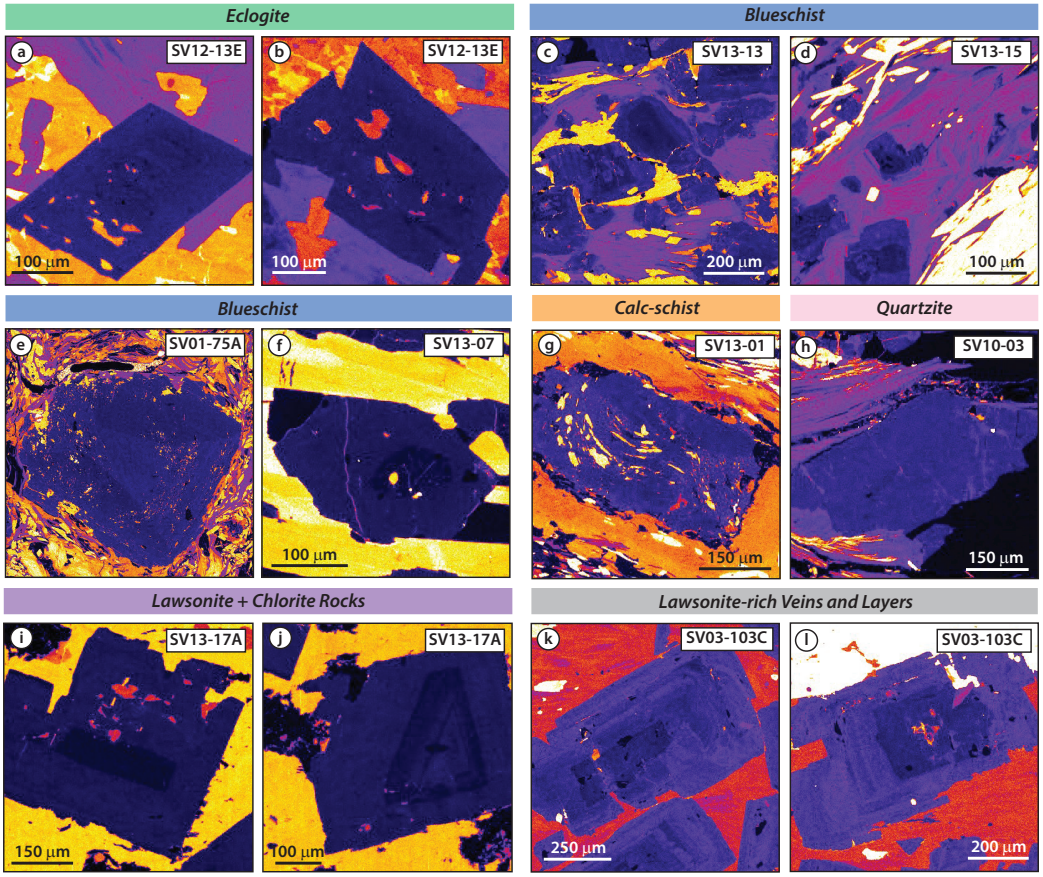

Figure 7. Representative Fe zoning in lawsonite from eclogite (a, b), blueschist (c, d, e, f), metasediments (g, h), metasomatic lawsonite + chlorite-rich rocks (i, j), and lawsonite-rich layers and veins (k, l) showing the variety of different zoning patterns possible (core-to-rim, sector, oscillatory).

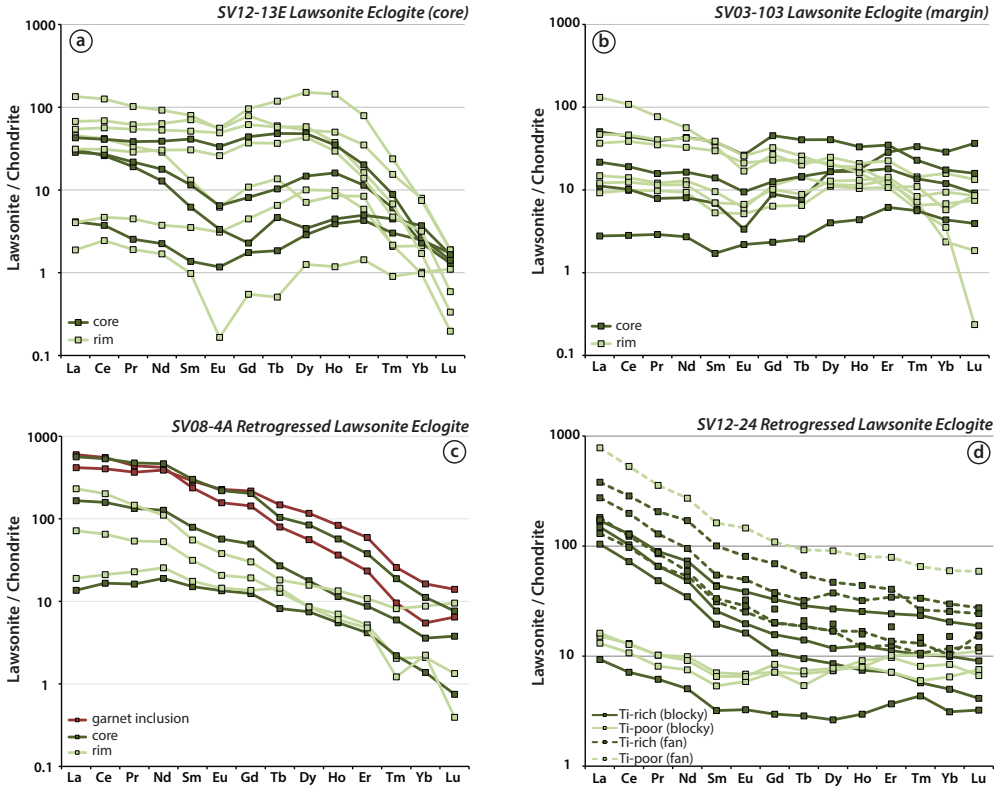

Figure 8. Chondrite-normalized REE patterns for lawsonite from representative fresh (a, b) and retrogressed (c, d) lawsonite eclogite samples.

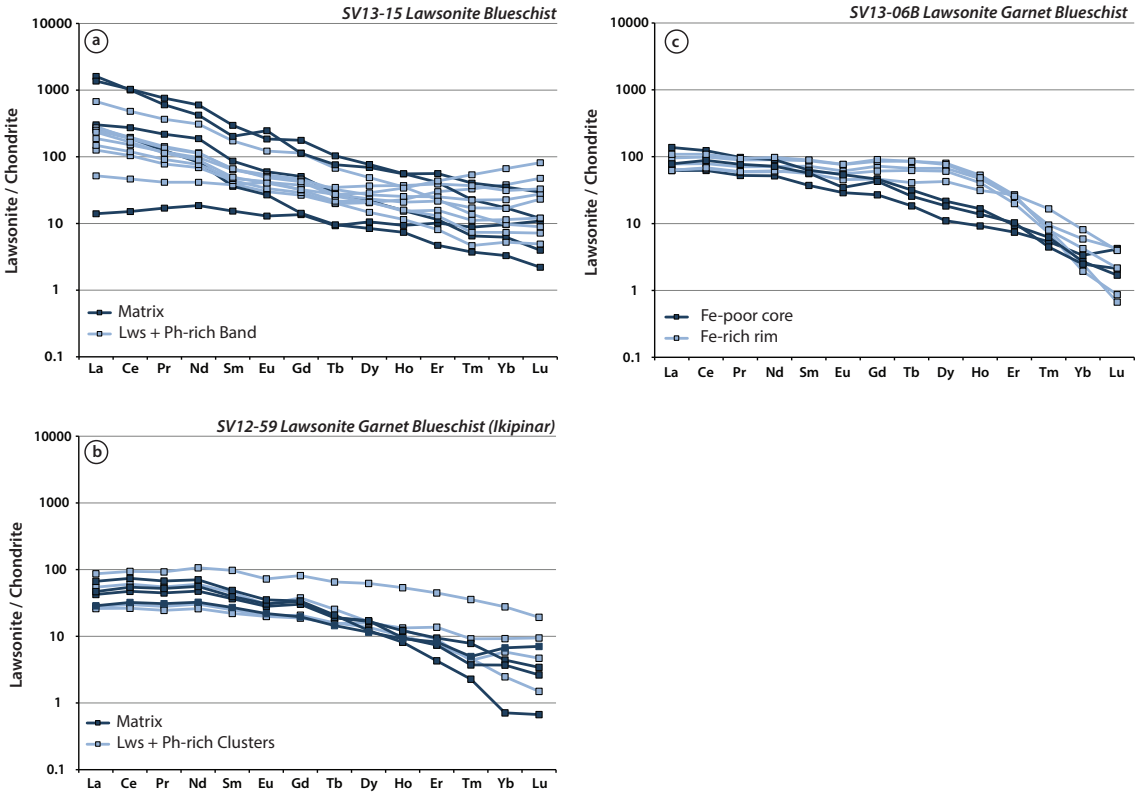

Figure 9. Chondrite-normalized REE patterns for lawsonite from representative lawsonite blueschist samples (a, b, c).

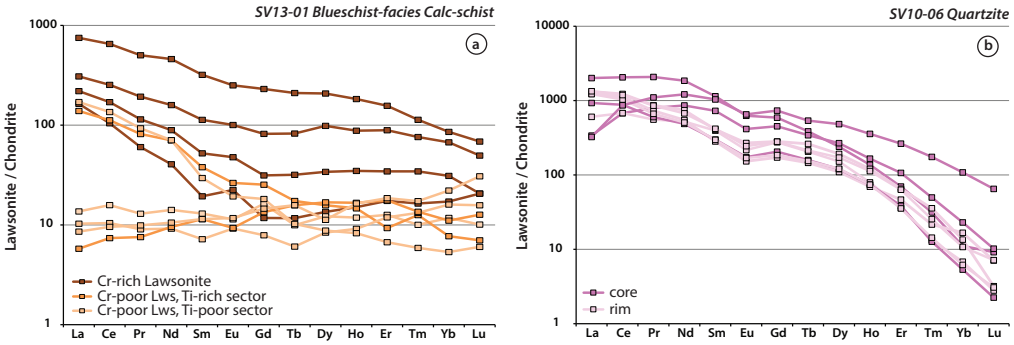

Figure 10. Chondrite-normalized REE patterns for lawsonite from lawsonite-bearing calc-schist (a) and quartzite (b).

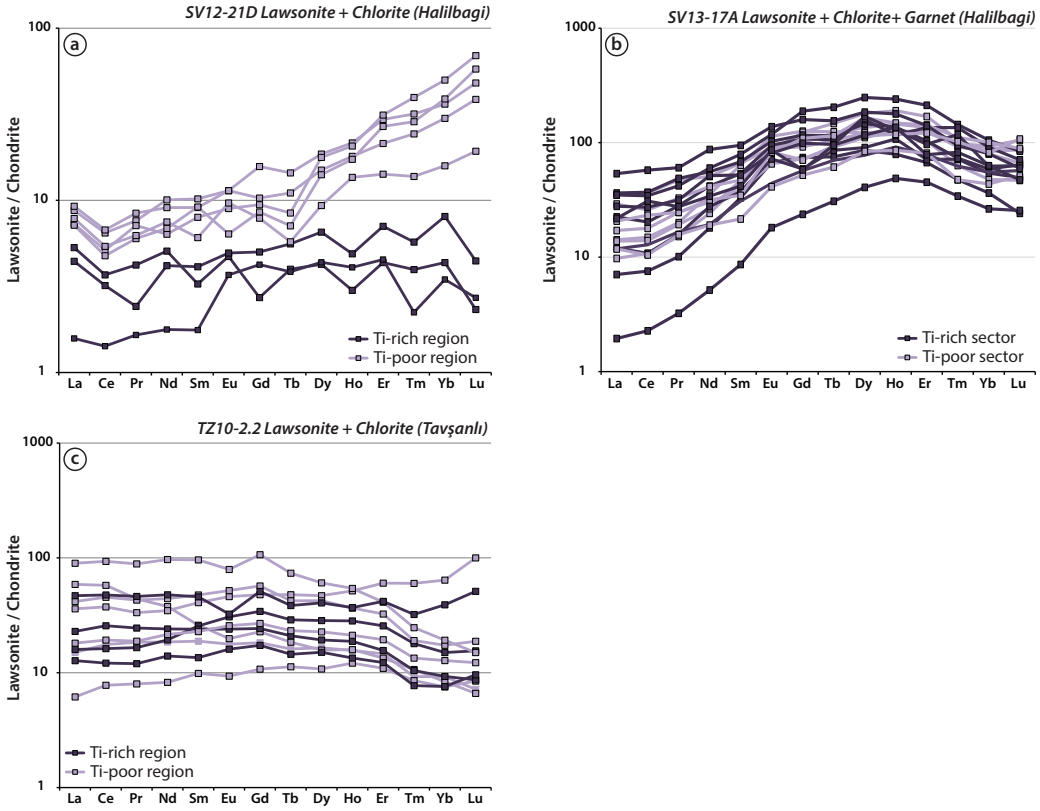

Figure 11. Chondrite-normalized REE patterns for lawsonite metasomatic lawsonite + chlorite-rich rocks from the Halilbağı region (a, b) and the western part of the Tavşanlı Zone (c).

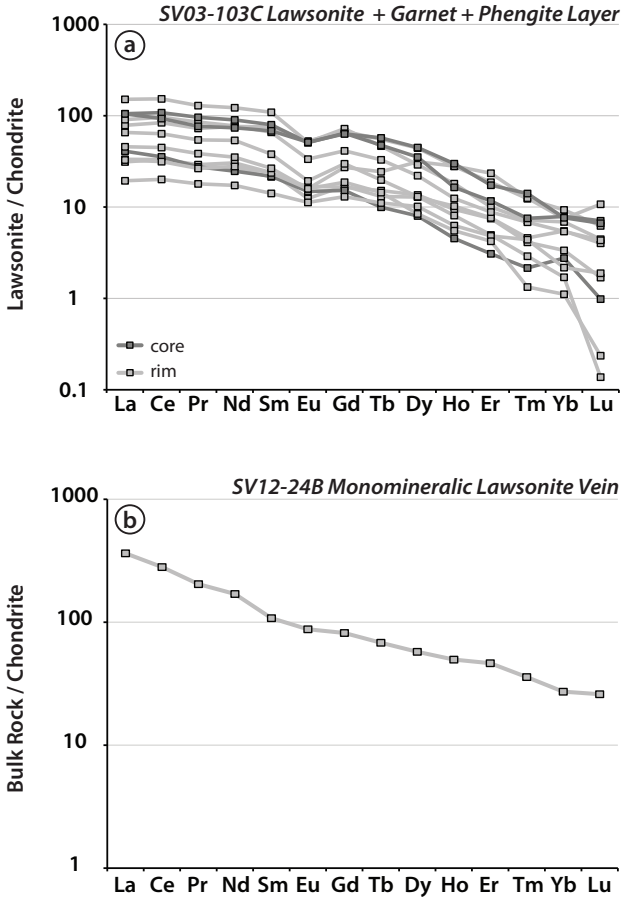

Figure 12. Chondrite-normalized REE patterns for lawsonite from a lawsonite + garnet + phengite-rich layer (a) and monomineralic lawsonite vein (b).

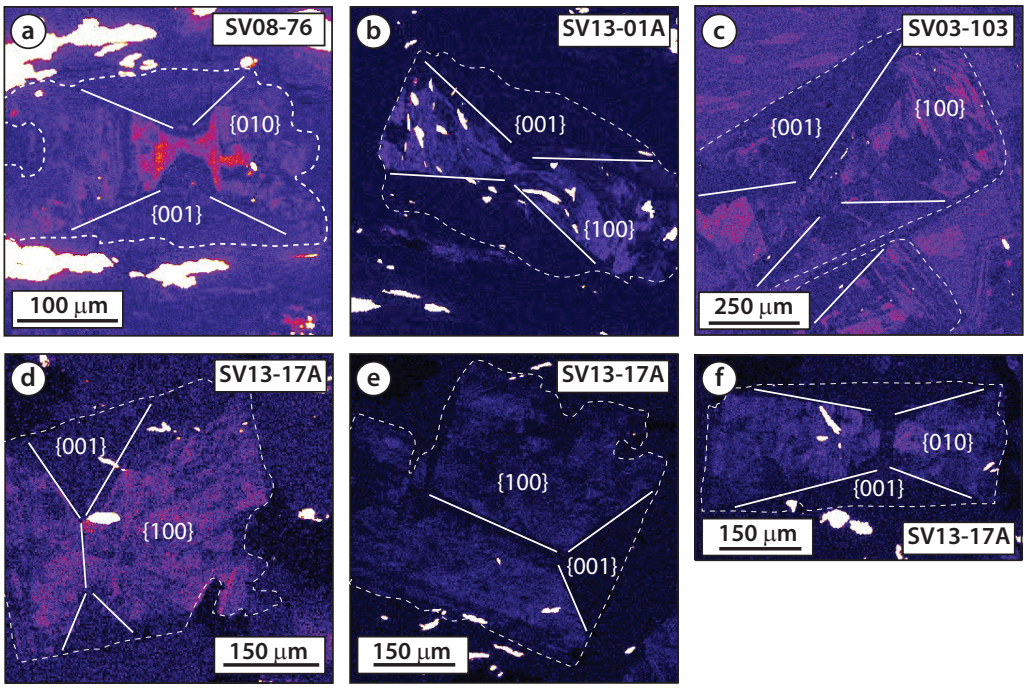

Figure 13. X-ray element maps highlighting the Ti hourglass sector zoning that is common in lawsonite from a variety of rock types including layered blueschists and eclogites (a), calc-schists (b), lawsonite-rich veins and layers (c), and metasomatic lawsonite + chlorite-rich rocks (d, e, f). Results from EBSD analysis of single lawsonite grains shows that Ti-rich sectors tend to grow in the direction of the {100} and {010} axis.

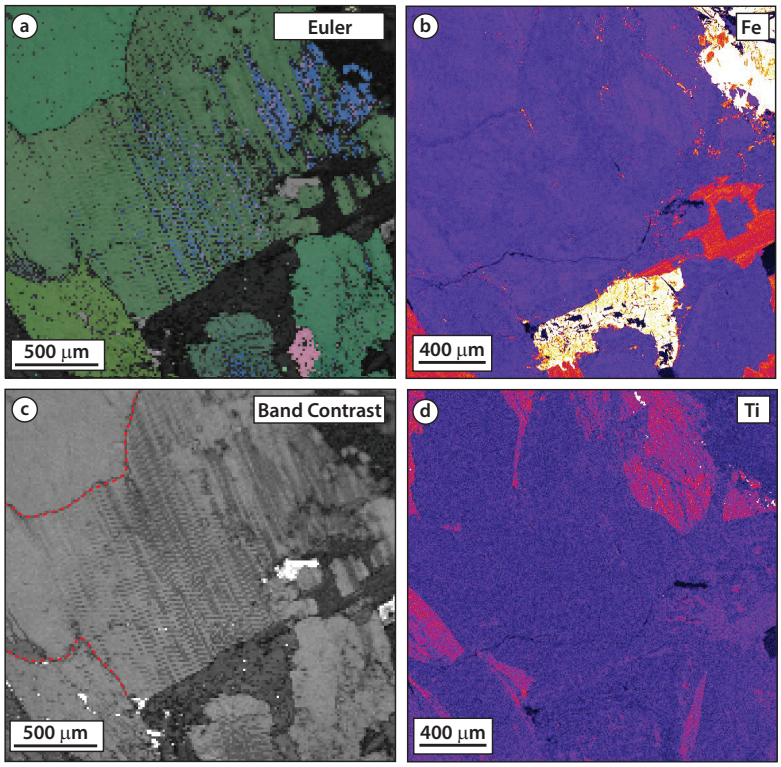

Figure 14. X-ray element maps showing the patchy Fe zoning (b) and irregular distribution of Ti (d) within a coarse-grained lawsonite from pod margin (SV03-305). Euler maps (a) and band contrast images (c) obtained from EBSD analysis shows that Ti is preferentially concentrated along lawsonite grain boundaries (shown in c, as dashed line) and regions with abundant polysynthetic twinning.

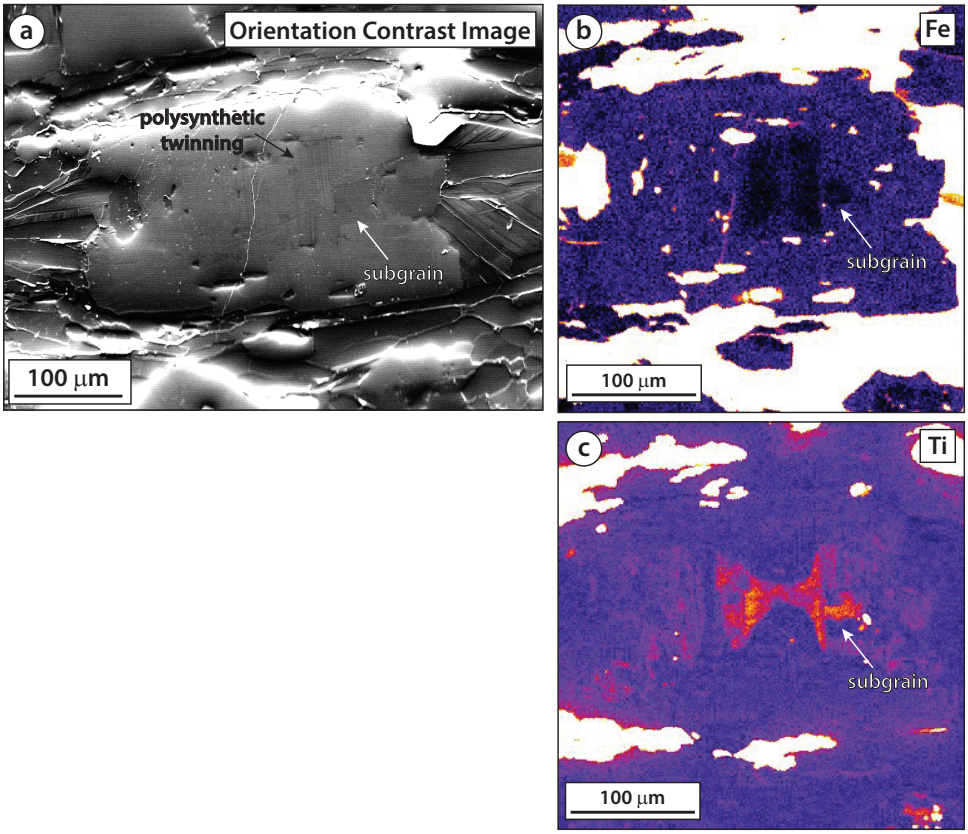

Figure 15. Orientation contrast image showing the presence of polysynthetic twinning and the presence of subgrains (a) in a lawsonite from a layered blueschist and eclogite (SV08-76). Fe (b) and Ti (c) X-ray element maps of the same lawsonite grain show distortion of the core-to-rim and sector zoning in the region of the subgrain.

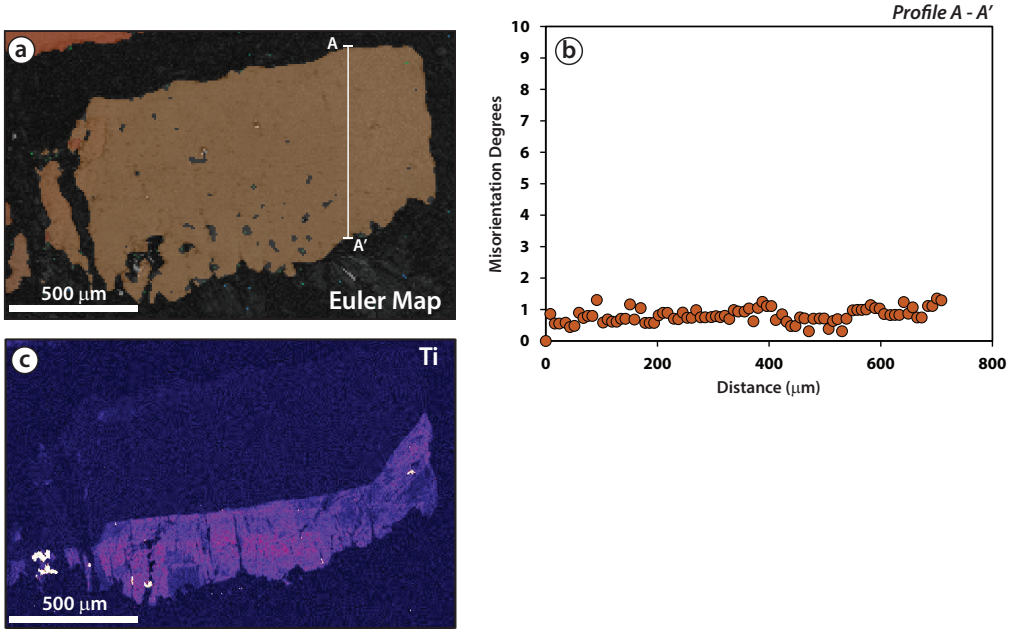

Figure 16. Euler map (a) of a coarse-grained lawsonite from a metasomatic lawsonite + chlorite-rich rock (SV12-21D). Despite the presence of a sharp compositional boundary within the grain (c), a profile across the grain shows that there is no significant lattice misorientation across the boundary (b).

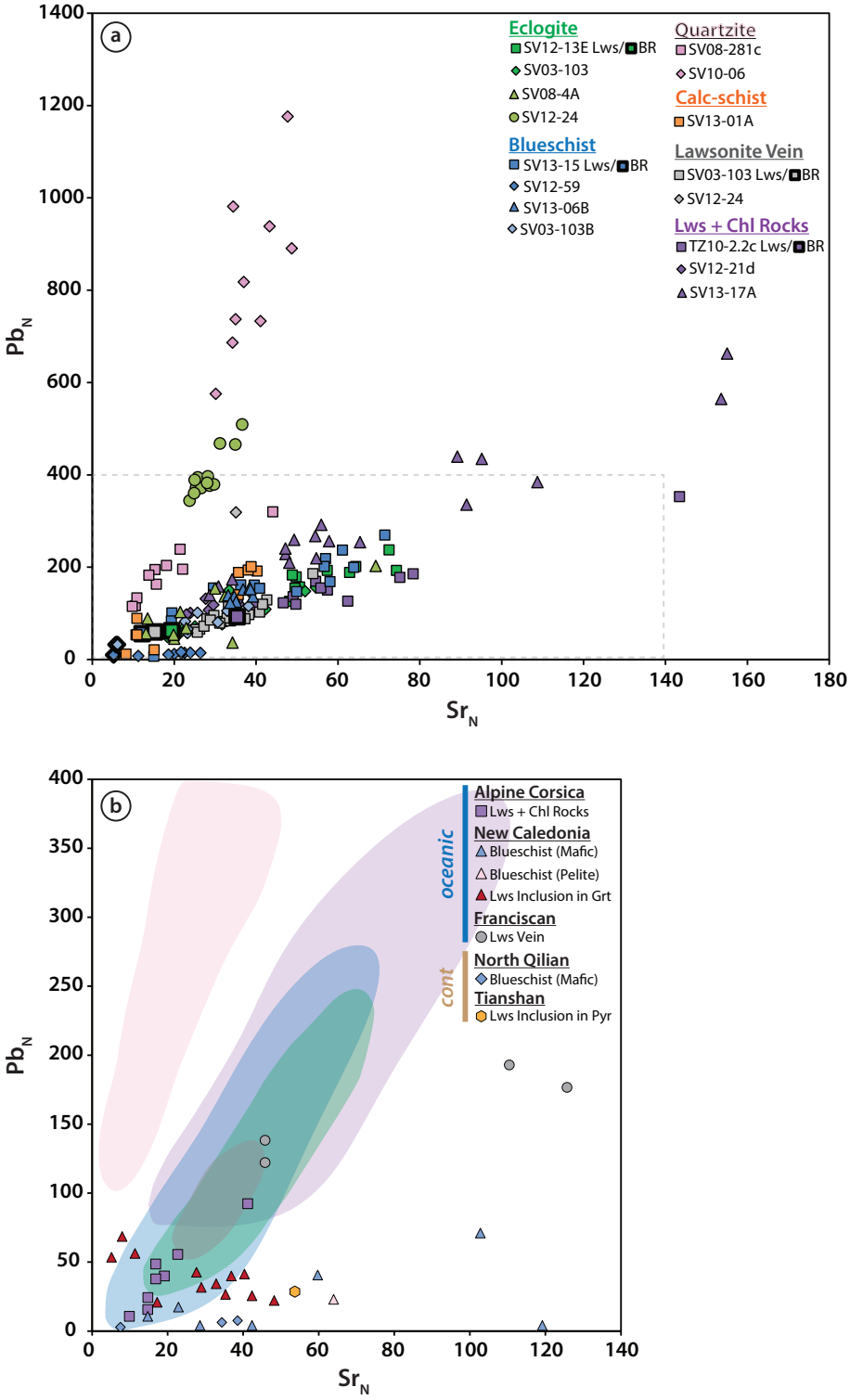

Figure 17. Plots of (primitive mantle normalized) Sr vs. Pb contents in lawsonite from the Tavşanlı Zone (a) and worldwide lawsonite-bearing localities (b).

Supplementary Material 1. Sample locations and analytical methods.

	UTM Coordinates[a]		Methods			
	Easting (m)	Northing (m)	Element Map	Major Elements	Trace Elements	EBSD Map
Eclogite Samples						
SV12-13E (core)	351574	4384265	x	x	x	x
SV03-103A (margin)	351574	4384265	x	x	x	
SV03-305 (margin)	351574	4384265	x			x
SV08-4A	350046	4385062		x	x	
SV12-24	344581	4386678	x	x	x	x
SV08-76	347773	4381019				
Blueschist Samples						
SV12-59	344596	4386992	x		x	
SV13-15	350572	4385194	x		x	
SV13-06B	350615	4385109	x		x	
SV13-07	350711	4384917	x			
Metasediment Samples						
SV13-01A	350295	4384946	x	x	x	x
SV08-281D	350194	4385116		x	x	
SV10-06	350066	4385206			x	
SV10-03	349975	4384913	x			x
Lawsonite + Chlorite Rocks						
TZ10-2.2[c]	741000	4400780	x	x	x	
SV13-17A	349839	4384940	x	x	x	x
SV12-21D	350042	4384924	x	x	x	x
Lawsonite Vein Samples						
SV03-103C	351574	4384265	x	x	x	x
SV12-24B	344581	4386678		x[b]	x[b]	

[a]Coordinates are reported using the ED 1950 (UTM) reference system, south hemisphere, zone 36, except when noted
[b]Major and trace elements obtained from a bulk rock analysis
[c]Coordinates reported are from Okay and Whitney (2010)

Chapter 4: Origin of Lawsonite-rich Veins and Layers in Eclogite and Blueschist, Sivrihisar Massif, Turkey

Chapter Summary

In the subduction complex of the Sivrihisar Massif, Tavşanlı Zone, Turkey, lawsonite eclogite occurs as meters-scale pods with lithologically complex margins characterized by finely interlayered lawsonite blueschist, eclogite, and, in some cases, lawsonite + phengite ± garnet-rich layers bordered by glaucophane-rich assemblages. Lawsonite-rich veins and layers are also found along the margins of retrogressed, chlorite + epidote-rich mafic pods, where they are comprised almost exclusively of lawsonite. To understand the origins and implications of these lawsonite-rich assemblages that are ubiquitous throughout the terrane, we present a bulk rock and mineral major and trace element study of two representative lawsonite-rich veins and layers and their associated host rocks. Bulk rock major element analyses indicate that the host lawsonite eclogite likely had a basaltic protolith, although trace element signatures suggest that it may have experienced interactions (via mechanical mixing and/or fluid-rock interaction) with more enriched reservoirs, such as sediments. Field relations, as well as petrological and geochemical evidence, suggest that the lawsonite + garnet + phengite-rich layer and its associated glaucophane-rich margin likely formed coevally with the host eclogite during prograde to peak metamorphism, as a result of differences in bulk rock composition imparted during fluid-rock interaction and subduction metamorphism. In addition to

altering the bulk rock composition, fluid-rock interaction along the pod margin may have also driven changes in fO_2, as minerals (omphacite, glaucophane, lawsonite, phengite) from the pod margin record a core-to-rim increase in Fe^{3+} compared to minerals from the pod core. In the case of lawsonite, fO_2 changes are also indicated by an overall decrease in V concentrations from pod core to pod rim, and intragrain shifts in the Eu anomaly. Results from X-ray Computed Tomography (XRCT) imaging suggest that high-field strength elements (HFSE) may have also been mobilized during the formation of the lawsonite + garnet + phengite-rich layer and associated glaucophane-rich margin, as HFSE-rich accessory minerals, such as zircon and rutile, are concentrated within these layers and depleted in the adjacent lawsonite eclogite.

1. Introduction

The subduction of hydrated oceanic lithosphere is accompanied by a series of dehydration reactions that release significant quantities of H_2O-rich fluid into the mantle. This fluid facilitates geochemical cycling between the crust and mantle, driving mantle wedge metasomatism and melting, and ultimately generating arc magmas. The release of H_2O during dehydration reactions may also affect the rheology of the subducting plate and the mechanical behavior of the slab-mantle interface (Wada et al. 2008, Angiboust et al. 2012), as well as the distribution of intermediate-depth intraslab earthquakes (Kirby et al. 1996, Hacker et al. 2003, Abers et al. 2006, Kita et al. 2006) and possibly episodic tremor and slip events (Obara 2002, Seno and Yamasaki 2003).

Knowledge of the processes and effects of fluids in subduction zones comes from geochemical studies of arc lavas, numerical models, high-pressure laboratory experiments, and geophysical imaging. The geochemical compositions of arc lavas have been used to evaluate the relative mobility of elements during subduction-related metamorphism. For example, the enrichment of the large ion lithophile elements (LILE) and light rare earth elements (LREE) in arc lavas is thought to result from fluid-mediated transport of those elements from the slab to the mantle, whereas the relative depletion of the high-field strength elements (HFSE) and heavy rare earth elements (HREE) is commonly attributed to the immobility of these elements in crustal fluids (McCulloch and Gamble 1991, Spandler and Pirard 2013). Experimental studies conducted at P-T conditions relevant to subduction zones, combined with thermal and phase equilibria modeling of subducted lithologies (mantle peridotite, basaltic oceanic crust, pelitic to calcareous seafloor sediments), have been used to determine the stability of high-pressure hydrous phases in these different bulk rock compositions, as well as the locations of the major dehydration reactions occurring in different thermal regimes (warm vs. cool) (Poli and Schmidt 1995, Domanik and Holloway 1996, Schmidt and Poli 1998, Hacker et al. 2003, van Keken et al. 2011). The distribution of hydrous phases in subducted oceanic crust, in particular lawsonite, have also been cited as a potential cause of the low-velocity layers that have been imaged to depths of ~ 150 km in active subduction zones, providing evidence for the transport of water to sub-arc depths and beyond (Fujimoto et al. 2010, Chantel et al. 2012, Reynard and Bass 2014).

Veins containing high-pressure mineral assemblages in high-pressure/low-temperature (HP/LT) rocks from exhumed subduction complexes provide an accessible and complementary record of fluid processes in subduction zones (e.g., Becker et al. 1999, Spandler and Hermann 2006, John et al. 2008, Spandler et al. 2011, Guo et al. 2012). Vein geometry, orientations, and microstructures can provide information about paleofluid transport systems, such as the stress fields during vein formation and variations in the fluid pressure (Passchier and Trouw 2005, Bons et al. 2012), and the major element, trace element, and isotopic composition of vein minerals can provide information on the metamorphic conditions of vein formation (P-T), the timing of fluid flow, as well as the source of the fluids (e.g., Nelson et al. 1991, Philippot and Selverstone 1991, Becker et al. 1999, Rubatto and Hermann 2003, Spandler and Hermann 2006, John et al. 2008, van der Straaten et al. 2008, Beinlich et al. 2010, Spandler et al. 2011, Guo et al. 2012, 2015). Fluid inclusions trapped within vein minerals can also provide information about the composition of fluids and how they evolved during subduction zone metamorphism (Selverstone et al. 1992. Giaramita and Sorensen 1994, Franz et al. 2001, Gao and Klemd 2001, Scambelluri and Philippot 2001).

Rare, but of potentially great significance for understanding the chemical and physical processes of fluids in subduction, are veins that contain lawsonite, a hydrous Ca-Al silicate that is stable over a wide range of depths in subducted oceanic crust. Lawsonite-rich veins or layers have only been described in a few localities: Franciscan, California (Davis 1960, Martin et al. 2014), New Caledonia (George and Grapes 1987); Tavşanlı Zone, Turkey (Davis and Whitney, 2008); and Alpine Corsica (Vitale

Brovarone et al. 2011), although possible lawsonite pseudomorphs have been reported in metamorphic veins from Monviso, Western Alps, Italy (Angiboust et al. 2011) and kyanite + quartz veins from the Dabie-Sulu ultrahigh-pressure terrane, China (Li et al. 2005).

Lawsonite-bearing veins and layers may be important archives of processes and conditions of water and trace element cycling in subduction zones because lawsonite is H_2O-rich (~12 wt.%) and a reservoir for many trace elements (Tribuzio et al. 1996, Ueno 1999, Spandler et al. 2003, Martin et al. 2014, Vitale Brovarone et al. 2014) and transition metals (Fe, Ti, Cr) (Mevel and Kienast 1980, Sherlock and Okay 1999, Ueno 1999, Vitale Brovarone et al. 2014). The bulk rock composition of lawsonite-rich veins and layers also closely approximates the CASH system, which extends the stability field of lawsonite to greater temperatures and pressures than the MORB + H_2O system (Pawley 1994). Therefore, lawsonite-rich veins and layers may serve as an important mechanism for transporting both water and trace elements to significant depths in subduction zones. Furthermore, the ability of lawsonite to incorporate a wide variety of trace elements and preserve compositional zoning may make it a sensitive monitor of changes in the reaction history and fluid sources during fluid-rock interaction (Martin et al. 2014).

In this study, we present a geochemical (bulk rock and mineral major and trace element) study of lawsonite-rich veins and layers from the Sivrihisar Massif, the only region of the Tavşanlı HP/LT Zone that contains lawsonite eclogite (Davis and Whitney, 2006, 2008; Whitney and Davis, 2006). In the lawsonite eclogite-bearing region of the

Sivrihisar Massif, lawsonite-rich veins and layers typically occur along the margins of metabasaltic pods. Two types of lawsonite-bearing veins and layers were analyzed: (1) a ~1 cm wide lawsonite + garnet + phengite-rich layer associated with finely interlayered (mm- to cm-scale) lawsonite eclogite- and blueschist-facies assemblages at the margin of a lawsonite eclogite pod (Davis and Whitney 2008), and (2) a ~5 cm wide, coarse-grained, monomineralic lawsonite vein associated with the epidote- and chlorite-rich margin of a metabasaltic pod. As these two lawsonite-bearing veins and layers preserve and coexist with different mineral assemblages, they may provide information about the chemical changes associated with fluid-rock interaction during the lawsonite eclogite-blueschist transition, as well as during retrograde metamorphism. These results provide insights into fluid-related processes as recorded by oceanic crustal rocks deformed and metamorphosed near the slab-mantle interface in the deep forearc (80-45 km) of a subduction zone.

2. Geology of the Sivrihisar Massif

The Sivrihisar Massif (Kulaksız 1978, Gautier 1984, Whitney 2002, Davis and Whitney 2006, 2008, Whitney and Davis 2006, Çetinkaplan et al. 2008, Seaton et al. 2009, 2014; Okay and Whitney 2010, Teyssier et al. 2010, Davis 2011, Whitney et al. 2011, 2014) is part of the Tavşanlı Zone, a Late Cretaceous paleosubduction zone exposed in northwest and south central Turkey, just south of the Izmir-Erzincan-Ankara suture (Figure 1a). The Sivrihisar Massif is comprised of a structurally coherent sequence of lawsonite blueschist and eclogite facies metabasaltic and metasedimentary rocks. The entire sequence is bounded to the north by a fault contact that juxtaposes HP/LT

metabasalts and metasedimentary rocks with a metamorphosed ultramafic-mafic complex containing serpentinite, diabase dikes, and (meta)gabbro (Teyssier et al. 2010, Whitney et al. 2014; Figure 1b). Locally, meter-scale slivers of antigorite serpentinite are incorporated into the high-pressure rocks; the contact between the two is a lawsonite + chlorite-rich reaction zone (Zack 2013, Whitney et al. 2014).

Blueschist facies metabasalts record P-T conditions of 1.2 – 1.6 GPa and 380 – 500 °C, although some blueschists record higher pressure conditions, similar to those of spatially- associated eclogite (Davis and Whitney 2006, 2008, Çetinkaplan et al. 2008). Peak metamorphic conditions for lawsonite eclogite, which occurs as 5 cm- to 3.5 m-long lens shaped pods hosted in lawsonite blueschist and in blueschist- and eclogite-facies metasedimentary rocks, are estimated at 500 – 550 °C and 2.4 – 2.6 GPa (Davis and Whitney 2006, 2008, Whitney and Davis 2006). Comparison of the P-T conditions recorded by lawsonite eclogite from the Sivrihisar Massif with estimates of slab-surface temperatures in modern subduction zones (e.g., Syracuse et al. 2010) indicates that the ~2.5 GPa, 550°C eclogites were likely metamorphosed at the slab-mantle interface (Teyssier et al. 2010, Whitney et al. 2014); this interpretation is consistent with high-pressure fabrics in the rocks, including a mylonite zone near the northern tectonic contact.

The presence in the interlayered metasedimentary rocks (quartzite, calc-schist) of HP minerals such as omphacite, glaucophane, garnet, lawsonite, phengite, and epidote-group minerals (e.g, piemontite in quartzite), as well as the columnar texture of calcite in marble (interpreted as pseudomorphs after aragonite, Seaton et al. 2009, 2014; Whitney

et al. 2014) is additional evidence that the entire sequence was metamorphosed at lawsonite blueschist- to eclogite-facies conditions. At least some of the blueschist formed from retrogression of eclogite during exhumation, as indicated by garnet zoning and glaucophane rims on omphacite (Davis and Whitney 2006, 2008; Whitney et al. 2014).

Lawsonite-rich veins and layers may also record different stages of the subduction and exhumation history, from lawsonite + garnet + phengite-rich layers that appear to be associated with the transition between eclogite and blueschist facies metamorphism to monomineralic lawsonite veins associated with the latest preserved stages of retrogression. (Note: We use the term 'layer' to refer to a lawsonite-rich rock that is concordant with lithological layering; 'vein' refers to a cross-cutting feature.) The lawsonite + garnet + phengite-rich layer analyzed in this study was collected from the margin of a lawsonite eclogite pod (Figure 2) that was previously studied for P-T conditions (Davis and Whitney 2008) and age of HP/LT metamorphism (Lu/Hf garnet-lawsonite: Mulcahy et al. 2014). However, the origin of this and other lawsonite-rich veins and layers and their significance for the fluid-rock history (if any) have not previously been studied. In the following sections, we describe petrologic, geochemical, and microstructural features of two representative lawsonite-rich veins and layers and associated HP rocks.

3. Methods

Two representative lawsonite-rich assemblages were collected for chemical and textural analysis (Figure 1; Supplementary Material 1). One is a lawsonite + garnet + phengite layer (SV03-103C) from the margin of a lawsonite eclogite pod hosted in

lawsonite blueschist and calc-schist (Figure 2a). Four different parts of the lawsonite eclogite pod were studied in order to document compositional changes from the core of the pod to its margin, where the lawsonite-rich layer is located: the lawsonite eclogite pod core (SV12-13E)), the lawsonite eclogite pod margin (SV03-103A), the glaucophane-rich margin that borders the lawsonite + garnet + phengite-rich layer (SV03-103B), and the lawsonite + garnet + phengite-rich layer (SV03-103C) (Figure 2). The eclogite core (SV12-13E) was sampled from the core of the lawsonite eclogite pod studied in detail by Davis and Whitney (2008), and a sample of the lithologically complex pod margin containing lawsonite eclogite, the lawsonite-rich layer, and the associated glaucophane-rich margin (SV03-103) was provided by P.B. Davis. The other sample analyzed is a monomineralic lawsonite vein (SV12-24B) that was collected from a retrogressed, chlorite + epidote-rich pod margin (Figure 2b). Bulk rock major and trace element analyses were acquired for both lawsonite-rich lithologies and the host rock(s) associated with the lawsonite + garnet + phengite layer (SV03-103C). Mineral major and trace element compositions were obtained for the primary mineral phases within the lawsonite + garnet + phengite layer and its associated host rocks.

3.1 Analysis of Whole-Rock and Mineral Compositions

To characterize the composition of the lawsonite-rich veins and layers, major and trace element abundances were determined for whole-rock samples by ICP-OES (major elements) and ICPMS (trace elements) (Table 1), and for minerals (garnet, lawsonite, omphacite, phengite, glaucophane, and rutile) within the lawsonite + garnet + phengite –

rich layers and associated host rocks by electron microprobe and LA-ICPMS (Tables 2-13).

3.1.1 Bulk Rock Major and Trace Element Analysis

Bulk rock major element analyses for the monomineralic lawsonite vein (SV12-24B) and 4 samples from a compositional traverse across the fresh lawsonite eclogite pod were conducted at the Department of Earth Sciences, University of Minnesota. Trace element analyses were conducted by Activation Laboratories in Canada

To obtain bulk compositional analyses for lithologic layers at the eclogite pod margin (SV03-103), individual layers were sawed out and then crushed and powdered. Given the small width of the layers (~ 3 – 5 mm) and the gradational boundary between the eclogite (SV03-103A) and glaucophane-rich margin of the lawsonite-rich layer (SV03-103B), it is possible that some powders contain small portions of other lithologic layers. It is also worth noting that trace and rare earth element-rich accessory phases (apatite, allanite, rutile, zircon) are heterogeneously distributed within the layers, so the small volumes of powders analyzed may not be representative. Nonetheless, the results provide a first-order estimate of the compositions for these three regions of the pod, and are useful for comparison.

3.1.2 Mineral Major Element Analysis by Electron Microprobe (EMP)

Mineral major element compositions were determined with a JEOL JXA-8900 electron microprobe in the Department of Earth Sciences at the University of Minnesota. For hydrous mineral phases, quantitative microprobe analyses (wavelength dispersive spectroscopy) were performed with a 15-kV accelerating voltage, 15 nA beam current,

and a defocused 5 μm beam diameter to minimize Na and K loss and beam damage to minerals. For anhydrous mineral phases, microprobe analyses were performed with a 15-kV accelerating voltage, 20 nA beam current, and a focused 1 μm beam diameter. Natural mineral standards were used in calibrations. O and OH were calculated by cation stoichiometry and included in the ZAF matrix corrections. X-ray element maps were acquired using a 15-kV accelerating voltage, 100 nA beam current, a focused beam, and stage-rastering step sizes ranging from 1 to 5 μm depending on mineral grain size.

3.1.3 Mineral Trace Element Analysis by LA-ICPMS

The trace element composition of minerals determined by *in situ* laser ablation inductively coupled plasma mass spectrometry (LA-ICPMS) at the Research School of Earth Sciences at the Australian National University. Trace elements were measured on an ArF excimer laser coupled to a quadrupole ICPMS Agilent 7700, using the set-up described in Eggins et al. (1998). The laser was tuned to a frequency of 5 Hz and an energy of 50 mJ (corresponding to an HV of around 26 – 27 kV), with spot sizes ranging from 28 μm to 47 μm in diameter depending on the size of the grain and compositional zoning features. Counting times were 20 s for the background and 50 s for sample analysis. The internal element used to quantify the analyses was Ti for rutile, and Si for garnet, omphacite, lawsonite, glaucophane, and phengite.

The NIST 610 glass was used as a primary standard for rutile. For silicate minerals, the NIST 612 glass was used as a primary standard, and the BCR-2G glass was used as a secondary standard. Trace element analyses of some minerals were compromised by abundant inclusions of rutile, zircon, and allanite; however, the effects

of these inclusions on the analysis were removed manually by examining the time-resolved spectra for each analysis prior to data reduction. The data were reduced with the freeware Iolite (Paton et al. 2011) and its data reduction scheme for trace elements (Woodhead et al. 2007). Accuracy and reproducibility of the secondary standard were generally within 10% of the reference value.

3.2 Microstructural Analysis of Lawsonite-rich Veins Layer and Associated Host Rock

X-ray Computed Tomographic (XRCT) scans of the core of the lawsonite eclogite pod (SV12-13E) and the compositionally layered pod margin (SV03-103A, B, C) were obtained to examine the distribution of garnet and high-density accessory phases (rutile, zircon) in the different lithologic layers of the pod to help evaluate petrogenesis of the lawsonite + garnet + phengite-rich layer. A cylindrical core (30 mm in height x 25 mm in diameter) cut from a hand sample of the core of the lawsonite eclogite pod (SV12-13E) and a rectangular billet (25 x 42 x 11 mm) of the compositionally layered pod margin (SV03-103) were scanned using the North Star X5000 instrument at the University of Minnesota XRCT Laboratory in the Department of Earth Sciences. The cylindrical core from the core of the lawsonite eclogite pod was scanned at 170 kV and 19.0 W and the billet from the margin of the pod was scanned at 150 kV and 21.0 W to optimize the contrast between the garnet and high-density accessory phases (rutile, zircon) and the matrix. Avizo Fire (version 9) was used for image processing and quantitative measurements (e.g., number of particles, particle volume) of the garnet and oxide crystals. Additional details about the analytical methods are supplied in Supplementary Material 2.

4. Petrography and Microstructures of the Lawsonite-rich Layer and Associated Host Rock

Lawsonite eclogite from the core of the pod (SV12-13E) is composed of omphacite + garnet + lawsonite + phengite + rutile, with texturally later glaucophane and minor amounts of epidote-group minerals. Apatite, florencite and zircon are present as accessory phases, and titanite forms rims on some rutile grains. Modal abundances of garnet, omphacite, lawsonite and phengite vary within the sample at the thin section (cm-) scale, with some regions containing more omphacite and garnet (Figure 3a), and other regions containing more phengite and lawsonite (Figure 3b), although these regions do not form distinct layers or compositional bands. XRCT imaging of the lawsonite eclogite pod core confirms variations in the modal abundance of garnet in the sample, and suggests that there may also be spatial variations in the concentrations of accessory phases within the sample (Figure 4). However, as the orientation of the XRCT core with respect to the pod margin is not known, we are unable to assess any systematic changes in pod core mineral assemblage with respect to the pod margin.

Garnet from all regions of the eclogite pod core is fractured, subhedral and has a diameter ranging from 0.2 mm to 1.0 mm. Garnet typically contains numerous inclusions of epidote ± white mica ± quartz ± zircon ± rutile (Figure 3c). Although quartz is a common inclusion in garnet, it does not occur as a matrix phase in any of the analyzed samples. Rutile from the core of the pod is generally coarse-grained and elongate (Figure 3d).

Two types of lawsonite textures are observed in the core of the lawsonite eclogite pod: (1) polycrystalline lawsonite that is dispersed throughout the omphacite + garnet matrix and that contains numerous high-angle (> 10°) grain boundaries (Figure 3e, f), and (2) euhedral to subhedral lawsonite that is ~ 300 – 500 μm in length and is typically found in phengite-rich regions (Figure 3g). The former is the most common texture of lawsonite in the core of the pod. Despite these differences, both textural types of lawsonite contain abundant inclusions of epidote, glaucophane, and zircon.

Omphacite in the omphacite + garnet rich regions tends to be relatively equant, whereas omphacite in the phengite + lawsonite regions tends to be more elongate (~1.0 mm in length x 0.10 mm in width). Glaucophane, which appears to be a texturally late phase, is zoned, with pale blue cores and darker blue rims in plane-polarized light (Figure 3h).

The margin of the eclogite pod is characterized by finely interlayered (cm-scale) lawsonite eclogite and blueschist facies assemblages, as well as the studied lawsonite + garnet + phengite vein (Figure 5). Eclogite at the margin of the pod (SV03-103A) consists of omphacite + garnet + lawsonite + phengite, with accessory epidote (with allanitic cores) and rutile (Figure 5a-d). In the eclogite layers at the pod margin, there appear to be two distinct garnet populations: (1) subhedral, inclusion-rich (quartz ± epidote ± white mica ± zircon) garnets, with diameters of ~ 0.90 – 1.45 mm (Figure 5b), and (2) smaller (~0.3 mm) euhedral to subhedral, inclusion-poor garnets (Figure 5c). The XRCT-derived dataset confirms the presence of garnets of different sizes in this layer (Figure 4, Supplementary Material 3). Omphacite in the pod margin eclogite is coarse-

grained (ranging from 0.5 to 1.0 mm in length), and zoned, with pale green cores and darker green rims in plane-polarized light. Omphacite typically lacks inclusions, but some omphacite cores contain quartz inclusions that are surrounded by radial fractures, as well as fine-grained inclusions of white mica ± epidote ± zircon; some omphacite rims also contain white mica inclusions (Figure 5a). Lawsonite is coarse-grained (1 – 1.3 mm in length) and forms euhedral to subhedral, blocky shapes. Compared to lawsonite in eclogite in the core of the pod (e.g., Figure 3f, g), lawsonite in pod-margin eclogite is inclusion-poor (containing only sparse inclusions of epidote and zircon), and is not polycrystalline (Figure 5b, c).

The glaucophane-rich margin (SV03-103B) adjacent to the lawsonite-rich layer consists of glaucophane + garnet + lawsonite, minor amounts of phengite and epidote (with allanitic cores), and accessory rutile (Figure 5d-f). It has a gradational boundary with the eclogite, characterized by decreasing amount of glaucophane over the scale of 1 – 2 mm (Figure 2a, inset). In contrast to the core of the lawsonite eclogite pod (SV12-13E) and the surrounding lithologic layers at the pod margin, where minerals are typically coarse-grained (≥ ~1 mm), minerals in the glaucophane-rich margin tend have a smaller grain size. For example, garnets are typically ~0.80 mm in diameter, and lawsonite is typically ~0.5 mm in length in the glaucophane-rich margin. Garnet in the glaucophane-rich margin is typically euhedral to subhedral, and contains inclusions of zircon ± quartz ± rutile ± epidote. Lawsonite in the glaucophane-rich margin is euhedral to subhedral, with inclusions of glaucophane ± rutile ± epidote. Phengite is sparse in the glaucophane-rich margin, but when present typically occurs along the flanks of garnets.

Similar to glaucophane from the core of the pod, glaucophane at the pod margin is zoned, displaying pale blue cores and darker blue rims in plane-polarized light (Figure 5d – f).

The transition from the glaucophane-rich margin to the lawsonite + garnet + phengite layer is well defined by an abrupt change in mineral assemblage and grain size (Figure 2a, 5f-h). The lawsonite-rich layer (SV03-103C) consists of lawsonite + garnet + phengite, with minor epidote (with allanitic cores; Figure 5f) and accessory zircon and rutile. Garnet in this layer displays a wide variety of morphologies and sizes: (1) large (~ 5 mm in diameter) subhedral garnet containing fine-grained inclusions in its core and coarse-grained inclusions in its rim (only one observed in the thin section analyzed, in the center of the layer; Figure 5g), (2) euhedral to subhedral garnets (~ 1.0 mm in diameter) containing fine-grained inclusions (Figure 5h), and (3) subhedral to anhedral, heavily fractured garnets (~ 0.5 to 1.5 mm in diameter) that contain coarse-grained inclusions (Figure 5h). Common inclusions in all garnet types include epidote ± white mica ± zircon ± quartz ± rutile. Jagged shards and fragments of garnet are also present throughout the layer. Lawsonite is coarse-grained (0.5 to 1 mm in length), and forms blocky, rectangular shapes. Rutile, epidote, and/or zircon are common inclusions in lawsonite.

5. Bulk Rock and Mineral Composition

5.1 Bulk Rock Major and Trace Element Analyses

The eclogite pod-core (SV12-13E), eclogite pod-margin (SV03-103A), and glaucophane-rich margin (SV03-103B) have similar bulk rock major element compositions, with 49 – 52 wt.% SiO_2, 3 – 4 wt.% Na_2O, and 1 – 2 wt.% K_2O (Figure 6a, b; Table 1). This is consistent with a basaltic protolith. CaO is systematically higher in

the eclogite portions of the pod (~10 – 13 wt. %) than in the blueschist layer (~ 4.5 wt. %), consistent with previous results for coexisting lawsonite eclogite and blueschist from the Sivrihisar Massif (Davis and Whitney, 2006) and elsewhere (Wei and Clarke 2011), although the scale at which the blueschist and eclogite are interlayered is smaller (cm-to-mm scale) for the samples analyzed in this study.

The concentration of TiO_2 is highest in the glaucophane-rich margin owing to a higher modal abundance of rutile. The core of the eclogite pod has the highest concentrations of P_2O_5 (0.60 wt.%), which likely reflects the presence of phosphate-rich accessory phases (apatite, florencite). Compared to the eclogite and blueschist regions of the pod, the lawsonite-rich layer (SV03-103C) has higher Al_2O_3 (21 wt.%) and K_2O (~ 6 wt.%) and lower Na_2O (0.46 wt.%) contents, consistent with the abundance of Al- and K-rich minerals such as lawsonite and phengite, as well as the absence of any major Na-bearing phase.

Results from trace element analyses of the individual lithologic layers from the lawsonite eclogite pod show that, with the exception of V, the glaucophane-rich margin has the highest concentrations of transition metal elements (Cr: 450 ppm, Zn: 220 ppm, Ni: 340 ppm, and Co: 252 ppm) (Table 1, Figure 6,7). Nb concentrations (135 ppm) are also highest in the glaucophane-rich margin and this likely reflects the high modal abundance of rutile. Other high-field strength elements (HFSE), such as Zr and Hf, are relatively enriched in the lawsonite + garnet + phengite layer (Zr 1200 ppm, Hf 27.7 ppm); likely reflecting the high modal abundance of zircon in the vein. The lawsonite + garnet + phengite layer (SV03-103C) also shows increased concentrations of the LILE

(Ba: 678 ppm, Rb: 111 ppm, Cs: 4.9 ppm) (Figure 6, 7); these typically strongly partition into phengite. The concentrations of the REE also vary between the layers, with the lawsonite + garnet + phengite layer (SV03-103C) having the highest concentrations of REE, followed by the eclogite pod core (SV12-13E), the glaucophane-rich margin (SV03-103B), and the pod margin eclogite (SV03-103A) (Figure 6f – h, 7).

Despite variations in the absolute abundance of the REE, chondrite-normalized REE plots from all layers of the lawsonite eclogite pod generally display a similar shape, characterized by an enrichment in the LREE (up to ~ 100 to 500 times chondrite) relative to the MREE and HREE (up to ~ 15 to 35 times chondrite), and a negative Eu anomaly (Figure 7). One notable difference between the layers is the slope of the MREE patterns, with eclogite from the pod margin (SV03-103C) and the glaucophane-rich margin (SV03-103B) displaying complementary patterns (Figure 7a).

As expected, the bulk-rock major element composition of the monomineralic lawsonite vein (SV12-24B) sampled from the chlorite + epidote-rich pod margin is similar to that of pure lawsonite, with 38.00 wt.% SiO_2, 27.92 wt.% Al_2O_3, and 18.93 wt.% CaO (Table 1). Small amounts of FeO* (2.69 wt.%) and TiO_2 (0.13 wt.%) are also present in this vein, consistent with electron microprobe analyses of lawsonite that occurs as a matrix phase in the HP/LT rocks of the Tavşanlı Zone (Davis and Whitney 2006, Martin et al. 2014, Plunder et al. 2015). Despite differences in the mineral assemblages of the two lawsonite-rich samples analyzed, the chondrite-normalized REE patterns for the monomineralic lawsonite vein (SV12-24B) and the lawsonite + garnet + phengite layer (SV03-103C), are similar, both in terms of the REE concentrations and the shape of the

pattern (Figure 7). The REE patterns differ, however, in the absence of a Eu anomaly in the monomineralic lawsonite vein. N-MORB normalized extended trace element patterns also show that the monomineralic lawsonite vein has higher concentrations of V (189 ppm), Co (56 ppm), Sr (740 ppm), Y (90.8 ppm), and Pb (53 ppm) compared to the lawsonite + garnet + phengite layer (Table 1, Figure 7).

5.2 Mineral Major and Trace Element Composition

5.2.1 Garnet

Garnet is present in all parts of the eclogite pod and vein sample (eclogite core/margin, glaucophane-rich margin, lawsonite-rich layer). Garnet in the core of the eclogite pod (SV12-13E) is Fe- and Ca-rich, and is zoned in both major and trace elements (Figure 8). Electron microprobe traverses across garnet grains show a major element zoning pattern characterized by an increase from core to rim of Fe, and Mg, and a decrease in Ca and Mn. A typical garnet from this eclogite has a core composition of $alm_{53}prp_{6}grs_{32}sps_{9}$ and an inner rim composition of $alm_{57}prp_{13}grs_{27}sps_{3}$ (abbreviations for minerals and components after Whitney and Evans, 2010). X-ray element mapping additionally reveals the presence of an oscillatory zoned, Mn-rich outer rim that has a composition of $alm_{58}prp_{6}grs_{28}sps_{8}$, although the spessartine component varies by several weight percent over a distance of <50 μm (Figure 8, Table 2). This compositionally distinct Mn-rich zone is also present along fractures and cracks that intersect the interior portions of the garnets.

Garnet from the core of the eclogite pod displays a REE pattern that is characterized by depletion in LREE (commonly below detection limits) and an HREE

enrichment of up to 100 times compared to chondrite (Figure 8). The outer Mn-rich, oscillatory-zoned rims have even higher HREE concentrations (Dy to Lu, up to 1000 times chondrite) compared with the interior portions (core, mantle/inner rim) of the garnets (Figure 8). In addition to enrichment in HREE, these rims also display increased concentrations of Y and Sc relative to the interior of the garnet (Table 4). The garnet core is enriched in Ti, V, and Zn relative to rim regions (Table 4).

Garnet in eclogite at the margin of the pod varies in size, distribution, and zoning patterns compared to garnet in the pod core; also, as noted in a previous section, there are at least two distinct populations of garnet (large, inclusion-rich; small, inclusion-poor). The large (0.90 – 1.45 mm), inclusion-rich garnets from the eclogite pod margin display growth zoning that mimics that of the garnet interiors in eclogite from the center of the pod, with a core composition of $alm_{54}prp_5grs_{31}sps_{10}$ and an inner rim composition of $alm_{59}prp_{13}grs_{25}sps_2$ (Figure 9, Table 2). Although too small to be analyzed (< 20 μm), a thin, discontinuous Mn-rich rim surrounds large garnets, similar to those observed in garnets from the core of the eclogite pod (Figure 8, 9). However, in contrast to pod-core garnets, which show embayment textures and evidence for internal modification of zoning, large garnets at the eclogite pod margin show no evidence for compositional modification. In contrast to the large garnets, small garnets in the same sample typically lack Mn-rich cores, but display thicker (~ 20 - 30 μm) Mn-rich, Mg-poor rims. Typical core compositions are $alm_{58}prp_9grs_{30}sps_3$, and typical rim compositions are $alm_{52}prp_6grs_{28}sps_{14}$ (Figure 9, Table 2). Rare earth element patterns from the larger garnets are characterized by enrichment in HREE (up to 100 times chondrite) and

depletion in LREE (Figure 9). Garnet cores display higher concentrations of HREE than the mantle or inner rim regions of the garnets; garnet inner rims tend to be enriched in the MREE compared to garnet cores or mantles.

Garnet in the glaucophane-rich margin shows major element zoning patterns similar to those observed in garnet from the eclogite margin and the interior portions of garnet from the eclogite pod core. Garnet core compositions are $alm_{55}prp_{7}grs_{26}sps_{12}$ and rim compositions are $alm_{62}prp_{8}grs_{24}sps_{6}$ (Figure 10a-e; Table 2). X-ray element maps show oscillatory and sector zoning features, and high beam current BSE imaging also display patchy zoning features (Figure 10a-d). REE patterns for garnets in the glaucophane-rich margin are similar to those for garnet in eclogite at the margin of the pod, and display enrichment in HREE and depletion in LREE relative to chondrite (Figure 10f). Garnet cores tend to be enriched in the HREE relative to garnet rims, and garnet rims tend to be enriched in MREE relative to the garnet cores. Compared to garnets from the other lithologic layers, garnets in the glaucophane-rich margin contain, on average, higher Cr contents (≥ 300 ppm) (Figure 11, Table 4).

The large (~5 mm in diameter) garnet in the lawsonite + garnet + phengite layer (Figure 4g) has a core composition of $alm_{71}prp_{1}grs_{18}sps_{10}$ and a rim composition of $alm_{69}prp_{9}grs_{21}sps_{1}$ (Table 3); Fe and Ca display oscillatory zoning near the rim (Figure 12). This change in zoning pattern occurs at the boundary between the garnet core (characterized by abundant fine-grained inclusions) and the fractured, garnet rim (characterized by abundant coarse-grained inclusions) With the exception of the large garnet, all other garnets in the layer display similar major element compositions and

zoning patterns, with core compositions of alm56prp4grs26sps9 and rim compositions of alm64prp10grs22sps1 (Figure 12, Table 3). Similar to garnets in the glaucophane-rich margin, high contrast BSE imaging reveals complex (patchy) internal zoning patterns that are truncated by a thin, discontinuous Mn-rich rim. REE patterns for garnets from this layer are similar to the REE patterns of garnets from the other lithologic layers at the pod margin, with relatively more HREE-enriched cores and MREE enriched inner rims. The cores of garnets from the lawsonite + garnet + phengite layer have elevated Cr contents (≥ 300 ppm), similar to those observed in the glaucophane-rich margin, whereas the rims tend to contain little to no Cr. The Cr-poor garnet rims tend to be enriched in Zn (≥ 100 ppm, Figure 11b).

5.2.2 Omphacite

Omphacite is present in both the core of the lawsonite eclogite pod (SV12-13E) and in eclogite layers at the margin of the pod (SV03-103A). Omphacite in the core of the lawsonite eclogite pod (SV12-13E) displays patchy zoning, with irregular variations in Al, Mg, Ca, and Na (Figure 13a, Table 5). Jadeite content ranges from 0.19 – 0.22 (light regions in BSE) to 0.30 – 0.38 (dark regions in BSE) (Figure 13a, b, Table 5). Lighter colored regions in BSE imaging also have higher diopside components (0.62) compared to darker colored regions in BSE (0.48 – 0.54). The aegirine component is relatively constant across the omphacite grains (0.14 – 0.16).

Omphacite from the margin of the pod (SV03-103A) displays core-to-rim zoning (Figure 13c). Cores (X_{jd} = 0.38 – 0.46) have higher jadeite content than rims (0.28 – 0.32). In contrast to omphacite in the core of the eclogite pod, omphacite in eclogite at

the pod-margin has a constant diopside component (0.50 – 0. 53) but displays variations in the aegirine component, with higher values at the rim (0.15 – 0.22) than in the core (0.03 – 0.08). Mn content also appears to be slightly elevated in the rims (0.11 – 0.22 wt.% MnO) compared to the cores (0.02 – 0.07 wt.% MnO) (Figure 13b, Table 5).

Trace element content in omphacite is generally low, consistent with analyses of clinopyroxene from other HP/LT terranes (Zack et al. 2002, Spandler et al. 2003, Spandler and Hermann 2006, Xiao et al. 2013). Nonetheless, intra-grain trace element zoning in Li, Ni, and the REE was observed in omphacite from the margin of the eclogite pod (Table 6). Omphacite cores have higher Li (~90 – 130 ppm) and Ni (100 – 150 ppm) contents than the rims (Li = 5 – 71 ppm, Ni = 63 – 75 ppm) (Table 6). Although the spot size used for omphacite trace element analyses (47 μm) was too large to resolve intra-grain trace element zoning in omphacite from the core of the eclogite pod, variations in trace element content between pod-core and pod-margin omphacite can be discerned (Figure 13d, e). Pod-core omphacite tends to have higher Mn (>1100 ppm) and Y (2.8 – 4.7 ppm) contents than pod-margin omphacite (Mn contents range from 200 – 900 ppm, Y contents range from 0.73 – 2.5 ppm) (Table 6). Chondrite-normalized REE patterns of omphacite from the core of the eclogite pod, although low, show enrichment in HREE compared to omphacite from the pod margin (where many of the REE are below detection limits). Zn content, however, is typically higher in omphacite from the eclogite margin (Zn = 107 – 160 ppm) than in omphacite from the core of the pod (Zn = 62 – 74 ppm) (Table 6).

5.2.3 Glaucophane

Glaucophane is present in both the core of the eclogite pod (SV12-13E) and in the blueschist-facies margin (SV03-103B) adjacent to the lawsonite-rich layer, and is compositionally classified as glaucophane. Glaucophane from the core of the lawsonite eclogite pod is texturally late relative to omphacite and displays core-to-rim zoning that may have experienced post-crystallization modification, as indicated by patchy zoning in the glaucophane cores and the fact that the cores are not always symmetric with respect to glaucophane grain boundaries (Figure 14a). Cores are Al_2O_3 rich (9 – 11 wt.%) and FeO* poor (9 – 12 wt.%) compared to rims (Al_2O_3 wt.% = 5 – 6, FeO* wt.% = 13 – 15); rims also contain higher concentrations of MnO (0.23 – 0.36 wt.%) (Table 7). Calculation of the Fe^{2+}/Fe^{3+} content assuming 13 cations and 23 oxygens suggests that the cores of the glaucophane contain less Fe^{3+} than the rims (Figure 14b).

Glaucophane in the glaucophane-rich margin generally displays core-to-rim zoning, with some elements, such as Mn, displaying oscillatory zoning at the rims (Figure 14c). Some grains, however, display patchy zoning and truncation of zoning features at grain boundaries. Similar to glaucophane from the core of the eclogite pod, cores are Al_2O_3 rich (10 – 11 wt.%) and FeO* poor (10 – 12 wt. %) compared to rims (Al_2O_3 wt. % = 7 – 9, FeO* wt. % = 12 – 15) (Table 7, Figure 14b).

With the exception of the transition metals, the concentration of many trace elements in the analyzed glaucophane is below detection level. Glaucophane from the margin of the eclogite pod displays core-to-rim zoning in some trace elements, with cores containing higher concentrations of Cr (~ 300 – 400 ppm), V (~80 ppm), Ni (1200 – 1300

ppm), and Zn (550 – 600 ppm) than the rims (Cr = ~75 ppm, V = ~ 60 ppm, Ni = ~450 ppm, Zn = 350 – 375 ppm) (Table 8). Similar to observations from major element analyses of glaucophane rims from eclogite in the core of the pod, glaucophane rims in the blueschist margin have higher Mn contents (cores = 260 – 350 ppm, Mn rims = 480 – 550 ppm).

Glaucophane from the core of the eclogite pod has higher concentrations of Mn and V than glaucophane at the pod margin (pod core: Mn ~600 – 800 ppm, V ~100 – 125 ppm; pod margin: Mn ~300 – 630 ppm, V ~55– 120 ppm). Zn concentrations, however, are higher and more variable in glaucophane from the margin of the pod (300 – 600 ppm) than in the pod core (225 – 270 ppm) (Table 8).

5.2.4 Lawsonite

Lawsonite is present in all analyzed samples (pod-core eclogite, pod-margin eclogite, glaucophane-rich margin, lawsonite-rich layer). Although two texturally different types of lawsonite are present in the core of the eclogite pod, both lawsonite types display similar major and trace element compositions. Lawsonite from the core of the eclogite pod deviates from the ideal composition, and contains FeO* (~1.2 – 1.5 wt. %), Ti (375 – 4000 ppm), and Cr (200 – 400 ppm). With the exception of Ti, which displays complex and irregular zoning that varies from grain to grain, no other significant major element zoning is observed (Figure 15, Table 9). Chondrite-normalized REE concentrations in lawsonite from the eclogite pod core vary by 1 – 2 orders of magnitude (1 – 100 times chondrite) and show varying degrees of enrichment in the LREE to MREE, even within a single grain. There does not appear to be any correlation between

variations in REE concentrations and the spatial position of the analysis (i.e., core vs. rim) or Ti concentration.

Lawsonite from eclogite at the pod margin also does not display strong major element zoning, with the exception of irregular Ti and Fe zoning. Ti-rich regions of the lawsonite contain 1750 – 4200 ppm Ti, whereas Ti-poor regions of the lawsonite contain only 350 – 375 ppm Ti. Fe and Cr contents vary little across individual grains, with FeO* contents ranging from 1.0 – 1.6 wt. % and Cr contents ranging from 30 – 150 ppm (Figure 16, Table 9). Although lawsonite from the eclogite pod margin displays similar chondrite-normalized REE concentrations as lawsonite from the pod core, ranging from 1 – 100 times chondrite, the REE patterns overall tend to be more flat.

Lawsonite in the glaucophane-rich margin displays core-to-rim zoning in Fe, with relatively Fe-poor cores (0.80 – 1.0 wt. % FeO*) and Fe-rich rims; Fe-rich rims display oscillatory zoning with variations in FeO* content ranging from 1.10 – 1.5 wt. % (Figure 17). Lawsonite in the glaucophane-rich margin also displays oscillatory Cr zoning, with variations in the Cr_2O_3 content ranging from 100 – 1100 ppm. Variations in TiO_2 concentrations are also observed, but are irregular (Figure 17); intragrain variations in Ti content range from ~300 – 2600 ppm (Table 9). Similar to lawsonite from the eclogite pod core, chondrite- normalized REE patterns show intra- and intergrain REE concentrations ranging from ~ 1 – 100 times chondrite, and variable enrichments in the LREE and MREE relative to the HREE (Figure 17).

Lawsonite in the lawsonite + garnet + phengite-rich layer displays core-to-rim zoning in Fe, with Fe-poor cores (~0.5 wt. % FeO*) and Fe-rich rims; Fe-rich rims

display oscillatory zoning with variations in FeO* content ranging from 0.8 – 1.5 wt. % (Figure 18). Fe-poor cores also tend to be Mn-poor (~ 8 ppm Mn) compared to Fe-rich rims (~ 20 ppm Mn). Weakly developed oscillatory Cr zoning is present in lawsonite located directly adjacent to the glaucophane-rich margin, but is not observed in lawsonite from the more interior regions of the lawsonite + garnet + phengite layer; this lawsonite contains little to no Cr (< 100 ppm). Faint Ti sector zoning is observed in lawsonite from all regions of the lawsonite vein; Ti-rich sectors contain 1170 - 3060 ppm Ti, whereas Ti-poor sectors contain < 950 ppm Ti (Table 9). Compared to lawsonite from other layers in the pod, lawsonite from the lawsonite-rich layer shows less intra- and intergrain variability in both the concentration and shape of the chondrite-normalized REE patterns, with REE concentrations ranging from 10 – 100 times chondrite and REE patterns characterized by an enrichment in the LREE compared to the HREE and a negative Eu anomaly (Figure 18). One lawsonite grain from the boundary between the glaucophane-rich margin and the lawsonite-rich layer, however, displays a shift in the Eu anomaly from positive in the core to negative in the rim and is accompanied by an increase in REE concentrations (and FeO* content) (Figure 18a, c).

A comparison of the trace element concentrations in lawsonite from the different pod regions analyzed shows that lawsonite in the core of the pod has the highest Sr (1000 – 1600 ppm), Pb (25 – 45 ppm), and V (250 – 450 ppm) contents. Although Sr and Pb contents in lawsonite from all regions of the pod margin (eclogite, glaucophane-rich margin, and lawsonite-rich layer) do not vary much, ranging between 400 – 800 ppm Sr and 10 -25 ppm Pb, V contents in lawsonite show a decrease from concentrations of ~

250 – 400 ppm V in the pod margin eclogite and glaucophane-rich margin to concentrations of ≤ 250 ppm in the lawsonite-rich layer. Cr contents in lawsonite appear to be highest in the blueschist-rich margin and in some lawsonite grains at the lawsonite-rich layer-blueschist margin contact (Figure 19, Table 10).

5.2.5 Phengite

Phengite from the core of the eclogite pod (SV12-13E) and from the lawsonite + garnet + phengite layer (SV03-103C) was analyzed for major and trace elements. Pod-core phengite is weakly zoned, with variations in Si and Fe at the rims and along the cleavage planes of some grains; in some cases this zoning is truncated at the grain boundary. The Si content for pod-core phengite ranges from 3.45 – 3.52 p.f.u, although some phengite inclusions in garnet have higher Si contents (~ 3.67 p.f.u.). Zircon and epidote commonly occur as inclusions in phengite.

Phengite in the lawsonite + garnet + phengite layer displays core-to-rim zoning: cores are Na-rich (~ 1 wt.%), Ti-rich (~0.5 wt.%), and Fe-poor (~2.4 wt.%) compared to rims that are Na-poor (~0.10 – 0.15 wt.%), Ti-poor (~0.10 – 0.20 wt.%), and Fe-rich (~ 3.5 wt.%). Phengite also shows a core-to-rim increase in Si content, from 3.22 – 3.32 Si p.f.u. in the cores to 3.38 – 3.50 near the rims (Table 11, Figure 20). Phengite inclusions in garnet, which occur in the outermost fractured portions of the larger garnets, are not zoned and tend to have similar Si contents, paragonite contents, and Mg# as phengite rims in the vein.

Trace element analyses of phengite from the core of the pod (SV12-13E) and in the lawsonite-rich layer (SV03-103C) show that phengite from the lawsonite + garnet +

phengite layer generally has higher Ba contents than phengite in the eclogite core of the pod. Cs concentrations in phengite from both the eclogite pod core and the lawsonite-rich layer are similar, although phengite from the lawsonite + garnet + phengite layer displays a greater variability in Cs content (Figure 20). Similar to compositional trends observed in other minerals from the pod margin (e.g., garnet, glaucophane, omphacite, rutile), phengite in the lawsonite-rich layer contains higher concentrations of Zn and Nb than phengite in the core of the eclogite pod.

5.2.6 Rutile

Rutile is present in both the pod core and the pod margin, but is most abundant in the glaucophane-rich vein-margin (SV03-103B) and in the portions of the lawsonite + garnet + phengite layer that are directly adjacent to the glaucophane-rich margin (Figure 4, Figure 5). In the core of the eclogite pod, rutile occurs both as an inclusion in garnet and as a matrix phase (Figure 3c ,d). Zr concentrations in rutile from the core of the eclogite pod vary widely, ranging from 20 – 150 ppm. There does not appear to be any correlation between measured Zr content and the size of the rutile grain or the textural position of the analysis (core vs. rim, inclusion in garnet vs. matrix grain), although this may be an artifact of the large spot size used for analyses (37 – 47 μm diameter). There is also no correlation between Zr content and whether the analyzed rutile was located in a more lawsonite + phengite-rich region of the matrix or a more omphacite + garnet-rich region. Zr content does, however, correlate with several other measured trace elements, showing a positive correlation with Hf and V contents, and a negative correlation with Mn, Sb, Sn, and W contents (Figure 21).

Given the small size of rutile from the margin of the pod, it was difficult to obtain LA-ICPMS analyses that were not contaminated by adjacent phases or (when present) thin, discontinuous rims of titanite, and the presented results are thus based on only a few grainss (n=4). Zr contents in rutile from the glaucophane-rich margin of the pod vary from 68 – 98 ppm.

Variations in the Nb/Ta and Zr/Hf ratios of rutile from the pod core (SV12-13E) and pod margin (SV03-103B, C) are observed. Rutile from the pod core contains fairly constant Nb/Ta ratios that are close to the chondritic Nb/Ta value of 17.4 (Jochum et al. 2000) but display a spread of measured Zr/Hf ratios that are subchondritic (chondritic Zr/Hf = 36.6, Sun and McDonough 1989) (Figure 21). However, rutile from the pod margin and vein displays a spread in Nb/Ta ratios that is generally superchondritic, and a fairly constant, subchondritic Zr/Hf ratio (Figure 21).

Compared to rutile in the core of the eclogite pod, rutile from the glaucophane-rich margin and lawsonite-rich layer has higher concentrations of Cr (>1500) and Nb (> 8000 ppm), although rutile from all regions of the pod has lower Cr and higher Nb contents than is typically found in rutile from metamafic rocks in other HP/LT terranes (Zack et al. 2004, Triebold et al. 2007, Meinhold et al. 2008; Figure 22) and display Nb/Cr compositions similar to rutile from metapelites.

6. Discussion

In the following sections, (1) evidence is evaluated for the nature of the eclogite protolith, to serve as a basis for understanding possible fluid-mediated changes in the pod-core and at the pod-margin; (2) the composition and zoning of minerals in the

lawsonite-garnet-phengite layer, associated glaucophane-rich margin, and host eclogite are considered in the context of the origin of the layer and the conditions and processes of eclogite-blueschist transformation; and (3) constraints on the possible sources of fluid involved in generation of the lawsonite-rich layers and veins – and in eclogite/blueschist transformation – are discussed. Although the abundant networks of monomineralic lawsonite veins observed at lawsonite-eclogite pod margins and in lawsonite blueschist are important evidence for the presence and pathways of H_2O-rich fluid, we focus mostly on the compositional information in the lawsonite + garnet + phengite layer and its host rocks because this sample's field setting and the layer's more complex mineral assemblage provide a good petrologic context for understanding its origin and significance.

6.1 Protolith

An important first step in evaluating the geochemical changes associated with subduction metamorphism (prograde and retrograde), including possible metasomatic effects of pervasive and/or channelized fluid flow, is identification of the starting composition (protolith). To date, the nature of the protolith for the Sivrihisar rocks has only been known from major element analyses that suggest the protolith for both eclogite and blueschist-facies metabasaltic rocks was likely N-MORB (Davis and Whitney 2006, 2008). Bulk rock major element analyses of the lawsonite eclogite pod core (SV12-13E) and the interlayered lawsonite eclogite and blueschist at the pod margin are also broadly consistent with a basaltic protolith, with 49 – 52 wt.% SiO_2, 3 – 4 wt.% Na_2O, and 1 – 2 wt.% K_2O. This is consistent with trace element data such as eclogite and blueschist

Zr/Hf ratios of ~ 36 – 38 (Table 1), which are similar to Zr/Hf ratios of oceanic basalts (cf. Pfander et al. 2007).

Other trace element abundances, however, suggest either a non-MORB protolith or chemical changes imparted during subduction. For example, the lawsonite eclogite pod core and interlayered lawsonite eclogite and blueschist at the pod margin show LREE-enriched chondrite-normalized patterns (La up to ~ 100 – 500 times chondrite) and are more similar to ocean island basalt (OIB) or "global subducted sediment" (GLOSS) than N-MORB or E-MORB (Figure 7a). N-MORB normalized trace element patterns for pod core and margin rocks also show enrichments in LREE and LILE relative to N-MORB and E-MORB and are similar to OIB, with the prominent exception of some of the fluid mobile elements, such as Cs, Rb, Ba, Sr, and Pb (Figure 7b). Although the observed enrichments in fluid mobile elements such as Cs, Rb, and Ba could also arise from pre-subduction seafloor alteration, the eclogite and glaucophane-rich margin show enrichments in K at constant Ba/Rb, as well as similar enrichment in Ba/Th and K/Th. These data are consistent with HP metasomatism trends rather than seafloor hydrothermal alteration (Bebout 2007).

Collectively, these results point either to an enriched protolith for these rocks (similar to OIB) or, enrichment resulting from mechanical mixing and/or fluid-driven interaction with LREE- and LILE-enriched reservoirs, such as sediments. Indeed, the N-MORB normalized trace element pattern for the average subducted sediment composition (GLOSS II, Plank et al. 2014) shows similar features and trace element concentrations to

the eclogite (SV12-13E, SV03-103C) and blueschist layers (SV03-103B), including enrichments in LILE and positive Pb anomalies (Figures 7a, b).

6.2 Origin of the lawsonite + garnet + phengite layer and glaucophane-rich margin

In HP terranes, veins and segregations containing HP minerals, and metasomatic rocks such as the lawsonitites of Corsica (Martin et al. 2011, Vitale Brovarone et al. 2014), are of interest because they provide information about the composition, transport scale, fluid sources, element solubilities, and extent and nature of fluid-rock reaction in subducted oceanic crust (Becker et al. 1999, Brunsmann et al. 2000, Gao and Klemd 2001, Scambelluri and Philippot 2001, Rubatto and Hermann 2003, Spandler and Hermann 2006, John et al. 2008, Spandler et al. 2011). Nevertheless, these rocks that record fluid-rock interaction have been interpreted in different ways. For example, some veins that contain HP minerals have been interpreted as features inherited from seafloor alteration (Widmer et al. 2000); products of crystallization from fluids during HP metamorphism (Becker et al. 1999); or the result of metasomatic reaction between rocks and fluids derived from local or external sources (Franz et al. 2001, Spandler and Hermann 2006). The occurrence of Al- and Ti-rich phases in veins has been cited as evidence that veins are ‘residues’, but experimental and other studies have shown that these elements are soluble in aqueous fluids under the HP conditions of subduction (Manning 2004), and yielding rutile-bearing veins that formed as a result of prolonged fluid-rock interaction.

In the Sivrihisar Massif, the lawsonite-garnet-phengite layer occurs at the margin of a lawsonite eclogite pod, in a region where some reaction textures suggest that eclogite

was in the process of transforming to blueschist (Davis and Whitney 2008). In addition, the presence of glaucophane-rich assemblages along the margin of the lawsonite + garnet + phengite layer indicates that layer formation may have occurred during the eclogite to blueschist transition. Evidence for a genetic relationship between the host eclogite, glaucophane-rich margin, and the lawsonite + garnet + phengite-rich layer is also suggested by the results of *in situ* UV laser $^{40}Ar/^{39}Ar$ phengite geochronology for this pod, as the range of ages obtained for phengite in each of these layers overlaps within uncertainty, indicating that phengite (re)crystallization in the eclogite pod-core, lawsonite + garnet + phengite rich layer, and associated glaucophane-rich margin was broadly coeval (Chapter 2).

In HP/LT terranes with coexisting blueschist- and eclogite-facies assemblages, blueschists have been interpreted as forming: (1) before eclogite along the prograde path (e.g. Federico et al. 2007); (2) coeval with eclogite owing to differences in bulk composition, H_2O content, or oxidation state (e.g. Barnicoat 1988, Krogh et al. 1994, Bucher et al. 2005, Beinlich et al. 2010, Vitale Brovarone et al. 2011); or (3) after eclogite along the retrograde path (Pognante 1991, Clarke et al. 1997, Och et al. 2003, Anczkiewicz et al. 2004, van der Straaten et al. 2008, Whitney et al. 2014). Based on the spatial and petrographic relationships between blueschist and eclogite assemblages in this pod, it seems unlikely that the blueschist-facies assemblages at the pod margin predated the formation of lawsonite eclogite in the core of the pod, so we consider here the following two scenarios: (1) the lawsonite + garnet + phengite layer formed during the initial stages of decompression, and fluids released by dehydration reactions triggered the

formation of retrograde blueschist-facies assemblages, or (2) the lawsonite + garnet + phengite layer formed at or near peak (lawsonite eclogite facies) P-T conditions and differences in bulk rock composition, either primary (Vitale-Brovarone et al. 2011) or imparted during metamorphism (Beinlich et al. 2010), stabilized different mineral assemblages in the pod-core and pod-margin. To evaluate these possibilities, we compare mineral compositions and zoning patterns for garnet, omphacite, glaucophane, lawsonite, phengite, and rutile in the different compositional layers in the pod (lawsonite eclogite from the pod core and margin, the glaucophane-rich margin and the lawsonite + garnet + phengite layer).

Despite variations in textural positions (pod core vs. pod margin) and mineral assemblages, garnet interiors (core, mantle/inner rim) from both the lawsonite eclogite and glaucophane-rich margin record similar major element zoning trends (core to rim increase in Mg and a core to rim decrease in Mn; Figures 8 – 10, 12) and compositions, inclusion assemblages, and REE patterns (core to rim decrease in HREE concentrations; Figures 8 – 10, 12). This suggests that, at least initially, garnet growth in the eclogite and the glaucophane-rich margin took place under similar P-T conditions on the prograde path. Although prograde-to-peak garnet growth likely took place under similar P-T conditions, the metamorphic environment in which the garnets grew may have been different, as garnets in the glaucophane-rich margin display oscillatory and sector zoning features that are distinct from zoning patterns observed in garnets from the lawsonite eclogite in the pod core and margin.

Trace element systematics in garnet also indicate that the availability of particular elements (Cr, Zn) varied across the layers during garnet growth (Figure 11). Garnets within the glaucophane-rich margin and some garnet cores in the lawsonite + garnet + phengite layer record high Cr contents (> 300 ppm) relative to garnets in the other lithologic layers (< 200 ppm Cr), and the inner rims (i.e., not the late Mn-rich rims) of garnets in the lawsonite + garnet + phengite layer record higher and more variable Zn concentrations (50 – 250 ppm Zn) that are not observed in garnets from other lithologic layers (≤ 100 ppm Zn). As the enrichment in Cr is observed in the cores of the garnets, this suggests that the increased availability of Cr occurred either at or prior to the time of garnet growth.

This relative enrichment in Cr is also documented in other minerals that form part of the glaucophane-rich assemblages at the lawsonite + garnet + phengite layer margin, such as glaucophane, lawsonite, and rutile. Glaucophane cores display high concentrations of Cr, and in some oscillatory zoned glaucophane along the boundary between the glaucophane-rich margin and lawsonite + garnet + phengite layer, these Cr-rich cores are co-enriched in Ni, V, and Zn. Lawsonite within and adjacent to the glaucophane-rich margin also displays oscillatory zoning in Cr that is approximately oppositely correlated with Fe zoning (Figure 17c).

This increased availability of Cr in the glaucophane-rich margin could reflect external addition of Cr to the system via fluids or local breakdown of a precursor Cr-rich mineral. An alternative interpretation of the systematic compositional variations observed at both the bulk rock and mineral scale is that the different assemblages within the pod

developed as a result of pre-existing compositional variations that were inherited from the protolith and not caused by subsequent fluid-rock interaction. This interpretation would also be consistent with evidence that garnet growth in the different lithologic layers likely took place under similar P-T conditions, and that phengite (re)crystallization in all of these layers was coeval.

The chondrite-normalized REE patterns of the individual lithologic layers at the pod margin also suggest that there may be limited evidence for fluid-rock interaction, as the patterns for all of the layers are nearly parallel (Figure 7a), suggesting that there has been little to no fractionation of the REE across the pod, as would be expected if fluid-rock reactions created the different assemblages present at the pod margin and has been documented in other studies of HP vein-selvage-host rock systematics (Spandler and Hermann 2006, John et al. 2008). However, despite the near-parallel REE patterns, LREE / HREE ratios show some variation across the transect from the eclogite pod core to the lawsonite + garnet + phengite layer, with the eclogite pod core, eclogite pod margin, and glaucophane-rich margin displaying nearly identical $[La/Yb]_N$ and $[Ce/Yb]_N$ ratios (~7 – 8 and 6, respectively) but the lawsonite + garnet + phengite-rich layer displaying much higher $[La/Yb]_N$ and $[Ce/Yb]_N$ ratios of 14 and 11, respectively. These ratios are identical to those obtained for the monomineralic lawsonite vein (SV12-24B) from the epidote + chlorite-rich margin of another mafic pod. Trace element ratios of fluid mobile elements to immobile elements with similar geochemical behavior (Sr/Ce, Pb/Ce, U/Th) also show changes across the transect, although in this case, the eclogite pod core shows more evidence for Sr and Pb enrichment (likely owing to aqueous fluid) than the pod margin.

Nonetheless, there is evidence for at least some localized element mobility across the pod.

The presence of oscillatory zoning in Cr in glaucophane and lawsonite in the glaucophane-rich layer-margin also indicates that Cr-enrichment in this zone may have involved a fluid-mediated reaction. It is possible that this involved breakdown of a Cr-rich phase that was also enriched in Ni, V, and Zn (e.g., chromite or spinel), but if so, it is difficult to explain why this only affected the mm-scale glaucophane-rich margin of the lawsonite-garnet-phengite layer. Similarly, protolith heterogeneities would also not explain the contrasting zoning patterns preserved in other minerals across the pod, for example, the presence of Ti sector zoning (indicative of rapid growth) and oscillatory Fe zoning in lawsonite from the lawsonite + garnet + phengite-rich layer (Figure 18) and irregular Fe and Ti zoning in lawsonite from the core of the pod (Figure 15). These observations suggest that although it is possible that there may have been some pre-existing compositional heterogeneity within the eclogite protolith, this cannot explain most of the observed differences in mineral composition and zoning patterns in the lawsonite + garnet + phengite layer, the glaucophane-rich margin, and the host eclogite. Oscillatory zoning and evidence for hydration reactions indicate the importance of fluid-rock interaction in the evolution of the eclogite pod margin, and rule out the possibility that these different assemblages were formed by solid-state transformation of precursor layers in the protolith.

Additional information about the evolution of the pod margin is provided by variations in the Fe^{2+}/Fe^{3+} ratio and other redox sensitive elements. With the exception of

glaucophane, which appears to be a texturally late phase in the core of the eclogite pod, and the Mn-rich oscillatory rims on garnet, which also appear to be a late-stage feature, most phases in the pod-core are unzoned. In contrast, omphacite, glaucophane, lawsonite, and phengite from the pod margin show core-to-rim and/or oscillatory Fe zoning (Figure 13, 14, 17, 18, 20). Estimates of the Fe^{2+}/Fe^{3+} ratio for these phases from mineral stoichiometry suggests an overall increase in Fe^{3+} from core to rim (Table 5, 7, 9).

In addition to Fe zoning, some lawsonite grains that are within the lawsonite + garnet + phengite layer but at its contact with the glaucophane-rich zone display inter- and intragrain variations in Eu anomaly: some grains have a positive Eu anomaly and some have a negative Eu anomaly. In one coarse-grained lawsonite crystal, the change in Eu anomaly occurs within a single grain, such that the Fe-poor core of the grain records a positive Eu anomaly, and the Fe-rich rim records a negative Eu anomaly (Figure 18c). This shift in Eu anomaly also correlates with a change in the REE concentration; from up to 20 times chondrite in the core to up to 85 times chondrite in the rim (Figure 18c).

Intragrain shifts in the Eu anomaly have been previously observed in lawsonite from a metasomatic rock in Alpine Corsica, where the change in Eu anomaly was attributed to growth under blueschist-facies (plagioclase-stable) conditions in the core to eclogite-facies (plagioclase-absent) conditions in the rim (Martin et al. 2011). In our sample, the observed core-to-rim shift in the Eu anomaly is reversed; however, as there is no existing plagioclase in the sample it is unlikely that the change in Eu anomaly is related to the growth of plagioclase under blueschist-facies conditions. The observed shift in the Eu anomaly could also be attributed to a change in oxidation state, as variations in

the Eu anomalies of other minerals (i.e., zircon) have been proposed as monitors of fluctuations in oxidation state (Burnham and Berry 2012, Trail et al. 2012). This interpretation is also consistent with the fact that the core-to-rim shift in the Eu anomaly is accompanied by a core-to-rim increase in Fe, which is likely Fe^{3+} in lawsonite.

Further support for a change in oxidation state at the pod margin is provided by the V contents of the bulk rock, as well as lawsonite and glaucophane, which show a decrease in V contents from the pod core to the pod rim (Figure 6, 19). As V becomes more incompatible with increases in fO_2, the observed decrease in V concentrations from pod core to pod rim at both the bulk rock and mineral scale is consistent with an increase in fO_2 at the pod margin. In igneous environments, the V/Sc ratio may be a more sensitive monitor of variations in redox conditions than V concentrations alone (Li and Lee 2004), as V is multivalent and Sc is homovalent, so only changes in oxidation state should lead to fractionation between these elements. Although bulk rock Sc data were not obtained, V/Sc ratios for lawsonite and glaucophane decrease from pod core to pod rim, also suggesting an increase in fO_2 in the pod margin assemblages. However, further work would be needed to determine whether V and V/Sc ratios could be used as monitors of redox conditions in metamorphic environments as well.

6.3 Fluid sources

Potential fluid sources contributing to fluid-rock interaction near the slab-mantle interface at forearc depths include sediment, seafloor-altered or subduction-metamorphosed oceanic crust, and serpentinized portions of the mantle in the subducting slab and/or overlying mantle wedge. As each of these rock types possesses a distinct

composition, fluids released from each of these reservoirs may impart a different geochemical signature. Differences in the bulk rock compositions may also affect the P-T conditions at which these lithologies undergo devolatilization reactions, potentially leading to variations in the sources of volatiles and trace elements during prograde and retrograde metamorphism. It is therefore a challenge to unambiguously track fluid sources in exhumed subduction complexes, including recognizing mixed fluid sources and changes in source along the P-T path during subduction and exhumation.

Geochemical studies of metamorphic veins hosted in HP/LT rocks have confirmed the diversity of fluid sources, with veins forming from fluids derived from metasediments (e.g., Bebout and Barton 1989, Nelson 1991), serpentinites, and dehydration of the host metabasalt. In some cases, HP/LT veins record complex interactions with multiple fluid sources, both internal (host-rock derived) and external (e.g., Spandler and Hermann 2006, van der Straaten et al. 2008, Spandler et al. 2011, Rubatto and Angiboust 2015).

The interlayering of metabasaltic and metasedimentary rocks, as well as the presence of antigorite serpentinite lenses, in the Sivrihisar Massif (Figure 1b) suggests that these are all potential fluid sources that may have contributed to the formation of HP (lawsonite-rich) layers and veins. The glaucophane-rich layer-margin contains a higher concentration of transition metals (Cr, Zn, Ni, Co) than either pod-core or pod–margin eclogite or the lawsonite + garnet + phengite layer. The increased concentrations of Cr, Co, and Ni in the glaucophane-rich margin show a trend from the eclogite host composition towards the composition of the antigorite serpentinite lenses incorporated

into the HP/LT terrane in the Halilbağı region (Supplementary Material 4), and may therefore indicate interactions with fluids derived from serpentinite. Given the inferred proximity of the HP unit to the slab-mantle interface (Teyssier et al. 2010; Whitney et al. 2014), it is likely that these slivers of serpentinite are from the mantle wedge.

Enrichment of transition metals such as Cr, Zn and Ni also occurred at the grain-scale in the glaucophane-rich layer-margin. Glaucophane cores contain higher concentrations of Cr, Zn, and Ni relative to rims and relative to the texturally late glaucophane in the core of the eclogite pod. In the context of the eclogite pod analyzed in this study, lawsonite within and adjacent to the glaucophane-rich margin consistently records higher levels of Cr than lawsonite from other regions of the pod. Few trace element studies have measured Zn, Ni, and Co concentrations in lawsonite, but the results presented here suggest that it is not a major host for these elements. Lawsonite can, however, incorporate significant amounts (weight percent levels) of Cr into its lattice (Mevel and Kienast 1980, Sherlock and Okay 1999, Vitale-Brovarone et al. 2014), and Cr-rich (3 – 6 wt.% Cr_2O_3) lawsonite has been documented throughout the Tavşanlı Zone (Sherlock and Okay 1999, Davis and Whitney 2006). Lawsonite analyzed in this study does not contain as much Cr, perhaps owing to preferential uptake of Cr by another phase (e.g., allanite) or to the location of the analyzed pod (further from the serpentinite than the Cr-rich lawsonite). It is also possible that lawsonite with higher Cr contents exist in the glaucophane-rich margin but were simply not analyzed in this study. Previous studies of HP/LT veins have shown that effects of fluid-rock interaction can be highly localized (Spandler et al. 2011); this is consistent with observations that only some glaucophane

cores record high Cr and Ni contents. Nonetheless, the important observation is that lawsonite within and adjacent to the glaucophane-rich layer-margin consistently records higher levels of Cr than lawsonite from other layers in the pod. These observations of high transition-element content in glaucophane, lawsonite, and rutile are consistent with enrichment related to layer-formation; i.e., by introduction of these elements in the fluid involved in layer formation and local metasomatism of the adjacent host rock.

Additional information about the composition of the fluid that drove reaction of eclogite can be gained from the distribution of HFSE-bearing accessory phases such as rutile and zircon, as experimental studies have shown that HFSE mobility at HP conditions is strongly affected by fluid composition. For example, rutile solubility has been shown to increase in halogen-bearing and albite-saturated fluids compared to pure H_2O fluids (Antignano and Manning 2008, Rapp et al. 2010), whereas the addition of CO_2 to H_2O-rich metamorphic fluids has been shown to reduce the solubility of rutile (Ayers and Watson 1993).

Evidence for the mobility of HFSE (Ti, Zr, Nb, Hf, and Ta) at HP to ultrahigh-pressure conditions has been documented in many metamorphic terranes, and includes the presence of rutile and zircon in HP veins and metasomatic selvages (Rubatto and Hermann 2003, Gao et al. 2007, Wu et al. 2009) and the presence of rutile in a primary fluid inclusion (Philipott and Selverstone 1991). In the lawsonite + garnet + phengite layer and associated glaucophane-rich margin studied here, evidence for the mobility of Ti, Zr, and other HFSE is also present. XRCT imaging of the pod margin (SV03-103A, B, C) shows that high density, HFSE-rich accessory phases are largely concentrated

within the lawsonite + garnet + phengite layer and glaucophane-rich margin and not in the adjacent lawsonite eclogite (Figure 4). Although we cannot distinguish between zircon and rutile using the XRCT-derived dataset alone, petrographic observations of the distribution of accessory phases and the difference in calculated volumes of the imaged accessory phases suggest that rutile is largely concentrated within the glaucophane-rich margin and zircon is largely concentrated within the lawsonite-rich layer. Bulk rock analyses of the lawsonite + garnet + phengite layer and glaucophane-rich margin also support these interpretations, as the glaucophane-rich margin contains the highest concentrations of TiO_2 and Nb of any analyzed layer, and the lawsonite-rich layer contains the highest concentrations of Zr and Hf (Table 1).

The source of the rutile and zircon components may have been the adjacent lawsonite eclogite at the pod margin (SV03-103A), as it contains a low proportion of accessory phases (Figure 4) and a depletion in elements commonly hosted in rutile and/or zircon, such as Ti, MREE, Zr, and Hf. This interpretation is also supported by the fact that the normalized REE and trace element patterns for the lawsonite eclogite from the pod margin, the glaucophane-rich layer-margin, and the lawsonite-rich layer show complementary relationships for some of these same elements (Figure 7a,b).

Trace element compositions of the rutile also suggest enhanced mobility of the HFSE near the lawsonite-rich layer and margin, with rutile from both having higher Nb concentrations (> 8000 ppm, Table 13) than rutile from the core of the eclogite pod (1600 - 3000 ppm Nb, Table 13). The observation of fluid-enhanced mobility of Nb may have implications for the use of rutile-based protolith discrimination diagrams. The Nb and Cr

content of rutile has been proposed as a tracer of the source lithology of rutile (i.e., rutile formed in metabasaltic rocks versus in metapelites) (e.g. Zack et al. 2004) (Figure 22). Compilations of rutile trace element compositions have shown that rutile from metamafic rocks is generally characterized by low Cr and low Nb concentrations, whereas rutile from metapelites is characterized by low Cr and high Nb concentrations. Although the boundaries for the fields of metabasalt vs. metapelite-derived rutile vary depending on which version of the discrimination diagram is used (Zack et al. 2004, Triebold et al. 2007, Meinhold et al. 2008), rutile from the Sivrihisar Massif consistently plots in the metapelite field, despite being in a mafic rock (Figure 22). This could indicate metasedimentary input via fluids (which then influenced the composition of rutile that crystallized in that layer), or, given the similarity between the chondrite-normalized REE patterns of the eclogite host (SV12-13) and GLOSS, that there was mechanical mixing of metasedimentary lithologies into the mafic rock, resulting in the transfer of detrital rutile grains from the metasediment into the host eclogite. Although we cannot distinguish between these two hypotheses using this dataset alone, caution should be used in interpreting rutile source lithologies based on the Nb and Cr systematics of rutile alone.

7. Conclusions

(1) Bulk rock major element analyses indicate that the host lawsonite eclogite likely had a basaltic protolith, although trace element signatures suggest that it may have experienced interactions (via mechanical mixing and/or fluid-rock interaction) with more enriched reservoirs, such as sediments. Interactions with metasedimentary reservoirs are also documented in the rutile trace element signatures, which record elevated Nb

concentrations and low Cr concentrations, typical of those found in rutile from metapelitic rocks.

(2) Field relations, as well as petrological and geochemical evidence, suggest that the lawsonite + garnet + phengite-rich layer and its associated glaucophane-rich margin likely formed coevally with the host eclogite during prograde to peak metamorphism, as a result of differences in bulk rock composition. The presence of oscillatory and/or sector zoning in minerals (garnet, lawsonite, glaucophane) within the lawsonite + garnet + phengite-rich layer and its adjacent glaucophane-rich margin suggest that these minerals were formed via precipitation from a fluid phase, indicating that the observed variations in bulk rock composition were likely imparted during fluid-rock interaction and not solid-state transformation of a precursor vein or compositional layer.

(3) Lawsonite eclogite immediately adjacent (within ~ 1 cm) to the lawsonite + garnet + phengite-rich layer and its glaucophane-rich margin shows a depletion in REE and HFSE compared to lawsonite eclogite from the pod-core, the glaucophane-rich layer margin, and the lawsonite + garnet + phengite-rich layer, suggesting that these elements may have been mobilized from the lawsonite eclogite at the pod margin to the lawsonite-rich layer and its associated margin. Results from XRCT imaging confirm these findings, showing that MREE- and HFSE-rich accessory minerals, such as zircon and rutile, are concentrated within these layers and depleted in the adjacent lawsonite eclogite.

(4) In addition to mobilizing elements at the pod margin, fluid-rock interaction may have also driven changes in fO_2, as minerals (omphacite, glaucophane, lawsonite, phengite)

from the pod margin record a core-to-rim increase in Fe^{3+} compared to minerals from the pod core.

REFERENCES

Abers GA, van Keken PE, Kneller EA, Ferris A, Stachnik JC (2006) The thermal structure of subduction zones constrained by seismic imaging: Implications for slab dehydration and wedge flow. Earth and Planetary Science Letters 241: 387 – 397.

Antignano A, Manning CE (2008) Rutile solubility in H2O, H2O-SiO2, and H2O-NaAlSi3O8 fluids at 0.7 – 2.0 GPa and 700 – 1000 degrees C: Implications for mobility of nominally insoluble elements. Chemical Geology 255: 283 – 293.

Angiboust S, Agard P, Raimbourg H, Yamato P, Huet B (2011) Subduction interface processes recorded by eclogite-facies shear zones (Monviso, W. Alps). Lithos 127: 222 – 238.

Angiboust S, Wolf S, Burov E, Agard P, Yamato P (2012) Effect of fluid circulation on subduction interface tectonic processes: Insights from thermo-mechanical numerical modeling. Earth and Planetary Science Letters 357 – 358: 238 – 248.

Anczkiewicz R, Platt JP, Thirwall MF, Wakabayashi J (2004) Franciscan subduction off to a slow start: evidence from high-precision Lu-Hf garnet ages on high grade-blocks. Earth and Planetary Science Letters 225: 147 – 161.

Ayers JC, Watson EB (1993) Rutile solubility and mobility in supercritical aqueous fluids. Contributions to Mineralogy and Petrology 114: 321 – 330.

Barnicoat AC (1988) Zoned High-Pressure Assemblages in Pillow Lavas of the Zermatt-Saas Ophiolite Zone, Switzerland. Lithos 21: 227 – 236.

Bebout GE, Barton MD (1989) Fluid-flow and Metasomatism in a Subduction Zone Hydrothermal System-Catalina-Schist Terrane, California. Geology 11: 976 – 980.

Bebout GE (2007) Metamorphic chemical geodynamics of subduction zones. Earth and Planetary Science Letters 260: 373 – 393.

Becker H, Jochum KP, Carlson RW (1999) Constraints from high-pressure veins in eclogites on the composition of hydrous fluids in subduction zones. Chemical Geology 160: 291 – 308.

Beinlich A, Klemd R, John T, Guo J (2010) Trace-element mobilization during Ca-metasomatism along a major fluid conduit: Eclogitization of blueschist as a consequence of fluid-rock interaction. Geochimica et Cosmochimica Acta 74: 1892 – 1922.

Bons PD, Elburg MA, Gomez-Rivas E (2012) A review of the formation of tectonic veins and their microstructures. Journal of Structural Geology 43: 33 – 62.

Brunsmann A, Franz G, Erzinger J, Landwehr D (2001) Zoisite- and clinozoisite-segregations in metabasites (Tauern Window, Austria) as evidence for high-pressure fluid-rock interaction. Journal of Metamorphic Geology 18: 1 – 21.

Bucher K, Fazis Y, De Capitani C, Grapes R (2005) Blueschists, eclogites, and decompression assemblages of the Zermatt-Saas ophiolite: High-pressure metamorphism of subducted Tethys lithosphere. American Mineralogist 90: 821 – 835.

Burnham AD, Berry AJ (2012) An experimental study of trace element partitioning between zircon and melt as a function of oxygen fugacity. Geochimica et Cosmochimica Acta 95: 196 – 212.

Çetinkaplan M, Candan O, Oberhansli R, Bousquet R (2008) Pressure-temperature evolution of lawsonite eclogite in Sivrihisar; Tavşanlı Zone-Turkey. Lithos 104:12 – 32.

Chantel J, Mookherjee M, Frost DJ (2012) The elasticity of lawsonite at high pressure and the origin of low velocity layers in subduction zones. Earth and Planetary Science Letters 349: 116 – 125.

Clarke GL, Aitchison JC, Cluzel D (1997) Eclogites and Blueschists of the Pam Peninsula, NE New Caledonia: a Reappraisal. Journal of Petrology 38: 843 – 876.

Davis GA (1960) Lawsonite and pumpellyite in glaucophane schist, North Berkeley Hills, California, with notes on the X-ray crystallography of lawsonite, by A. Pabst. American Journal of Science 258: 689 – 704.

Davis PB, Whitney DL (2006) Petrogenesis of lawsonite and epidote eclogite and blueschist, Sivrihisar Massif, Turkey. Journal of Metamorphic Geology 24: 823 – 849.

Davis PB, Whitney DL (2008) Petrogenesis and structural petrology of high-pressure metabasalt pods, Sivrihisar, Turkey. Contributions to Mineralogy and Petrology 156: 217 – 241.

Davis PB (2011) Petrotectonics of lawsonite eclogite exhumation: Insights from the Sivrihisar Massif, Turkey. Tectonics 30: doi:10.1029/2010TC002713.

Domanik KJ, Holloway JR (1996) The stability and composition of phengitic muscovite and associated phases from 5.5 to 11 GPa: Implications for deeply subducted sediments. Geochemica et Cosmochimica Acta 60: 4133 – 4150.

Eggins SM, Rudnick RL, McDonough WF (1998) The composition of peridotites and their minerals: a laser ablation ICP-MS study. Earth and Planetary Science Letters 154: 53 – 71.

Franz G, Romer RL, Klemd R, Schmid R, Oberhansli R, Wagner T, Shuwen D (2001) Eclogite-facies quartz veins within metabasites of the Dabie Shan (eastern China): pressure-temperature-time-deformation path, composition of the fluid phase and fluid flow during exhumation of high-pressure rocks. Contributions to Mineralogy and Petrology 141: 322 – 346.

Fujimoto Y, Kono Y, Hirajima T, Kanagawa K, Ishikawa M, Arima M (2010) P-wave velocity and anisotropy of lawsonite and epidote blueschists: constraints on water transportation along subducting oceanic crust. Physics of the Earth and Planetary Interiors 183: 219 – 228.

Gao J, Klemd R (2001) Primary fluids entrapped at blueschist to eclogite transition: evidence from the Tianshan meta-subduction complex in northwestern China. Contributions to Mineralogy and Petrology 142: 1 – 14.

Gao J, John T, Klemd R, Xiong X (2007) Mobilization of Ti-Nb-Ta during subduction: Evidence from rutile-bearing dehydration segregations and veins hosted in eclogite, Tianshan, NW China. Geochimica et Cosmochimica Acta 71: 4974 – 4996.

Gautier Y (1984) Deformations et Metamorphismes Associes a la Fermeture Tethysienne en Anatolie Centrale (Region de Sivrihisar, Turquie. Ph.D. Thesis University Paris-Sud, 236 pp.

George A, Grapes R (1987) Lawsonite-bearing veins in Torlesse rocks. New Zealand Journal of Geology and Geophysics 30: 203 – 205.

Giaramita MJ, Sorensen SS (1994) Primary Fluids in Low-Temperature Eclogites-Evidence from 2 Subduction Complexes (Dominican Republic, and California, USA). Contributions to Mineralogy and Petrology 117: 279 – 292.

Guo S, Ye K, Chen Y, Liu J, Mao Q, Ma Y (2012) Fluid-rock interaction and element mobilization in UHP metabasalt: Constraints from an omphacite-epidote vein and host eclogites in the Dabie orogen. Lithos:145 – 167.

Guo S, Chen Y, Ye K, Su B, Yang Y, Zhang L, Liu J, Mao Q (2015) Formation of multiple high-pressure veins in ultrahigh-pressure eclogite (Hualiangting, Dabie terrane, China): Fluid source, element transfer, and closed-system metamorphic veining. Chemical Geology 417: 238 – 260.

Hacker BR, Peacock SM, Abers GA, Holloway SD (2003) Subduction factory 2. Are intermediate-depth earthquakes in subducting slabs linked to metamorphic dehydration reactions? Journal of Geophysical Research 108: 1 – 16.

Jochum KP, Stolz AJ, McOrist G (2000) Niobium and tantalum in carbonaceous chondrites: constraints on the solar system and primitive mantle niobium/tantalum, zirconium/niobium, and niobium/uranium ratios. Meteoritics and Planet Science 35: 229 – 235.

John T, Klemd R, Gao J, Garbe-Schonberg C-D (2008) Trace element mobilization in slabs due to non steady-state fluid-rock interaction: Constraints from an eclogite-facies transport vein in blueschist (Tianshan, China). Lithos 103: 1 – 24.

Ketcham RA (2005) Computational methods for quantitative analysis of three-dimensional features in geological specimens. Geosphere 1: 32 – 41.

Kirby SH, Engdahl ER, Denlinger RP (1996) Intermediate-depth intraslab earthquakes and arc volcanism as physical expressions of crustal and uppermost mantle metamorphism in subducting slabs. In: Bebout, G.E., Scholl, D.W., Kirby, S.H., Platt, J.P. (Eds.), Subduction top to bottom. American Geophysical Union, Washington, pp. 195 – 214.

Kita S, Okada T, Nakajima J, Matsuzawa T, Hasegawa A (2006) Existence of a seismic belt in the upper plane of the double seismic zone extending in the along-arc direction at depths of 70-100 km beneath NE Japan. Geophysical Research Letters 33: L24310.

Krogh EJ, Oh CW, Liou JG (1994) Polyphase and anticlockwise P-T evolution for Franciscan eclogites and blueschists from Jenner, California, USA. Journal of Metamorphic Geology 12: 121 – 134.

Kulaksız S (1978) Sivrihisar kuzeybatı eklojitleri. Yerbilimleri 4:89 – 94.

Li Z-X A, Lee C-T A (2004) The constancy of upper mantle fO_2 through time inferred from V/Sc ratios in basalts. Earth and Planetary Science Letters 228: 483 – 493.

Li XP, Li YL, Shu GM (2005) Breakdown of lawsonite subsequent to peak UHP metamorphism in the Dabie terrane and its implication for fluid activity. Chinese Science Bulletin 50: 1366 – 1372.

Lu Z, Zhang L, Du J, Yang X, Tian Z, Xia B (2012) Petrology of HP metamorphic veins in coesite-bearing eclogite from western Tianshan, China: Fluid processes and

elemental mobility during exhumation in a cold subduction zone. Lithos 136-139: 168 – 186.

Manning CE (2004) The chemistry of subduction-zone fluids. Earth and Planetary Science Letters 223: 1 – 16.

Martin LAJ, Rubatto D, Vitale Brovarone A, Hermann J (2011) Late Eocene lawsonite-eclogite facies metasomatism of a granulite sliver associated to ophiolites in Alpine Corsica. Lithos 125: 620 – 640.

Martin LAJ, Hermann J, Gauthiez-Putallaz L, Whitney DL, Vitale Brovarone A, Fornash KF, Evans NJ (2014) Lawsonite geochemistry and stability – implication for trace element and water cycles in subduction zones. Journal of Metamorphic Geology 32: 455 – 487.

McCulloch MT, Gamble AJ (1991) Geochemical and geodynamical constraints on subduction zone magmatism. Earth and Planetary Science Letters 102: 358 – 374.

Meinhold G, Anders B, Kostopoulos D, Reischmann T (2008) Rutile chemistry and thermometry as provenance indicator: an example from Chios Island, Greece. Sedimentary Geology 203: 98- 111.

Mevel C, Kienast JR (1980) Chromian jadeite, phengite, pumpellyite, and lawsonite in a high-pressure metamorphosed gabbro from the French Alps. Mineralogical Magazine 43: 979 – 984.

Mulcahy SR, Vervoort JD, Renne PR (2014) Dating subduction-zone metamorphism with combined garnet and lawsonite Lu-Hf geochronology. Journal of Metamorphic Geology 32: 515-533.

Nelson BK (1991) Sediment-derived fluids in subduction zones: Isotopic evidence from veins in blueschist and eclogite of the Franciscan Complex, California. Geology 19: 1033 – 1036.

Obara K (2002) Nonvolcanic deep tremor associated with subduction in southwest Japan. Science 296: 1679 – 1681.

Och DJ, Leitch EC, Caprarelli G, Watanabe T (2003) Blueschist and eclogite in tectonic mélange, Port Macquarie, New South Wales, Australia. Mineralogical Magazine 67: 609 – 624.

Okay AI, Whitney DL (2010) Blueschists, eclogites, ophiolites and suture zones in northwest Turkey: A review and a field excursion guide. Ofioliti 35: 131 – 172.

Passchier CW, Trouw RAJ (2005) Microtectonics. Berlin, Springer Verlag, 366 p., doi:10.1007/3-540-29359-0.

Paton C, Hellstrom J, Paul B, Woodhead J, Hergt J (2011) Iolite: Freeware for the visualization and processing of mass spectrometric data. Journal of Analytical Atomic Spectrometry 26: 2508 – 2518.

Pawley AR (1994) The pressure and temperature stability limits of lawsonite: implications for H_2O recycling in subduction zones. Contributions to Mineralogy and Petrology 118: 99 – 108.

Pfander JA, Munker C, Stracke A, Mezger K (2007) Nb/Ta and Zr/Hf in ocean island basalts – Implications for crust-mantle differentiation and the fate of Niobium. Earth and Planetary Science Letters 254: 158 – 172.

Philippot P, Selverstone J (1991) Trace Element-rich Brines in Eclogitic Veins – Implications for Fluid Composition and Transport During Subduction. Contributions to Mineralogy and Petrology 106: 417 – 430.

Plank T (2014) The Chemical Composition of Subducting Sediments. Treatise on Geochemistry 4: 607 – 629.

Pognante U (1991) Petrological Constraints on the Eclogite-Facies and Blueschist-Facies Metamorphism and P-T-T Paths in the Western Alps. Journal of Metamorphic Geology 9: 5 – 17.

Poli S, Schmidt MW (1995) H2O transport and release in subduction zones: Experimental constraints on basaltic and andesitic systems. Journal of Geophysical Research 100:22,299 – 22, 314.

Rapp JF, Klemme S, Bulter IB, Harley SL (2010) Extremely high solubility of rutile in chloride and fluoride-bearing metamorphic fluids: An experimental investigation. Geology 38: 323 – 326.

Reynard B, Bass JD (2014) Elasticity of lawsonite and seismological signature of metamorphism and water cycling in the subducting oceanic crust. Journal of Metamorphic Geology 32: 479 – 487.

Rubatto D, Hermann J (2003) Zircon formation during fluid circulation in eclogites (Monviso, Western Alps): implications for Zr and Hf budget in subduction zones. Geochimica et Cosmochimica Acta 67: 2173 – 2187.

Rubatto D, Angiboust S (2015) Oxygen isotope record of oceanic and high-pressure metasomatism: a P-T-time-fluid path for the Monviso eclogites (Italy). Contributions to Mineralogy and Petrology 170:doi:10.1007/s00410-015-1198-4.

Scambelluri M, Philippot P (2001) Deep fluids in subduction zones. Lithos 55: 213 – 227.

Schmidt MW, Poli S (1998) Experimentally based water budgets for dehydrating slabs and consequences for arc magma generation. Earth and Planetary Science letters 163: 361 – 379.

Seaton NCA, Whitney DL, Teyssier C, Toraman E, Heizler M (2009) Recrystallization of high-pressure marble (Sivrihisar, Turkey). Tectonophysics 479: 241 – 253.

Seaton NCA, Teyssier C, Whitney DL, Heizler MT (2014) Quartzite and calcite microfabric transitions in a pressure and temperature gradient, Sivrihisar, Turkey. Geodinamica Acta 26: 191 – 206.

Selverstone J, Franz G, Thomas S, Getty S (1992) Fluid variability in 2 GPa eclogites as an indicator of fluid behavior during subduction. Contributions to Mineralogy and Petrology 112: 341 – 357.

Seno T, Yamasaki T (2003) Low-frequency tremors, intraslab and interpolate earthquakes in Southwest Japan-from a viewpoint of slab dehydration. Geophysical Research Letters 30: doi:10.1029/2003GL018349.

Sherlock SC, Okay AI (1999) Oscillatory zoned chrome lawsonite in the Tavşanlı Zone, northwest Turkey. Mineralogical Magazine 63: 687 – 692.

Spandler C, Hermann J, Arculus R, Mavrogenes J (2003) Redistribution of trace elements during prograde metamorphism from lawsonite blueschist to eclogite facies; implications for deep subduction-zone processes. Contributions to Mineralogy and Petrology 146: 205 – 222.

Spandler C, Hermann J (2006) High-pressure veins in eclogite from New Caledonia and their significance for fluid migration in subduction zones. Lithos 89: 135 – 153.

Spandler C, Pettke T, Rubatto D (2011) Internal and External Fluid Sources for Eclogite-facies Veins in the Monviso Meta-ophiolite, Western Alps: Implications for Fluid Flow in Subduction Zones. Journal of Petrology 52: 1207 – 1236.

Spandler C, Pirard C (2013) Element recycling from subducting slabs to arc crust: A review. Lithos 170: 208 – 223.

Sun SS, McDonough WF (1989) Chemical and isotopic systematic of oceanic basalts; implications for mantle composition and processes. In: Saunders, A.D., Norry, M.J., (Eds.), Magmatism in the Ocean Basins. Special Publications of the Geological Society of London, vol. 42, pp. 313 – 345.

Syracuse EM, van Keken PE, Abers GA (2010) The global range of subduction zone thermal models. Physics of the Earth and Planetary Interiors 183: 73 – 90.

Teyssier C, Whitney DL, Toraman E, Seaton NCA (2010) Lawsonite vorticity and subduction kinematics. Geology 38:1123-1126.

Trail D, Watson EB, Tailby ND (2012) Ce and Eu anomalies in zircon as proxies for the oxidation state of magmas. Geochimica et Cosmochimica Acta 97: 70 – 87.

Tribuzio R, Messiga B, Vannucci R, Bottazzi P (1996) Rare earth element redistribution during high-pressure – low-temperature metamorphism in ophiolitic Fe-gabbros (Liguria, northwestern Italy): Implications for light REE mobility in subduction zones. Geology 24: 711 – 714.

Triebold S, von Eynatten H, Luvizotto GL, Zack T (2007) Deducing source rock lithology from detrital rutile geochemistry: an example from the Erzgebirge, Germany. Chemical Geology 244: 421 – 436.

Ueno T (1999) REE-bearing sector-zoned lawsonite in the Sanbagawa politic schists of the eastern Kii Peninsula, central Japan. European Journal of Mineralogy 11: 993 – 998.

Van der Straaten F, Schenk V, John T, Gao J (2008) Blueschist-facies rehydration of eclogites (Tian Shan, NW-China): Implications for fluid-rock interaction in the subduction channel. Chemical Geology 255: 195 – 219.

Van Keken PE, Hacker BR, Syracuse EM, Abers GA (2011) Subduction factory: 4. Depth dependent flux of H2O from subducting slabs worldwide. Journal of Geophysical Resarch 116:B01401, doi:10.1029/2010JB007922.

Vitale Brovarone A, Groppo C, Hetenyi G, Compagnoni R, Malavielle J (2011) Coexistence of lawsonite-bearing eclogite and blueschist: Phase equilibria modelling of Alpine Corsica metabasalts and petrological evolution of subducting slabs. Journal of Metamorphic Geology 29: 583 – 600.

Vitale Brovarone A, Alard O, Beyssac O, Martin L, Picatto M (2014) Lawsonite metasomatism and trace element recycling in subduction zones. Journal of Metamorphic Geology 32: 489 – 514.

Wada I, Wang K, He J, Hyndman RD (2008) Weakening of the subduction interface and its effects on surface heat flow, slab dehydration, and mantle wedge serpentinization. Journal of Geophysical Research 113: doi:10.1029/2007JB005190.

Wei CJ, Clarke GL (2011) Calculated phase equilibria for MORB compositions: a reappraisal of the metamorphic evolution of lawsonite eclogite. Journal of Metamorphic Geology 29: 939 – 952.

Whitney DL (2002) Coexisting andalusite, kyanite, and sillimanite: Sequential formation of three Al2SiO5 polymorphs during progressive metamorphism near the triple point, Sivrihisar, Turkey. American Mineralogist 87:405 – 416.

Whitney DL, Davis PB (2006) Why is lawsonite eclogite so rare? Metamorphism and preservation of lawsonite eclogite, Sivrihisar, Turkey. Geology 34:473-476.

Whitney DL, Evans BW (2010) Abbreviations for names of rock-forming minerals. American Mineralogist 95: 185 – 187.

Whitney DL, Teyssier C, Toraman E, Seaton NCA, Fayon AK (2011) Metamorphic and tectonic evolution of a structurally continuous blueschist-to-Barrovian terrane, Sivrihisar Massif, Turkey. Journal of Metamorphic Geology 29:193 – 212.

Whitney DL, Teyssier C, Seaton NCA, Fornash KF (2014) Petrofabrics of high-pressure rocks exhumed at the slab-mantle interface from the ‘point of no return’ in an oceanic

subduction zone (Sivrihisar, Turkey). Tectonics 33:2315-2341, doi: 10/1002/2014TC003677.

Widmer T, Ganguin J, Thomson AB (2000) Ocean floor hydrothermal veins in eclogite facies rocks of the Zermatt-Saas Zone, Switzerland. Schweizerische mineralogische und petrographische Mitteilungen 80: 63 – 73.

Woodhead JD, Hellstrom J, Hergt JM, Grieg A, Maas R (2007) Isotopic and elemental imaging of geological materials by laser ablation inductively coupled plasma-mass spectrometry. Geostandards and Geoanalytical Research 31: 331 – 343.

Wu YB, Gao S, Zhang HF, Yang SH, Liu XC, Jiao WF, Liu YS, Yuan HL, Gong HJ, He MC (2009) U-Pb age, trace-element, and Hf-isotope compositions of zircon in a quartz vein from eclogite in the western Dabie Mountains: Constraints on fluid flow during early exhumation of ultra high-pressure rocks. American Mineralogist 94: 303 – 312.

Xiao Y, Niu Y, Song S, Davidson J, Liu X (2013) Elemental responses to subduction-zone metamorphism: Constraints from the North Qilian Mountain, NW China. Lithos 160 – 161: 55 - 67.

Zack T, Kronz A, Foley SF, Rivers T (2002) Trace element abundances in rutiles from eclogites and associated garnet mica schists. Chemical Geology 184: 97 – 122.

Zack T, von Eynatten H, Kronz A (2004) Rutile geochemistry and its potential use in quantitative provenance studies. Sedimentary Geology 171: 37 – 58.

Zack T, John, T (2007) An evaluation of reactive fluid flow and trace element mobility in subducting slabs. Chemical Geology 239: 199- 216.

Zack TA (2013) Cold slab-mantle interface: constraints from exceptionally well preserved lawsonite eclogites. Mineralogical Magazine 77:2574.

Table 1. Bulk rock major element (ICP-OES) and trace element (ICP-MS) composition of samples from the eclogite pod core and margin

Lithology	Eclogite Core	Eclogite Margin	Glaucophane Margin	Lws + Grt + Ph Layer	Monomineralic Lws Vein
Sample #	SV12-13E	SV03-103A	SV03-103B	SV03-103C	SV12-24B
SiO_2	49.32	51.8	49.14	44.53	38
TiO_2	0.88	0.68	1.27	0.62	0.13
Al_2O_3	16.03	12.87	16.49	21.38	27.92
Fe_2O_3	8.57	9.32	11.33	13.03	2.69
MnO	0.27	0.21	0.25	0.34	0.01
MgO	4.89	6.32	6.44	3.43	0.05
CaO	12.87	10.3	4.53	4.6	18.93
Na_2O	3.19	4.36	3.37	0.46	0.05
K_2O	1.41	1.46	2.38	5.95	0.07
P_2O_5	0.6	0.07	0.07	0.17	0.01
LOI	3.71	2.5	3.25	2.93	13.13
Total (Wt.%)	101.74	99.89	98.52	97.44	100.99
V	185	178	122	117	189
Cr	140	250	450	140	<20
Co	55	122	252	18	56
Ni	90	140	340	50	<20
Cu	20	50	20	40	<10
Zn	50	110	220	100	<30
Ga	23	18	21	30	23
Ge	2	1.7	1.5	2.2	1.9
As	<5	<5	<5	<5	<5
Rb	33	39	60	111	2
Sr	432	122	130	322	740
Y	46.3	19.4	41.6	66.2	90.8
Zr	182	142	283	1200	6
Nb	18.3	34.4	135	51.5	0.8
Mo	<2	<2	<2	<2	<2
Ag	<0.5	<0.5	0.6	3.7	<0.5
In	0.2	0.2	0.1	0.2	<0.1
Sn	4	2	4	4	3
Sb	0.8	0.8	0.8	0.7	0.5
Cs	1.4	1.8	2.4	4.9	<0.1
Ba	176	218	357	678	15
La	52	24.8	38.6	121	86.2
Ce	95.7	49.7	79.5	246	172
Pr	11.9	5.82	9.06	26.9	19.4
Nd	46.9	22.9	36.7	100	79.2
Sm	10.1	4.68	7.03	19	16.5
Eu	2.57	1.07	1.71	3.59	5.08
Gd	9.49	4.15	6.63	15.7	16.8
Tb	1.48	0.61	1.27	2.37	2.55
Dy	8.42	3.44	7.82	13.2	14.6
Ho	1.58	0.7	1.49	2.44	2.81
Er	4.43	2.23	4.27	6.68	7.69
Tm	0.695	0.361	0.586	0.936	0.914
Yb	4.45	2.49	3.65	6.06	4.63
Lu	0.694	0.362	0.527	0.903	0.66
Hf	5.4	3.8	7.4	27.2	0.2
Ta	5.24	7.17	11.8	5.33	2.88
W	886	1690	3140	21.7	728
Tl	0.11	0.16	0.23	0.53	<0.05
Pb	16	6	6	11	59
Bi	0.3	<0.1	<0.1	0.4	0.4
Th	13.3	6.16	6.72	15.5	1.33
U	4.05	1.19	1.39	3.52	2.28

LOI, loss on ignition

Table 2. Representative Major Element Compositions of Garnet in Eclogite and Blueschist

Lithology	Eclogite Core				Eclogite Margin						Glaucophane-rich Margin			
Sample #	SV12-13E	SV12-13E	SV12-13E	SV12-13E	SV03-103A	SV03-103A	SV03-103A	SV03-103A	SV03-103A	SV03-103A	SV03-103B	SV03-103B	SV03-103B	SV03-103B
Garnet Type					large, ~ 1mm	large, ~ 1mm	large, ~ 1mm	small, ~ 0.3 mm	small, ~ 0.3 mm	small, ~ 0.3 mm				
Textural Position	core	mantle	rim	late osc rim	core	mantle	rim	core	rim	late osc rim	core	mantle	rim	late osc rim
SiO_2	37.48	37.49	37.91	37.18	37.46	38.10	38.13	37.89	37.43	37.09	37.18	37.51	37.68	37.48
TiO_2	0.16	0.14	0.09	0.07	0.13	0.08	0.09	0.06	0.06	0.03	0.14	0.21	0.01	0.13
Al_2O_3	20.86	20.72	21.14	20.53	21.25	21.34	21.58	21.66	21.08	20.96	21.43	21.30	21.59	21.20
FeO*	24.78	27.56	27.28	26.86	24.29	25.48	27.24	26.13	25.82	23.07	27.13	27.69	28.14	25.47
MnO	3.85	0.83	1.04	2.64	4.44	3.23	0.90	1.32	1.17	6.24	2.68	2.50	1.18	4.38
MgO	1.35	2.21	2.49	1.61	1.31	1.80	3.42	2.40	3.36	1.54	1.55	1.83	2.12	1.72
CaO	11.78	10.65	10.59	10.26	10.73	10.72	9.07	10.62	9.46	9.70	9.62	9.08	9.42	9.31
Na_2O	0.02	bdl	0.01	0.02	0.02	0.04	0.03	0.03	0.03	0.01	0.01	0.01	bdl	0.02
K_2O	bdl	0.01	bdl	0.01	0.01	bdl	0.02	bdl	bdl	bdl	bdl	0.01	0.01	0.02
Cr_2O_3	0.02	bdl	0.02	0.06	0.01	bdl	bdl	bdl	0.03	0.10	bdl	0.05	bdl	bdl
Total (Wt.%)	100.3	99.61	100.57	99.24	99.65	100.79	100.48	100.11	98.44	98.74	99.74	100.19	100.15	99.73
Cations calculated on 12 oxygen basis, with Fe^{2+}/Fe^{3+} calculated assuming full occupancy														
Si	2.98	2.99	2.99	2.99	2.99	3.00	2.99	2.99	2.99	2.99	2.97	2.99	2.99	2.99
Al^{iv}	0.02	0.01	0.01	0.01	0.01	0.00	0.01	0.01	0.01	0.01	0.03	0.01	0.01	0.01
Al^{vi}	1.94	1.94	1.95	1.94	1.99	1.98	1.99	2.00	1.98	1.99	1.99	1.98	2.00	1.99
Ti	0.01	0.01	0.01	0.00	0.01	0.00	0.01	0.00	0.00	0.00	0.01	0.01	0.00	0.01
Cr	0.00	0.00	0.00	0.00	0.00	0.00	0.00	0.00	0.00	0.01	0.00	0.00	0.00	0.00
Fe^{3+}	0.05	0.05	0.04	0.05	0.00	0.01	0.01	0.00	0.01	0.00	0.00	0.00	0.00	0.00
Fe^{2+}	1.60	1.79	1.76	1.76	1.63	1.67	1.78	1.73	1.72	1.55	1.82	1.84	1.87	1.70
Mn	0.26	0.06	0.07	0.18	0.30	0.22	0.06	0.09	0.08	0.43	0.18	0.17	0.08	0.30
Mg	0.16	0.26	0.29	0.19	0.16	0.21	0.40	0.28	0.40	0.18	0.18	0.22	0.25	0.20
Ca	1.00	0.91	0.89	0.88	0.92	0.91	0.76	0.90	0.81	0.84	0.82	0.77	0.80	0.80
Total (cations)	8.02	8.02	8.01	8.00	8.01	8.00	8.01	8.00	8.00	8.00	8.00	7.99	8.00	8.00
Endmembers (mol%)														
Almandine	52.23	58.89	57.95	57.96	54.02	55.42	59.15	57.59	56.90	51.56	59.96	61.16	62.17	56.65
Andradite	2.4	2.41	1.85	2.33	0.22	0.05	0.31	0.00	0.59	0.02	0.00	0.04	0.00	0.04
Grossular	31.21	28.02	28.02	27.07	30.44	29.78	25.18	30.03	26.40	27.51	27.71	25.74	26.77	26.58
Pyrope	5.39	8.79	9.80	6.44	5.23	7.07	13.37	9.44	13.37	6.17	6.21	7.27	8.41	6.84
Spessartine	8.71	1.88	2.32	6.02	10.05	7.21	1.99	2.94	2.65	14.24	6.11	5.63	2.65	9.89
Uvarovite	0.07	0.00	0.06	0.18	0.03	0.00	0.00	0.00	0.09	0.33	0.01	0.15	0.01	0.00

bdl, below detection limit

Table 3. Representative Major Element Compositions of Vein Garnet

Lithology	Lawsonite Layer			Lawsonite Layer			Lawsonite Layer		
Sample #	SV03-103C	SV03-103C	SV03-103C	SV03-103C	SV03-103C	SV03-103C	SV03-103C	SV03-103C	SV03-103C
Garnet Type	large, ~ 5mm	large, ~ 5mm	large, ~ 5mm	inclusion-rich	inclusion-rich	inclusion-rich	inclusion-poor	inclusion-poor	inclusion-poor
Textural Position	core	mantle	rim	core	mantle	rim	core	mantle	rim
SiO_2	36.87	36.84	37.02	37.42	37.55	38.00	37.28	37.60	37.73
TiO_2	0.22	0.14	0.05	0.17	0.16	0.06	0.16	0.06	0.07
Al_2O_3	20.59	20.58	20.96	20.75	20.57	21.29	20.43	20.87	21.12
FeO*	31.03	31.66	32.90	29.92	30.57	29.41	26.31	27.67	29.33
MnO	4.28	3.44	0.03	0.20	0.14	0.40	4.04	0.85	0.38
MgO	0.22	0.26	1.65	1.34	1.41	3.17	1.27	2.58	3.38
CaO	6.65	6.53	6.58	10.16	9.61	7.84	9.83	9.93	7.95
Na_2O	0.04	0.08	0.02	0.07	0.05	0.06	0.05	0.01	0.02
K_2O	bdl	bdl	0.01	0.01	bdl	0.02	bdl	bdl	0.01
Cr_2O_3	0.01	0.05	bdl	bdl	bdl	bdl	0.06	bdl	0.04
Total (Wt.%)	99.91	99.58	99.22	100.04	100.06	100.25	99.43	99.57	100.03
Cations calculated on 12 oxygen basis, with Fe^{2+}/Fe^{3+} calculated assuming full occupancy									
Si	3.00	3.00	3.00	2.99	3.00	3.00	3.00	2.99	2.99
Al^{iv}	0.00	0.00	0.00	0.01	0.00	0.00	0.00	0.01	0.01
Al^{vi}	1.97	1.98	2.00	1.95	1.94	1.98	1.94	1.95	1.96
Ti	0.01	0.01	0.00	0.01	0.01	0.00	0.01	0.00	0.00
Cr	0.00	0.00	0.00	0.00	0.00	0.00	0.00	0.00	0.00
Fe^{3+}	0.01	0.00	0.00	0.03	0.05	0.01	0.04	0.04	0.03
Fe^{2+}	2.10	2.15	2.23	1.97	2.01	1.94	1.73	1.80	1.91
Mn	0.29	0.24	0.00	0.01	0.01	0.03	0.28	0.06	0.03
Mg	0.03	0.03	0.20	0.16	0.17	0.37	0.15	0.31	0.40
Ca	0.58	0.57	0.57	0.87	0.82	0.66	0.85	0.85	0.67
Total (cations)	7.99	7.98	8.00	8.00	8.01	7.99	3.01	8.01	8.00
Endmembers (mol%)									
Almandine	69.80	71.81	74.25	65.05	66.37	64.38	57.08	59.58	63.20
Andradite	0.65	0.22	0.03	1.74	2.28	0.42	1.98	1.89	1.43
Grossular	18.76	18.78	19.01	27.41	25.38	21.80	26.34	26.41	21.02
Pyrope	0.88	1.07	6.64	5.35	5.64	12.49	5.14	10.21	13.37
Spessartine	9.88	7.97	0.08	0.45	0.33	0.90	9.26	1.91	0.85
Uvarovite	0.02	0.15	0.00	0.00	0.00	0.00	0.21	0.00	0.13

bdl, below detection level

Table 4. Representative Trace Element Compositions of Garnet

Lithology	Eclogite Core			Eclogite Margin			Glaucophane-rich Margin			Lawsonite Layer		
Sample #	SV12-13E	SV12-13E	SV12-13E	SV03-103A	SV03-103A	SV03-103A	SV03-103B	SV03-103B	SV03-103B	SV03-103C	SV03-103C	SV03-103C
Textural Position	core	mantle/rim	late osc rim	core	mantle	rim	core	mantle	rim	core	mantle	rim
(ppm)												
Li	6.6	2.5	0.9	7.3	6.2	2.7	5	6.3	5.9	2.2	6.4	7
P	26.5	29.4	20	29.4	22.4	30.3	36.7	30.4	20.8	34.1	29	37
Sc	58.3	24.9	88.7	59.4	47.6	59.4	64.8	53.5	61.7	153.6	201	71.2
Ti	620	341	291	1043	938	364	1102	1340	1170	723	1313	403
V	103.3	40.8	42	63.9	63.8	64.5	72.9	57.5	36.8	53.1	58.1	23.4
Cr	65.2	91.8	115.8	160.3	191.7	137.9	461.8	535.2	397.4	414.9	372.9	314.4
Ni	0.62	0.94	0.61	1.01	1.33	1.05	1.11	0.08	1.2	0.19	2.2	1.9
Zn	43.4	86.9	31.3	53.1	51.6	70	78.9	84.9	105.4	68.1	85.3	145.2
As	0	0.53	bdl	0.38	0.84	0.65	0.17	0.7	0.24	0.24	0.43	0.2
Rb	0	0.04	bdl	0.09	0.26	0.01	0.27	0	bdl	bdl	0.57	0.42
Sr	0	0.02	0.023	0.034	0.033	bdl	0.05	0.083	0.004	bdl	0.24	0.026
Y	50.5	27.3	359	67.1	33.32	91.4	64	110.7	211.9	231	216	209.4
Zr	1.31	0.74	0.129	1.22	7.2	1.03	34.7	7.6	3.36	9.8	1.6	2.21
Nb	0.6	bdl	bdl	0.88	1.18	0	0.81	3.36	4.43	0.4	14.3	bdl
Cs	0.05	0.16	0.3	bdl	0.096	0.05	0.11	bdl	0.031	bdl	bdl	bdl
Ba	0	0	0	0	0	0	0	0.02	0	bdl	bdl	bdl
La	0	0.091	0.057	0.0079	0.0022	0	0	0.026	0	bdl	bdl	bdl
Ce	0	1.21	0.63	0.023	0.05	0	0.028	0.168	0.0092	bdl	0.03	bdl
Pr	0	0.0083	0.02	0.0021	0.0015	bdl	0.0034	0.033	bdl	bdl	0.0055	bdl
Nd	0	0.046	0.013	0.032	0.035	bdl	0.042	0.33	0.069	bdl	0.117	0.041
Sm	0	0.012	0.012	0.00296	0.017	0.017	0.05	0.37	0.66	0.029	0.075	0.45
Eu	0.0061	0.0019	0.0074	0.022	0.0133	0.04	0.036	0.168	0.84	0.048	0.097	0.72
Gd	0.21	0.046	0.61	0.185	0.071	0.6	0.21	2.01	10.53	1.25	1.92	10
Tb	0.113	0.051	0.7	0.19	0.061	0.514	0.296	1.44	5.53	1.07	1.48	6.1
Dy	3.1	1.34	20	3.58	1.88	9.52	4.97	17.7	49.9	21.6	23.9	52.6
Ho	1.59	0.715	10.9	2.16	1.03	3.19	2.25	4.48	8.19	8.09	7.19	8.96
Er	9.52	5.59	61.5	14.4	6.21	11.25	11.59	11.93	16.79	35.1	26.3	16
Tm	2.18	1.94	11.5	3.44	1.45	1.662	2.59	1.61	1.83	6.41	3.53	1.62
Yb	17.4	20.96	81.5	28.7	13.49	11.14	18.99	8.93	9.4	42.2	20.4	9.16
Lu	2.62	3.55	10.7	4.44	2.278	1.54	3.08	0.99	1.286	6.03	2.8	1.11
Hf	0	bdl	bdl	0.0067	0.108	0.0059	0.71	0.13	0.076	0.25	bdl	bdl
Ta	0.12	0	0	0.063	0.052	0	0.034	0.076	0.072	0.0067	0.79	bdl
Pb	0.01	0.014	0.043	0.0123	0.209	0.0022	0.0061	0.055	0.057	0.005	0.033	0.009
Th	0	0.081	0.044	0.0026	0.0031	0	0.038	0.0082	0	0.031	bdl	bdl
U	0	0	0	0.112	0.053	0	0.096	0.024	0.0125	0.046	bdl	bdl

bdl, below detection limit

Table 5. Representative Major Element Compositions of Omphacite

Lithology	Eclogite Core		Eclogite Margin		
Sample #	SV12-13E	SV12-13E	SV03-103A	SV03-103A	SV03-103A
Textural Position	BSE dark	BSE light	core	mantle	rim
SiO_2	55.42	54.88	55.69	54.69	54.52
TiO_2	0.04	0.09	0.22	0.07	0.08
Al_2O_3	8.29	4.78	11.54	6.59	6.90
Cr_2O_3	0.02	0.10	0.04	bdl	0.02
FeO*	9.59	9.91	6.19	10.77	10.17
MnO	0.18	0.13	0.02	0.10	0.11
MgO	7.02	9.40	7.16	7.32	7.80
CaO	12.46	15.61	12.78	13.07	13.60
Na_2O	7.20	5.08	7.02	6.69	6.56
K_2O	0.01	0.01	bdl	bdl	0.01
Total (Wt.%)	100.23	99.99	100.66	99.29	99.77
Cations calculated on 8 oxygen basis, with Fe^{2+}/Fe^{3+} calculated assuming full occupancy					
Si	1.99	2.00	1.98	2.00	1.98
Ti	0.00	0.00	0.01	0.00	0.00
Al	0.35	0.21	0.48	0.28	0.29
Fe^{3+}	0.16	0.14	0.03	0.19	0.21
Cr	0.00	0.00	0.00	0.00	0.00
Fe^{2+}	0.13	0.16	0.15	0.14	0.10
Mn	0.01	0.00	0.00	0.00	0.00
Mg	0.38	0.51	0.38	0.40	0.42
Ca	0.48	0.61	0.49	0.51	0.53
Na	0.50	0.36	0.48	0.47	0.46
K	0.00	0.00	0.00	0.00	0.00
Total (cations)	4.00	3.99	4.00	3.99	3.99
Endmembers(mol%)					
Wo	48.81	47.63	47.85	48.71	50.16
En	38.26	39.91	37.29	37.98	40.05
Fs	12.93	12.46	14.86	13.31	9.78
Aegirine	16.42	14.73	3.37	19.21	20.76
Jadeite	34.70	22.34	46.46	28.86	25.84
Diopside	48.88	62.94	50.17	51.93	53.4

bdl, below detection limit

Table 6. Representative Trace Element Compositions of Omphacite

Lithology	Eclogite Core		Eclogite Margin	
Sample #	SV12-13E	SV12-13E	SV03-103A	SV03-103A
Textural Position	BSE dark	BSE light	core	rim
(ppm)				
Li	108.2	58	131	64.2
P	23.5	38	24.2	19.3
Sc	50.9	52.8	26.27	53.7
Ti	383	137	477	160.5
V	214.4	166.4	180.9	177.7
Cr	291.6	153	38	78.5
Mn	1302	1319	467.5	892
Ni	122.9	170.8	139.6	75.7
Zn	64.5	74.3	166.9	116.8
As	bdl	bdl	bdl	1.22
Rb	0	0	bdl	bdl
Sr	9.99	13.92	12.28	11.99
Y	4.08	3.86	2.49	0.96
Zr	1.37	0.5	2.75	0.41
Nb	0.27	0.199	bdl	0.0048
Cs	bdl	0	bdl	bdl
Ba	0.22	0.71	0	0
La	0	0.039	0.0008	0
Ce	0	0.076	0.014	0.0015
Pr	0	0.012	bdl	bdl
Nd	0	0.035	bdl	bdl
Sm	0.045	0	bdl	bdl
Eu	0	bdl	0.027	bdl
Gd	0.028	0	0.014	0
Tb	0.035	0.019	0.045	0.0175
Dy	0.41	0.54	0.413	0.092
Ho	0.135	0.119	0.098	0.037
Er	0.52	0.36	0.28	0.077
Tm	0.087	0.05	0.0145	0.0025
Yb	0.58	0.49	0.147	0.096
Lu	0.026	0.063	0.0073	bdl
Hf	0.207	bdl	0.265	bdl
Ta	bdl	bdl	0	0.0009
Pb	0.638	1.01	0.244	0.462
Th	0	0.085	0	0
U	0.029	0.061	0	0.0018

bdl, below detection limit

Table 7. Representative Major Element Compositions of Glaucophane

Lithology	Eclogite Core		Glaucophane-rich Margin	
Sample #	SV12-13E	SV12-13E	SV03-103B	SV03-103B
Textural Position	core	rim	core	rim
SiO_2	59.30	58.09	55.69	56.09
TiO_2	bdl	bdl	0.02	bdl
Al_2O_3	11.00	5.17	11.48	10.32
Cr_2O_3	0.10	bdl	0.10	bdl
FeO*	9.83	15.66	10.98	12.89
MnO	0.13	0.36	0.03	0.07
MgO	10.91	11.13	9.93	9.31
CaO	1.00	1.27	1.21	0.37
Na_2O	6.93	6.60	6.64	7.06
K_2O	bdl	0.01	0.02	0.03
Total (Wt.%)	99.20	98.29	96.10	96.14
Cations calculated on a 13 cation/23 oxygen basis, with Fe^{2+}/Fe^{3+} calculated assuming full occupancy				
Si	7.95	8.02	7.76	7.84
Al^{iv}	0.05	0.00	0.24	0.16
Al^{vi}	1.69	0.08	1.64	1.54
Ti	0.00	0.00	0.00	0.00
Cr	0.01	0.00	0.01	0.00
Fe^{3+}	0.26	0.98	0.43	0.58
Fe^{2+}	0.85	0.83	0.85	0.93
Mn	0.01	0.04	0.00	0.01
Mg	2.18	2.29	2.06	1.94
Ca	0.00	0.00	0.18	0.06
Na	0.00	0.00	1.79	1.92
K	0.00	0.00	0.00	0.00
Total (cations)	16.95	16.96	16.98	16.98
$Mg/ (Mg + Fe^{2+})$	0.72	0.73	0.71	0.68
$Fe^{3+}/ (Fe^{3+} + Al^{vi})$	0.13	0.54	0.21	0.27

bdl, below detection limits

Table 8. Representative Trace Element Compositions of Sodic Amphibole

Lithology	Eclogite Core		Glaucophane-rich Margin	
Sample #	SV12-13E	SV12-13E	SV03-103B	SV03-103B
Textural Position			core	rim
(ppm)				
Li	138.7	152.6	175.6	126.8
P	14.4	28.7	30.1	23.3
Sc	11.4	12.09	18.63	18
Ti	130	100.9	145.7	79.4
V	121.5	106.9	80.8	57
Cr	226.1	234.4	459.6	77.9
Mn	748	600.4	355.6	486.9
Ni	316.3	458	1262	462.7
Zn	254	246.9	575	373.8
As	0.57	1.33	0.45	1.09
Rb	0	0	0.23	0
Sr	1.9	1.48	0.184	0.537
Y	0.008	0.128	0.044	0.089
Zr	0.015	0.085	0.045	0.041
Nb	0.008	0	0.028	0.027
Cs	0	0	0.01	0
Ba	0	0	0	0.015
La	0	0.0074	0	0
Ce	0.006	0.01	0	0
Pr	0	0.0012	0	0
Nd	0.012	0.012	0	0
Sm	0	0	0	0
Eu		0.0022	0	0
Gd	0	0	0	0
Tb	0	0	0	0.0029
Dy	0	0	0.009	0.012
Ho	0	0	0	0.002
Er	0	0.012	0.001099	0.001035
Tm	0	0	0	0
Yb	0	0	0	0
Lu	0	0.0034	0	0
Hf	0	0	0	0
Ta	0	0	0	0
Pb	0.058	0.114	0.03	0.174
Th	0	0	0	0
U	0	0	0	0

Table 9. Representative Major Element Compositions of Lawsonite

Lithology	Eclogite Core		Eclogite Margin		Gl-rich Margin		Lawsonite Layer (margin)		Lawsonite Layer (interior)	
Sample #	SV12-13E	SV12-13E	SV03-103A	SV03-103A	SV03-103B	SV03-103B	SV03-103C	SV03-103C	SV03-103C	SV03-103C
Textural Position	Ti-rich	Ti-poor	Ti-rich	Ti-poor	core	rim	Fe-poor core	Fe-rich rim	Fe-poor core	Fe-rich rim
SiO_2	37.94	38.29	38.44	38.42	38.45	38.20	38.36	38.31	38.36	38.54
TiO_2	0.31	0.07	0.26	0.04	0.57	0.61	0.48	0.41	0.03	0.38
Al_2O_3	31.21	31.99	31.96	31.97	31.99	31.60	32.18	31.97	32.67	31.70
Cr_2O_3	0.02	0.01	0.01	0.01	bdl	0.03	0.01	0.08	0.00	0.00
FeO*	1.45	1.47	1.08	1.31	0.94	1.20	0.67	1.45	0.65	1.45
MnO	bdl	bdl	bdl	bdl	bdl	bdl	bdl	bdl	bdl	bdl
MgO	bdl	bdl	bdl	bdl	bdl	bdl	bdl	bdl	bdl	bdl
CaO	17.92	17.86	17.95	17.75	17.97	17.99	17.91	17.67	18.00	17.83
Na_2O	bdl	bdl	bdl	bdl	bdl	bdl	bdl	bdl	bdl	bdl
K_2O	bdl	bdl	bdl	bdl	bdl	bdl	bdl	bdl	bdl	bdl
Total (Wt.%)	88.85	89.69	89.70	89.50	89.92	89.63	89.61	89.89	89.71	89.90
Cations calculated on 8 oxygen basis										
Si	2.00	1.99	2.00	2.00	1.99	1.99	1.99	1.99	1.99	2.00
Ti	0.01	0.00	0.01	0.00	0.02	0.02	0.02	0.02	0.00	0.01
Al	1.94	1.96	1.96	1.96	1.94	1.95	1.97	1.96	1.99	1.94
Fe^{3+}	0.06	0.06	0.05	0.06	0.05	0.04	0.03	0.06	0.03	0.06
Cr	0.00	0.00	0.00	0.00	0.00	0.00	0.00	0.00	0.00	0.00
Mn	0.00	0.00	0.00	0.00	0.00	0.00	0.00	0.00	0.00	0.00
Mg	0.00	0.00	0.00	0.00	0.00	0.00	0.00	0.00	0.00	0.00
Ca	1.01	1.00	1.00	0.99	1.00	1.00	1.00	0.98	1.00	0.99
Na	0.00	0.00	0.00	0.00	0.00	0.00	0.00	0.00	0.00	0.00
K	0.00	0.00	0.00	0.00	0.00	0.00	0.00	0.00	0.00	0.00
Total (cations)	5.02	5.01	5.02	5.01	5.00	5.00	5.01	5.01	5.01	5.00

bdl, below detection level

Table 10. Representative Trace Element Compositions of Lawsonite

Lithology	Eclogite Core		Eclogite Margin		Glaucophane-rich Layer Margin		Lawsonite Layer Margin		Lawsonite Layer Interior			
Sample #	SV12-13E	SV12-13E	SV03-103A	SV03-103A	SV03-103B	SV03-103B	SV03-103C	SV03-103C	SV03-103C	SV03-103C	SV03-103C	SV03-103C
Textural Position	high Ti	low Ti	high Ti	low Ti	high Ti	low Ti	Fe-poor core	Fe-rich rim	Fe-poor core	Fe-rich rim	Ti-poor sector	Ti-rich sector
(ppm)												
P	25	18.2	19	28	21.6	26	23.9	29	34	28.5	17	30.4
Sc	2.38	2.55	2.52	2.41	5.22	2.97	2.45	3.59	2.6	2.74	2.29	2.55
Ti	1437	455	2637	364	2642	319	930	2349	883	2368	200	3060
V	262.2	429.3	284.8	250.7	316.1	306.9	199.2	148.7	38.8	47.9	42.9	45.8
Cr	305.2	317.2	95	91.9	172.8	84.7	836	783	17.6	4.01	5.3	14.58
Mn	12.77	17.2	21.4	18.5	25.2	25.1	20.2	8.21	6.3	20.9	22.2	26.8
Sr	1326	1567	484	669	410.4	647	899	553	877	541.1	1137	626
Y	18.84	8.41	17.5	20.51	11.5	10.63	20.81	12.54	40.6	7.1	19.8	36.4
Zr	0	0	31	0.18	0	0.014	0	0.017	158	0.02	3.2	0
Nb	0.035	0	0	0	0	0	0	7.01	0.12	0.005	0	0.44
Cs	0	0	0	0	0	0	0.11	0.14	0.07	0.1	0	0
Ba	0	0.23	0	0.1	0	0.045	0	0	0	0	0.26	0.26
La	0.956	0.98	2.19	3.52	4.37	26.92	11.81	3.96	7.76	9.7	35.8	18.6
Ce	2.86	2.29	6.06	8.62	12.09	65.5	32.23	8.71	19.25	21.7	93.7	51.3
Pr	0.426	0.241	0.93	1.15	1.6	7.84	4.42	1.112	2.52	2.62	12.25	6.9
Nd	1.75	1.05	4.37	6.02	8.61	35.9	22.5	5.21	13	11.54	57.1	35.6
Sm	0.54	0.21	0.81	1.46	2.46	5.69	6.14	1.7	3.63	3.32	16.7	11.52
Eu	0.18	0.068	0.3	0.351	0.772	1.39	1.38	0.86	0.92	0.86	2.97	3.06
Gd	0.92	0.36	1.31	2.32	2.97	4.48	6.7	2.94	5.6	3.13	14.8	13.8
Tb	0.244	0.069	0.243	0.534	0.34	0.535	1.1	0.7	0.91	0.373	1.74	2.07
Dy	2.55	0.73	2.82	2.95	2.33	2.47	5.43	3.56	7.94	2.03	7.38	11.26
Ho	0.557	0.221	0.59	0.64	0.39	0.351	0.772	0.433	1.59	0.257	1.02	1.58
Er	0.97	0.71	1.78	2.19	1.01	0.62	1.13	0.49	3.88	0.51	1.66	3.1
Tm	0.055	0.077	0.281	0.166	0.116	0.053	0.091	0.021	0.32	0.055	0.183	0.315
Yb	0.166	0.42	0.98	1.16	0.49	0.43	0.32	0.08	1.27	0.47	1.17	1.58
Lu	0.005	0.044	0.22	0.19	0.078	0.064	0.0052	0.0029	0.273	0.025	0.113	0.158
Hf	0	0	0.82	0	0	0	0	0	3.9	0	0.12	0
Ta	0.0015	0	0	0	0	0	0	0.063	0.051	0.0048	0	0.0097
Pb	34.89	35.7	11.15	14.11	12	14.96	23.87	12.18	22.2	10.97	34.4	17.65
Th	0.046	0.0087	0.035	0.113	0.325	0.103	1.24	0.052	1.23	0.301	0.97	0.573
U	0.0056	0.0067	0.055	0.025	0.036	0.0104	0.11	0.097	0.61	0.9	0.08	0.225

Table 11. Representative Major Element Compositions of Phengite

Lithology	Eclogite Core		Lawsonite Layer	
Sample #	SV12-13E	SV12-13E	SV03-103B	SV03-103B
Textural Position			core	rim
SiO_2	51.87	51.18	48.30	51.45
TiO_2	0.16	0.19	0.46	0.11
Al_2O_3	23.73	23.72	30.13	23.65
Cr_2O_3	bdl	0.01	0.02	0.07
FeO*	3.69	3.77	2.65	3.87
MnO	bdl	bdl	bdl	0.03
MgO	4.29	4.30	2.49	4.40
CaO	bdl	0.05	0.01	bdl
Na_2O	0.16	0.19	1.16	0.10
K_2O	11.11	11.26	9.73	11.27
Total (Wt.%)	95.01	94.67	94.95	94.95
Cations calculated on a 11 oxygen basis				
Si	3.51	3.48	3.24	3.49
Al	1.89	1.90	2.38	1.89
Ti	0.01	0.01	0.02	0.01
Cr	0.00	0.00	0.00	0.00
Fe	0.21	0.21	0.15	0.22
Mn	0.00	0.00	0.00	0.00
Mg	0.43	0.44	0.25	0.44
Ca	0.00	0.00	0.00	0.00
Na	0.02	0.02	0.15	0.01
K	0.96	0.98	0.83	0.98
Total (cations)	7.03	7.04	7.02	7.04

bdl, below detection limits

Table 12. Representative Trace Element Compositions of Phengite

Lithology	Eclogite Core		Lawsonite Layer	
Sample #	SV12-13E	SV12-13E	SV03-103C	SV03-103C
Textural Position			core	rim
(ppm)				
Li	12.58	12.4	15.5	14.1
P	25	23.2	19.6	19.7
Sc	5.68	4.65	5.11	4.59
Ti	935	1140	1717	980
V	124.3	116	156.2	109.6
Cr	295	223	645.7	252.2
Mn	55.22	74.4	49.3	80.9
Ni	50.2	120	157.6	104
Zn	75.6	42.9	95.3	90.6
As	1.04	1.16	0.79	0.9
Rb	299.7	289.7	262.7	269.8
Sr	10.18	6.87	32.37	6.98
Y	0.0021	0.026	0	0.0062
Zr	0.048	0.017	0	0.003
Nb	1.67	0.563	13	2.97
Cs	14.75	13.57	5.38	10.8
Ba	1333	1207	1500	1631
La	0.0093	0.109	0	0
Ce	0.0021	0.22	0	0
Pr	0	0.026	0	bdl
Nd	0	0.107	0	bdl
Sm	0	0	0	bdl
Eu	0.035	0.058	0.0077	0.0149
Gd	0	0	0	0
Tb	0	0	0	0
Dy	0	0.017	0	0
Ho	0	0	0	0
Er	0	0	0.001	0.00155
Tm	0	0	0	bdl
Yb	0	0	0	bdl
Lu	0	0	0	0
Hf	0	0	0	bdl
Ta	0.033	0.028	0.046	0.074
Pb	1.94	1.55	2.62	1.113
Th	0	0.05	0	0.0018
U	0	0.017	0	0

bdl, below detection limit

Table 13. Representative Trace Element Compositions of Rutile

Lithology	Eclogite Core				Gl-rich Layer Margin/Lws Layer	
Sample #	SV12-13E	SV12-13E	SV12-13E	SV12-13E	SV03-103B/C	SV03-103B/C
Textural Position	low Zr	med Zr	high Zr	garnet incl	low Zr	high Zr
(ppm)						
Al	630	98.9	89.2	72.3	217	48.9
Si	4060	3150	2807	2726	2810	2320
P	27.1	20.8	20.9	18.4	12	15.6
Ca	430	810	10	9	0	95
Sc	1.43	1.14	1.53	0.89	0.094	1.52
V	364.6	433.1	534	455.6	480	479.4
Cr	1059	524	439.6	316.6	2066	1551
Mn	25	8.46	5.86	11.56	5.1	2.4
Co	0.202	0.114	0.156	0.107	0	0
Ni	1.5	2.32	1.41	1.27	3	3.2
Cu	33.1	22.3	20.3	18.5	15.5	14.6
Zn	11	7.7	8.07	7.03	8.3	6.3
Rb	0.1	0	0	0	0.6	0.01
Y	6	1.2	0	0.0062	0.17	0.0043
Zr	19.81	83.6	150.5	103.7	68.1	98.5
Nb	2062	2984	1850	2969	19390	12530
Mo	5.44	3.23	2.4	3.97	3.2	6.44
Sn	101.7	50.5	44.5	24.9	93.6	70.9
Sb	23.4	7.28	1.17	2.33	5.9	2.88
Hf	1.47	4.39	5.9	5.31	2.88	4.37
Ta	131.4	201.8	134.7	176.1	1421	296.9
W	87.5	23.54	6.44	10.32	36.7	23.9
Pb	3.08	0.84	0.047	0.06	0.55	0.057
Th	9.4	0.78	0	0.001	0.041	0
U	3.21	0.82	0.098	0.303	0.89	0.646
Nb/Ta	15.69	14.79	13.73	16.86	13.65	42.20
Zr/Hf	13.48	19.04	25.51	19.53	23.65	22.54

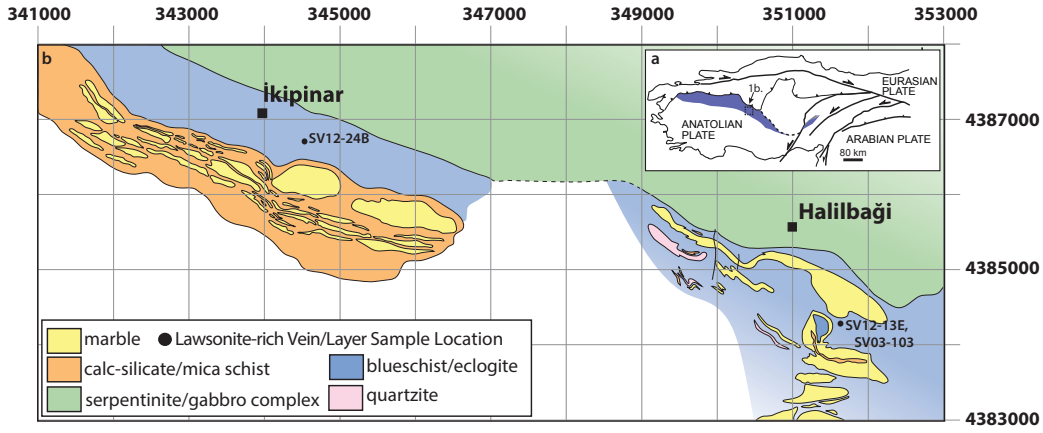

Figure 1. (a) Tectonic map showing the location of the Tavşanlı Zone HP/LT belt (shaded region) in Turkey. (b) Simplified geologic map of the Sivrihisar Massif near the villages of Halilbağı and İkipınar; sample locations for the mono-minerallic lawsonite vein (SV12-24B) and the lawsonite + garnet + phengite-rich layer (SV03-103) and host eclogite (SV12-13E) are shown. Sample coordinates are provided in Supplementary Material 1.

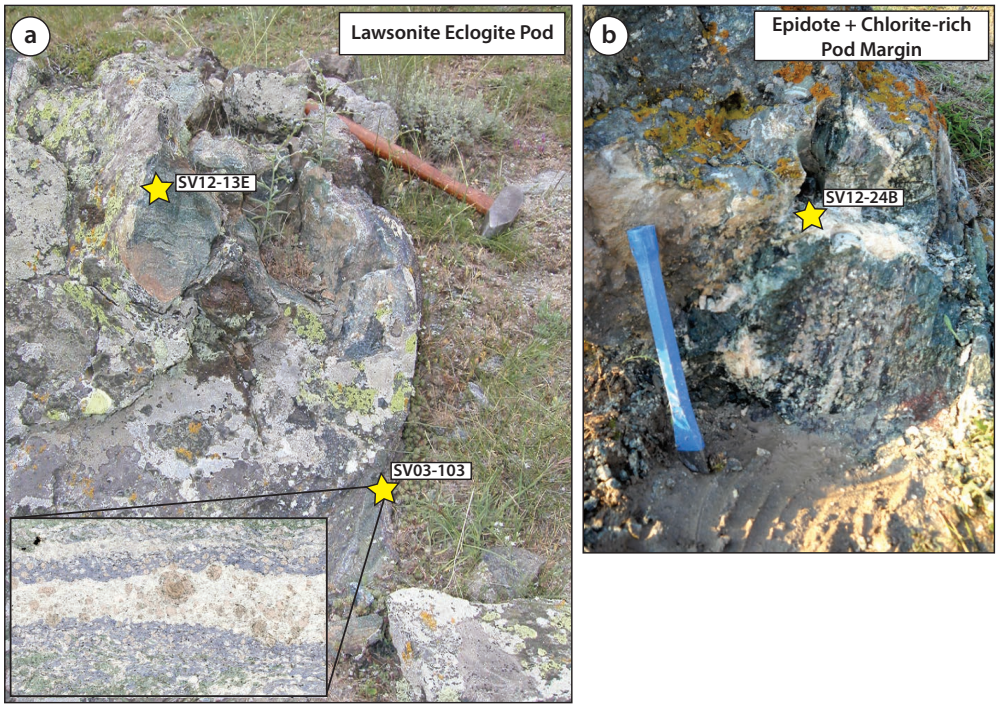

Figure 2. Photograph of the lawsonite eclogite pod from which samples SV12-13E (pod core) and SV03-103 (pod margin) were collected. Inset shows a thin section scan of the pod margin highlighting the mm-to-cm scale interlayering of blueschist and eclogite, as well as the relationship of these layers to the lawsonite + garnet + phengite-rich layer (a). Photograph of the epidote + chlorite-rich pod margin from which the mono-minerallic lawsonite vein (SV12-24B) was sampled (b).

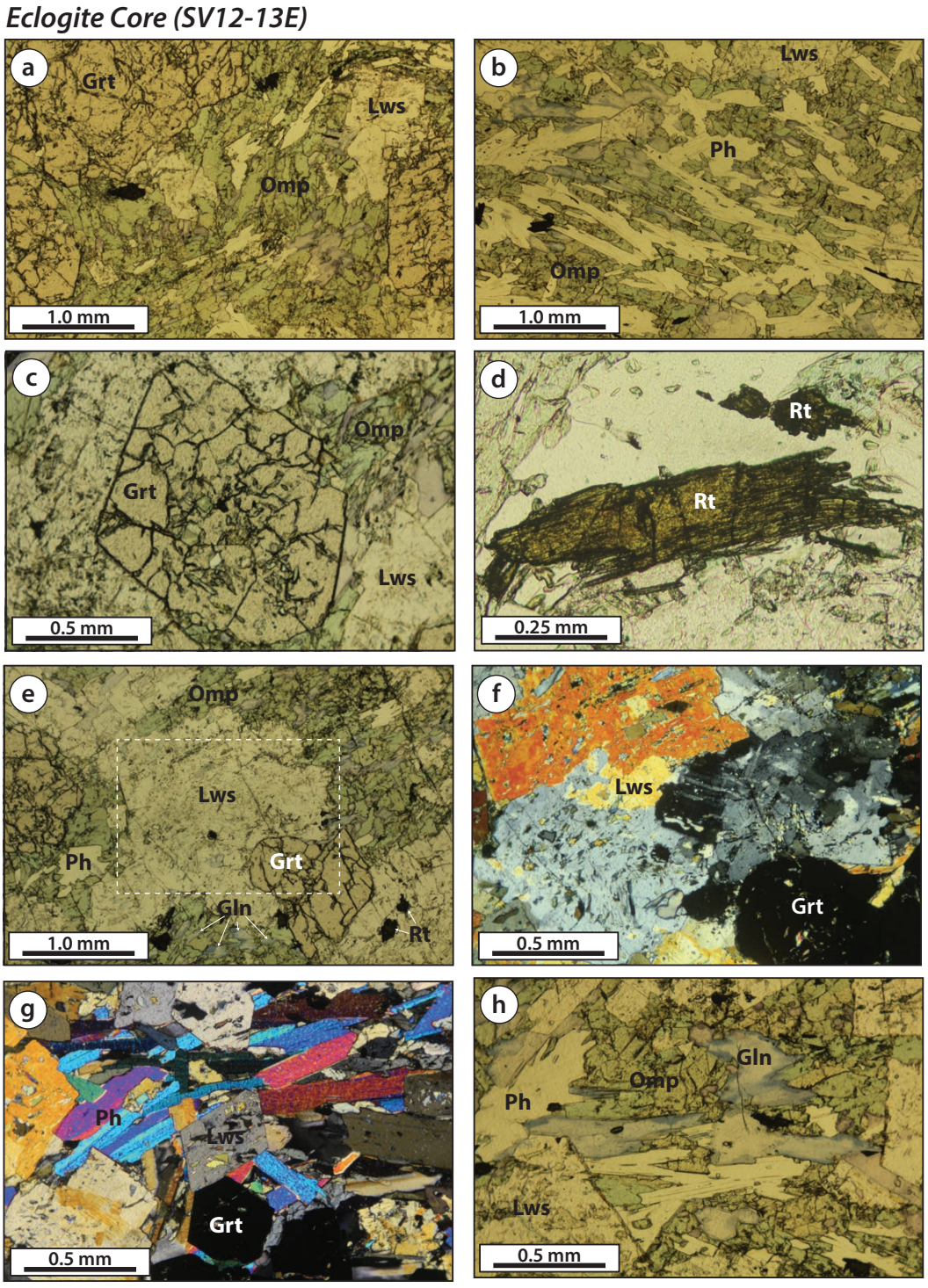

Figure 3. Photomicrographs from the core of the lawsonite eclogite pod (SV12-13E).

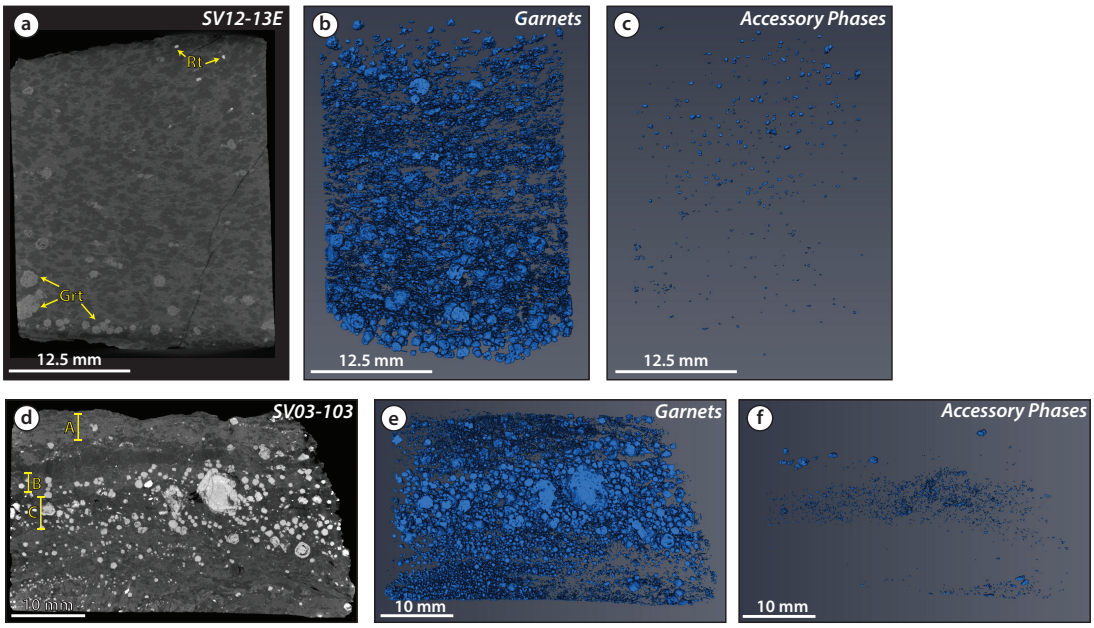

Figure 4. X-ray Computed Tomography (XRCT) reconstruction of the lawsonite eclogite core (sampled from the core of the pod, a) and the billet containing the lawsonite + garnet + phengite-rich layer, associated glaucophane-rich margin and host lawsonite eclogite (sampled from the margin of the pod, d). The distribution of garnets (b,e) and accessory phases (zircon and rutile; c and f) within each of these samples are shown.

Pod Margin (SV03-103)

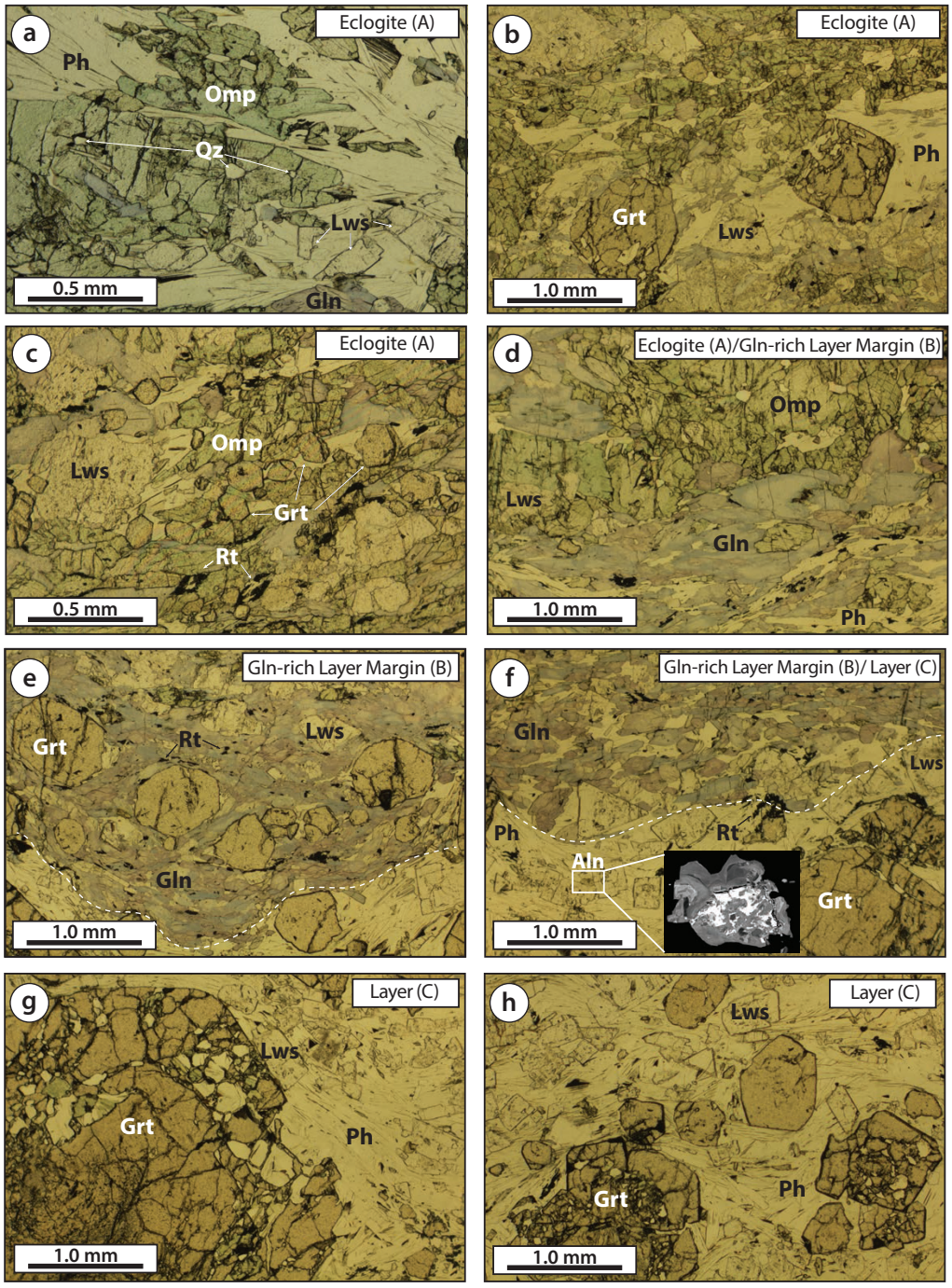

Figure 5. Photomicrographs from the margin of the lawsonite eclogite pod, highlighting the textural relationships between the interlayered lawsonite eclogite (SV03-103A), glaucophane-rich margin (SV03-103B), and lawsonite + garnet + phengite layer (SV03-103C) and their mineral assemblages.

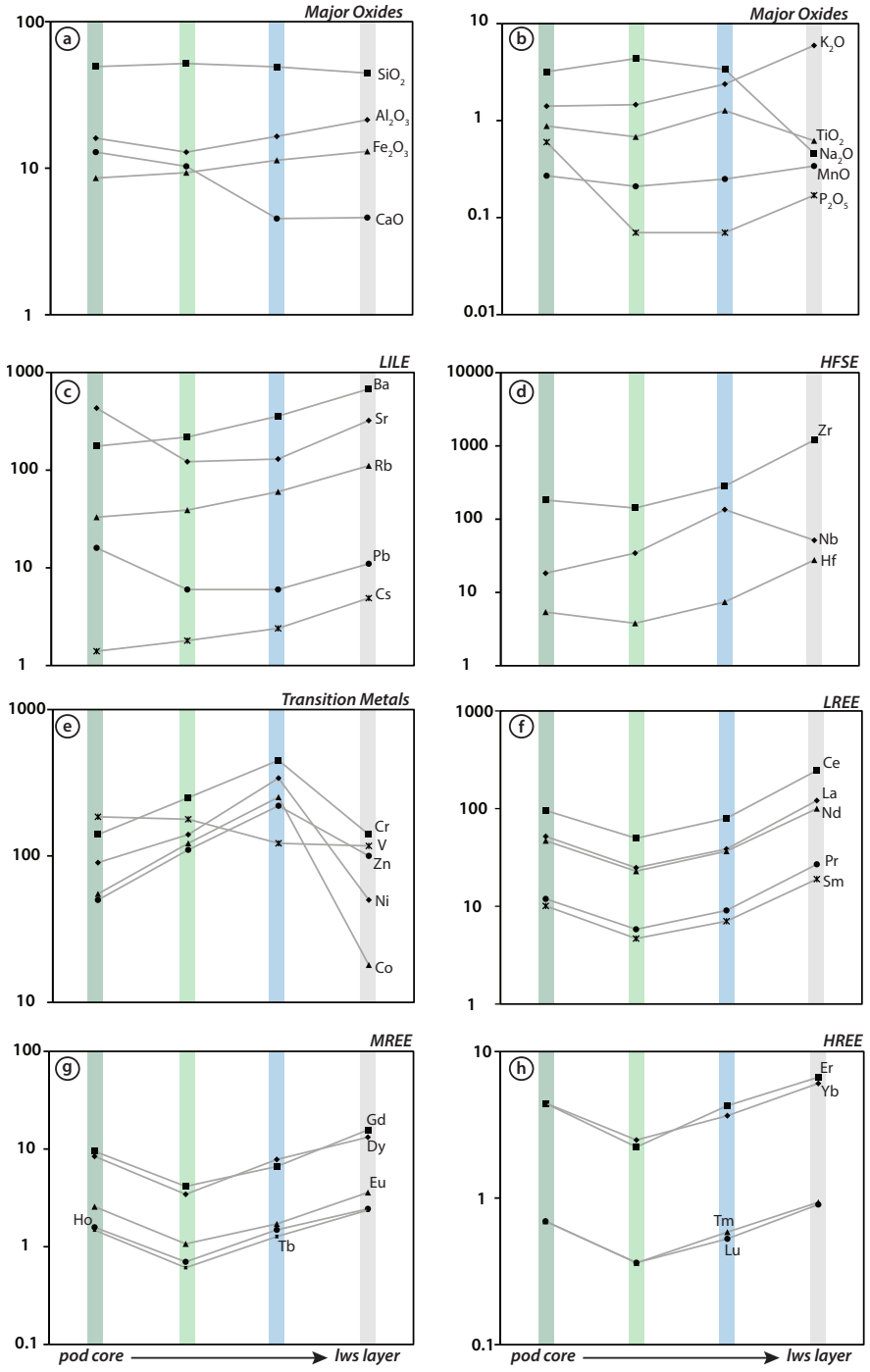

Figure 6. Changes in the bulk rock concentrations of the major oxides (a,b), large ion lithophile elements (LILE) (c), high-field strength elements (HFSE) (d), transition metals (e), light rare earth elements (LREE) (f), middle rare earth elements (MREE) (g), and heavy rare earth elements (HREE) (h) along the profile from the pod core to the lawsonite + phengite + garnet-rich layer at the pod margin.

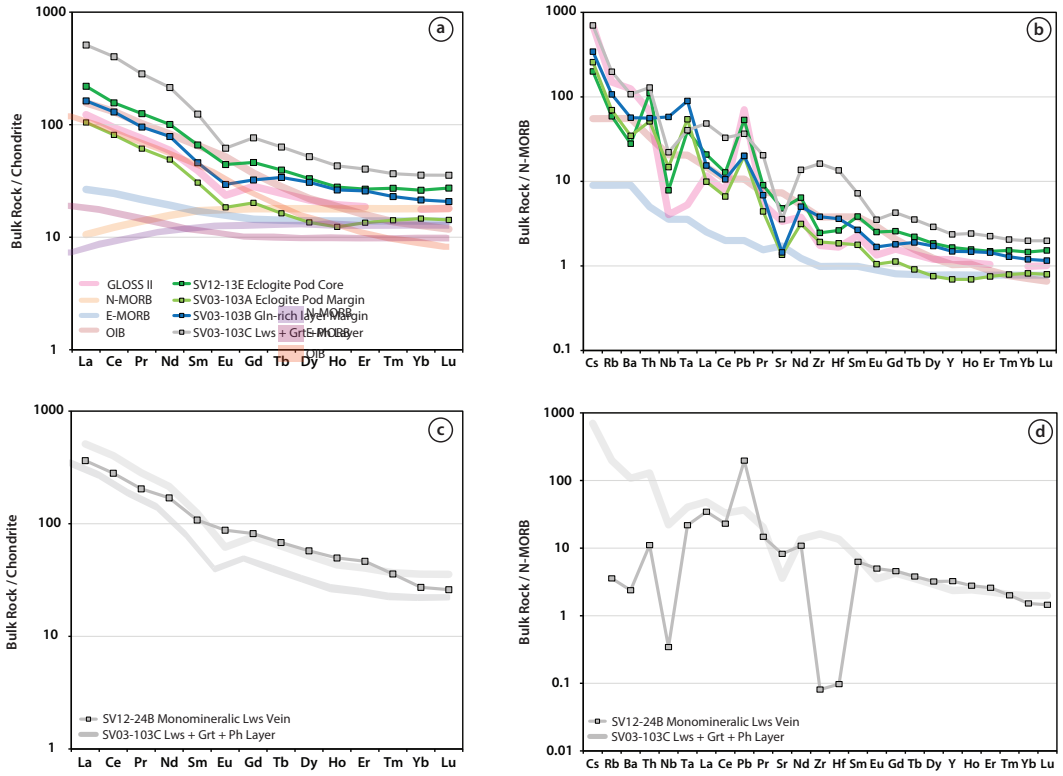

Figure 7. Chondrite-normalized rare earth element (REE) and N-MORB normalized extended trace element patterns for the lawsonite eclogite pod core, lawsonite eclogite pod margin, glaucophane-rich margin, and lawsonite + phengite + garnet-rich layer (a,b), as well as the mono-minerallic lawsonite vein (c,d). For comparison, the normalized compositions of N-MORB, E-MORB, OIB, and GLOSS are presented in (a, b), and the composition of the lawsonite + garnet + phengite-rich layer are presented in (c, d). Chondrite, N-MORB, E-MORB, and OIB element concentrations were obtained from Sun and McDonough (1989), and GLOSS II element concentrations were obtained from Plank et al. (2014).

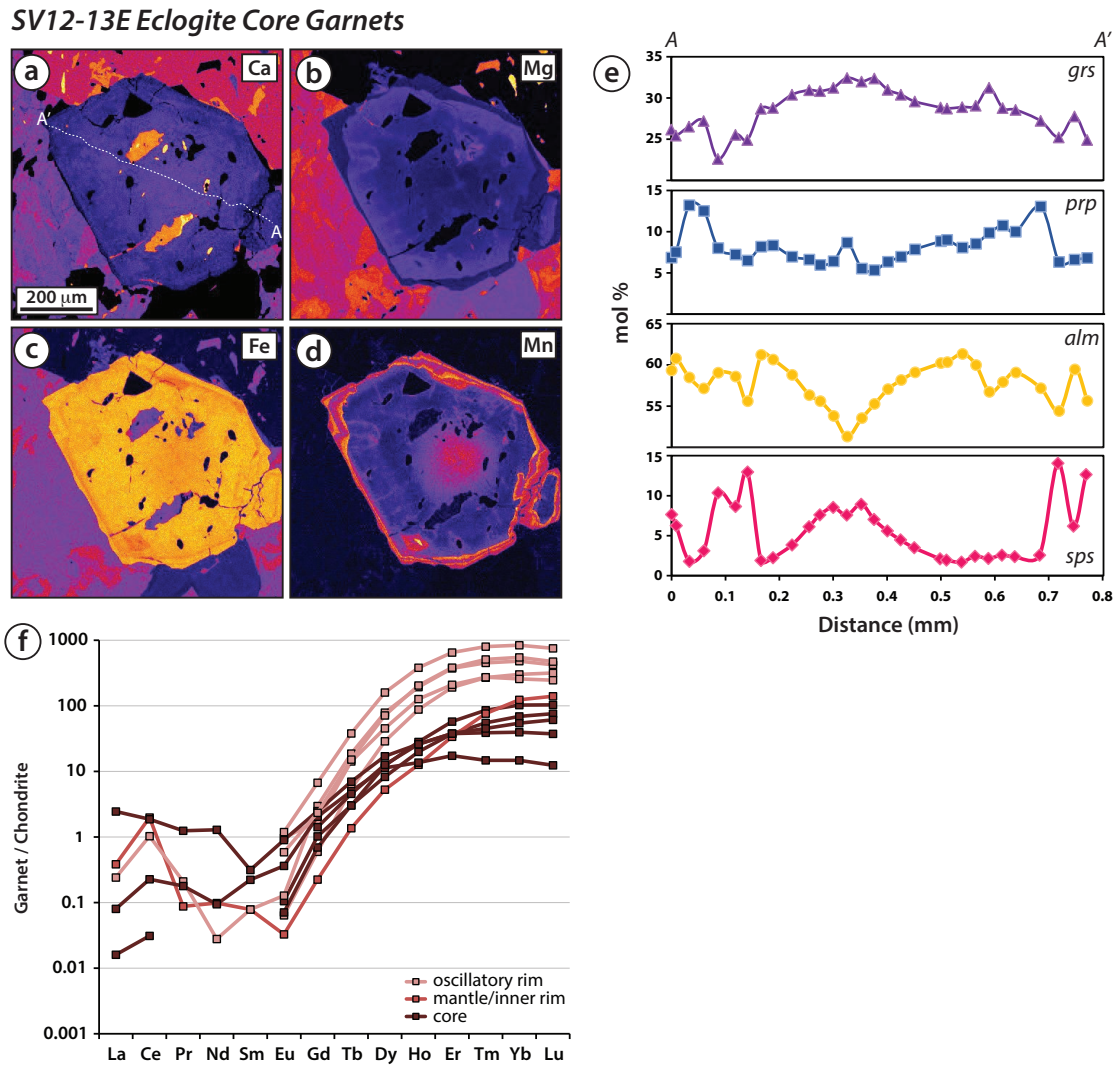

Figure 8. Representative major element zoning (a,b,c,d) and major (e) and trace (f) element compositional profiles of garnet from the core of the eclogite pod (SV12-13E).

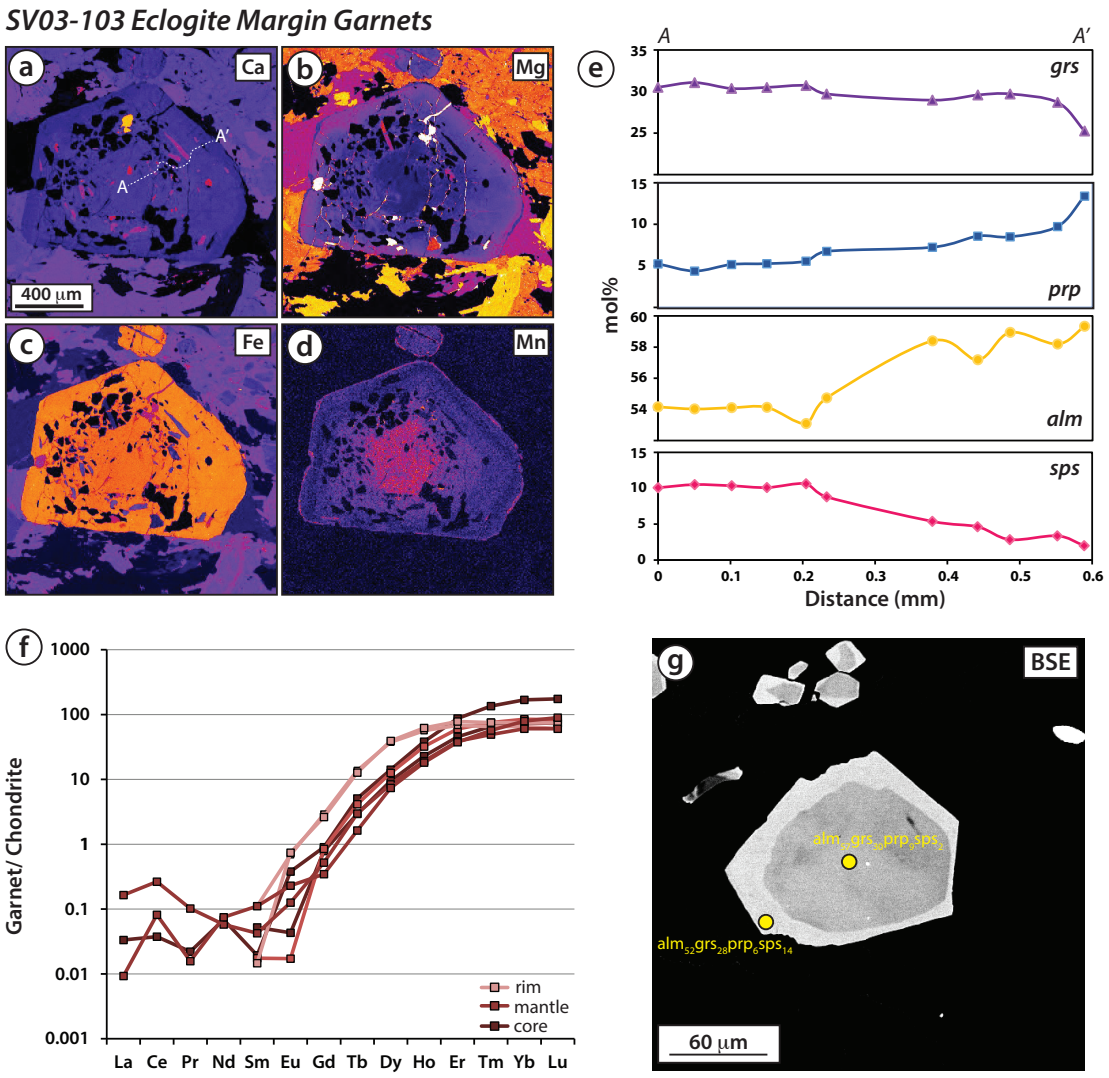

Figure 9. Representative major element zoning (a,b,c,d) and major (e) and trace (f) element compositional profiles of large (~ 0.90 – 1.45 mm in diameter) garnet from the margin of the eclogite pod (SV03-103A). Backscattered electron (BSE) image of small garnets in the eclogite layer show core-to-rim zoning; representative microprobe analyses for the core and rim are shown (g).

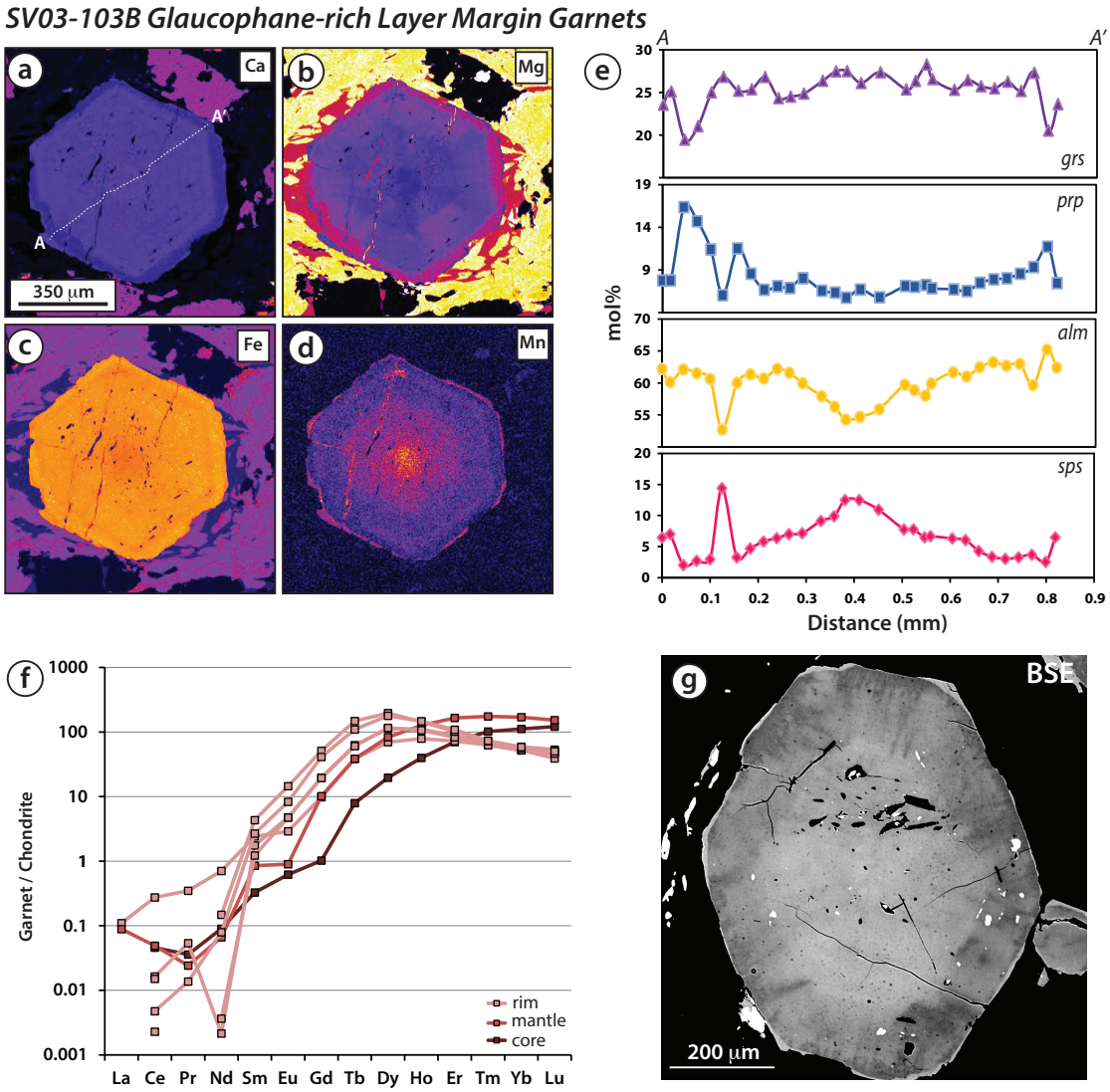

Figure 10. Major element zoning (a,b,c,d) and major (e) and trace (f) element compositional profiles of garnet from the glaucophane-rich margin of the lawsonite + garnet + phengite layer. High contrast backscattered electron (BSE) imaging of garnet from the glaucophane-rich vein margin shows patchy zoning features, as well as the presence of a late thin rim that truncates existing zoning features (g).

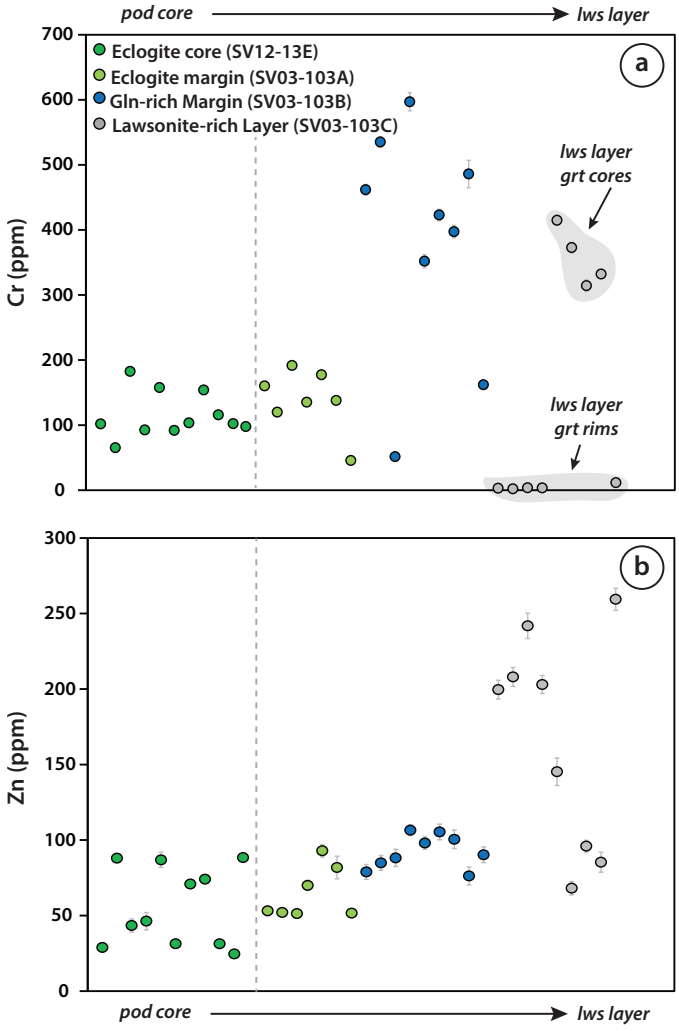

Figure 11. Changes in the concentration of Cr (a) and Zn (b) in garnet along a transect from the lawsonite eclogite pod core to the lawsonite + garnet + phengite layer. Dashed line denotes the separation between garnet analyses from the core of the pod, and garnet analyses from the individual lithologic layers at the pod margin.

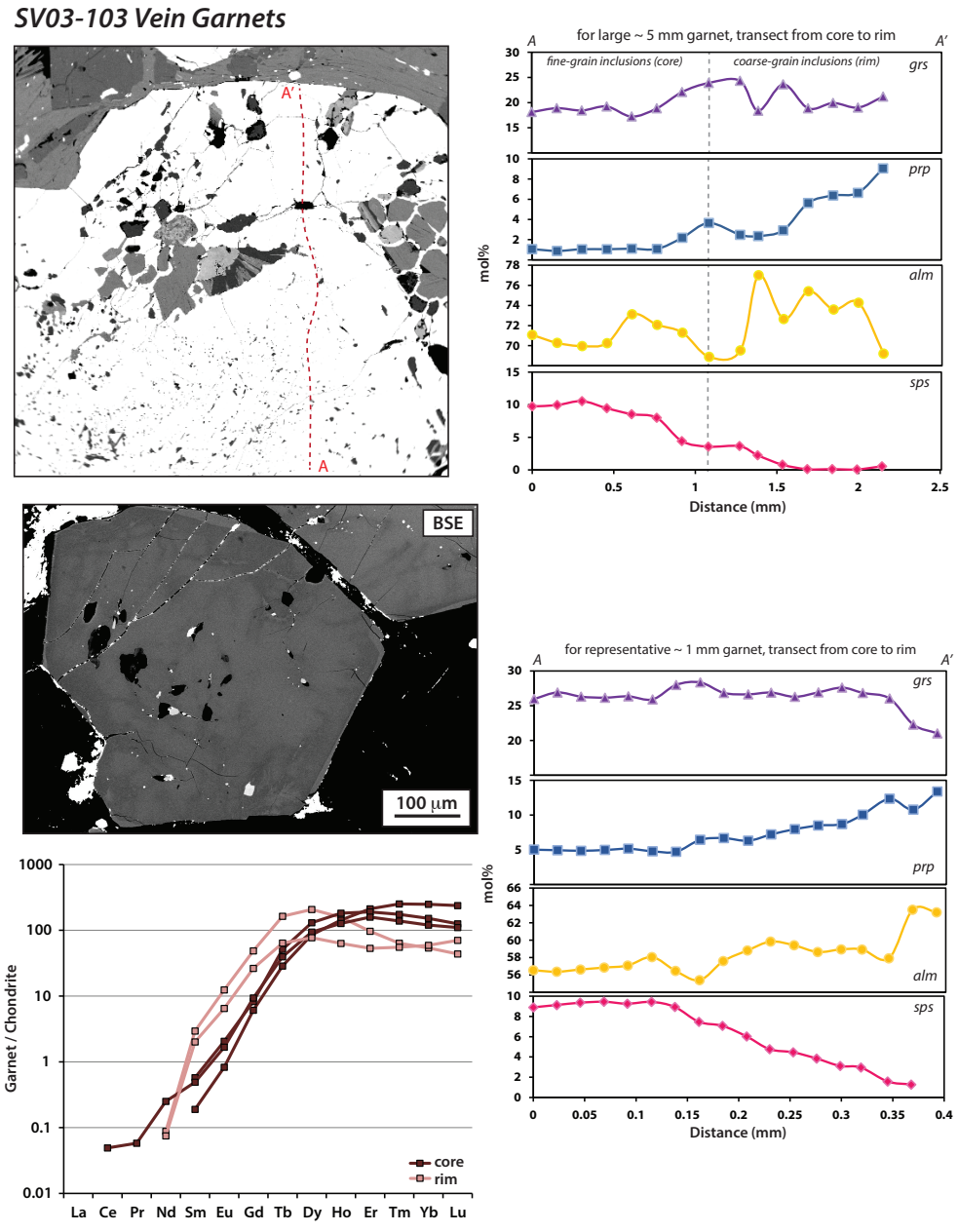

Figure 12. Backscattered electron (BSE) images of the large, ~ 5 mm garnet in the lawsonite + garnet + phengite-rich layer showing the transition from the core (characterized by fine-grained inclusions) to the rim (characterized by coarse-grained inclusions) and oscillatory zoning in Ca and Fe. Representative BSE image and major and trace element compositional profiles of the ~ 1 mm garnet population in lawsonite + garnet + phengite-rich layer.

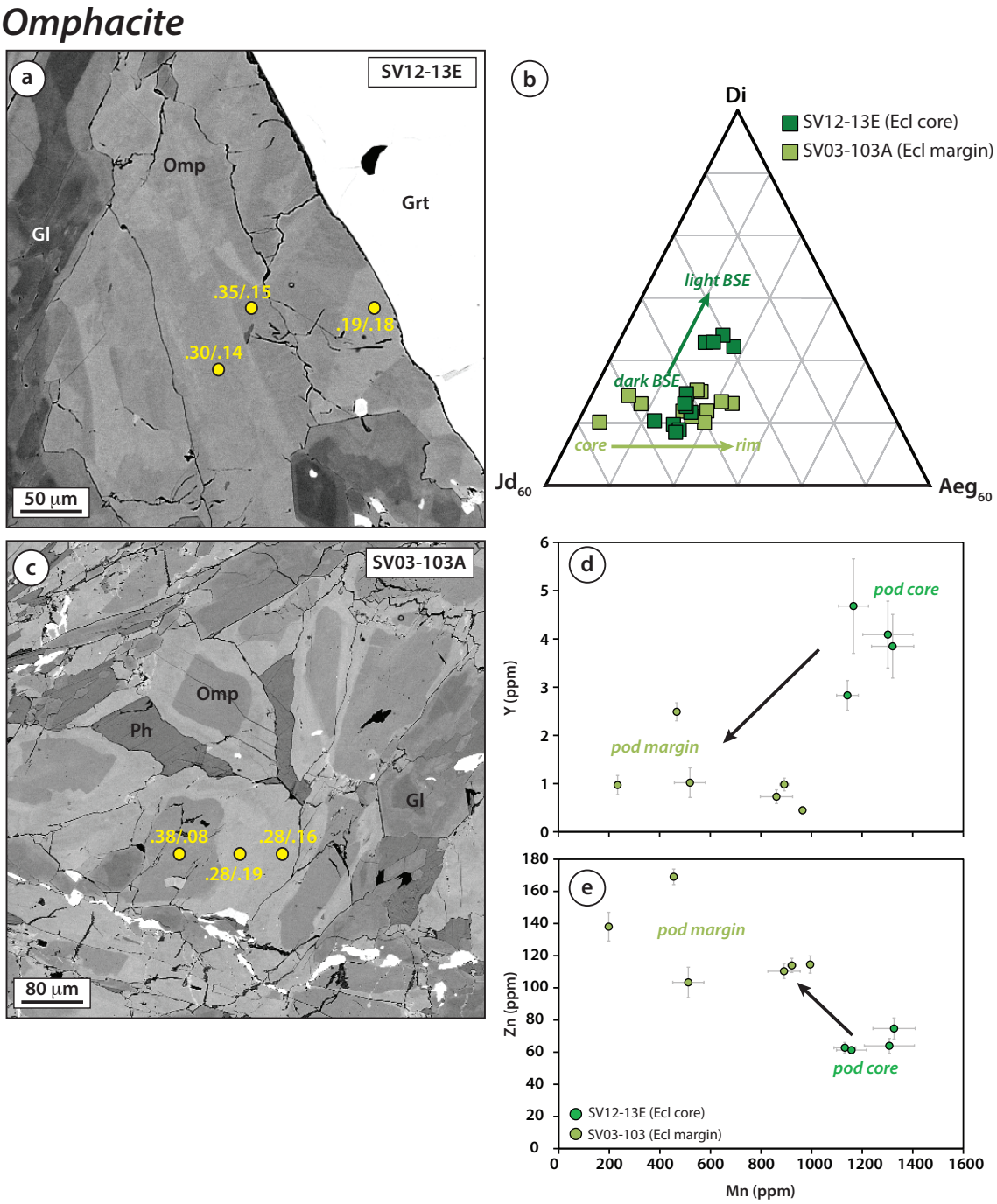

Figure 13. Backscattered electron (BSE) images of omphacite from the core of the lawsonite eclogite pod (SV12-13E; a) and the eclogite at the margin of the lawsonite eclogite pod (SV03-103A; c). X_{jd} / X_{ae} content obtained from microprobe analyses in different compositional domains are shown. Variations in major elements and Mn, Y, and Zn contents between omphacite from the core of the pod and the margin of the pod are shown in b, and d and e, respectively.

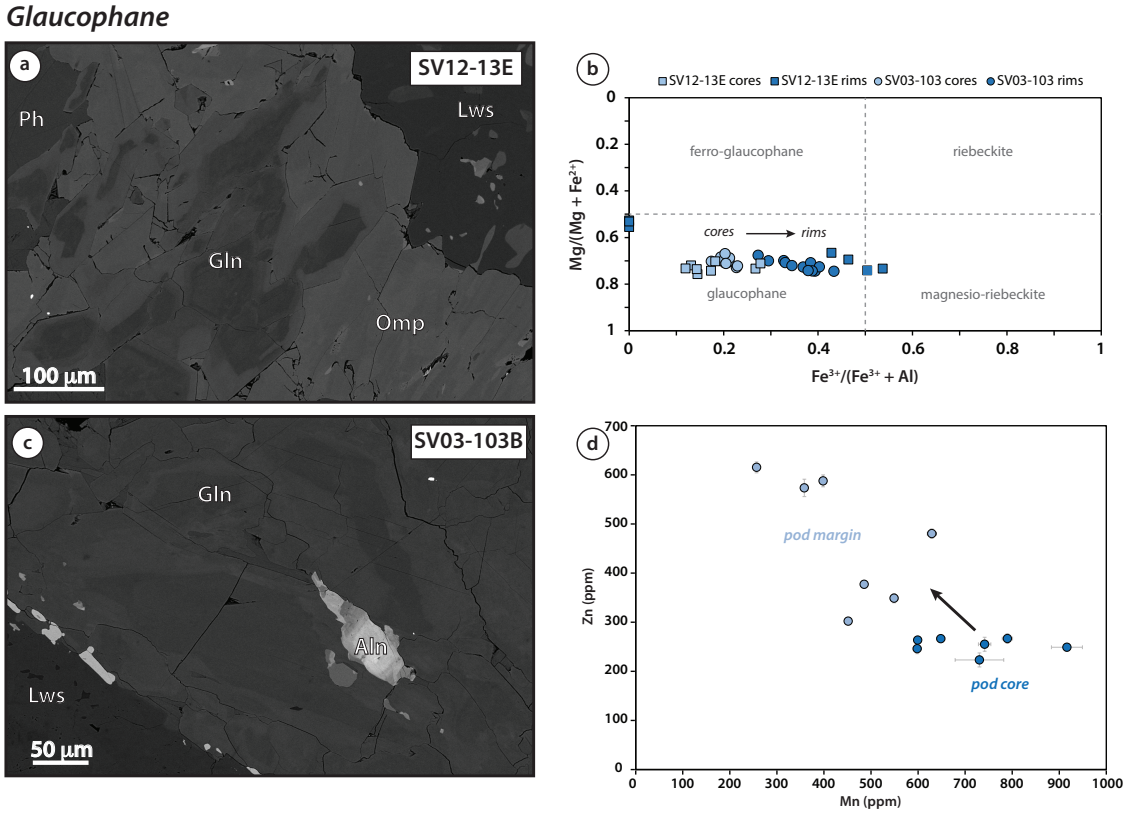

Figure 14. Backscattered electron (BSE) images of glaucophane from the core of the lawsonite eclogite pod (SV12-13E, a) and the glaucophane-rich margin (SV03-103B, c). Variations in major elements, and Mn and Zn contents between glaucophane from the core of the pod and the margin of the pod are shown in b and d, respectively.

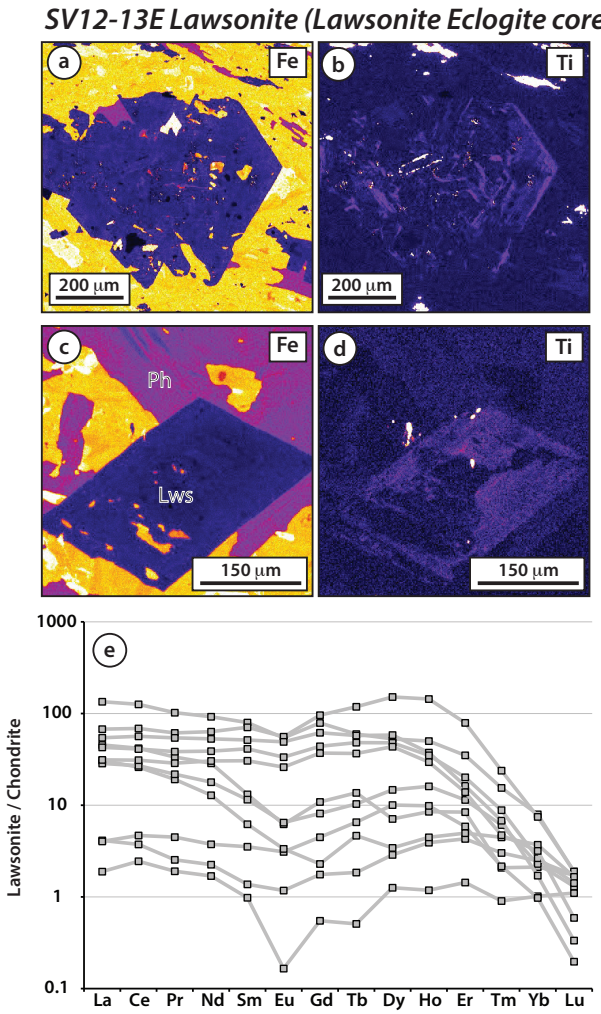

Figure 15. Fe and Ti X-ray element maps for polycrystalline lawsonite (a,b) and euhedral lawsonite (c,d), as well as the chondrite-normalized REE patterns for all lawsonite types from the core of the eclogite pod (SV12-13E).

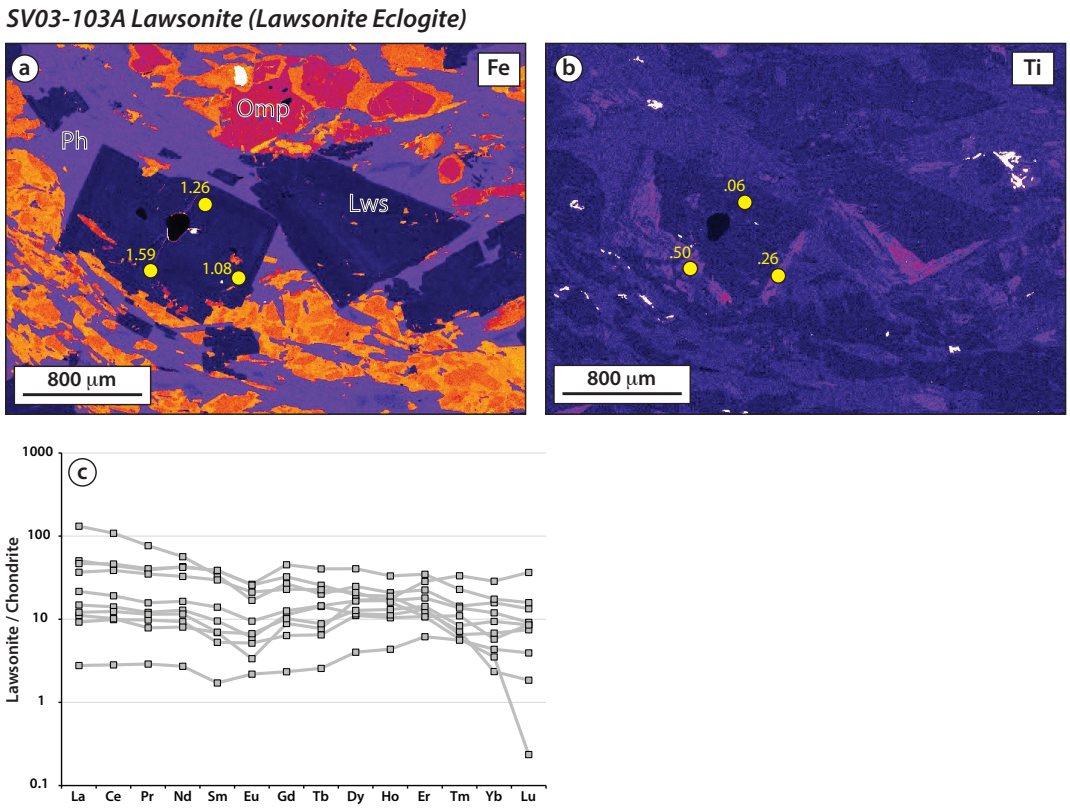

Figure 16. Fe (a) and Ti (b) X-ray element maps and chondrite-normalized REE patterns (c) for lawsonite in eclogite layers at the pod margin (SV03-103A). FeO (a) and TiO_2 (b) contents (in wt.%) for sample microprobe analyses are also shown.

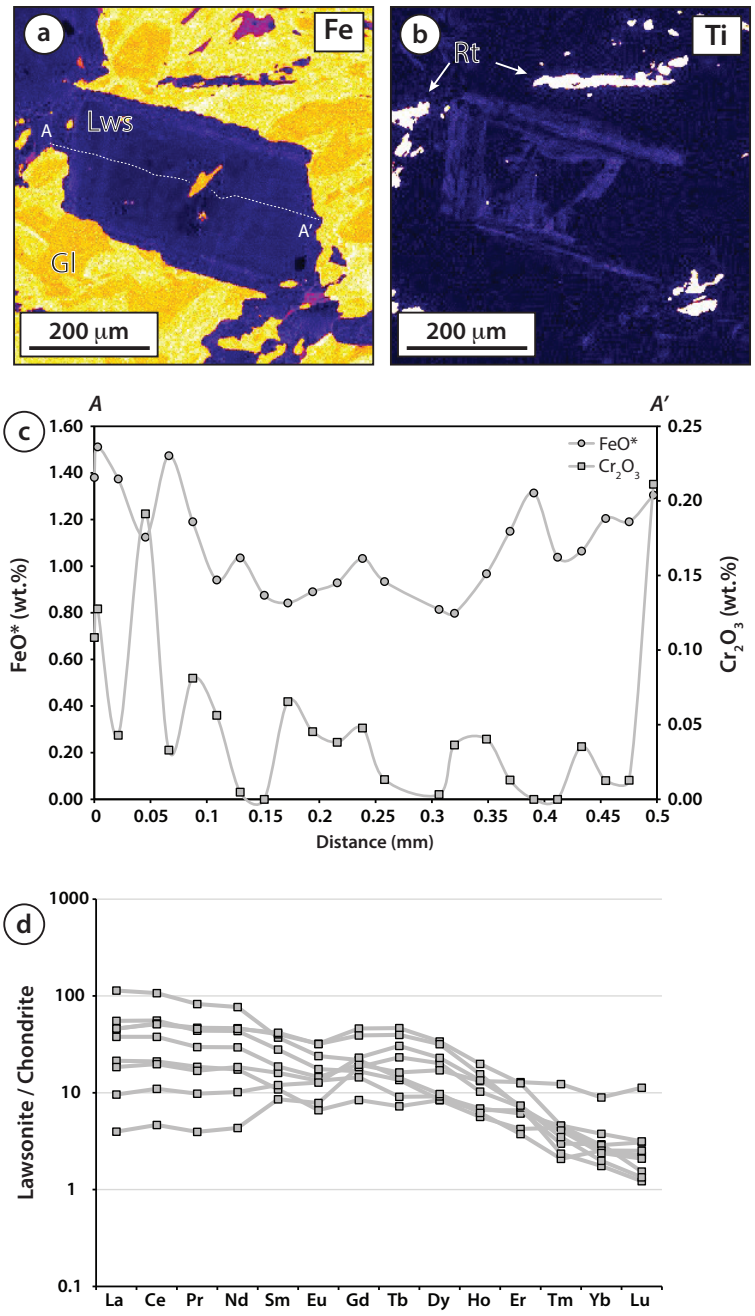

Figure 17. Representative Fe (a) and Ti (b) X-ray element maps, and chondrite-normalized REE patterns (d) for lawsonite in the glaucophane-rich margin. Microprobe traverses across the grain highlight the oscillatory Fe and Cr zoning (c).

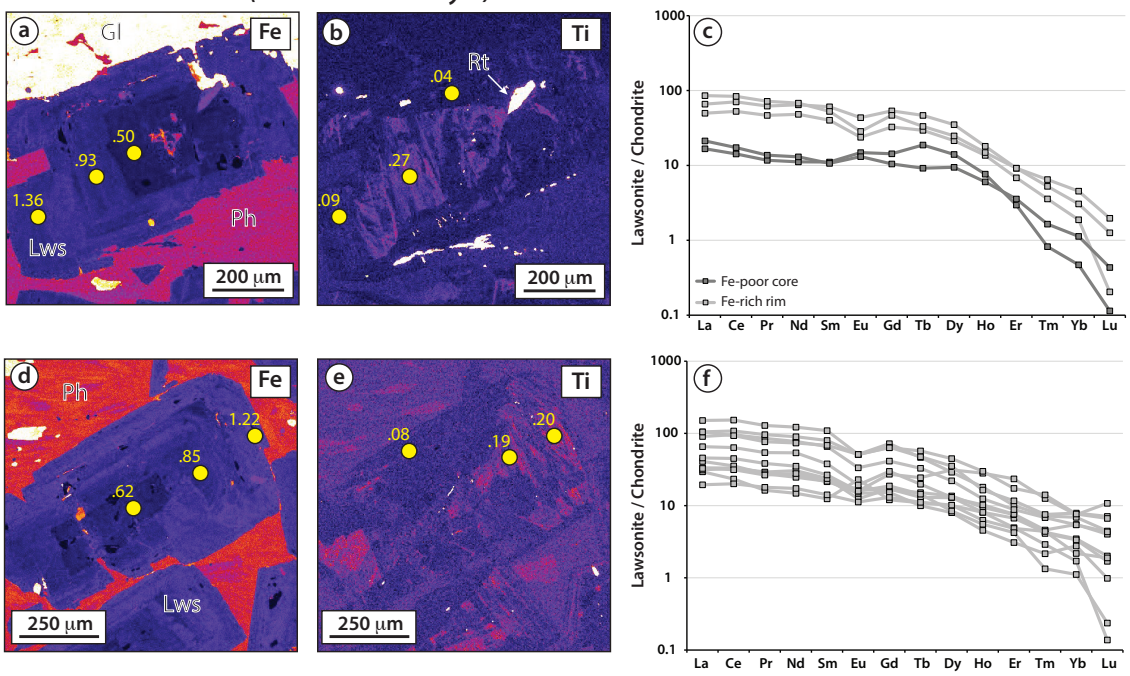

Figure 18. Representative Fe and Ti X-ray element maps and rare earth element patterns for lawsonite from the lawsonite + garnet + phengite-rich layer margin (a, b, c) and layer center (d, e, f). FeO* (a, d) and TiO_2 (b, e) contents (in wt.%) for sample microprobe analyses are also shown.

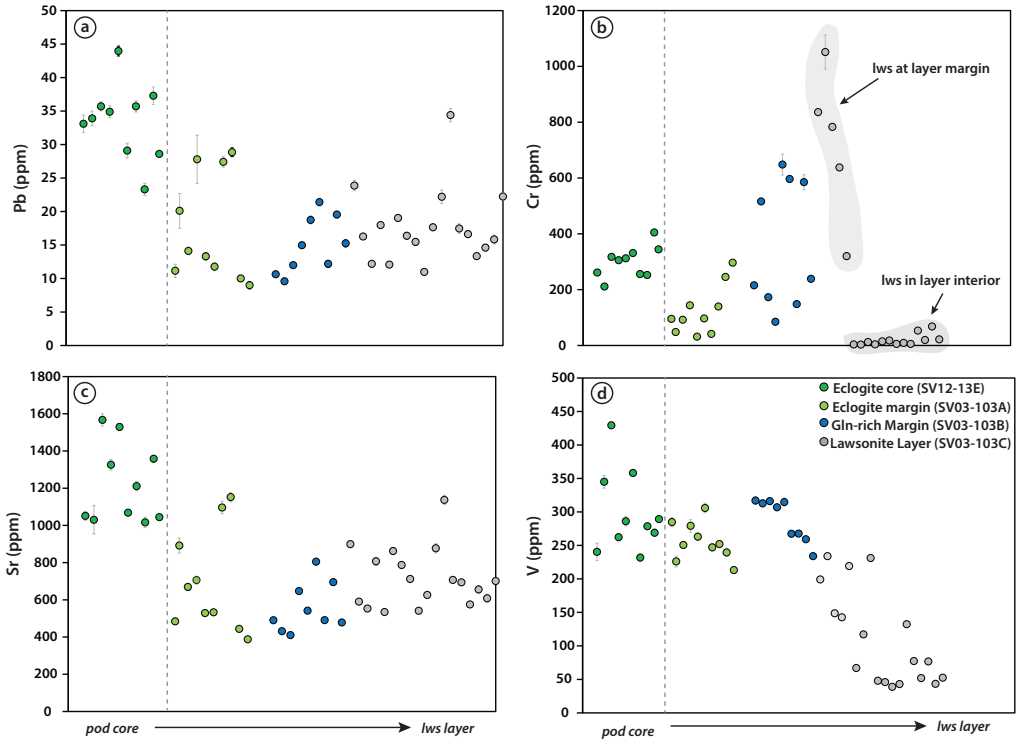

Figure 19. Changes in the concentration of Pb (a), Cr (b), Sr (c), and V (d) in lawsonite along a transect from the lawsonite eclogite pod core to the lawsonite + garnet + phengite-rich layer. Dashed line denotes the separation between lawsonite analyses from the core of the pod, and lawsonite analyses from the individual lithologic layers at the pod margin.

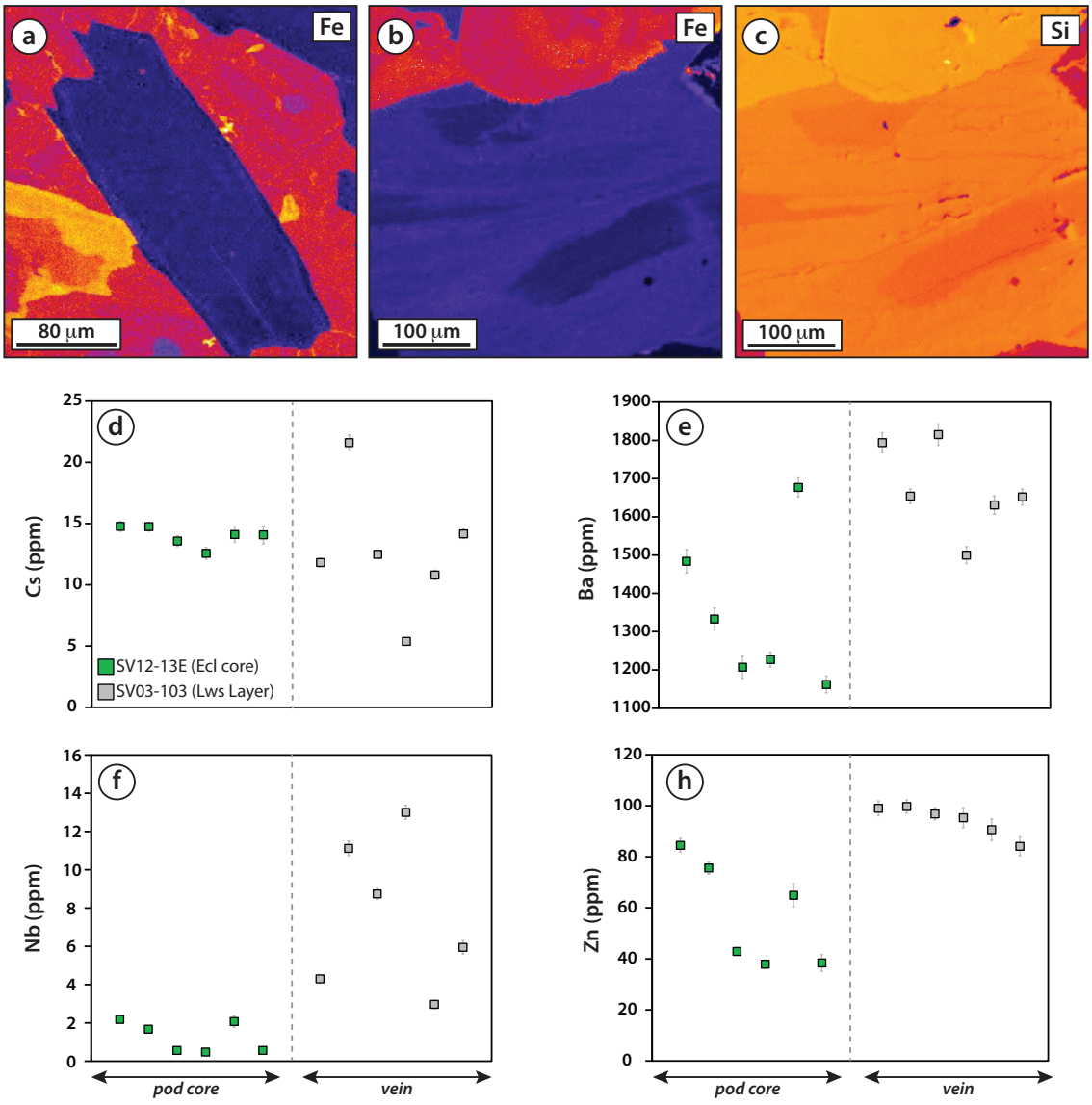

Figure 20. Representative Fe and Si X-ray element maps for phengite from the pod core (a) and phengite from pod margin (b, c) highlighting intra-grain zoning features. Variations in Cs, Ba, Nb, and Zn concentrations between phengite from the pod core and phengite from the pod margin are also shown in d, e, f, and g, respectively. Dashed line denotes the separation between phengite analyses from the pod core and phengite analyses from the lawsonite + garnet + phengite-rich layer.

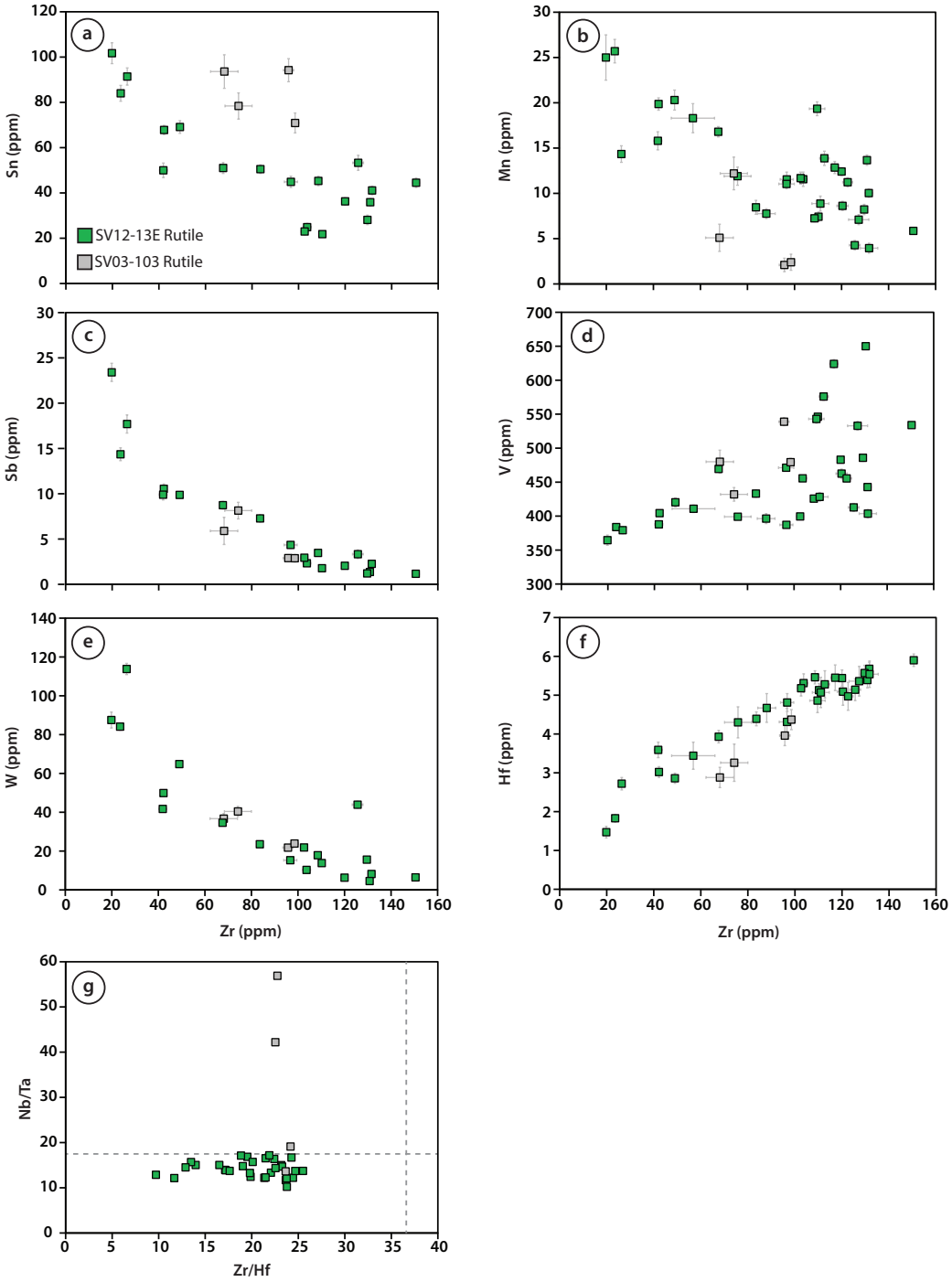

Figure 21. Correlations between Zr content (ppm) in rutile and Sn (a), Mn (b), Sb (c), V (d), W (e), and Hf (f) content (ppm) in rutile. Plot of Zr/Hf vs. Nb/Ta ratios in rutile from the core of the eclogite pod and rutile from the glaucophane-rich margin and lawsonite + garnet + phengite-rich layer (g); dashed lines indicate the chondritic Nb/Ta (Jochum et al. 2000) and Zr/Hf (Sun and McDonough 1989) values.

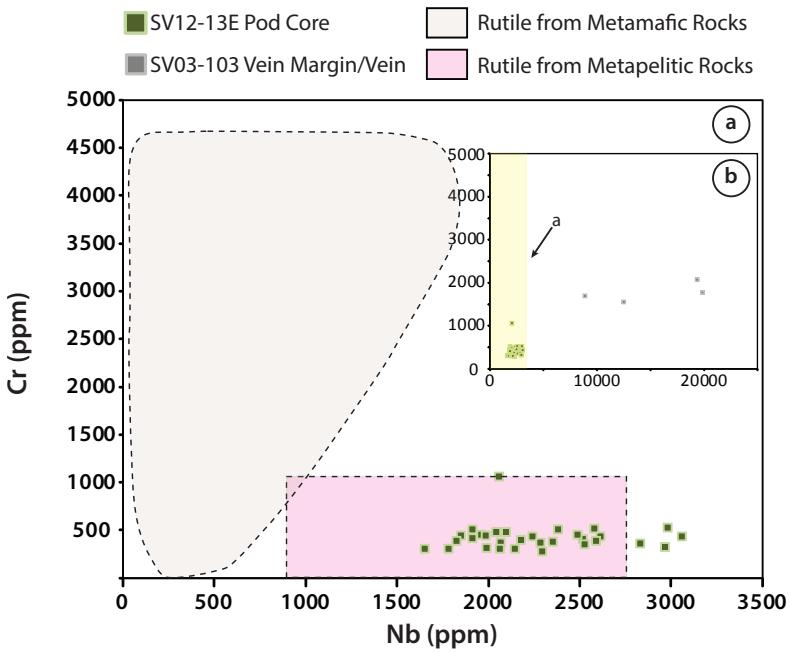

Figure 22. Plot of Nb (ppm) vs. Cr (ppm) content in rutiles from the core of the eclogite pod (a) and the glaucophane-rich margin and lawsonite + garnet + phengite-rich layer (b). Fields denoting boundaries for metamafic-derived rutiles and metapelite-derived rutiles follow the recommendations of Zack et al. 2004. Inset within each figure shows the region where rutile from the glaucophane-rich margin and lawsonite vein plot compared to the rutiles from the core of the eclogite pod (shown in shaded region labeled a).

Supplementary Material 1. Sample locations

	UTM Coordinates[a]	
	Easting (m)	**Northing (m)**
Lawsonite + Garnet + Phengite Vein and Eclogite Host		
SV12-13E; SV03-103A,B,C	351574	4384265
Monomineralic Lawsonite Vein		
SV12-24B	344581	4386678

[a]Coordinates are reported using the ED 1950 (UTM) reference system, south hemisphere, zone 36

Supplementary Material 2. XRCT scanning conditions

UMN XRCT
CT Acquisition
Technique Sheet

Sample SV12-13E

Xray source: Feinfocus FXE
- voltage: 170 kV
- focal spot size: 6 microns
- focal spot mode: n/a

Detector: Dexela 2923 [2237]
- pixel pitch: [75 x 75] microns
- mode: Sequence (Low gain)
- gain:
- binning: 1x1
- framerate: 1.3 fps (769.234 ms integration time)

- flip: horizontal
- rotation: none
- crop: none

- defect map: 89318 defective pixels (0.74737486232205%)
- offset map: 0.0969, dev 0.00567, 150 fravg, 1.3 fps
- gain map 0: 0.763, dev 0.0546, 150 fravg, 1.3 fps
- gain map 1: 0.46, dev 0.0326, 150 fravg, 1.3 fps
- gain map 2: 0.0841, dev 0.00532, 150 fravg, 1.3 fps

Distances:
- tube to detector: 750 [mm] (FDD)
- tube to part: 115 [mm] (FOD)
- calculated Ug: 0.03313 [mm](0.442 pixels)
- zoom factor: x6.52

Fixturing:
Filter: 170kv 19.0w 1.3fps 0.005" Cu

CT Scan:
- project name: E:\SV12-13F\SV12-13F.nsipro
- type: step
- # projections: 1080
- # frames averaged: 3
- delay: 0 ms
- monitor xray down: max allowed image variation 4%
- start: 6/23/2015 11:57:31 AM
- end: 6/23/2015 1:06:45 PM
- duration: 1h09m13s

UMN XRCT
CT Acquisition
Technique Sheet

Sample SV03-103

Xray source: Feinfocus FXE
- voltage: 150 kV
- focal spot size: 6 microns
- focal spot mode: n/a

Detector: Dexela 2923 [2237]
- pixel pitch: [75 x 75] microns
- mode: Sequence (Low gain)
- gain:
- binning: 1x1
- framerate: 1.9 fps (526.314 ms integration time)

- flip: horizontal
- rotation: none
- crop: none

- defect map: 89318 defective pixels (0.74737486232205%)
- offset map: 0.0946, dev 0.00549, 200 fravg, 1.9 fps
- gain map 0: 0.77, dev 0.0606, 200 fravg, 1.9 fps
- gain map 1: 0.449, dev 0.0381, 200 fravg, 1.9 fps
- gain map 2: 0.0767, dev 0.00536, 200 fravg, 1.9 fps

Distances:
- tube to detector: 747.657 [mm] (FDD)
- tube to part: 145.191 [mm] (FOD)
- calculated Ug: 0.0249 [mm](0.332 pixels)
- zoom factor: x5.15

Fixturing:
Filter: 150kv 21.0w 1.9fps

CT Scan:
- project name: E:\SV03-103-billet\SV03-103-billet.nsipro
- type: step
- # projections: 1080
- # frames averaged: 3
- delay: 0 ms
- monitor xray down: max allowed image variation 4%
- start: 6/24/2015 10:29:31 AM
- end: 6/24/2015 11:17:11 AM
- duration: 47m39s

Supplementary Material 3. Histograms of garnet volume (determined from XRCT analyses)

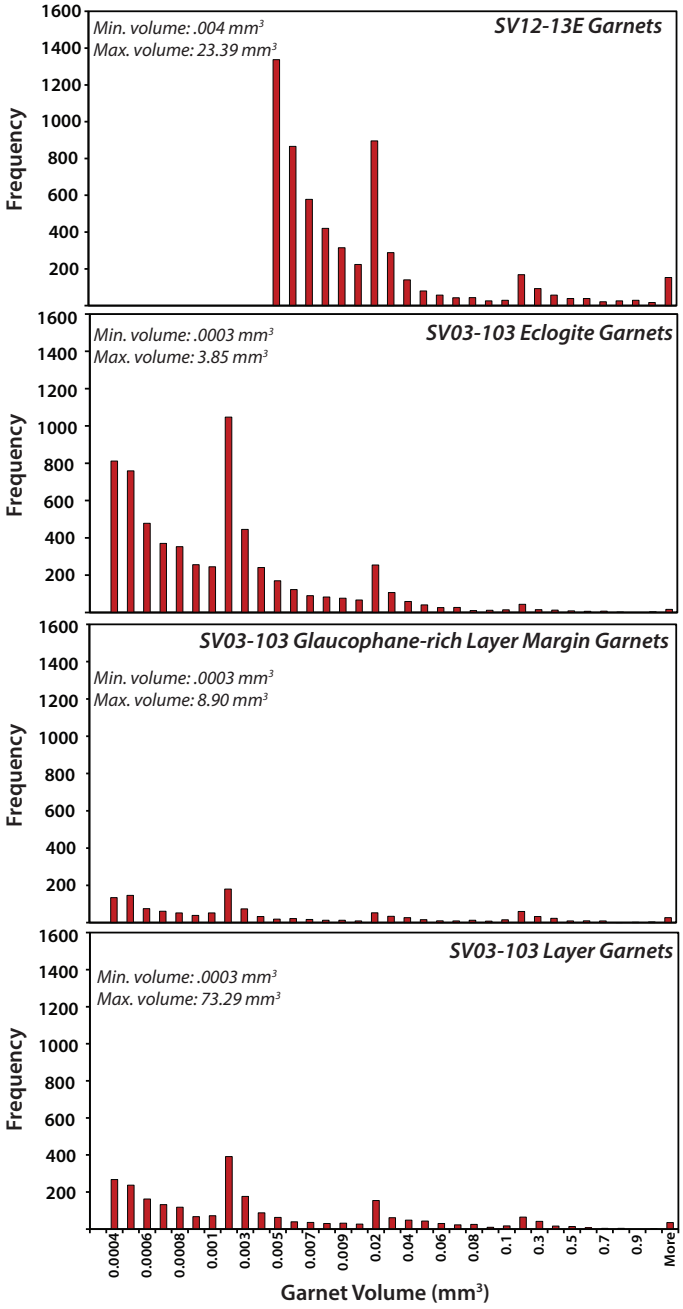

Supplementary Material 4. Plot of Ni vs. Cr bulk rock systematics

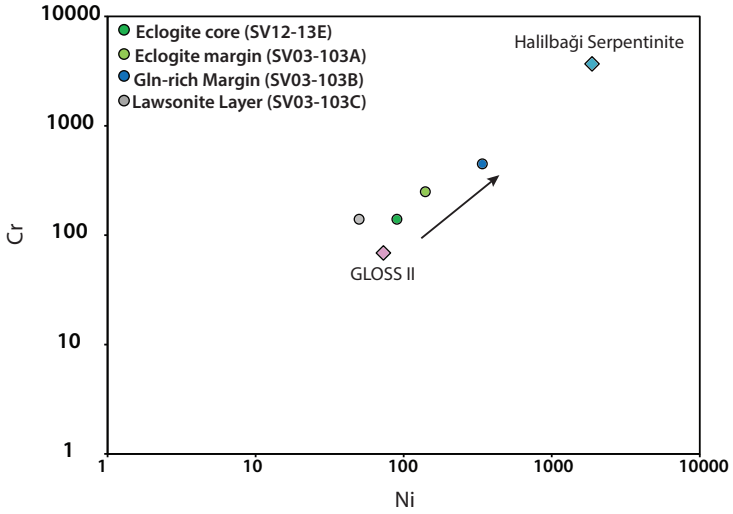

Chapter 5. Conclusion

Subduction zones are some of the most geologically active regions on the Earth. Not only are they sites of some of the largest earthquakes, but they are also the location where a significant fraction of the Earth's magmatism is generated. Thermal models of modern subduction zones, as well as geochemical studies of arc magmas and geophysical observations, have suggested that much of the geologic activity found in subduction zones may ultimately be the result of fluids expelled during the dehydration of the subducting slab.

While the mechanisms for the addition of water to the slab are relatively well-constrained, the fate of the fluids after they have been released is largely unknown. HP-LT metamorphic rocks, and the hydrous phases and metasomatic features preserved in them, provide an accessible record of fluid processes in subduction zones that can be interrogated using a variety of petrologic, geochemical, and microstructural techniques. Application of these techniques to the HP/LT rocks of the Sivrihisar Massif, Tavşanlı Zone, Turkey, provides new insights into the timing of HP/LT metamorphic events in the region, as well as evidence for geochemical interactions between the different lithologies interlayered within the terrane (metasediment, metabasaltic, and ultramafic). As the rocks of the Sivrihisar Massif were metamorphosed and deformed at the slab-mantle interface (Teyssier et al. 2010, Whitney et al. 2014), information about the timing of metamorphism, deformation and fluid-rock interaction (prograde, peak, retrograde), as well as the sources, compositions, and pathways of fluids in this paleosubduction

complex, may provide constraints on the geochemical and geodynamic evolution of this otherwise inaccessible interface.

The slab-mantle interface is a structurally and geochemically complex region, characterized by the juxtaposition of different lithologies, such as altered oceanic crust, sediments, and ultramafic material, which vary not only in their compositions and water content, but also in their rheology and deformation behavior. Field-based studies of exhumed subduction complexes have shown that the tectonic juxtaposition of these lithologies can occur at different scales (mm – to –km), leading to the suggestion that there may be different "tectonic styles" preserved at the slab – mantle interface (e.g., structurally coherent vs. mélange). In exhumed subduction complexes where the mafic material occurs as blocks in an ultramafic or metasedimentary mélange, the blocks commonly show evidence for substantial fluid-rock interaction and transport of fluid-mobile elements, resulting in the formation of metasomatic alteration rinds on the blocks. In subduction complexes that were exhumed as structurally coherent terranes, on the other hand, there appears to be evidence for only limited element mobility and fluid-rock interaction. However, in the Sivrihisar Massif, which was exhumed as a largely coherent but intensely deformed terrane, HP/LT rocks record evidence for complex interactions amongst metasedimentary, metabasaltic, and ultramafic reservoirs at a variety of scales, similar to what is observed in mélange. Although the mechanism (mechanical mixing and/or fluid-rock interaction) for mass transfer between these different lithologies is not always clear, the common occurrence of oscillatory and/or patchy zoning in minerals, the abundance of hydrous phases (20 – 40 % modal abundance in some rocks), and the

development of lawsonite-rich veins and layers at pod margins, suggests that fluid-rock interaction played an important role.

The timing of fluid-rock interaction in the Sivrihisar Massif remains an open question. *In situ* UV laser $^{40}Ar/^{39}Ar$ geochronology of phengite from a lawsonite + garnet + phengite-rich layer hosted in lawsonite eclogite yields ages ranging from 86.1 ± 3.7 Ma to 102.8 ± 3.9 Ma. These ages overlap within error the $^{40}Ar/^{39}Ar$ ages obtained for lawsonite eclogites (87.7 ± 2.5 Ma to 99.8 ± 3.7 Ma) in the region, suggesting that the lawsonite-rich layer may have formed coevally with peak eclogite facies metamorphism (Chapter 2). Although scatter in the age data precludes a definitive interpretation, this conclusion is broadly consistent with interpretations about the relative timing of lawsonite + garnet + phengite layer formation based on petrographic observations and systematic variations in the zoning patterns and compositions of minerals from the lawsonite + garnet + phengite-rich layer and its associated host rocks (Chapter 4). Monomineralic lawsonite veins and vein networks at the margins of lawsonite blueschist and chlorite + epidote-rich pods, on the other hand, likely document fluid-rock interaction occurring during retrograde metamorphism.

In addition to differences in mineral assemblages, lawsonite from these different vein generations also record differences in their Sr/Pb ratios, with lawsonite from the lawsonite + garnet + phengite-rich layer recording high Sr/Pb ratios and lawsonite from the monomineralic lawsonite vein recording low Sr/Pb ratios (Chapter 3), suggesting that the source of the fluids (mafic/ultramafic vs. metasedimentary) may have also varied along the P-T path. However, additional work linking Sr/Pb ratios in lawsonite, with

other monitors of fluid-rock interaction, such as stable isotopes (O, H) in lawsonite, would be needed to confirm that variations in lawsonite Sr/Pb ratios track fluid-rock interaction, as Sr/Pb ratios in lawsonite from other HP/LT terranes does not always exhibit consistent behavior.

In the Sivrihisar Massif, as in other HP/LT terranes, there is evidence that fluid-rock interaction enhanced element mobility, even for elements such as the HFSE and the transition metals (Fe, Ti, Cr) that are commonly assumed to immobile in aqueous fluids. This evidence includes the preferential concentration of HFSE-bearing accessory phases, such as rutile and zircon, in lawsonite + garnet + phengite-rich layers and their associated glaucophane-rich reaction margins (Chapter 4), as well as the concentration of Ti along grain boundaries in some lawsonite grains (Chapter 3). In some lawsonite, there is also evidence that the development of subgrains modified the intra-grain distribution of Fe and Ti (Chapter 3), indicating that deformation may also enhance the mobility of transition metals in the subduction system.

COMPREHENSIVE BIBLIOGRAPHY

Abers GA, Sarker G (1996) Dispersion of regional body waves at 100-150 km depth beneath Alaska: in situ constraints on metamorphism of subducted crust. Geophysical Research Letters 23: 1171–1174.

Abers GA, van Keken PE, Kneller EA, Ferris A, Stachnik JC (2006) The thermal structure of subduction zones constrained by seismic imaging: Implications for slab dehydration and wedge flow. Earth and Planetary Science Letters 241: 387 – 397.

Abers GA, Nakajima J, van Keken PE, Kita S, Hacker BR (2013) Thermal-petrological controls on the location of earthquakes within subducting plates. Earth and Planetary Science Letters 369: 178 – 187.

Agard P, Monie P, Jolivet L, Goffe B (2002) Exhumation of the Schistes Lustres complex: in situ laser probe $^{40}Ar/^{39}Ar$ constraints and implications for the Western Alps. J Metamorph Geol 20:599 – 618.

Antignano A, Manning CE (2008) Rutile solubility in H2O, H2O-SiO2, and H2O-NaAlSi3O8 fluids at 0.7 – 2.0 GPa and 700 – 1000 degrees C: Implications for mobility of nominally insoluble elements. Chemical Geology 255: 283 – 293.

Angiboust S, Agard P, Raimbourg H, Yamato P, Huet B (2011) Subduction interface processes recorded by eclogite-facies shear zones (Monviso, W. Alps). Lithos 127: 222 – 238.

Angiboust S, Wolf S, Burov E, Agard P, Yamato P (2012) Effect of fluid circulation on subduction interface tectonic processes: Insights from thermo-mechanical numerical modeling. Earth and Planetary Science Letters 357 – 358: 238 – 248.

Anczkiewicz R, Platt JP, Thirwall MF, Wakabayashi J (2004) Franciscan subduction off to a slow start: evidence from high-precision Lu-Hf garnet ages on high grade-blocks. Earth and Planetary Science Letters 225: 147 – 161.

Arnaud NO, Kelley SP (1995) Evidence for excess argon during high pressure metamorphism in the Dora Maira Massif (western Alps, Italy), using an ultra-violet laser ablation microprobe ^{40}Ar-^{39}Ar technique. Contrib Mineral Petr 121:1 – 11.

Ayers JC, Watson EB (1993) Rutile solubility and mobility in supercritical aqueous fluids. Contributions to Mineralogy and Petrology 114: 321 – 330.

Ballevre M, Pitra P, Bohn M (2003) Lawsonite growth in epidote blueschists from the Ile de Groix (Armorican Massif, France): a potential geobarometer. Journal of Metamorphic Geology 21: 723 – 735.

Barnicoat AC (1988) Zoned High-Pressure Assemblages in Pillow Lavas of the Zermatt-Saas Ophiolite Zone, Switzerland. Lithos 21: 227 – 236.

Baxter EF, DePaolo DJ, Renne PR (2002) Spatially correlated anomalous $^{40}Ar/^{39}Ar$ "age" variations in biotites about a lithologic contact near Simplon Pass, Switzerland: A mechanistic explanation for excess Ar. Geochim Cosmochim Ac 66:1067 – 1083.

Beane RJ, Liou JG (2005) Metasomatism in Serpentinite Melange Rocks from the High-Pressure Maksyutov Complex, Southern Ural Mountains, Russia. International Geology Review 47: 24 – 40.

Bebout GE, Barton MD (1989) Fluid-flow and Metasomatism in a Subduction Zone Hydrothermal System-Catalina-Schist Terrane, California. Geology 11: 976 – 980.

Bebout GE (2007) Metamorphic chemical geodynamics of subduction zones. Earth and Planetary Science Letters 260: 373 – 393.

Becker H, Jochum KP, Carlson RW (1999) Constraints from high-pressure veins in eclogites on the composition of hydrous fluids in subduction zones. Chemical Geology 160: 291 – 308.

Beinlich A, Klemd R, John T, Guo J (2010) Trace-element mobilization during Ca-metasomatism along a major fluid conduit: Eclogitization of blueschist as a consequence of fluid-rock interaction. Geochimica et Cosmochimica Acta 74: 1892 – 1922.

Beltrando M, Lister GS, Forster M, Dunlap WJ, Fraser G, Hermann J (2009) Dating microstructures by the $^{40}Ar/^{39}Ar$ step-heating technique: Deformation-pressure-temperature-time history of the Penninic Units of the Western Alps. Lithos 113:801 – 819.

Beltrando M, Di Vincenzo G, Ferraris C (2013) Preservation of sub-microscopic structural relicts in micas from the Gran Paradiso Massif (Western Alps): Implications for Ar-40-Ar-39 geochronology. Geochim Cosmochim Ac 119:359 – 380.

Bons PD, Elburg MA, Gomez-Rivas E (2012) A review of the formation of tectonic veins and their microstructures. Journal of Structural Geology 43: 33 – 62.

Bosse V, Feraud G, Ballevre M, Peucat J, Corsini M (2005) Rb-Sr and $^{40}Ar/^{39}Ar$ ages in blueschists from the Ile de Groix (Armorican Massif, France): Implications for closure mechanisms in isotopic systems. Chem Geol 220:21 – 45.

Bröcker M, Baldwin S, Arkudas R (2013) The geological significance of $^{40}Ar/^{39}Ar$ and Rb-Sr white mica ages from Syros and Sifnos, Greece: a record of continuous (re)crystallization during exhumation? J Metamorph Geol 31: doi: 0.1111/jmg.12037.

Brunsmann A, Franz G, Erzinger J, Landwehr D (2001) Zoisite- and clinozoisite-segregations in metabasites (Tauern Window, Austria) as evidence for high-pressure fluid-rock interaction. Journal of Metamorphic Geology 18: 1 – 21.

Bucher K, Fazis Y, De Capitani C, Grapes R (2005) Blueschists, eclogites, and decompression assemblages of the Zermatt-Saas ophiolite: High-pressure metamorphism of subducted Tethys lithosphere. American Mineralogist 90: 821 – 835.

Burnham AD, Berry AJ (2012) An experimental study of trace element partitioning between zircon and melt as a function of oxygen fugacity. Geochimica et Cosmochimica Acta 95: 196 – 212.

Cao Y, Jung H, Song S (2014) Microstructres and petro-fabrics of lawsonite blueschist in the North Qilian suture zone, NW China: Implications for seismic anisotropy of subducting oceanic crust. Tectonophysics 628: 140 – 157.

Cao Y, Jung H (2016) Seismic properties of subducting oceanic crust: Constraints from natural lawsonite-bearing blueschist and eclogite in Sivrihisar Massif, Turkey, Physics of the Earth and Planetary Interiors: doi: http://dx.doi.org/10.1016/j.pepi.2015.10.003.

Çetinkaplan M, Candan O, Oberhansli R, Bousquet R (2008) Pressure-temperature evolution of lawsonite eclogite in Sivrihisar; Tavşanlı Zone-Turkey. Lithos 104:12 – 32.

Chantel J, Mookherjee M, Frost DJ (2012) The elasticity of lawsonite at high pressure and the origin of low velocity layers in subduction zones. Earth and Planetary Science Letters 349: 116 – 125.

Clarke GL, Aitchison JC, Cluzel D (1997) Eclogites and Blueschists of the Pam Peninsula, NE New Caledonia: a Reappraisal. Journal of Petrology 38: 843 – 876.

Coğulu E, Krummenacher D (1967) Problemes geochronometriques dans la partie NW de l'Anatolie Centrale (Turquie). Schweizerische mineralogische und petrographische Mitteilungen 47: 825 – 833.

Connolly JAD, Kerrick DM (2002) Metamorphic controls on seismic velocity of subducted oceanic crust at 100-250 km depth. Earth and Planetary Science Letters 204: 61–74.

Cosca MA, Giorgis D, Rumble D, Liou JG (2005) Limiting effects of UHP Metamorphism on Length Scales of Oxygen, Hydrogen, and Argon Isotope Exchange: An Example from the Qinglongshan UHP Eclogites, Sulu Terrain, China. Int Geol Rev 47:716 – 749.

Dahl PS (1996) The crystal-chemical basis for Ar retention in micas: inferences from interlayer partitioning and implications for geochronology. Contrib Mineral Petr 123:22 – 39.

Davis GA (1960) Lawsonite and pumpellyite in glaucophane schist, North Berkeley Hills, California, with notes on the X-ray crystallography of lawsonite, by A. Pabst. American Journal of Science 258: 689 – 704.

Davis PB, Whitney DL (2006) Petrogenesis of lawsonite and epidote eclogite and blueschist, Sivrihisar Massif, Turkey. Journal of Metamorphic Geology 24: 823 – 849.

Davis PB, Whitney DL (2008) Petrogenesis and structural petrology of high-pressure metabasalt pods, Sivrihisar, Turkey. Contributions to Mineralogy and Petrology 156: 217 – 241.

Davis PB (2011) Petrotectonics of lawsonite eclogite exhumation: Insights from the Sivrihisar Massif, Turkey. Tectonics 30: doi:10.1029/2010TC002713.

Delaloye M, Bingol E (2000) Granitoids from Western and Northwestern Anatolia: Geochemistry and Modeling of Geodynamic Evolution. Int Geol Rev 42:241 – 268.

Dempster TJ (1992) Zoning and recrystallization of phengitic micas: implications for metamorphic equilibrium. Contrib Mineral Petr 109:526 – 537.

Dilek Y, Whitney DL (1997) Counterclockwise P-T-t trajectory from the metamorphic sole of a Neo-Tethyan ophiolite (Turkey). Tectonophysics 280: 295 – 310.

Di Vincenzo G, Ghiribelli B, Giorgetti G, Palmeri R (2001) Evidence of a close link between petrology and isotope records: constraints from SEM, EMP, TEM and in situ ^{40}Ar-^{39}Ar laser analyses on multiple generations of white micas (Lanterman Range, Antarctica). Earth Planet Sc Lett 192:389- 405.

Di Vincenzo G, Carosi R, Palmeri R (2004) The Relationship between Tectono-metamorphic Evolution and Argon Isotope Records in White Mica: Constraints from in situ ^{40}Ar-^{39}Ar Laser Analysis of the Variscan Basement of Sardinia. J Petrol 45:1013 – 1043.

Di Vincenzo G, Tonarini S, Lombardo B, Castelli D, Ottolini L (2006) Comparison of ^{40}Ar-^{39}Ar and Rb-Sr Data on Phengites from the UHP Brossasco-Isasca Unit (Dora Maira Massif, Italy): Implications for Dating White Mica. J Petrol 47: 1439 – 1465.

Dodson MH (1973) Closure Temperature in Cooling Geochronological and Petrological Systems. Contrib Mineral Petr 40: 259 – 274.

Domanik KJ, Holloway JR (1996) The stability and composition of phengitic muscovite and associated phases from 5.5 to 11 GPa: Implications for deeply subducted sediments. Geochemica et Cosmochimica Acta 60: 4133 – 4150.

Droop GTR, Karakaya MC, Eren Y, Karakaya N (2005) Metamorphic evolution of blueschists of the Altinekin Complex, Konya area, south central Turkey. Geological Journal 40: 127 – 153.

Eggins SM, Rudnick RL, McDonough WF (1998) The composition of peridotites and their minerals: a laser ablation ICP-MS study. Earth and Planetary Science Letters 154: 53 – 71.

Federico L, Capponi G, Crispini L, Scambelluri M, Villa I.M (2005) ^{39}Ar/^{40}Ar dating of high-pressure rocks from the Ligurian Alps: Evidence for a continuous subduction-exhumation cycle. Earth Planet Sc Lett 240:668 – 680.

Foland KA (1979) Limited mobility of argon in a metamorphic terrain. Geochim Cosmochim Ac 43:793 – 801.

Forster MA, Lister GS (2014) $^{40}Ar/^{39}Ar$ geochronology and the diffusion of ^{39}Ar in phengite-muscovite intergrowths during step-heating experiments *in vacuo*. In: Jourdan F, Mark DF, Verati C (eds) Advances in $^{40}Ar/^{39}Ar$ Dating: from Archaology to Planetary Sciences, Geological Society, London, Special Publications, 378, pp 117 – 135.

Franz G, Romer RL, Klemd R, Schmid R, Oberhansli R, Wagner T, Shuwen D (2001) Eclogite-facies quartz veins within metabasites of the Dabie Shan (eastern China): pressure-temperature-time-deformation path, composition of the fluid phase and fluid flow during exhumation of high-pressure rocks. Contributions to Mineralogy and Petrology 141: 322 – 346.

Fujimoto Y, Kono Y, Hirajima T, Kanagawa K, Ishikawa M, Arima M (2010) P-wave velocity and anisotropy of lawsonite and epidote blueschists: constraints on water transportation along subducting oceanic crust. Physics of the Earth and Planetary Interiors 183: 219 – 228.

Gao J, Klemd R (2001) Primary fluids entrapped at blueschist to eclogite transition: evidence from the Tianshan meta-subduction complex in northwestern China. Contributions to Mineralogy and Petrology 142: 1 – 14.

Gao J, John T, Klemd R, Xiong X (2007) Mobilization of Ti-Nb-Ta during subduction: Evidence from rutile-bearing dehydration segregations and veins hosted in eclogite, Tianshan, NW China. Geochimica et Cosmochimica Acta 71: 4974 – 4996.

Gauthiez-Putallaz L, Rubatto D, Hermann J, Martin L, Fornash KF, Whitney D (2014) Sediment-Eclogite Fluid Exchanges during Subduction in the Tavsanli Zone, Turkey. Goldschmidt Abstracts, 778.

Gautier Y (1984) Deformations et Metamorphismes Associes a la Fermeture Tethysienne en Anatolie Centrale (Region de Sivrihisar, Turquie. Ph.D. Thesis University Paris-Sud, 236 pp.

George A, Grapes R (1987) Lawsonite-bearing veins in Torlesse rocks. New Zealand Journal of Geology and Geophysics 30: 203 – 205.

Giaramita MJ, Sorensen SS (1994) Primary Fluids in Low-Temperature Eclogites-Evidence from 2 Subduction Complexes (Dominican Republic, and California, USA). Contributions to Mineralogy and Petrology 117: 279 – 292.

Giorgis D, Cosca MA, Li S (2000) Distribution and significance of extraneous argon in UHP eclogite (Sulu terrain, China): insight from in situ $^{40}Ar/^{39}Ar$ UV-laser ablation analysis. Earth Planet Sc Lett 181:605- 615.

Gray DR, Miller J, Foster DA, Gregory RT (2004) Transition from subduction- to exhumation-related fabrics in glaucophane-bearing eclogites, Oman: evidence from relative fabric chronology and 40Ar/39Ar ages. Tectonophysics 389:35 – 64.

Guo S, Ye K, Chen Y, Liu J, Mao Q, Ma Y (2012) Fluid-rock interaction and element mobilization in UHP metabasalt: Constraints from an omphacite-epidote vein and host eclogites in the Dabie orogen. Lithos:145 – 167.

Guo S, Ye K, Wu TF, Chen Y, Yang YH, Zhang LM, Liu JB, Mao Q, Ma YG (2013) A potential method to confirm the previous existence of lawsonite in eclogite: the mass

imbalance of Sr and LREEs in multistage epidote (Ganghe, Dabie UHP terrane). Journal of Metamorphic Geology 31: 415 – 435.

Guo S, Chen Y, Ye K, Su B, Yang Y, Zhang L, Liu J, Mao Q (2015) Formation of multiple high-pressure veins in ultrahigh-pressure eclogite (Hualiangting, Dabie terrane, China): Fluid source, element transfer, and closed-system metamorphic veining. Chemical Geology 417: 238 – 260.

Hacker BR (1996) Eclogite formation and the rheology, buoyancy, seismicity, and H2O content of oceanic crust. In: Subduction: Top to Bottom (eds Bebout, G.E., Scholl, D. & Kirby, S.), pp. 337–346. AGU, Washington, DC.

Hacker BR, Peacock SM, Abers GA, Holloway SD (2003) Subduction factory 2. Are intermediate-depth earthquakes in subducting slabs linked to metamorphic dehydration reactions? Journal of Geophysical Research 108: 1 – 16.

Halama R, Konrad-Schmolke M, Sudo M, Marschall HR, Wiedenback M (2014) Effects of fluid-rock interaction on $^{40}Ar/^{39}Ar$ geochronology in high-pressure rocks (Sesia-Lanzo Zone, Western Alps). Geochim Cosmochim Ac 126:475 – 494.

Harris NBW, Kelley S, Okay AI (1994) Post-collision magmatism and tectonics in northwest Anatolia. Contributions to Mineralogy and Petrology 117:241 – 252.

Harrison TM, Celerier J, Aikman AB, Hermann J, Heizler MT (2009) Diffusion of ^{40}Ar in muscovite. Geochim Cosmochim Ac 73:1039 – 1051.

Jochum KP, Stolz AJ, McOrist G (2000) Niobium and tantalum in carbonaceous chondrites: constraints on the solar system and primitive mantle niobium/tantalum,

zirconium/niobium, and niobium/uranium ratios. Meteoritics and Planet Science 35: 229 – 235.

John T, Klemd R, Gao J, Garbe-Schonberg C-D (2008) Trace element mobilization in slabs due to non steady-state fluid-rock interaction: Constraints from an eclogite-facies transport vein in blueschist (Tianshan, China). Lithos 103: 1 – 24.

Kelley SP, Wartho JA (2000) Rapid kimberlite ascent and the significance of Ar-Ar ages in xenolith phlogopites. Science 289:609 – 611.

Ketcham RA (2005) Computational methods for quantitative analysis of three-dimensional features in geological specimens. Geosphere 1: 32 – 41.

Kim D, Katayama I, Michibayashi K, Tsujimori T (2013) Rheological contrast between glaucophane and lawsonite in naturally deformed blueschist from Diablo Range, California. Island Arc 22: 63 – 73.

Kim D, Katayama I, Wallis S, Michibayashi K, Miyake A, Seto Y, Azuma S (2015) Deformation microstructures of glaucophane and lawsonite in experimentally deformed blueschists: implications for intermediate-depth intraplate earthquakes. Journal of Geophysical Research: Solid Earth 120: 1229 – 1242.

Kirby SH, Engdahl ER, Denlinger RP (1996) Intermediate-depth intraslab earthquakes and arc volcanism as physical expressions of crustal and uppermost mantle metamorphism in subducting slabs. In: Bebout, G.E., Scholl, D.W., Kirby, S.H., Platt, J.P. (Eds.), Subduction top to bottom. American Geophysical Union, Washington, pp. 195 – 214.

Kita S, Okada T, Nakajima J, Matsuzawa T, Hasegawa A (2006) Existence of a seismic belt in the upper plane of the double seismic zone extending in the along-arc direction at depths of 70-100 km beneath NE Japan. Geophysical Research Letters 33: L24310.

Krogh EJ, Oh CW, Liou JG (1994) Polyphase and anticlockwise P-T evolution for Franciscan eclogites and blueschists from Jenner, California, USA. Journal of Metamorphic Geology 12: 121 – 134.

Kramar N, Cosca MA, Hunziker JC (2001) Heterogeneous ^{40}Ar* distributions in naturally deformed muscovite: in situ UV-laser ablation evidence for microstructurally controlled intragrain diffusion. Earth Planet Sc Lett 192:377 – 388.

Kuiper KF, Deino A, Hilgen FJ, Krijgsman W, Renne PR, Wijbrans JR (2008) Synchronizing rock clocks of Earth history. Science 320, 500 – 504.

Kulaksız S (1978) Sivrihisar kuzeybatı eklojitleri. Yerbilimleri 4:89 – 94.

Lee J-Y, Marti K, Severinghaus JP, Kawamura K, Yoo H-S, Lee JB, Kim JS (2006) A redetermination of the isotopic abundances of atmospheric Ar. Geochim Cosmochim Ac 70: 4507 – 4512.

Li S, Wang S, Chen Y, Liu D, Qui J, Zhou H, Zhang Z (1994) Excess argon in phengite from eclogite: Evidence from dating of eclogite minerals by Sm-Nd, Rb-Sr, and ^{40}Ar/^{39}Ar methods. Chem Geol 112:343 – 350.

Li Z-X A, Lee C-T A (2004) The constancy of upper mantle fO_2 through time inferred from V/Sc ratios in basalts. Earth and Planetary Science Letters 228: 483 – 493.

Li XP, Li YL, Shu GM (2005) Breakdown of lawsonite subsequent to peak UHP metamorphism in the Dabie terrane and its implication for fluid activity. Chinese Science Bulletin 50: 1366 – 1372.

Li J.-L, Gao J, John T, Klemd R, Su W (2013) Fluid-mediated metal transport in subduction zones and its link to arc-related giant ore deposits: Constraints from a sulfide-bearing HP vein in lawsonite eclogite (Tianshan, China). Geochimica et Cosmochimica Acta 120: 326 - 362.

Lister GS, Baldwin SL (1996) Modelling the effect of arbitrary P-T-t histories on argon diffusion in minerals using the MacArgon program for the Apple Macintosh. Tectonophysics 253:83 -109.

Lister GS, Forster MA (2016) White mica $^{40}Ar/^{39}Ar$ age spectra and the timing of multiple episodes of high-P metamorphic mineral growth in the Cycladic eclogite-blueschist belt, Syros, Aegean Sea, Greece. J Metamorph Geol. doi: 10.1111/jmg.12178.

Lu Z, Zhang L, Du J, Yang X, Tian Z, Xia B (2012) Petrology of HP metamorphic veins in coesite-bearing eclogite from western Tianshan, China: Fluid processes and elemental mobility during exhumation in a cold subduction zone. Lithos 136-139: 168 – 186.

Mallman G, O'Neill H St. C. (2009) The Crystal/Melt Partitioning of V during Mantle Melting as a Function of Oxygen Fugacity Compared with some other Elements (Al, P, Ca, Sc, Ti, Cr, Fe, Ga, Y, Zr, and Nb). Journal of Petrology 50: 1765 – 1794.

Manning CE (2004) The chemistry of subduction-zone fluids. Earth and Planetary Science Letters 223: 1 – 16.

Martin LAJ, Rubatto D, Vitale Brovarone A, Hermann J (2011) Late Eocene lawsonite-eclogite facies metasomatism of a granulite sliver associated to ophiolites in Alpine Corsica. Lithos 125: 620 – 640.

Martin LAJ, Hermann J, Gauthiez-Putallaz L, Whitney DL, Vitale Brovarone A, Fornash KF, Evans NJ (2014) Lawsonite geochemistry and stability – implication for trace element and water cycles in subduction zones. Journal of Metamorphic Geology 32: 455 – 487.

Maruyama S, Liou JG (1988) Petrology of Franciscan Metabasites Along the Jadeite-Glaucophane Type Facies Series, Cazadero, California. Journal of Petrology 29: 1 – 37.

McCulloch MT, Gamble AJ (1991) Geochemical and geodynamical constraints on subduction zone magmatism. Earth and Planetary Science Letters 102: 358 – 374.

Meinhold G, Anders B, Kostopoulos D, Reischmann T (2008) Rutile chemistry and thermometry as provenance indicator: an example from Chios Island, Greece. Sedimentary Geology 203: 98- 111.

Mevel C, Kienast JR (1980) Chromian jadeite, phengite, pumpellyite, and lawsonite in a high-pressure metamorphosed gabbro from the French Alps. Mineralogical Magazine 43: 979 – 984.

Min K, Mundil R, Renne PR, Ludwig KR (2000) A test for systematic errors in $^{40}Ar/^{39}Ar$ geochronology through comparison with U/Pb analysis of a 1.1-Ga rhyolite. Geochim Cosmochim Ac 64:73 – 98.

Mookherjee M, Bezacier L (2012) The low velocity layer in subduction zone: structure and elasticity of glaucophane at high pressures. Physics of the Earth and Planetary Interiors 208–209: 50–58.

Mulcahy SR, King RL, Vervoort JD (2009) Lawsonite Lu-Hf geochronology: A new geochronometer for subduction zone processes. Geology 37: 987 – 990.

Mulcahy SR, Vervoort JD, Renne PR (2014) Dating subduction-zone metamorphism with combined garnet and lawsonite Lu-Hf geochronology. Journal of Metamorphic Geology 32: 515-533.

Mulch A, Cosca MA, Handy MR (2002) In-situ UV-laser $^{40}Ar/^{39}Ar$ geochronology of a micaceous mylonite: an example of defect-enhanced argon loss. Contrib Mineral Petr 142: 738 – 752.

Nelson BK (1991) Sediment-derived fluids in subduction zones: Isotopic evidence from veins in blueschist and eclogite of the Franciscan Complex, California. Geology 19: 1033 – 1036.

Obara K (2002) Nonvolcanic deep tremor associated with subduction in southwest Japan. Science 296: 1679 – 1681.

Och DJ, Leitch EC, Caprarelli G, Watanabe T (2003) Blueschist and eclogite in tectonic mélange, Port Macquarie, New South Wales, Australia. Mineralogical Magazine 67: 609 – 624.

Okay AI (1980) Mineralogy, petrology and phase relations of glaucophane-lawsonite zone blueschist from the Tavşanlı region, north-west Turkey. Contributions to Mineralogy and Petrology 72: 243- 255.

Okay AI (1984) Distribution and characteristics of the northwest Turkish blueschist. In: The Geological Evolution of the Eastern Mediterranean, Special Publication 17 (eds Dixon, J.E. & Robertson, A.H.F.), pp. 455 – 466. Geological Society, London.

Okay AI (1986) High-pressure/low-temperature metamorphic rocks of Turkey. In: Blueschists and Eclogites (eds Evans, B.W. & Brown, E.H.), Geological Society of America Memoir 164: 333- 347.

Okay AI, Kelley SP (1994) Tectonic setting, petrology and geochronology of jadeite + glaucophane and chloritoid + glaucophane schists from northwest Turkey. Journal of Metamorphic Geology 12: 455 – 466.

Okay AI (1998) Exhumation of blueschists along a Tethyan suture in northwest Turkey. Tectonophysics 285: 275 – 299.

Okay AI (2002) Jadeite-chloritoid-glaucophane-lawsonite blueschists in northwest Turkey: unusually high P/T ratios in continental crust. Journal of Metamorphic Geology 20: 757 – 768.

Okay AI, Whitney DL (2010) Blueschists, eclogites, ophiolites and suture zones in northwest Turkey: A review and a field excursion guide. Ofioliti 35: 131 – 172.

Önen AP, Hall R (2000) Sub-ophiolite metamorphic rocks from NW Anatolia, Turkey. J Metamorph Geol 18:483 – 495.

Önen AP (2003) Neotethyan ophiolitic rocks of the Anatolides of NW Turkey and comparison with Tauride ophiolites. Journal of the Geological Society 160: 947 – 962.

Passchier CW, Trouw RAJ (2005) Microtectonics. Berlin, Springer Verlag, 366 p., doi:10.1007/3-540-29359-0.

Paton C, Hellstrom J, Paul B, Woodhead J, Hergt J (2011) Iolite: Freeware for the visualization and processing of mass spectrometric data. Journal of Analytical Atomic Spectrometry 26: 2508 – 2518.

Pawley AR (1994) The pressure and temperature stability limits of lawsonite: implications for H_2O recycling in subduction zones. Contributions to Mineralogy and Petrology 118: 99 – 108.

Peacock SM (2001) Are the lower planes of double seismic zones caused by serpentinite dehydration in subducting oceanic mantle? Geology 29: 299 – 302.

Pfander JA, Munker C, Stracke A, Mezger K (2007) Nb/Ta and Zr/Hf in ocean island basalts – Implications for crust-mantle differentiation and the fate of Niobium. Earth and Planetary Science Letters 254: 158 – 172.

Philippot P, Selverstone J (1991) Trace Element-rich Brines in Eclogitic Veins – Implications for Fluid Composition and Transport During Subduction. Contributions to Mineralogy and Petrology 106: 417 – 430.

Plank T (2014) The Chemical Composition of Subducting Sediments. Treatise on Geochemistry 4: 607 – 629.

Plunder A, Agard P, Chopin C, Okay AI (2013) Geodynamics of the Tavşanlı Zone, western Turkey: Insights into subduction/obduction processes. Tectonophysics 608: 884 – 903.

Plunder A, Agard P, Chopin C, Pourteau A, Okay AI (2015) Accretion, underplating and exhumation along a subduction interface: From subduction initiation to continental subduction (Tavşanlı zone, W. Turkey). Lithos: http://dx.doi.org/10.1016/j.lithos.2015.01.007.

Pognante U (1991) Petrological Constraints on the Eclogite-Facies and Blueschist-Facies Metamorphism and P-T-T Paths in the Western Alps. Journal of Metamorphic Geology 9: 5 – 17.

Poli S, Schmidt MW (1995) H2O transport and release in subduction zones: Experimental constraints on basaltic and andesitic systems. Journal of Geophysical Research 100:22,299 – 22, 314.

Pourteau, A., Scherer E. E., Schmidt, A., Bast, R., 2014. Internal P-T-t Structure of Subduction Complexes- Insights from Lu-Hf Geochronology on Garnet and Lawsonite (Halilbağı, Central Anatolia). Abstract #V24C-02 presented at 2014 Fall Meeting, AGU, San Francisco, Calif., 15 -19 Dec.

Putlitz B, Cosca MA, Schumacher JC (2005) Prograde mica $^{40}Ar/^{39}Ar$ growth ages recorded in high pressure rocks (Syros, Cyclades, Greece). Chem Geol 214:79- 98.

Rapp JF, Klemme S, Bulter IB, Harley SL (2010) Extremely high solubility of rutile in chloride and fluoride-bearing metamorphic fluids: An experimental investigation. Geology 38: 323 – 326.

Reddy SM, Kelley SP, Wheeler J (1996) A $^{40}Ar/^{39}Ar$ laser probe study of micas from the Sesia Zone, Italian Alps: implications for metamorphic and deformation histories. J Metamorph Geol 14:493 – 508.

Reynard B, Bass JD (2014) Elasticity of lawsonite and seismological signature of metamorphism and water cycling in the subducting oceanic crust. Journal of Metamorphic Geology 32: 479 – 487.

Rubatto D, Hermann J (2003) Zircon formation during fluid circulation in eclogites (Monviso, Western Alps): implications for Zr and Hf budget in subduction zones. Geochimica et Cosmochimica Acta 67: 2173 – 2187.

Rubatto D, Angiboust S (2015) Oxygen isotope record of oceanic and high-pressure metasomatism: a P-T-time-fluid path for the Monviso eclogites (Italy). Contributions to Mineralogy and Petrology 170:doi:10.1007/s00410-015-1198-4.

Ruffet G, Feraud G, Balevre M, Kienast J-R (1995) Plateau ages and excess argon in phengites: an 40Ar-39Ar laser probe study of Alpine micas (Sesia Zone, Western Alps, northern Italy). Chem Geol 121:327 – 343.

Ruffet G, Gruau G, Ballevre M, Feraud G, Philippot P (1997) Rb-Sr and 40Ar-39Ar laser probe dating of high-pressure phengites from the Sesia Zone (Western Alps): underscoring of excess argon and new age constraints on the high-pressure metamorphism. Chem Geol 141:1 – 18.

Scaillet S, Feraud F, Ballevre M, Amouric M (1992) Mg/Fe and [(Mg,Fe)Si-Al_2] compositional control on argon behavior in high-pressure white micas: A $^{40}Ar/^{39}Ar$

continuous laser-probe study from the Dora-Maira nappe of the internal western Alps, Italy. Geochim Cosmochim Ac 56:2851 – 2872.

Scaillet S (1996) Excess ^{40}Ar transport scale and mechanism in high-pressure phengites: A case study from an eclogitized metabasite of the Dora-Maira nappe, western Alps. Geochim Cosmochim Ac 60:1075 - 1090.

Scambelluri M, Philippot P (2001) Deep fluids in subduction zones. Lithos 55: 213 – 227.

Schmidt MW, Poli S (1994) The stability of lawsonite and zoisite at high pressures: Experiments in CASH to 92 kbar and implications for the presence of hydrous phases in subducted lithosphere. Earth and Planetary Science Letters 124: 105 – 118.

Schmidt MW, Poli S (1998) Experimentally based water budgets for dehydrating slabs and consequences for arc magma generation. Earth and Planetary Science letters 163: 361 – 379.

Seaton NCA, Whitney DL, Teyssier C, Toraman E, Heizler M (2009) Recrystallization of high-pressure marble (Sivrihisar, Turkey). Tectonophysics 479: 241 – 253.

Seaton NCA, Teyssier C, Whitney DL, Heizler MT (2014) Quartzite and calcite microfabric transitions in a pressure and temperature gradient, Sivrihisar, Turkey. Geodinamica Acta 26: 191 – 206.

Selverstone J, Franz G, Thomas S, Getty S (1992) Fluid variability in 2 GPa eclogites as an indicator of fluid behavior during subduction. Contributions to Mineralogy and Petrology 112: 341 – 357.

Seno T, Yamasaki T (2003) Low-frequency tremors, intraslab and interpolate earthquakes in Southwest Japan-from a viewpoint of slab dehydration. Geophysical Research Letters 30: doi:10.1029/2003GL018349.

Sherlock S, Kelley S, Inger S, Harris N, Okay A (1999) ^{40}Ar-^{39}Ar and Rb-Sr geochronology of high-pressure metamorphism and exhumation history of the Tavşanlı Zone, NW Turkey. Contributions to Mineralogy and Petrology 137:46 – 58.

Sherlock SC, Okay AI (1999) Oscillatory zoned chrome lawsonite in the Tavşanlı Zone, northwest Turkey. Mineralogical Magazine 63: 687 – 692.

Shin TA, Catlos EJ, Jacob L, Black K (2012) Relationships between very high pressure subduction complex assemblages and intrusive granitoids in the Tavşanlı Zone, Sivrihisar Massif, central Anatolia. Tectonophysics 595:183 – 197.

Smye AJ, Warren CJ, Bickle MJ (2013) The signature of devolatisation: Extraneous ^{40}Ar systematics in high-pressure metamorphic rocks. Geochim Cosmochim Ac 113:94 – 112.

Spandler C, Hermann J, Arculus R, Mavrogenes J (2003) Redistribution of trace elements during prograde metamorphism from lawsonite blueschist to eclogite facies; implications for deep subduction-zone processes. Contributions to Mineralogy and Petrology 146: 205 – 222.

Spandler C, Hermann J (2006) High-pressure veins in eclogite from New Caledonia and their significance for fluid migration in subduction zones. Lithos 89: 135 – 153.

Spandler C, Pettke T, Rubatto D (2011) Internal and External Fluid Sources for Eclogite-facies Veins in the Monviso Meta-ophiolite, Western Alps: Implications for Fluid Flow in Subduction Zones. Journal of Petrology 52: 1207 – 1236.

Spandler C, Pirard C (2013) Element recycling from subducting slabs to arc crust: A review. Lithos 170: 208 – 223.

Sun SS, McDonough WF (1989) Chemical and isotopic systematic of oceanic basalts; implications for mantle composition and processes. In: Saunders, A.D., Norry, M.J., (Eds.), Magmatism in the Ocean Basins. Special Publications of the Geological Society of London, vol. 42, pp. 313 – 345.

Syracuse EM, van Keken PE, Abers GA (2010) The global range of subduction zone thermal models. Physics of the Earth and Planetary Interiors 183: 73 – 90.

Teyssier C, Whitney DL, Toraman E, Seaton NCA (2010) Lawsonite vorticity and subduction kinematics. Geology 38:1123-1126.

Trail D, Watson EB, Tailby ND (2012) Ce and Eu anomalies in zircon as proxies for the oxidation state of magmas. Geochimica et Cosmochimica Acta 97: 70 – 87.

Tribuzio R, Messiga B, Vannucci R, Bottazzi P (1996) Rare earth element redistribution during high-pressure – low-temperature metamorphism in ophiolitic Fe-gabbros (Liguria, northwestern Italy): Implications for light REE mobility in subduction zones. Geology 24: 711 – 714.

Triebold S, von Eynatten H, Luvizotto GL, Zack T (2007) Deducing source rock lithology from detrital rutile geochemistry: an example from the Erzgebirge, Germany. Chemical Geology 244: 421 – 436.

Tsujimori T, Sisson VB, Liou JG, Harlow GE, Sorensen SS (2006) Very-low-temperature record of the subduction process: A review of worldwide lawsonite eclogites. Lithos 92: 609 – 624.

Tsujimori T, Ernst WG (2014) Lawsonite blueschists and lawsonite eclogites as proxies for palaeo-subduction zone processes: a review. Journal of Metamorphic Geology 32: 455 – 478.

Ueno T (1999) REE-bearing sector-zoned lawsonite in the Sanbagawa politic schists of the eastern Kii Peninsula, central Japan. European Journal of Mineralogy 11: 993 – 998.

Usui T, Nakamura E, and Helmstaedt H (2006) Petrology and geochemistry of eclogite xenoliths from the Colorado Plateau: implications for the evolution of subducted oceanic crust. Journal of Petrology 47: 929-964.

Van der Straaten F, Schenk V, John T, Gao J (2008) Blueschist-facies rehydration of eclogites (Tian Shan, NW-China): Implications for fluid-rock interaction in the subduction channel. Chemical Geology 255: 195 – 219.

Van Keken PE, Hacker BR, Syracuse EM, Abers GA (2011) Subduction factory: 4. Depth dependent flux of H2O from subducting slabs worldwide. Journal of Geophysical Resarch 116:B01401, doi:10.1029/2010JB007922.

Vitale Brovarone A, Groppo C, Hetenyi G, Compagnoni R, Malavielle J (2011) Coexistence of lawsonite-bearing eclogite and blueschist: Phase equilibria modelling of Alpine Corsica metabasalts and petrological evolution of subducting slabs. Journal of Metamorphic Geology 29: 583 – 600.

Vitale Brovarone A, Herwartz D (2013) Timing of HP metamorphism in the Schistes Lustres of Alpine Corsica: New Lu-Hf garnet and lawsonite ages. Lithos 172 – 173: 175 – 191.

Vitale Brovarone A, Alard O, Beyssac O, Martin L, Picatto M (2014) Lawsonite metasomatism and trace element recycling in subduction zones. Journal of Metamorphic Geology 32: 489 – 514.

Wada I, Wang K, He J, Hyndman RD (2008) Weakening of the subduction interface and its effects on surface heat flow, slab dehydration, and mantle wedge serpentinization. Journal of Geophysical Research 113: doi:10.1029/2007JB005190.

Wada I, Wang K (2009) Common depth of slab-mantle decoupling: Reconciling diversity and uniformity of subduction zones. Geochemistry Geophysics Geosystems 10: doi:10.1029/2009GC002570.

Warren CJ, Sherlock SC, Kelley SP (2011) Interpreting high-pressure phengite $^{40}Ar/^{39}Ar$ laserprobe ages: an example from Saih Hatat, NE Oman. Contrib Mineral Petr 161:991 – 1009.

Warren CJ, Smye AJ, Kelley SP, Sherlock SC (2012a) Using white mica $^{40}Ar/^{39}Ar$ data as a tracer for fluid flow and permeability under high-P conditions: Tauern Window, Eastern Alps. J Metamorph Geol 30:63 – 80.

Warren CJ, Hanke F, Kelley SP (2012b) When can muscovite $^{40}Ar/^{39}Ar$ dating constrain the timing of metamorphic exhumation? Chem Geol 291:79- 86.

Wei CJ, Clarke GL (2011) Calculated phase equilibria for MORB compositions: a reappraisal of the metamorphic evolution of lawsonite eclogite. Journal of Metamorphic Geology 29: 939 – 952.

Whitney DL (2002) Coexisting andalusite, kyanite, and sillimanite: Sequential formation of three Al2SiO5 polymorphs during progressive metamorphism near the triple point, Sivrihisar, Turkey. American Mineralogist 87:405 – 416.

Whitney DL, Davis PB (2006) Why is lawsonite eclogite so rare? Metamorphism and preservation of lawsonite eclogite, Sivrihisar, Turkey. Geology 34:473-476.

Whitney DL, Evans BW (2010) Abbreviations for names of rock-forming minerals. American Mineralogist 95: 185 – 187.

Whitney DL, Teyssier C, Toraman E, Seaton NCA, Fayon AK (2011) Metamorphic and tectonic evolution of a structurally continuous blueschist-to-Barrovian terrane, Sivrihisar Massif, Turkey. Journal of Metamorphic Geology 29:193 – 212.

Whitney DL, Teyssier C, Seaton NCA, Fornash KF (2014) Petrofabrics of high-pressure rocks exhumed at the slab-mantle interface from the 'point of no return' in an oceanic subduction zone (Sivrihisar, Turkey). Tectonics 33:2315-2341, doi: 10/1002/2014TC003677.

Widmer T, Ganguin J, Thomson AB (2000) Ocean floor hydrothermal veins in eclogite facies rocks of the Zermatt-Saas Zone, Switzerland. Schweizerische mineralogische und petrographische Mitteilungen 80: 63 – 73.

Wijbrans JR, McDougall I (1986) $^{40}Ar/^{39}Ar$ dating of white micas from an Alpine high-pressure metamorphic belt on Naxos (Greece): the resetting of the argon isotopic system. Contrib Mineral Petr 93:187 – 194.

Woodhead JD, Hellstrom J, Hergt JM, Grieg A, Maas R (2007) Isotopic and elemental imaging of geological materials by laser ablation inductively coupled plasma-mass spectrometry. Geostandards and Geoanalytical Research 31: 331 – 343.

Wu YB, Gao S, Zhang HF, Yang SH, Liu XC, Jiao WF, Liu YS, Yuan HL, Gong HJ, He MC (2009) U-Pb age, trace-element, and Hf-isotope compositions of zircon in a quartz vein from eclogite in the western Dabie Mountains: Constraints on fluid flow during early exhumation of ultra high-pressure rocks. American Mineralogist 94: 303 – 312.

Xiao Y, Niu Y, Song S, Davidson J, Liu X (2013) Elemental responses to subduction-zone metamorphism: Constraints from the North Qilian Mountain, NW China. Lithos 160 – 161: 55 - 67.

Zack T, Kronz A, Foley SF, Rivers T (2002) Trace element abundances in rutiles from eclogites and associated garnet mica schists. Chemical Geology 184: 97 – 122.

Zack T, von Eynatten H, Kronz A (2004) Rutile geochemistry and its potential use in quantitative provenance studies. Sedimentary Geology 171: 37 – 58.

Zack T, Rivers T, Brumm R, Kronz A (2004) Cold subduction of oceanic crust: Implications from a lawsonite eclogite from the Dominican Republic. European Journal of Mineralogy 16: 909 – 916.

Zack T, John, T (2007) An evaluation of reactive fluid flow and trace element mobility in subducting slabs. Chemical Geology 239: 199- 216.

Zack TA (2013) Cold slab-mantle interface: constraints from exceptionally well preserved lawsonite eclogites. Mineralogical Magazine 77:2574.

Zheng J, Meng F (2006) Lawsonite-bearing eclogites in the north Qilian and north Altyn Tagh: Evidence for cold subduction of oceanic crust. Chinese Science Bulletin 51: 1238 – 1244.